

DYNAMIC ENHANCED RECOVERY TECHNOLOGIES
CLASS I

Final Report
Part I

July 1994 - October 1995

By
Roger N. Anderson

Performed Under Contract No. DE-FC22-93BC14961

Columbia University New York, New York

**National Petroleum Technology Office
U. S. Department Of Energy
Tulsa, Oklahoma**

DISCLAIMER

This report was prepared as an account of work sponsored by an agency of the United States Government. Neither the United States Government nor any agency thereof, nor any of their employees, makes any warranty, expressed or implied, or assumes any legal liability or responsibility for the accuracy, completeness, or usefulness of any information, apparatus, product, or process disclosed, or represents that its use would not infringe privately owned rights. Reference herein to any specific commercial product, process, or service by trade name, trademark, manufacturer, or otherwise does not necessarily constitute or imply its endorsement, recommendation, or favoring by the United States Government or any agency thereof. The views and opinions of authors expressed herein do not necessarily state or reflect those of the United States Government.

This report has been edited and reduced in length to meet the requirements of publication. The original report was submitted as required in 1996. Many of the original illustrations and formulas were insufficiently clear to be reproduced in electronic format. A separate file of related figures is added to replace the figures deleted from the text. Editing was done through NPTO in 1999-2000.

**Dynamic Enhanced Recovery Technologies
Class I**

By
Roger N. Anderson

Work Performed Under Contract No. DE-FC22-93BC14961

Prepared for
U.S. Department of Energy
Assistant Secretary for Fossil Energy

Chandra Nautiyal, Technology Manager National Petroleum Technology Office
P.O. Box 3628 Tulsa, OK 74101

Prepared by:
Columbia University New York, NY 10021
Edited by:
National Petroleum Technology Office

ABSTRACT

We chose the Eugene Island 330 field for our oil migration study because it is the largest Pleistocene oil field in the world, it is geologically well-characterized, and most importantly, it shows a variety of indications of geologically recent hydrocarbon migration (Holland et al, 1990 and Whelan et al, 1994). The Eugene Island 330 Field is a typical Gulf of Mexico mini-basin (Alexander and Flemings, 1994). Structurally, a regional growth-fault system (the "Red Fault Zone") forms the northern boundary of alternating sequences of Plio-Pleistocene sands and shales overlying deep-water turbidities and basin-floor fan deposits from the ancestral Mississippi River delta. As the Red Fault Zone accommodated extension toward the deep-water Gulf of Mexico, the sediments in the depobasin formed rollover anticlines that are now filled with oil and gas. Extension was caused by withdrawal to the south of an extensive salt sill initially present near the surface of the mini-basin from 6 to at least 2.2 Ma (Rowan, Weimer and Flemings 1994). A counter-regional, down-to-the-north fault zone forms the southern boundary of the mini-basin. A thick shale sequence separates the shallow-water shelf sands from geopressured, deep-water deposits (Alexander and Flemings, 1994). Remnant salt feeder stocks and remobilized salt diapirs bound the mini-basin, exclusively upthrown to the bounding fault system. The deep turbidities are still geopressured (He and Anderson, 1994), even after the removal of the impermeable salt seal, because high sedimentation rates combined with the thick, deepwater shale accumulations in the Pliocene resulted in rapid burial and permeabilities too low for the excess pore fluids to escape (Mello, et al, 1994).

Migration of hydrocarbons is occurring today in the Eugene Island 330 Field (Anderson, et al, 1993). Seeps are active at the sea floor outcrop of the Red Fault Zone system. Oil and gas are being produced in reservoirs as young as 400,000-years-old beneath these seeps. Geochemical monitoring over the last twenty years has recorded temporal changes in the composition of the oils being produced from the shallow reservoirs; these changes may reflect recent injection of wet gas and gasolines (Whelan, et al, 1994). Also, biodegraded oils have been replaced by less biodegraded oils over time in the shallowest reservoirs.

Executive Summary

Task One - Management Start-Up
Roger N. Anderson - Task Manager

OBJECTIVE:

The purpose of this task was to equip the project with staff and resources (computer and otherwise) to accomplish the other 6 tasks of this project; to negotiate contracts with several industry and university subcontractors to achieve the task objectives; and to initiate the technology transfer to industry and the public from the very beginning of this project

Task Two - Database Management
Roger N. Anderson - Task Manager

OBJECTIVE:

The objectives of this task were to accumulate, archive, and disseminate the geological information available within the area of research of this project; networked database creation, generation of new seismic interpretation with high-tech software, and real-time visualization of the on-line database

SUMMARY:

Fluid-Flow Monitoring Using Industry Multiple 3-D Seismic Data Sets has been one of the outstanding new discoveries of the project. We have developed and submitted a patent for 4-D seismic processing software that can recognize amplitude and impedance changes caused by the addition and subtraction of oil and gas from reservoirs over time intervals as short as a few years. The technique has been developed using the 1992 Shell/Exxon data set (received in December 1994) with two previously acquired 3-D seismic surveys, the Texaco/Chevron data set (acquired in 1988) and the Pennzoil et al data set (acquired in 1985). This DOE project is one of the first Case Histories of 4-D seismic reservoir monitoring in the oil industry.

Liqing Xu developed the LDEO 4-D Software as a set of AVS modules that are networked to form a 4-D package library. He has written, modLFied, debugged and mounted more than 100,000 lines of code that form the AVS modules making up the code. He worked out the 4-D imaging and visualization requirements, and has completed a new 4-D software homepage.

Houston in October 1995. LDEO 4-D Software is copyrighted by Columbia University in the City of New York, and ownership remains with Columbia University, for whom a United States Letters Patent is pending.

Task Three - Field Demonstration Experiment
Roger N. Anderson - Task Manager

OBJECTIVE:

Task three drilled one well extension to test the Dynamic Enhanced Recovery Technologies objectives of this project. In November and December, 1993, we drilled into the fault zone in Eugene Island Block 330 (A20-ST) and performed the following experiments: whole coring, wireline logging, sidewall coring, formation pressure tests, stress tests, completion with frac-pack, flow test and pressure transient test.

SUMMARY:

The A-20ST, Pathfinder well was drilled by Pennzoil Exploration and Production Co., on behalf of partners Exxon, Mobil and Cockrell, into the 01-4 reservoir just above the "Red" growth fault zone that forms the northern boundary of the Eugene Island 330 minibasin. The well was then extended across the fault zone and into the footwall. The GBRN Field Demonstration Project consisted of three phases: whole coring, extensive logging, and stress and production testing in the Pathfinder extension. Measurements were made to determine in situ conditions within and surrounding the fault zone and to test the hypothesis that hydrocarbons could be produced from a fault zone.

We found and sampled oil and gas from silty shales within the fault zone and discovered that the oils have similar chemistry to those being produced from the reservoirs directly above the fault zone. Whole coring revealed that faulting and fracturing extended at least 350 feet into the shales of the upthrown block. Many of the faults and fractures contained oil. Hydrocarbons would not flow at economically viable rates during drill-stem tests. The larger the drawdown pressure applied across the perforations, the lower the permeability of the fault zone became.

Where the A-20ST crossed the fault zone, the horizontal closure stress was 500 psi greater than the fluid pressure. An increase in the pore pressure of 500 psi was then found to induce significant permeability within the fault zone.

A related well, the A-10ST, was drilled into the fault zone in Eugene Island 330 in October, 1993, in anticipation of the Pathfinder well. In contrast to the "tight" fault encountered in the Pathfinder well, fluids flowed strongly when the fault zone was penetrated by the shallower A-10ST well. Fluid flow within the high-pressured fault zone was sufficient to cause differential sticking and the loss of two bottom-hole assemblies in the well. A pulsed-neutron, Thermal Decay Time log run through the stuck drillpipe recorded increased gamma ray radiation from oxygen activation indicating that water was flowing at rates of up to 700 barrels/day within the fault zone.

Task Four - Reservoir Characterization
Peter Flemings - Task Manager

OBJECTIVE:

The purpose of this task was to integrate the geological and geophysical data to construct the minibasin and reservoir models in the Eugene Island 330 Area in order to understand the hydrodynamics of the minibasins. The minibasins are analyzed through stratigraphic interpretation, salt analysis, pressure and temperature mapping. Temporal seismic amplitude analysis is to monitor the dynamic changes occurred in the reservoir.

SUMMARY:

Though the final year of the project we continued to acquire important data for the 330 field. These included: 1) complete wire- line data for Blocks 338 and 339 (donated by Texaco), 2) fracture completion data, and leak off data for Blocks 330, 338, and 339, and 3) The entire 316 A-12 core (now housed in the Penn State Core Repository) which was recently drilled by Pennzoil.

Task Five - Modeling
Larry Cathles - Task Manager

OBJECTIVE:

The objectives of the modeling task: (1) the cause of pressure, temperature, fluid chemical, and porosity anomalies near the Red Fault; (2) the possible sources of oil and gas moving up the fault; and (3) the causes of organic and inorganic chemical alteration near the fault.

Particular attention was to be focused on: (1) porosity and excess pressure development in the RVE, (2) hydrocarbon maturation (3) detailed fluid flow near the fault focusing on the detailed distribution of high permeability sands, (4) the effects of salt diapirism on subsurface temperatures, (5) the effects of fault movement on fault permeability and fluid venting out of the fault (6) the effects of gas venting on oil migration, (7) the transport of oil as a separate phase up the fault, and (8) the effects of fluid flow (water, gas, and oil) on rock chemistry and mineralogy. The modeling was to be carried out in 3-D as well as 2-D.

No computer software existed that was adequate to these tasks. In collaboration with Computational Mechanics Corp. of Knoxville, Tennessee, we developed a basin modeling system capable of investigating the highly coupled phenomena associated with hydrocarbon migration up the Red Fault of the South Eugene Island minibasin, and applied that modeling system to the geologic data collected.

The AKCESS.BASIN Modeling System was developed and applied to the South Eugene Island (SEI) Block 330 region. Preparation of the geologic data in a fashion that takes account of diapirism, overpressuring, and faulting in three dimensions, proved far more difficult and time

consuming than we had anticipated. Substantial effort was also devoted to developing algorithms that accurately describe critical parameters such as thermal conductivity and permeability in the data cube. A powerful modeling capability has been created that is supported by a private company and a growing group of academics spread over five separate institutions.

SUMMARY:

The principal accomplishments to date under this proposal are:

1. Development of a 3-D finite element basin modeling system with sound and fully articulated fundamentals, and accurate algorithms for thermal conductivity and sand permeability. It provides for easy input of highly detailed three-dimensional geologic data with options to infer salt diapirism from the surface pattern of sedimentation and sea level. It takes into account all major physical and chemical phenomena (e.g., isostasy, salt diapirism, faulting, overpressuring, seals, hydrocarbon maturation, fluid flow driven by haline or thermal convection, water table topography, or overpressuring, salt dissolution and transport, etc.). It solves the coupled equations with an easy to use, but versatile and controllable finite element solver, which can execute rapidly on parallel machines. It provides convenient and easy to use visualization tools at all stages.
2. Distribution of that modeling system across 5 institutions (Cornell, LSU, Michigan Tech., and Bowling Green) with appropriate training of professionals and students at each.
3. Extensive benchmarking demonstration of the validity of various aspects of the modeling system.
- 4 Application of the Modeling System to eight ~100km long 2-D seismic lines centered on the South Eugene Island Block 330 area of the Gulf of Mexico and one 1200km interpreted N-S section. The history of salt movement over the last 20 Ma inferred directly from sedimentation shows evolution from a salt sheet to multiple minibasins and domes. The domes have a major impact on subsurface temperature (70°C temperature anomalies above and below the salt domes).
5. Construction of highly detailed 3-D data cube in the SEI 330 area resolving all principal sands and their displacement across four NE-SW faults over the last 3.4 Ma. The salt movement inferred from the pattern of sedimentation shows the burial of a local salt sill and its remobilization into the South Eugene Island Block 330 minibasin with the Red Fault at its northern margin.
6. Detailed analysis of bottom hole temperature data shows a positive temperature anomaly of about 5°C below the Pennzoil oil and gas fields roughly along the Red Fault and a negative (-5°C) temperature anomaly above the oil reservoirs. Modeling shows that temperature anomalies of this magnitude or greater will be produced by the insulating hydrocarbon-filled sand reservoirs. Fluid flow could produce the positive anomaly below the reservoirs along the Red Fault, but not the negative anomaly above the reservoirs. This suggests that the present day temperature field in the South Eugene Island Block 330 minibasin is due to thermal conductivity anomalies associated with hydrocarbon reservoirs and not rapid fluid flow.

A variety of data support ongoing filling of the GA sand via rapid injection, and high fluid flux in the fault zone in the past. Repeated sampling of wells over a period of 10 years has led to the finding that unbiodegraded oils are injected into the GA sand on the time scale of years

or less. Biodegradation occurs rapidly there, and the presence of unaltered oil is interpreted to reflect rapid influx from depths at which biodegradation does not take place. A variety of other organic geochemical data corroborate this conclusion. In the A6ST well, which penetrates the main growth fault at a point 1000 feet from the fault intercept in the Pathfinder Well, sediments from within the growth fault are characterized by anomalously high vitrinite reflectances relative to sediments outside the fault, indicating that the fault is locally a paleothermal anomaly. Combined with stable isotopic composition of minerals from the fault in that well, these data support the conclusion that the fault, at least at some locations, acted as a conduit of relatively high-temperature fluids.

The Pathfinder core contains three structurally distinct fault domains only the deepest of which contains oil. Based on structural and geologic data, this deepest domain is concluded to have been the most recently active. Structural and geochemical data indicate the other two fault domains were active prior to oil migration. The oil-barren domains contain fractures that are favorably oriented to transmit oil, and oil is furthermore present in sands in these domains. It is evident that fault zone oil migration took place only within that part of the fault that was active during the time migratable oil was available to the fault. Despite the variability of hydrogeologic characteristics of faults as evident in the core, the geochemical data indicate that none of these cored faults transmitted significant amounts of fluid in the Pathfinder well. The same fault in the A6ST well has apparently acted as a fluid conduit, indicating relatively short-range lateral variability in fluid flow behavior in the fault.

Task Seven - Technology Transfer
Roger N. Anderson - Task Manager

OBJECTIVE:

The purpose of this task was to integrate the results into one comprehensive perspective of the project's objectives and to transfer the results to industry. We made special efforts to patent and license technology developed as part of this project so that it would become commercially available to the oil industry. We commissioned a study using the United States Geological Survey's fractal oil and gas reserves techniques to identify whether we were dealing with an additional source of oil and gas in the Eugene Island 330 field's recharge-along-faults.

SUMMARY:

The DOE field Demonstration Project "Dynamic Enhanced Recovery Technologies" has spawned important new technologies such as 4-D Seismic Monitoring, resulted in the placement of successful new wells to drain new and bypassed oil and gas in one of the most prolific oil fields in the U.S. offshore, grown into industry-only funding consortia for all its major tasks, and promoted Internet collaboration across institutional boundaries. In addition, there is every prospect that the U.S. Treasury will be repaid many times over for the direct investment of funds into the future of the oil industry in America.

Task Two – Database Management

Software Development

LDEO 4-D Software was developed at Lamont-Doherty Earth Observatory of Columbia University. Software implementation started in 1994. It was initiated on the Global Basin Research Network (GBRN) which is headed by Dr. Roger N. Anderson. LDEO 4-D software was written by Liqing Xu with design input from Wei He and Albert Boulanger.

LDEO 4-D Software has applications to the interpretation of time dependent changes in multiple 3-D seismic surveys acquired over the same subsurface volume at different times to monitor the changes in impedance caused by drainage and migration of hydrocarbons and other subsurface fluids. A United States Letters Patent is pending. LDEO 4-D Software also has modules for seismic data processing, image processing, data interpretation and data visualization in 2-D and 3-D. It is built on top of Advanced Visual Systems, which provides the modular programming environment and basic modules for image display and 3-D rendering. The LDEO 4-D software currently contains more than 100,000 lines of code in the, which cover seismic data input, well log analysis, and horizon data input into AVS. Modules are provided for 4-D seismic data interpretation, horizon extraction and interpretation, volume processing and imaging which form the backbone of the LDEO 4-D software. Because LDEO 4-D Software is built on top of AVS, users can dynamically connect our software modules to create 4-D seismic analysis networks. Each module is small and specifically designed to accomplish one task within the 4-D analysis framework. The LDEO 4-D Software divides major applications into groups of AVS modules which can be either independently executed in stages, or networked together to perform analyses of 4-D Seismic datasets.

The major purpose of the LDEO 4-D Software is to provide a "Quick Look" tool to track changes of seismic amplitude and impedance over the time as hydrocarbon pool drainage proceeds. The LDEO 4-D software modules are designed to extract differences and similarities among multiple generations of 3-D seismic surveys (4-D seismic data). LDEO 4-D Software provides a methodology whereby hydrocarbon migration and drainage pathways and reservoir fluid locations and volumes can be mapped over time.

The LDEO 4-D Software provides all required data processing functions for 4-D analysis, such as amplitude and frequency spectral normalization, seismic attribute computation, and a rich set of data filters. The processing flow of the LDEO 4-D Software proceeds from the rebinning and pre-processing of multiple 3-D seismic data, to procedures for amplitude and frequency normalization, cross correlated to minimize spatial shift and navigation errors. Then each seismic dataset is converted to the seismic attribute domain, and reflection strength, or the amplitude envelope of the seismic signal, is computed for each waveform. The individual 3-D seismic datasets are then grown about seed points of the highest amplitudes within each seismic dataset to obtain volumetric representations of the hydrocarbon reservoirs. Another important part of the LDEO 4-D Software is visualization capabilities to display and recognize the dimouts, amplitude brightening and sustained amplitude regions that delineate drainage, water encroachment, gas cap formation, and most importantly, locations of bypassed pay. LDEO 4-D software provides a rich set of visualization modules such as slicing (orthogonal and arbitrary slicing), volumetric rendering of reservoirs, seismic and well log visualization along wellpaths

(regardless of deviation), multiple horizon slicing, amplitude extraction, horizon visualization, skeleton building, migration pathway manLFolding and 2-D particle flow simulation. All visualization is implemented in real 3-D space, but since we image only within grown regions, the datasets have been downsized for rapid manipulation with standard workstation graphics capabilities. LDEO 4-D Software provides an added set of utility modules to generate print-ready and Internet mountable html output easily.

LDEO 4-D Software contains five basic operations: data loading, data preprocessing, data interpretation, 4-D dLFferencing, and visualization. It provides the ability to multiple 3-D seismic datasets for 4-D drainage and fluid migration changes.

Geological Analyses of Industry 3-D Seismic Surveys

Landmark compared the traditional interpretation of the horizons and faults, and the reinterpreted reflector horizons and faults in Phase I of this project. The reinterpreted geologic data was convened and exported to other databases. Integration of several data sets aided in the reassessment of the drilling location and the field demonstration experiment

Lincoln Fratson has completed the development of an algorithm for well log/time series correlation. Development of a robust, non-parametric correlation statistic for testing and ranking the similarity of any two, related time Series, specifically the well logs from Eugene Island 330, continues. A study of the morphology of the sea floor in the Gulf of Mexico has been completed and published in Geology. In this study, the intraslope basin morphology of the Louisiana slope, which is the evolutionary precursor of the Eugene Island 330 basin, is compared to the morphology of other US continental slopes. The study shows that the Louisiana Slope morphology, though rugged, is flatter and more random at both regional ($>1,500 \text{ km}^2$) and local ($<0.1 \text{ km}^2$) measurement scales than any of the other US continental slopes, which span a range of sedimentary and tectonic setting. The low grade of the Louisiana slope is undoubtedly tied to the allochthonous salt that underlies the region. It is suggested that the salt may not be competent enough to support steep seafloor slopes, and/or, in moving, it may frequently trigger slope re-adjustment through failure. Evidence for the latter are the numerous debris aprons that emanate from the base of the Sigsbee Escarpment where allochthonous salt has been thrusting seaward.

Real-Time Visualization of Database

Reservoir characterization of the LF reservoir in the Eugene bland Block 330 Field of offshore Louis- Gulf of Mexico

The dynamic changes we have observed in the LF reservoir during hydrocarbon production suggest that this reservoir is very complex and internally heterogeneous. We characterize this complexity with a fine-scale reservoir characterization model that describes petrophysical properties such as lithology, porosity, and effective oil saturation.

For many years, reservoir characterization has played an essential role in oil field management. Reservoir simulations are used by geologists and reservoir engineers to optimize and maximize recovery efficiency. Traditionally, only wireline logging data and well production

histories have been used in these characterizations. Consequently, the characterizations are often too smooth due to the lack of lateral resolution. As 3-D seismic imaging has improved, its usefulness in reservoir characterization has increased (Doyen et al., 1992; Martinez et al., 1992 and He et al., 1994). Reservoir characterization has become increasingly accurate and reliable. However, the static reservoir descriptions cannot predict dynamic behavior of hydrocarbon reservoirs under production.

The combination of static reservoir characterization and 4-D seismic monitoring techniques can be used to achieve much more accurate oil field management and higher economic returns (Anderson et al, 1995a and 1995b). We foresee that such a combination involving multiple 3-D seismic datasets will play a more and more important role in future reservoir management and surveillance, and become the industry norm in the near future.

Reservoir characterization can be performed in micro-, meso-, macro-, and megascales depending on data availability. Well logs and surface reflection seismic data are useful for mesoscopic and macroscopic scales (i.e., reservoirs are characterized in terms of bed boundaries, stratification types, lithology and porosity).

The lack of a unified theory that can account for all geophysical and geological observations at different scales severely affects the development of reservoir characterization techniques. Numerous empirical relationships between reservoir petrophysical and acoustic properties have been developed (Archie, 1942; Gardner et al., 1974; Brock, 1984 and Han et al., 1986). These relationships are of limited effectiveness because the correlation between petrophysical properties are imprecise. These *in situ* relationships based on high frequency data (e.g., 10 KHz sonic log and 1 MHz ultrasonic core analysis frequency) are often very inaccurate when applied to lower frequency seismic surveys.

The imprecise relationship between rock lithology and acoustic properties is often a problem when multiple lithologies are present. However, stochastic simulations can be used to assess this ambiguity and to determine the spatial distribution of reservoir properties. The physics behind the use of stochastic simulation is that the petrophysical and acoustic properties (e.g., impedance) made over the same reservoir are closely associated even though they have different frequency bandwidth. These associations can be imaged through cross-correlations between the properties and between the impedance data measured in space.

In this chapter, we present a systematic technique for determining reservoir lithology, porosity, and oil saturation distributions and applied it to the LF reservoir. Our method consists of a combination of well data analysis for lithology determination, spatial cross-correlation computations between lithology and acoustic impedance, and a robust stochastic simulation technique (Deutsch et al, 1992).

We first investigate the lithology distribution within the LF reservoir because lithology is the dominant factor affecting the acoustic impedances. Reservoir lithology interpreted from well log data analysis is assumed to be the most reliable (hard data), while lithology derived from estimated acoustic impedances is assumed to be imprecise (soft data). We used the Markov-Bayes conditional sequential indicator simulation technique to simulate the most probable Lithology distribution of the LF reservoir. This simulation technique integrates the shale volume fractions derived from the 1992 acoustic impedance volume with shale volume fractions derived from the wireline logging data. The porosity and effective oil saturation distributions are then inferred using a time-average equation along with the 3-D lithology model. The likelihood of the

Lithology model of the LF reservoir determines other properties, such as porosity and oil saturation.

Conditional soft indicator simulations

The conditional soft indicator simulation is a stochastic optimization technique, which integrates data from different sources with various probability and confidence levels assigned to produce multiple images of the spatial distribution of an attribute related to these data. The simulated images provide a rich family of characterized attribute distribution with equal probability. When this technique is used to simulate spatial distributions of Lithology using well and seismic data, the estimated Lithology images preserve the spatial statistic of the original well data. In addition, the Lithology images also possess the higher lateral resolution of seismic data.

Uncertainties in an attribute, such as lithology, can be estimated by examining the statistics of an ensemble of estimated images to create probability maps. The simulated stochastic images are globally conditioned to all available information, and also locally conditioned by hard data. The sparse hard data is honored exactly while the soft data has influence in proportion to its degree of uncertainty.

The concept of indicator variables

Many geological properties, such as lithology, permeability and pore fluid pressure, can be simulated as indicator variables because the classification of these parameters tends to be categorical. For instance, the continuous variables, shale volume fraction, can be categorized into sandy and silty regions. The indicator is represented by a binary number that takes the value 0 or 1. The indicator is assigned to be either 0 or 1 depending on the value of the underlying continuous variable. The indicator categorizes the value of the continuous variable. Thus indicator variables have the characteristics of both continuous and categorical variables. Indicator variables are useful when the number of hard data points is too few to produce reasonable statistical simulations of a continuous variable. The concept of indicator variables was introduced, developed and applied to spatial statistics by Switzer (1977), Journel (1982, 1983, 1984 and 1986).

The sequential, conditional, soft indicator simulation

The sequential, conditional indicator simulation is aggressive in practice. Once the lithology indicator at a location is simulated this location is recategorized into the hard indicator and joins the stochastic simulation for the next location, depending upon the physical and statistical analysis of the soft data. In our case, we simulate reservoir lithology using shale volume fraction from wells as hard data and those from impedance as soft data. Minimization only requires knowledge of the spatial autocovariance and cross variance of hard and soft indicators.

The simulations reproduce the indicator means, autocovariances, and cross covariances. The simulated spatial distribution of an indicator variable honors both hard data (directly, as constraint) and soft data (indirectly, through its indicator).

Geological and geophysical logging data analysis in the LF reservoir

Reservoir characterizations are performed in the same area where we have performed the 4-D analysis.

Well log analysis for lithology of the LF reservoir

The lithology of the LF reservoir is first studied using twenty logged wells in the study area. In sand and shale sequences gamma ray (GR) and spontaneous potential (SP) logs are used to calculate the fractional shale volume by using empirical relationships. The well log analysis is then used to derive the hard lithology data of the LF reservoir and its surroundings. Because the spatial cross-correlation plays a very important role in the conditional sequential indicator simulation algorithm, these 20 wells have been chosen very carefully to have a good spatial coverage.

Qualitative description of the LF reservoir

The LF reservoir belongs to a vertically stacked, deltaic sand package (JD~KE-LF sands) deposited during the proximal deltaic phase in the lowstand pro-ding wedge system tract in the EI-330 minibasin (Alexander et al., 1995). Holland et al (1990) used well logs and production data to analyze the overall reservoir properties.

The LF sand is a distributary-mouth bar deposit. The sand progressively thins up-dip and is shaled-out on the crest of the antic line. It is very fine-grained and clean, with a high irreducible water saturation. Unusually low resistivity is observed on resistivity logs. It consists of predominantly quartz with various, but minor amounts of detrital shale. Feldspars and other minerals may constitute as much as 30% of the total rock volume. Hard, unLFormly cemented "streaks" of calcite precipitates, along with authigenic clay, silica, dolomite, and pyrite, are found toward the top of the sand in two cores (Flemings et al., 1996 and Hoover, 1996, personal communication).

As is typical with deltaic sand deposits, the sand bodies of the LF reservoir contain variable shale and other distributed fine-grained compositions that vary spatially. Using well data alone in traditional reservoir characterization, one must interpolate reservoir properties within each reservoir in order to estimate the spatial distributions of these properties. Simple contouring and kriging techniques are used to make the image of the characterized LF reservoir. The LF reservoir is the most prolific oil-producing reservoir in the field. It has excellent water drive support, and a gas cap exists near the structural crest of the EI-330 rollover anticline. The average porosity is about 30%, and the net pay thickness averages about 17 m.

The characterizations of the LF reservoir from well data alone are qualitative. Only ranges of porosity and permeability have been estimated (Holland et al., 1990). These characterizations do not describe spatial variabilities, and cannot satisfy our needs for quantifying the 4-D analysis, because the image is too smooth to capture the true heterogeneity of the reservoir. The addition of 3-D seismic data enables a much more realistic reservoir characterization.

The geometry of the LF reservoir

The estimated 1992 acoustic impedance volume contains the SD, KE and LF reservoirs. This impedance volume is used along with the reservoir lithology derived from well logs within it to characterize the lithology and porosity distributions of the LF reservoir.

The estimated acoustic impedance volume is converted from two-way travelttime to depth

using conversion table created by averaging fourteen sonic logs. The converted acoustic impedance volume is then resampled every 1.5 m. The top and bottom of the LF reservoir in this impedance volume are consistent with the well tops, indicating that the conversion from two way traveltime to depth has been successful.

The thickest part of the LF reservoir is in the center of the study area. There appears to be a thick sand trend running along the north-east to south-west direction, consistent with the interpretation that the LX sand is in a deltaic mouth bar deposit. The map of depth to the top of the LF reservoir based on both seismic and log data has much greater spatial resolution than the map based on log data alone. Dramatic stratigraphic thinning of the SD, KE, and LF sands onto the crest of anticline in the study area is also seen in the east-west cross-section.

The relationship between acoustic impedances and lithology in the LF reservoir

Correlations between lithology, porosity and acoustic impedance are often ambiguous. The classified reservoir lithologies do not always correspond to a particular impedance interval, and impedance ranges of different lithologies often overlap one another. The more the overlap, the greater the ambiguity of direct classification.

The statistical distribution of the extracted acoustic impedance data and the shale volume fraction data differ. Shale volume fraction data has strong bi-modal statistics, while acoustic impedance has a single-modal statistics, but a long-tailed distribution. Empirical relationships between volume fraction and impedance are difficult to justify, given such large difference in their statistics. Even within the narrow specified depth interval (91 m), the relation between the shale volume fraction and acoustic impedance is very poor.

The variogram models estimated from hard and soft data

Variogram is the variance of a random variable with respect to discrete distance increments. The shale volume fractions in the hard data clearly exhibit sand and shale categories. However, the distribution of the soft data does have a long tail at the lower impedance end, which probably corresponds to clean sand saturated with either oil or gas.

The spatial correlation between the hard (shale volume fraction measured by logs) and the derived secondary data (shale volume fractions derived from the estimated acoustic impedance) is quantified using directional semivariograms. Experimental semivariograms of both hard and soft shale volume fractions in the east-west, north-south, and depth directions were computed and correspond to one another. The hard shale volume fractions have much greater spatial variability than the soft data in all three directions. Introduction of the soft data will significantly improve estimates of the spatial distributions of reservoir properties.

We computed semivariograms of the three indicators using both hard and soft data. The observed semivariograms are then approximated by a simple, "spherical" semivariogram model (Deutsch et al., 1992). The hard and soft indicators have similar semivariograms. The maximum correlation length is larger in downdip and along-strike directions, than in the depth direction (152 m corresponds to 15 m). Sand has the least spatial variability with a maximum correlation length (183 m) in the across-strike (down-dip) direction. The variability of shaly sand and sandy shale is twice that of the sand in lateral directions.

Our stochastic simulation is carried out in a finite difference 3-D grid (it is also the 3-D seismic

grid) with dimensions of 134 node points in the downdip direction, 125 node points in the across-strike direction, and 61 node points in the depth direction. The spacing in the down-dip, across-strike, and depth directions are 23 m, 15 m, and 1.5 m, respectively.

The Markov-Bayes calibration of the hard and soft indicators

The Markov-Bayes calibration was performed using the calibration dataset, which contains 1235 collocated hard and soft data pairs. These collocated data pairs give the prior conditioned cumulative frequency table for each class. The table then gives the linear scaling factors that ensure that the probability of random drawing of the realization at each data point is constrained to the collocated hard and soft data calibrations (Kulkarni, 1984). At this time, the shale volume fractions, which are not directly analyzed through the variogram studies, are incorporated implicitly into the simulation.

The simulated lithology distributions of the LF reservoir

Twenty simulations, using four different random seed points, were computed using the conditioned Markov-Bayes calibration table and the spatial semivariogram models. The simulated shale volume fraction realizations are compared with the estimated acoustic impedance distributions in the top, middle, and bottom of the LF reservoir. Remarkable lateral continuity of the simulated sand distributions is observed, even though such lateral continuity is not in either the estimated acoustic impedance or the well data. Similar sand and shale distribution patterns are observed in all twenty simulated images.

Because all the simulated lithologic images exactly honor the hard data, it is difficult to determine which image is the best description of the LF reservoir. We arithmetically average the twenty simulated shale volume fraction distributions to obtain a final estimate of the lithology. We then computed a probability volume that described the probability that the lithology is sand, shaly sand, silty shale, or shale at each point. The LF sand gradually shales out towards the east, as expected. The shale line runs nearly north-south even though the structural contours wrap around the anticline. The thickening of the LF sand reservoir in the center just north of the F fault defines the depocenter. The clean sand distribution shows the greatest discontinuity on the upper slice and the greatest continuity along the middle slice. On the lower slice, clean sands are primarily located in the depocenter.

Analysis of the estimated LF reservoir properties

The net sand thickness of the LF reservoir is computed by multiplying the reservoir thickness by the average sand volume fractions within LF sand interval. The LF sand thins toward the east. A sharp decrease in sand thickness is found in the eastern part of the reservoir along the structural highs. The boundary between significant and insignificant net sand thickness runs north-south, and does not follow the structural contours. By the time the LF sand was deposited, the minibasin had significant relief, and fresh sediments were transported to the depocenter. Modification to the LF sand thickness by the ocean waves was apparently not significant. The cleaner sands are found in the depocenter.

We assess the accuracy of the simulated lithology and porosity distributions by

extracting four cross-sections of simulated shale volume fractions and estimated porosities along four well paths. Excellent correlation between the estimated and between resistivity and the estimated porosity are observed. The spatial consistency between the well logs and the simulated lithology and estimated porosity distributions is thus established. In this sense, we have obtained accurate lithology and porosity volumes that both honor the well logs and estimated acoustic impedances.

Calcite precipitation near the top of the LF reservoir sand in the down-dip direction has been observed both in cores and sonic log measurements (Flemings et al., 1996). The thickness of the cemented sand is less than 5 m. Acoustic velocity and density of this interval tends to be greater than that of the sands without such precipitation, but less than that of surrounding shales. Thus seismic amplitudes observed near the top of the LF reservoir are primarily caused by two interfaces. The interfaces are located between the shale and cemented sand and between the cemented sand and uncemented sand. The calcite precipitation causes velocity of cemented sands to increase. The magnitude of such an increase is about one third to one half of the velocity difference between shale and uncemented sand. The increase of velocity in this zone is also observed in the estimated porosity distribution (low porosity zone), which is consistent with the well log data. The characterized main body of the LF reservoir is not significantly affected by the occurrence of calcite precipitation.

In deriving the porosity, the fluid acoustic impedance was set to saline acoustic impedance. The estimated porosities may thus be considered "effective hydrocarbon saturation" indicators, because the porosities in the areas saturated with oil or gas are overestimated. Thus, the areas of higher porosities in the LF sand are, in fact, areas of high hydrocarbon saturations, enable us to derive a map of effective oil saturation from the estimated porosity volume. Remarkable similarities between the bypassed hydrocarbon map from our 4-D acoustic impedance analysis and the derived effective oil saturation map are observed. This observation substantiates the effectiveness of using acoustic impedance to estimate oil saturation. While the distinct oil and water boundaries have been smeared by the thickness of the LF sand, the map indicates that the thickest oil-saturated sand can be found in the depocenter of the LF reservoir. In the future, we can use the effective oil saturations computed in this way as the soft data and the oil saturations derived from well log and production data as hard data to further simulate the hydrocarbon saturations. These saturations will substantially improve the accuracy of oil field management.

Conclusion

We have presented an integrated method to quantitatively characterize the LF reservoir in the EI-330 Field in terms of lithology, porosity, and effective hydrocarbon saturation. The results show great consistency throughout the LF reservoir and the surrounding shale formations. The constructed lithology models exactly honor the well log data. The porosity model is less accurate than the lithology model because no porosity measurements are available in the study area. Inaccuracy of the estimated porosities is caused primarily by the hydrocarbon saturation in pore spaces. We developed a new concept that uses the discrepancy to locate hydrocarbons. In practice, we have found the Markov-Bayes sequential indicator simulation technique to be powerful and robust. The technique systematically integrates the hard and soft data into a statistically optimized 3-D model.

Reservoir characterization based on the stochastic simulations is of great importance, especially in the integration of legacy 4-D seismic datasets. Multi-disciplinary data, including geological, geophysical, and production data, can all be
 AVS analyzed system, and we dLFference that data set with the Pennzoil and Texaco/Chevron 3-D surveys. We have completed the inversion of the seismic volumes from Shell and Pennzoil and have performed the 4-D analysis of them.

Nonlinear inversion of 4-D seismic datasets in the Eugene Isand Block 330 Field of offshore Louisiana, Gulf of Mexico

Introduction

Parameters derived from seismic reflection data have been used to identify hydrocarbon reservoirs for decades. Variations of seismic amplitude, such as brightspots and flat spots, are associated with oil- or gas-bearing strata. As 3-D seismic technologies merge with the reservoir characterization, acoustic impedances estimated from seismic waveforms are becoming more and more important. Unlike seismic amplitudes, which measure the acoustic impedance variations, the acoustic impedance itself is directly associated with petrophysical properties of sedimentary rocks and the fluids that fill pore spaces. The techniques by which the acoustic impedance are obtained are the bridge connecting reflection seismic data and rock petrophysical properties.

Acoustic impedance volumes estimated from 3-D seismic surveys have only recently begun to be used in reservoir characterization. The nonlinear seismic inversion technique described in Chapter 1 is a robust method of estimating acoustic impedance. It contains features particularly useful for analyzing 4-D (time-lapse 3-D) seismic datasets. The time-variant, dynamic wavelet extraction eliminates the dLFferences caused by most of the post-stack seismic processes applied to the various 3-D seismic datasets used in the 4-D analysis. The low-frequency constraints imposed on the estimated impedance functions can preserve the unchanging nature of the overall regional geological settings. As a result, dynamic changes of reservoir fluids can be imaged.

In this chapter, we have applied our nonlinear seismic inversion technique to two time-lapse 3-D seismic datasets to estimate acoustic impedance volumes in the EI-330 minibasin. The same geological and geophysical constraints derived from well log analysis are incorporated into the nonlinear seismic inversion of both seismic datasets. Both the technique and procedure used to construct the acoustic impedance constraints are presented in detail. Independent estimations of the accuracy and reliability of the estimated acoustic impedance are performed using acoustic well logging data. Our seismic inversion technique is found to be stable and consistent throughout the computation.

Geological background

The Eugene Island (EI) 330 minibasin is located approximately 270 Km southwest of New Orleans, which is one of the most prolific minibasins in the offshore Gulf of Mexico region. The EI-330 minibasin is oblong, approximately 19 Km by 15 Km (11.9 miles by 9.4 miles), and fault-bounded. It sits on a major shelf margin deltaic depocenter of Plio-Pleistocene

age. Hydrocarbons of the EI-330 Field are produced from over twenty-five different Plio-Pleistocene sand reservoirs that are segmented into at least a hundred structural and stratigraphic traps (Holland et al., 1990).

Alexander et al. (1995) suggest that the minibasin evolved in three phases: prodelta, proximal deltaic, and fluvial. In the prodelta phase, bathymal and outer neritic shales and turbidities loaded and mobilized an underlying salt sheet. During the proximal deltaic phase, salt continued to withdraw from beneath the minibasin and lowstand shelf margin deltas deposited large volumes of sediment. Regional growth faults bound the northern margin of the minibasin. Sediment accumulation and fault slip rates were high as thick sequences of deltaic sands were deposited adjacent to the fault system. During the final fluvial phase, salt withdrawal waned, and the creation of accommodation space within the minibasin ceased. The minibasin was filled and lowstands deltaic systems prograded southward (Alexander et al., 1995). Most of the hydrocarbon reservoirs discovered in the EI-330 Field were formed during the second and third phases. The seismic data input to the nonlinear inversion has a time window large enough to include all major sand reservoirs in the study area (0-3 seconds).

4-D seismic datasets: registration and wireline logging database

Since the discovery of the EI-330 Field, more than five hundred wells were drilled to explore and produce this most prolific oil field in offshore US Gulf of Mexico. Well data collected in this area from several oil companies provide substantial control to the inversion and subsequent analyses. In addition to extensive 2-D seismic surveys, three partially overlapping 3-D seismic surveys have been acquired since 1985. Two of the 3-D seismic surveys, acquired in 1985 and 1992 were selected for 4-D analysis. The overlapping area is centered at the Block 330/331 boundary and covers approximately equal amounts of each block. Structurally, this area is situated on the western flank of the Block 330 rollover anticline, which forms the closure trapping hydrocarbons against the northern growth fault system.

Registration of 4-D seismic datasets

To date, no 4-D seismic dataset has been acquired for the expressed purpose of fluid monitoring in the offshore Gulf of Mexico. The 3-D seismic surveys were acquired with different orientations and spacings, and processed with different parameters by different geophysical service companies. Despite these disadvantages, we found that these "legacy" 4-D seismic datasets are sufficiently similar to be used for fluid monitoring purposes.

Legacy 4-D seismic datasets must be properly registered in space and time. Differences between the results of two surveys can be caused by differences in seismic data acquisition and processing as well as by dynamic changes that occur in the reservoirs. Changes caused by data acquisition and processing must be eliminated before hydrodynamic changes can be identified. Difference caused by acquisition in different directions, at different spacing or different cable length, cannot be corrected after stacking and migration have been performed. Fortunately, modern seismic imaging technologies are much better than a decade ago. Differences due to different directions are often small in areas of low subsurface relief such as the Eugene Island Area. Especially helpful: the 1985 3-D survey was re-processed in 1992 using new processing techniques.

The general geology (locations of faults geometry, lithology and porosity) should be in

the same location between the surveys. Indeed, the two 3-D seismic datasets are remarkably similar, at least in regions where no steeply dipping geological structures (salt and large faults) occur. Salt withdrawal structures do occur in our study area, but do not distort the seismic images of the hydrocarbon reservoirs because they are usually deeper. We assume that the dLFferences observed in the stacked and migrated datasets are dominantly affected by hydrocarbon drainage caused by production and different post-stack processing parameters, and not by different acquisition geometry.

The 1985 seismic survey was acquired in the northwest-southeast oriented lines, while the 1992 survey was acquired in north-south lines. The "bin" spacing of the two surveys is also different. A re-gridding process is applied to relocate the two surveys into a common grid before any farther seismic analysis is performed. We use an algorithm that interpolates one three-dimensional mesh into another three-dimensional mesh slice-by-slice in travelttime and orient the 1985 seismic survey onto the 1992 grid. The algorithm computes the areal weights in a moving window in depth, and interpolates new data values into the destination survey coordinates. After the re-gridding process, only data points common to both surveys are preserved, the rest being assigned null values. Seismic sections extracted from these two volumes at the same location from the two volumes are generally similar, although some dLFferences are evident. The loss of high frequency content in seismic data becomes signLFficant in the deeper portion of seismic volumes.

Spectral matching between the two seismic datasets is not necessary in the seismic inversion approach to the analysis of 4-D seismic datasets, unlike 4-D seismic amplitude dLFferencing technologies (Anderson et al., 1995). But phase matching is performed in order to compare the inversion results. Our nonlinear inversion technique is capable of eliminating other post-stack processing artLFfacts using dynamically extracted seismic source functions. However, since the true amplitudes of seismic datasets are unknown, amplitude renormalization must be performed. We first normalize each seismic volume by mapping the histogram of amplitudes onto one another. The normalized seismic traces are rescaled to the proper amplitude by comparing them to synthetic seismograms computed from impedance measurements (i.e., sonic and density logs) from wells in the area. Scaling factors of 0.15 and 0.25 are used for the 1985 and 1992 seismic surveys, respectively. The extracted seismic source functions are normalized to unity so that the reflectivity functions derived from the estimated acoustic impedances are realistic (i.e., within the range of ± 0.15). Normally, Tertiary sedimentary basins filled with sand and shale sequences have seismic amplitudes less than ± 0.3 .

Digital wireline logging database

The nonlinear inversion of seismic data requires a good *a priori* reference model. There are more than seventy wells in our study area overlapped by the two seismic datasets. However, sonic and bulk density logs, which are needed to compute impedance, are only available in fourteen of these wells. The limited sonic data availability may be overcome by using the correlation between sonic and other logs to empirically calculate a "pseudo" sonic log (a common technique in petrophysical analysis). In wells without density logs, we use the inverse Gardner relationship to calculate density logs from measured or estimated sonic logs (Gardner et al., 1976).

Well log analysis for the impedance inversion

The band-limited nature of observed seismic datasets requires that the estimated acoustic impedance functions, i.e., the short-wave length model parameter (Tarantola, 1982 and 1984), should also be within a confined frequency bandwidth in order to have physical meanings. Detailed trend analysis for predicting long-wavelength constraints on impedance is essential. Such constraints derived independently from acoustic measurements in wells not only increase accuracy of the estimated impedance, but also stabilize the iterative seismic inversion (He et al., 1995). The low-frequency impedance constraints derived from well logs are sufficient to allow our nonlinear seismic inversion to converge on true acoustic impedance solutions.

The principles of wireline logging and data interpretation

Geophysical log data are recorded using probes, which are lowered, on the end of a wireline through the drillpipe and into the previously drilled borehole. The depth at which the measurements are made is determined by measuring the length of cable run into the hole. Modern logging technologies can measure many different physical properties. Three major types of log data are in general available for well data analysis: electrical, radioactive, and sonic logs. The well log database in our study area includes natural gamma ray (GR), spontaneous potential (SP), resistivity (RES), induction %WD), bulk density (RHOB), sonic (DT) and caliper (CALI) measurements. Some wells also contain porosity measurements made on sidewall cores.

The natural gamma ray log utilizes a scintillation detector to measure the natural radiation emitted by the rocks surrounding the borehole. The response of the tool is a simple function of the concentration by weight of radioactive materials and the rock density. The average investigation depth into sedimentary formations is about 0.3 m, and actual resolution is 0.15 m. GR is used principally as a sand/shale discriminator since shales contain abundant radioactive minerals such as clays, whereas sandstones do not.

Density is measured by the lithodensity logging tool. A radioactive source is mounted in the tool body, and a bow-spring forces it and a pair of detectors against the borehole wall. The two detectors measure the returned flux of scattered gamma rays in a series of energy bands, which is used to determine formation density (RHOB) and photo-electric factor (PEF). A measure of tool performance based on the energy distribution at the near and far receivers (DRHO) is also provided. The interaction between the gamma ray and electrons in the formation causes Compton scattering. The density logging tool measures electron density directly, and formation density is determined using the fact that in most rock-forming elements atomic weight is roughly twice atomic number. This measurement is almost independent of porosity and can be used as a matrix lithology indicator. The depth of investigation of the lithodensity tool depends on the density of the rock: the higher the density, the lower the penetration. In porous and permeable formations, the density tool does not read deeper than 0.15 m. The vertical resolution is about 0.3 m.

The array induction tool string indirectly measures electrical resistivity and gamma ray "shaliness", which are related to porosity and hydrocarbon content. The array induction tool is a resistivity logging device that provides measurements of spontaneous potential (SP) and resistivity. Resistivity is reported for three different depths (deep, medium, and shallow).

Differences between shallow and deep resistivity measurements can be related to the invasion of drilling fluids into permeable horizons. Resistivity is controlled mainly by the

amount and connectivity of the porosity and the conductivity of the pore fluids, since the solid constituents are orders of magnitude more resistive than pore fluids in most rocks.

Sonic tools are designed to measure the compressional wave velocity of the rock surrounding the borehole. The sonic tool can be thought of as a miniature seismic refraction experiment carried out within the cylindrical borehole. The tool is centered in the hole by means of bowsprings, and contains one or more acoustic sources and receivers. A source emits acoustic waves that are transmitted into the borehole fluid. A refracted compressional wave is generated when the wavefront impinges on the borehole wall. Waves arrive at the receivers at a time, which is linearly proportional to their offset from the source. Compressional wave velocities can be determined by differencing the arrival times at multiple receivers a known distance apart.

The Caliper log measures wellbore diameter, and is run at the top of both array induction and sonic combinations. It is primarily used to indicate "washouts", where other logs may read inaccurately, and to correct logs whose response is sensitive to hole diameter. However, caliper response can also be indicative of lithology. For instance, in zones with swelling clays, hole constrictions are observed where the caliper reads less than the bit size. Variations in hole diameter may correlate with lithologic changes, since hole conditions are in general a consequence of rock properties.

Lithology can be obtained from GR and SF logs. Resistivity and induction logs are used to identify pore fluid composition. Formation porosity is one of the primary physical property measurements made in a wellbore, and direct measurements are made by neutron logging tools. The difference between thermal and epithermal neutron porosity is a measure of the amount of bound water in clay minerals. Since neutron logging tools were not run in most of production wells drilled in the study area, porosities in our wellbores are indirectly derived from sonic, density, and resistivity logs. The relationship between resistivity and porosity has been quantified by "Archie's Law" (Archie, 1942), which relates the resistivity to an inverse power of the porosity. This empirical relationship works reasonably well in the sands found in hydrocarbon reservoirs.

Well log interpretation for nonlinear seismic inversion

The estimated acoustic impedance functions are sampled in travelttime whereas well logs are sampled in depth. We converted logs from depth to two-way travelttime using sonic logs and velocity measured by "checkshot" vertical seismic profiles (VSP). Synthetic seismograms, generated from the sonic logs, are compared with seismic data to verify the depth-time conversion.

Acoustic velocity and density logs estimated from other logs

Empirical relationships between well logs have been widely used in the oil industry for many years. In wells that have only density logs, the pseudo-sonic velocity can be estimated using the Gardner's relationship (Gardner et al., 1974).

Velocity-depth profile varies laterally due to formation structure and stratigraphy. We compensate by adjusting the regressed sand and shale compaction curves according to stratigraphic horizons in our study area. For example, the structure maps of two sand tops (the tops of JD and LF reservoirs) indicate that the sands dip about 20 degrees westwards along the west flank of the EI-330 roll-over anticline. The regressed sand and shale compaction curves are adjusted for the amount of structural uplift at each well location by an amount determined from wells with sonic measurements. The low-frequency trends are consistent with both geological structure, and direct measurements made in neighboring wells. Both the measured and estimated pseudo-sonic logs were then used to compute acoustic impedance logs and to convert logs in depth to logs in two-way traveltime. When no density log is available for a well, the pseudo-density log can be computed from the sonic log by using the inverse Gardner relationship.

Calibrations are performed on wells with full suites of log measurements to determine the constants in the above empirical relationships. Due to the crossover of the sand and shale compaction curves, the sand sections are high-velocity anomalies in the shallow portion of the well (above 1067 m) and are low-velocity anomalies at depth. We can see that the estimated velocity and density logs are very similar to the measured logs. The low-frequency trend in the estimated pseudo-velocity log agrees with the measured trend as well. The relative error between the estimated and measured velocity logs is 6% and that of density logs is 6.7%. The average relative error between the estimated and measured impedance logs is 5.5%. The velocity, density, and acoustic impedance logs are in agreement throughout the depth range, justifying the use of the empirical relationships. These results also indicate that superimposing the regressed low-frequency trend of velocity to the high-frequency velocity variations derived from resistivity and lithology logs is viable. We will also use only the low-frequency impedance functions to constrain the estimation of high-frequency impedance functions.

The seismic section is an arbitrary seismic line extracted from the 1985 seismic survey. Several sand tops identified in well logs show good ties with the corresponding seismic reflectors in traveltime.

A priori acoustic impedance model construction

The nonlinear inversion employs a one-dimensional inversion algorithm. An *a priori* impedance model has to be constructed for each trace of both 3-D seismic surveys. We use impedance logs from twelve wells with sonic and density measurements in the study area to construct the reference impedance model. The acoustic impedance logs from these twelve wells are first analyzed to extract compaction trends at each location. Depth is then converted to two-way traveltime using the velocity logs at each well. We then construct a 3-D impedance model by linearly interpolating these impedance trend curves into the common seismic grid. The interpolated 3-D impedance model contains only the low-frequency trend of the acoustic impedance function. Each vertical trace of this model is then treated as the *a priori* impedance model and the initial model for the corresponding seismic trace. Data and model space covariance functions are also needed to constrain the inversion process, in addition to an *a priori* impedance model. These covariance functions represent uncertainties associated with data and model parameter optimization.

Nonlinear inversion of 4-D seismic datasets

The two seismic datasets are independently inverted with the same *a priori* low-frequency impedance and initial impedance models. The covariance functions that describe uncertainties in estimated impedance functions and the observed seismic traces are treated in the same manner for each seismic trace of both seismic surveys, so the inversion of the two seismic datasets is under a uniform constraints and uncertainties.

Dynamic extraction of seismic source functions

The first step of the full-scale nonlinear seismic inversion is to extract seismic source functions from the observed seismic trace. We dynamically extract a time-variant source function from each seismic trace in the dataset. The time-variant source function actually contains three source functions that are applied to different time windows within the seismic trace. These source functions are determined from a moving-window autocorrelation function computed for each seismic trace, along with assumption that they are zero-phase. These dynamic source functions eliminate data processing artifacts that were introduced by using different processing parameters after the stacking and migration processes. Using the method, the spatial variation of frequency bandwidth of the impedance function in the estimated acoustic impedance volumes are made internally consistent.

Two seismic traces were extracted from the same location of the 1985 and 1992 3-D seismic surveys. The two traces have significant differences in frequency content and shape. The trace from the 1992 survey has the higher data quality, but its frequency content is lower than that of its 1985 counterpart. Frequency segmentation observed in both traces suggests that three seismic source functions are necessary to properly retain the frequency bandwidth of the estimated impedance functions, acting in three distinct time windows (0.1 seconds, 1-2 seconds and 2-3 seconds). Similar behavior is observed in other traces within the surveys, leading us to use three seismic source functions in three time windows for the inversion.

Estimation of impedance volumes from 4-D seismic datasets

We focus on seismic data from 0.9 to 2.8 seconds two-way traveltime. Each seismic trace in these surveys is sampled at 4 ms interval and contains 476 samples. The full-scale nonlinear seismic inversion is applied to each seismic trace of both surveys independently. The similarity in the estimated acoustic impedance volumes is an independent check of the success of the inversion.

The seismic data contain multiple reflections, side reflections, and noise, which affect the quality of the inversion. This contamination is modeled as random noise described by a Gaussian data covariance functions. Uncertainty in the model parameters is also modeled by a Gaussian distribution law. The *a priori* acoustic impedance at each sample location is expressed in terms of a mean and a covariance. The covariance expresses our degree of certainty that the true impedance is close to the *a priori* impedance. We use the low-frequency impedance model derived from well logs in section 2.4.4 as the *a priori* impedance. The variance of the impedance is taken to be about 20% of its mean.

Discussion and conclusion

Like the seismic volumes, the estimated 1985 and 1992 acoustic impedance volumes are in general similar to one another. However, significant small-scale differences, occur. These changes are possibly caused by hydrocarbon production drainage in reservoirs.

Vertical wells drilled in offshore oil fields are rare, most of the wells were drilled with deviations. Thus the best way to compare the estimated impedance functions with the measurements from logs is to use arbitrary impedance cross-sections that follow the deviation pattern of the wells. Excellent match can be seen between the sonic logs and estimated impedance section along the well paths on both sections. The low impedance anomalies are often correlated to the hydrocarbon reservoirs.

There is significant evidence for hydrocarbon drainage from areas of low impedance observed in 1985. In 1992, these regions have matched of both increased impedances and decreased impedances. The increase in acoustic impedance often indicates that reservoir voids, which were occupied by hydrocarbons in 1985, have been replaced by formation brine by 1992 (Anderson et al., 1995).

Accuracy and reliability of estimated impedance volumes

Evaluation of the estimated acoustic impedance volumes is usually difficult to implement because we do not have exact knowledge of the acoustic properties in the entire sediment volume. We analyze the accuracy and reliability of our inversion results by examining the estimated impedances by using sonic, density, GR, and resistivity logs. These well logs are well-correlated to the acoustic impedance, in general. Because the initial and *a priori* impedance models are based on only the low-frequency part of impedance logs, the high-frequency data from those wells constitute independent data.

We plotted the measured impedance log in a vertical well, 331-SH-1, against the estimated acoustic impedance function. The estimated impedance function has the same low-frequency trend as the impedance log. The high-frequency content in the estimated impedance is not as high as that of the impedance log. However, the relative error between the impedance log and the estimated impedance function in well 331_SH_1 is small, only 8.0%. A good linear correlation is observed between the impedance log and the estimated acoustic impedance. Similar results were also obtained from several other logs.

These tests demonstrate that the estimated acoustic impedance volumes are acceptable for use in 4-D and other geological analyses. Although the estimated impedance function has less resolution than the sparsely distributed well logs, the lateral continuity makes the impedance results much more useful.

2 Conclusion

We have developed a full-scale, nonlinear 4-D seismic inversion technique to invert two-time lapse, 4-D seismic volumes under low-frequency acoustic impedance constraints. Prior to the inversion process, *a priori* information about the acoustic impedance model is constructed from a limited number of wells that have sonic and density logs. We do not use all available wells to construct the reference impedance model, so that control wells can be used after the inversion to analyze the reliability and accuracy of the computed impedance volumes. Independent examinations of the estimated acoustic impedance volumes using these control well logs indicate that the inversion is able to recover accurate acoustic impedance functions to less

than $\pm 10\%$. The consistency observed between impedance volumes suggests that our nonlinear inversion avoids serious artifacts.

The geological features observed in the two impedance volumes are remarkably similar. Good agreements between the estimated impedance functions and well logs are observed, suggesting that the nonuniqueness of the estimated impedance volumes is not significant. The impedance volumes are now ready for 4-D seismic monitoring analysis and reservoir characterization.

Time-varying seismic source functions are also obtained for all seismic traces in the two inverted seismic data volumes. These wavelets may be of some usefulness in estimating spatial frequency variations caused by both acquisition and processing variability. We have not implemented phase adjustment into source extraction process. In the future, such refinements may further improve the inversion process.

Our estimated impedance volumes are well behaved and laterally continuous. We believe that the integration of high lateral resolution from the estimated acoustic impedance volumes and high vertical resolution from sparsely distributed well logs can be used to achieve a much better characterization of changes in oil and gas reservoirs overtime than today's standard analysis techniques.

References

- Alexander, L., and P.B. Flemings, 1995, Geologic evolution of a Plio-Pleistocene salt-withdrawal minibasin: Eugene Island Block 330, offshore Louisiana: American Association of Petroleum Geologists Bulletin, v.79, p.1737-1756.
- Anderson, R.N., A. Boulanger, W. He, Y.F. Sun, L Xu, and B. Han, 1995, 4-D seismic monitoring of drainage in the Eugene Island 330 Field in the offshore Gulf of Mexico: American Association of Petroleum Geologist special publication, in press.
- Archie, G.E., 1942, The electrical resistivity log as an aid in determining some reservoir characteristics: Transactions AIME 146, p. 5~62.
- Brock, J., 1984, Analyzing Your Logs, Vol. 11-Advanced Open Hole Log Interpretation: Petromedia, Tyler, 173 p.
- Gardner, G.H.F., L.W. Gardner and A.L Gregory, 1974, Formation Velocity and Density-The Diagnostic Basics for Stratigraphic Traps: Geophysics, V.39, No.6, p.770-780.
- He, W., R.N. Anderson, and Y. C. Teng, 1995, Application of seismic inversion to quantitative mapping geopressure transition zones in the Pleistocene, offshore Louisiana, Gulf of Mexico: The 2nd International Conference on Theoretical and Computational Acoustics, Honolulu, Hawaii.
- Tarantola, A, and B. Valette, 1982, Inversion = Quest for information: Geophysics, v. 50, p.159-170.

Tarantula, A., 1984, Inversion of seismic reflection data in the acoustic approximation: *Geophysics*, v.49, p.1259-1266.

4-D seismic monitoring of subsurface fluids in the El-330 Field of offshore Louisiana, Gulf of Mexico

3-D seismic images have improved to the point that they are being applied to reservoir production and engineering problems. 4-D (time-lapse 3-D) seismic imaging may soon be applied to oil field monitoring. However, this technology will require a better understanding of the link between stratigraphy, fluid content and changes in seismic response.

Time-dependence of individual reservoirs has long been observed in production wells. The use of 4-D seismic datasets to monitor fluid movements dates back to more than a decade when thermal and CO₂ injection enhanced oil recovery Projects were carried out (Nur, 1982; Dunlop et al., 1988 and Breitenbach et al., 1989). Petrophysical studies indicate that seismic datasets may be used to monitor subsurface fluid movement in sandstone reservoirs saturated with medium-to-light weight hydrocarbons (Wang et al., 1992). The acoustic contrasts caused by lightweight, gas saturated hydrocarbons (oils with high gas:oil ratio, GOR) can produce even greater seismic amplitude changes.

Changes in seismic amplitude within a given reservoir can be caused by changes in gas:oil:water ratios, fluid pressures and/or fluid contact levels. Time-lapse 3-D seismic surveys acquired can quantify these changes. These seismic datasets can be used to decipher both temporal and spatial distributions of oil, gas and water in reservoirs under production. We believe that such 4-D seismic technologies, integrated with petrophysics and other related multidisciplinary principles, will become the industry standard in hydrocarbon exploitation.

4-D seismic technology is still in its infancy. New techniques are being developed yearly, as the great potential of using such datasets in reservoir surveillance and management is recognized (Nur, 1989; Lumbly, 1995; Anderson, et al., 1995a, 1995b and 1995c).

In order to extract 4-D seismic changes, we examine successive 3-D seismic surveys and examine their similarities and differences. The temporal changes allow us to predict the locations and compositions of bypassed hydrocarbons. We also use wireline logs (sonic, density, porosity, oil saturation variations over time) and production data (pressure, water cut, GOR variations over time) to calibrate our models of acoustic impedance changes. The model results will allow us to predict the quantitative changes in seismic response.

Because the time-lapse 3-D seismic datasets used in this study were acquired for other purposes, we must pay special attention to their registration in space and time. The acquisition and processing parameters of different surveys were not the same, and thus we must correctly register the seismic datasets to preserve the maximum amount of common information of these surveys.

Despite these disadvantages, the results obtained from analyzing these "legacy" datasets are rather encouraging. Elimination of artifacts caused by differences in data processing enables us to distinguish the actual acoustic changes in hydrocarbon reservoirs. Many such legacy 4-D seismic datasets are available, especially for the producing oil fields in the offshore Gulf of Mexico. We expect that the application of 4-D seismic techniques to these seismic

datasets will result in the recovery of a large volume of bypassed oil. Nevertheless, much research will be needed to advance 4-D seismic techniques so that they can be used to view of the true dynamic of the drainage of oil and gas from reservoirs.

In this chapter, we present a seismic amplitude analysis technique, applied to the LF reservoir in the Eugene Island 330 Field. A 4-D seismic dataset consisting of two SD seismic surveys (acquired in 1985 and 1992, respectively) is used to locate regions where seismic amplitudes have changed over time. These changes are qualitatively analyzed in term of brightening, dim-outs, and unchanged areas that might contain bypassed hydrocarbons (pay). We then examine the spatial and temporal changes in acoustic impedance, as determined by the nonlinear 4-D seismic inversion techniques. The changes in the estimated 4-D acoustic impedances are better imaged than those changes observed in seismic amplitudes alone.

Seismic prediction of dynamic changes in hydrocarbon reservoirs

Laboratory experiments indicate that the acoustic reflection coefficients varies with oil, gas and water mix, effective pressure and temperature (Wyllie et al. 1958; King, 1965; Domenico, 1976; Gregory, 1976 and Wang et al, 1988). This behavior is also observed in the field in water and steam floods, which have produced noticeable acoustic differences over time (Nur, 1982 and 1989; Dunlop et al, 1988; Breitenbach et al., 1989 and Wang et al., 1992).

Changes in seismic data expected from the production of hydrocarbons in the LF hydrocarbon reservoir are summarized using a Simple seismic modeling approach. Seismic amplitudes were modeled by varying the acoustic properties across a hypothetical, constant thickness sandstone reservoir undergoing pressure depletion and GOR changes. The 1985-1992 petrophysical changes match the production data for the LF reservoir. The acoustic property changes are computed using the experimental data from Ottawa sand (Domenico, 1976). The changing gas/water contact (G/W), gas/oil contact (G/O), and oil/water contact (O/W) also causes changes in seismic amplitudes across the reservoir boundaries. Effective pressure (overburden pressure minus pore fluid pressure) increases as hydrocarbons are drained from a reservoir, reducing seismic amplitudes in both oil and gas sands. LF, however, a GOR increase occurs during production, as with the formation of a secondary gas cap, seismic amplitudes are predicted to increase (brighten) over time, because the acoustic effects of the fluid change dominate over the pressure depletion effects. Similarly, seismic amplitudes can dramatically decrease (dim-out), LF, in addition to pressure depletion of a high GOR oil, the O/W contact migrates across a reservoir. The amplitude decrease caused by pressure depletion is further enhanced by the drop in the impedance contrast caused by the replacement of low velocity oil and/or gas by relatively high velocity water.

Our seismic modeling investigation suggests that bypassed hydrocarbons are associated with near-zero changes in regions of high seismic amplitude over time, LF there has been little change in effective pressure (as within a water-drive reservoir). Areas of sustained high seismic amplitudes are either the highest permeability drainage pathways through which the hydrocarbons move, or isolated pressure compartments that are not connected to the wellbore drainage system. Bypassed hydrocarbon can be located on the basis of changes in seismic amplitudes only after the cause for impedance changes is understood.

4-D seismic monitoring technology

Our 4-D seismic analysis technology consists of imaging, feature extraction, and pattern recognition functions, coupled iteratively with high resolution, seismic forward and inverse modeling. Due to the practical limitations, systematic seismic forward modeling methods are only discussed briefly because they are still being developed. Pattern recognition, rather than interpolation and recomputation, is used to examine similarities and differences among the seismic amplitudes, and acoustic impedances of the datasets in the hope that we can use a large amount of legacy 3-D seismic datasets to monitor hydrocarbon drainage and to locate bypassed pay in the mean time.

The Eugene Island Block 330 Field

The Eugene Island Block 330 (EI-330) Field has produced more than 5×10^8 barrels of oil since 1972. The oil and gas are produced from more than twenty-five stacked sand reservoirs in rollover anticlines abutting against the large growth fault system (the Red fault) and associated smaller antithetic faults.

The ongoing development of this field and the remarkable amount of seismic, production, geological and wireline data available from the field make it an ideal location to research the effects of production and fluid migration on changing acoustic (seismic) signals over time. Multiple vintages of 3-D seismic data, large amounts of digital wireline logging data, and production histories from multiple wells enable us to study the reservoir fluid dynamics of the LF in great detail within the EI-330 Field.

The study area is centered along the Block 330/331 boundary where two vintages of 3-D seismic surveys overlap. The two 3-D seismic surveys are the 1985 survey centered on Block 330 and the 1992 survey centered on Block 331. Well logs and production data from nineteen wells are available in the overlap area. Combined stratigraphic, structural and seismic attribute analyses of the legacy 3-D seismic datasets have shown how depositional features and faults compartmentalize reservoirs in this field. Geopressures in the study area are also predicted and characterized (He et al., 1995a and 1995b) as part of the larger study. It is believed that hydrodynamic disequilibrium that has produced dramatic variations along the top-of-geopressure surface over short distances in the minibasin, coupled with periodic fluid release up the large regional growth fault system, is the primary cause for the active hydrodynamic fluid flow in this region. The well-connected aquifer supporting the water drive mechanism within the LF is one result from this dynamic system.

4-D seismic data registration

Amplitude measurements from two 3-D seismic surveys cannot be directly used because the data acquisition and processing parameters applied to them originally were very different. Seismic attributes, such as amplitude, phase, and frequency bandwidth, differ considerably. We use special matching, amplitude normalization, and phase corrections to correct the data.

The 1985 and the 1992 3-D seismic surveys were first re-binned into the same common grid. When comparing the two 3-D seismic volumes acquired seven years apart, navigation efforts may have been introduced because the resolution of navigational systems at sea has been constantly improved. In our case, we found that there is a 62 m displacement in the east-west direction between the two seismic volumes. The offset was determined from a global cross-correlation between the two seismic volumes in both the north-south and the east-west directions.

The global cross correlations are computed from sequential time slices through the entire two volumes.

The frequency bandwidth of the 1985 volume differs from that of the 1992 seismic volume because seismic sources have been steadily improved over the years. To match the frequency bandwidth, we first computed the global frequency spectrum of each volume, determined the bandwidth that common to both, and used it to bandpass filter both datasets. A zero phase filter is used.

Different static shifts were applied to seismic datasets in the original processing. We correct for this shift by cross correlating corresponding traces to determine the relative offset. The offset is then averaged over all the seismic traces, and the average is applied to the 1985 seismic survey to correct it to that of the 1992 survey.

Phase shifts between legacy seismic surveys are determined using a cross-correlation technique to determine the phase angle difference between the two volumes. We held the seismic traces from the 1985 survey fixed, while phase-shifting the traces of the 1992 survey with all possible angles (0-360 degree). The phase angle that maximizes the correlation between the two traces is applied to the 1992 survey to correct it. Numerical experiments carried out in our volume matching techniques indicate that the matching of conventional post-stack seismic volumes can be best performed by applying time-variant filters to different time windows because the seismic waveform characteristics vary with traveltime.

Amplitudes of the two seismic volumes are normalized by requiring that the cumulative amplitude histograms of the two seismic volumes be similar. The two surveys have rather different amplitude distributions. We choose the 1992 seismic volume as the amplitude reference, performed a global histogram renormalization of the 1985 survey. The amplitudes are rescaled by a factor appropriate for real acoustic variations in the earth by comparison with synthetic traces computed from sonic and density logs. Amplitudes of the two surveys are generally similar, but significant differences occur within the producing reservoirs. We will next focus on the time window from 1.7 to 2.2 seconds, which includes the LF reservoir, to perform our 4-D seismic analysis.

The LF reservoir in the study area

The LF reservoir is centered along the boundary of blocks EI-330/331. It dips gently to the west from the crest of the rollover anticline in the center of EI-330, and is bounded on the north by the south-dipping B fault and on the south by the north-dipping F antithetic fault. It is one in a stack of reservoirs (JD-KE-LF) that are main oil and gas producers in the field. Structural dips are of the order of 10-20 degrees, and the sand top deepens from about 2,012 m (6600 ft) to over 2,316 m (7,600 ft) in this fault. The locations of production wells, and the positions of estimated fluid contacts at the beginning of production in 1972 and those estimated at the beginning of our 4-D study in 1992, indicate their movement with time as interpreted from the production data. The regions in red are the original gas cap. Regions in pink are areas that have had oil replaced by gas due to expansion of a secondary gas cap down-dip. Regions in green are predicted to be oil-filled and are thought to have undergone no change in fluid composition. Regions in dark blue are water. Regions in light blue in the west are water sweep occurred since 1972. A large region to the west that has been water swept between 1972 and 1992, whereas between the wells 330_Pz_C-iS and 330_Pz_A-I6ST to the east of the 330/331

block boundary, a secondary gas cap has grown between the time production started in 1972 and 1992. Low permeability gas is also detected from logs near the crest of the structure (regions in dark pink). The original oil-water contact in the LF reservoir is interpreted to be at the 2,307 m (7,568 ft) level from the production data. UnLForm, gravity driven, up-dip movement of the oil-water contact is predicted from production data- The oil-water contact as deduced from the sparse well data is not horizontal in 1992, but appears to cut across structural contours in the south of the F fault. The dip could indicate that the thick LF sand located in these zones is more permeable, and fluids are being preferentially drawn from these high quality sands.

4-D Seismic amplitude analysis technique

The region-growing algorithms

In practice, the amplitude normalization, frequency and phase matching techniques cannot totally correct for differences in original seismic surveys, so the match is never perfect. The inter comparisons are accomplished in attribute-derivative space since we have found that only the lowest frequency in amplitude spectra preserve the best commonality among the differently-processed seismic datasets. Comparison based on wavefield envelope are more robust than those based on the seismic trace itself. Therefore, we use the reflection strength, or instantaneous amplitude (Taner et al., 1979) of the seismic amplitude in our analysis. These reflection strength volumes computed and divided into volumes of similar high amplitude regions (HARs) through the use of region-growing algorithms that we have developed. The conventional isosurfacing technique bounds regions by connecting data points with the same amplitude values on the surface. The usefulness of this technique applied to as noisy seismic data is very limited. Our region-growing technique is more robust. The technique employs nonlinear, 3-D operators to isolate HAR's within the seismic datasets. Beginning from a set of initial "seed" points (with large amplitude values), we track the magnitude of the change-in-amplitude in 3-D. A threshold value of amplitude gradient is selected to bound the regions. The HAR's are bounded by surfaces of high amplitudes that exceed the threshold in the gradient of amplitudes away from the seed points. Data points outside HAR's are excluded from analysis, downsizing the overall amount of data. Rough-cut connectivity between HAR's within each dataset are obtained by properly choosing threshold operator so that lowpass spatial filtering, dilation and erosion "grows" the connections between segmented HAR seed points.

We then difference the two 3-D datasets within each of the HAR's. Corresponding HAR'S defined from the two separate surveys are merged into a single set of HAR's by a volume union operation (Anderson et al., 1995b). Each HAR's is characterized as having undergone near-zero change, brightening, or dim-out. Fine-scaled structure within a single HAR may be indicative of bypassed pay. Intervals of sustained high amplitudes that are within 10% of each other can be used to reveal inter-connectivity. The 3-D pattern of bypassed hydrocarbons has a surprising inter-connectivity. The amplitude pattern is aligned 30 degrees to the major bounding faults in this portion of the LF reservoir. The apparent lineation may be due to small faults caused by westward shear in the vicinity of the LF reservoir. This pattern is not evident in either of the primary 3-D seismic surveys.

Misregistration errors can cause edge effects on the differentiated seismic data, as can be created by velocity differences caused by the changing fluid composition. For example, the

formation of a gas cap significantly lowers the velocities within the top of the reservoir, resulting in a mismatch between the two times. These edge effects must be removed from the final image of the reservoir.

Volumetric analysis of drainage of the LF reservoir

Regions of near-zero seismic amplitude differences may possibly contain bypassed hydrocarbons. Dim-outs could be caused by water encroachment or pressure depletion. Brightened regions could be from GOR increases and secondary gas dissolution.

This detailed hydrocarbon distribution image can be combined with production data to further analyze the drainage patterns caused by production. More than 470,000 barrels of oil with low GOR has been produced from this part of the LF reservoir from 1985 to 1992, mostly from wells A-12A, A-6, A-S, and BA. The other thirteen wells in both Blocks 330 and 331 stopped producing due to water intrusion or mechanical failure early in the production history (before the 1985 3-D survey was acquired).

The estimated initial (1972) and current (1992) oil/water and oil/gas contacts from the production data. The oil/water contact has moved about 107 m (350 ft) in vertical distance up-dip and to the east, and the gas expansion should have deepened the gas/oil contact by about 15 m (50 ft) down-dip and to the west. From these production history interpretations, new wells would have to be placed in a very narrow (< 610 m or 2,000 ft wide) band along the structure contours in the fault block B.

However, the 4-D image of the LF reservoir predicts a significant different drainage pattern from the interpretation derived based on the gravitational assumptions of the production history. The drainage is much more heterogeneous than indicated by the production data. The drainage patterns of the LF reservoir do not follow structure contours. Instead, the bypassed hydrocarbons appear to be related to fingered sands trending in the north-west to south-east direction. Water intrusions appear to have fingered into the reservoir in the same direction. The isolated regions with water invasion appear to be caused by water conning.

Horizon amplitude extraction of the LF reservoir

We sample the 3-D amplitude along the 2-D top horizon of the LF reservoir, which corresponds to a strong seismic reflector. The 1985 2-D image clearly shows dim-outs that are approximately parallel to structural contours, especially in the west and near the bounding faults B and F in the north and south. These amplitude boundaries correspond to the 1985 oil/water contacts. The amplitude pattern is more continuous in the east. However, by 1992, the amplitudes have become discontinuous. The total area of high reflectivity has decreased with time, as expected for an actively produced reservoir with decreasing fluid pressures and oil saturations.

Amplitude changes in the top of the LF reservoir also indicate brightened areas marking gas formation and dim-out areas marking water invasion. However, the boundaries are more complex and less clearly tied to structure than in the gravitational model derived from production data. Depletion of the gas cap from 1985 to 1992 is imaged as an amplitude dim-out in the eastern portion of the reservoir, with brightening indicated within the newly depleted oil zone (down-dip to the west). Areas of near-zero amplitude change are primarily located in regions where no active production wells were operated (e.g., Block 331). We predict that there is

significant bypassed oil located in the LF reservoir of this fault block.

Significant edge effects are caused by traveltimes misalignment of the LF reservoir in the southwest and south of the fault block (just north of the F fault). This misalignment is probably caused by velocity changes from the significant drainage in the shallower JD reservoir, which is a large gas producer.

Volumetric variations of seismic amplitude differences

The HAR analysis measures the acoustic thickness of the LF reservoir, and allows variations within the volume to be examined. We difference HARs to create volumetric representations of the seismic amplitude changes between the 1985 and 1992 seismic surveys. Because 3-D variations are difficult to convey on paper, we slice the difference volume through its top, middle and bottom along planes parallel to the LF structure surface. We present both a fluid contact interpretation of the differences, and the absolute difference images.

We then compared these HAR slices with a slice made along the top of the reservoir, as defined by the seismic reflector. Both show the gas formation, but the HAR slices demonstrate that the high amplitude anomalies have migrated much deeper into the reservoir and to the west by 1992. However, in the eastern portion of the reservoir (up-dip), water sweep has changed the original gas distribution dramatically due to the active production in Block 330. For example, the A-6 well (in Block 330) produced oil since 1981. The A-6 well was shut-in in 1987 because of a sudden water intrusion, and it was producing hydrocarbon at a GOR of 3,000 before the shut-in. The case of amplitude increase (brightening) in Block 331 is unknown. It contains no active production wells. Perhaps pressure decreases within the overall reservoir caused gas to come out of solution. However, the brightened amplitudes moved more than 305 m (1,000 feet) to the northwest from 1985 to 1992, so we believe the amplitude increases to be real.

4-D acoustic impedance analysis technique

Volumetric reservoir descriptions based upon seismic amplitude data are less physical than those based upon acoustic impedance. Because acoustic impedance is more closely associated with the petrophysical and fluid properties of reservoirs than amplitudes, we apply the same region-growing technique to the estimated acoustic impedance volumes. We therefore inverted the amplitude-normalized, phase-matched seismic datasets to produce the estimated impedance volumes. The constrained, full-scale nonlinear seismic inversion technique is applied. The estimated 4-D acoustic impedance volumes from the 1985 and 1992 seismic volumes is within the time window from 1.7 to 2.2 seconds. The hydrocarbon reservoirs correspond to low impedance regions within these two impedance volumes.

Differences in acoustic impedance between 1985 and 1992 in the LF reservoir

Using our region-growing algorithms, the 1985 and 1992 acoustic impedance volumes are then segmented into similar Low Impedance Regions (LIRs) and data from outside these LIRs are excluded from future analysis.

The shape of the LIRs (derived from acoustic impedance volumes) differs from that of the HARs (derived from seismic amplitude volumes). Because seismic amplitudes are sensitive to reservoir boundaries, to fluid contacts, and to impedance contrasts, while acoustic impedances are more sensitive to internal continuity and heterogeneity within the reservoir itself. Reservoir

thicknesses derived from the estimated acoustic impedance volumes are much more accurate than those resolved from seismic amplitudes. As we will see later in this section, our region-growing techniques are more robust when applied to the estimated acoustic impedance data.

Reservoir drainage from the shallower JD reservoir causes vertical traveltime delays in the LF reflections. There is up to 20 ms of delay in the 1992 survey versus the 1985 survey. We compensate the traveltime delays by applying a horizon-balancing technique. We interpreted the top of the LF reservoir sand on both estimated acoustic impedance volumes. We then corrected the traveltime differences between the 1985 and 1992 LF reservoir tops by shifting the 1985 data. The edge effects shown in are thus eliminated.

The differences within the LIRs of the LF reservoir between 1985 and 1992 were then computed. Changes in acoustic impedance over time are quantitatively related to the drainage of hydrocarbons. Near-zero impedance differences indicate locations where there was minimal change within the LIRs of the surveys, which we interpret to be possible bypassed hydrocarbons. Increases in impedance are likely caused by water encroachment or pressure depletion between the times of the two surveys, and decreases from GOR increases and secondary gas dissolution. A visualization of the volumetric changes within the LF reservoir is created by slicing through the upper-, mid-, and lower-intervals of the LF LIR. Comparing this result to the similar figure made from seismic amplitude differences, more coherences are observed within the LIR than in the seismic amplitude HAR. However, water appears to have encroached in what might be fingers through high permeability sand from several directions, not just from the deeper portion of the reservoir in the west

Horizon acoustic impedance extraction of the LF reservoir

The acoustic impedances were extracted from along the LF reservoir top structure from each impedance volume. The extracted impedances can be directly used to delineate distributions of hydrocarbons remaining within the reservoir.

The reservoirs are outlined by the boundaries between high and low impedances. The reservoir dim-outs and brightenings have higher coherence than in the corresponding analysis that used seismic amplitudes. The hydrocarbon contacts are clearly seen on both images. The similarities and differences between the 1985 and 1992 extractions show the quantitative hydrocarbon changes that have occurred within the LF reservoir. Such changes indicate reservoir dim-outs and brightening inside the reservoir from 1985 to 1992.

As with the qualitative results obtained from the amplitude analysis, the dim-outs (increased impedance) are approximately parallel to structural contours, particularly in the western part of reservoir. These impedance boundaries correspond to the oil/water contact. No obvious water intrusion is detected perpendicular to structural contours in the northwest. However, long distance water encroachment perpendicular to the structural contours has occurred along the north of the F fault. In 1985, the region of low impedances show continuity to the eastern part of the reservoir. But by 1992, the continuity has markedly decreased. In general, the area of low impedances decreases with time, as might be expected for an actively produced reservoir.

Volumetric variations of acoustic impedance differences in the LF reservoir

Impedance differences within the LIRs are related to hydrocarbon movement. Brightened

volumes mark gas cap formation and volumes with dim-outs mark water sweep. But the boundaries are more complex and less tied to the reservoir structure than described by production data analysis. Low impedance regions above the initial gas/oil contact in fault block B are considered to be gas. Depletion of the gas cap from 1985 to 1992 is not obvious in these regions. However, areas with decreasing impedances occur further down-dip to the west within the oil zone, suggesting down-dip migration of the gas cap and gas dissolution from oil. The areas with near-zero impedance change in Block 331 are greater than those in Block 330, indicating that there may be more bypassed hydrocarbon reserves in Block 331 of the fault block. However, as we have noted previously, the cause of these regions with decreased impedance is unknown because there was no well producing from 1985 to 1992.

We present a fluid contact interpretation of the differences based on the analysis of images. Both volumetric impedance extractions and planar extractions show the low impedance anomalies migrated much deeper down-dip. This information is not present in the 2D surface extraction analysis.

The total volume of decreased impedance and near-zero impedance change is larger than those observed in the HAR analysis, and these volumes are more continuous as well. This improvement occurs because traveltimes delays caused by production of shallower reservoirs have been eliminated.

The regions with near-zero impedance changes within the original gas cap to the east should still be gas. However, significant water encroachment is detected, and the original gas distribution (gas/oil contact) has been changed dramatically by the production in Block 330.

The well data in Block 330 are consistent with the predicted hydrocarbon drainage patterns from the 4-D amplitude and impedance analyses. For example, in 1985, A-S well produced oil, gas, and water as the water front moves up-dip toward east and south, the well was shut-in in mid 1987 because of water encroachment. This well is located in the area of water sweep predicted by our 4-D analysis. The nearby A-6 well (in the up-dip direction to the south of A-S) has a similar history, but it saw water about six months earlier (instead of later) than A-S, indicating that either the water intrusion in the LF reservoir is preferentially oriented in certain directions or it is caused by water conning. Another example is the B-4 well, which came into production in 1984; it has produced oil steadily with low GOR into 1991. It is on the edge of the area of bypassed oil predicted by our 4-D analysis.

The water conning is observed much more clearly in the Block 331. Although production from wells in Block 331 has stopped because of water encroachment or sand-flow induced mechanical failures before 1985, there are water encroachment "halos" detected from our 4-D analysis existing around the watered-out wells (e.g., wells A-4, A-7 and A-S). Nevertheless, the predicted water encroachment are not radially isotropic, instead, the drainage appears to have been significantly affected by sand quality variations and other permeability heterogeneities.

Quantitative 4-D seismic monitoring technique

In an effort to further quantify our 4-D seismic monitoring techniques (He et al., 1994 and 1995b), we have used a multi-dimensional seismic forward model based on the finite element method (FEM) and fluid substitution technique (Sun, 1994) to verify whether the hydrocarbon drainage changes can produce the observable seismic amplitude changes. We constructed a velocity model of the LF reservoir as it appeared in 1985. To change the reservoir petrophysical properties, we use Gassman's equation combined with the dynamical theory of

porous media (Sun, 1994) for estimating the acoustic velocity of rock containing a multi-phase pore fluid. We incorporate changes in gas cap development, water intrusion, GOR increase and unchanged oil saturation into the 1992 model. We then compare its FEM seismic response to the 1985 response. The FEM model results indicate that surface seismic data can be used to monitor the hydrocarbon drainage process.

Conclusion

When applied to data from the LF reservoir in the EI-330 Field of offshore Louisiana, our 4-D seismic monitoring techniques are effective in determining the locations and volumes of bypassed hydrocarbons. Corrections for spatial data registration and traveltimes from delays caused by drainage above the reservoir are very important. Without them, the resulting edge effects may cause the 4-D analysis to fail.

The application of our 4-D seismic monitoring techniques to seismic amplitude and estimated acoustic impedance data suggested that: a) the amplitude analysis is the better prediction of reservoir drainage patterns; and b) the impedance analysis is better prediction of reservoir petrophysical property changes. The integration of the two techniques produces quantitative understandings of the drainage of hydrocarbon reservoirs over time.

Our analysis suggests that drainage patterns are very sensitive to heterogeneities in lithology, porosity, and permeability of the reservoir. Water intrusion and gas cap expansion is found to be almost independent of the LF reservoir structure. Instead, we found that they are determined by potential fluid pathways provided by faults and fine-scale sediment fairways with high permeability.

Production wells within the LF reservoir in fault block B were found to have produced very limited, heterogeneous and contorted drainage radii. The drainage pathways in the LF reservoir are elongated along directions of high permeability (northwest-southeast) and shortened along directions with lower permeability (northeast-southwest), which indicates that the production wells have greater drainage efficiencies in selected directions. The wells that were shut-in because of water intrusions were seen to have "suffered" from much more water-coning from below than from lateral, up-dip gravity driven water invasion. The use of 4-D seismic data has significantly improved the understanding of reservoir dynamics of the LF reservoir, compared to what is possible with the traditional interpretations based on well logs and production history.

References

Alexander, L., and P.B. Flemings, 1995, Geologic evolution of a Plio-Pleistocene salt-withdrawal minibasin: Eugene Island Block 330, offshore Louisiana: American Association of Petroleum Geologists Bulletin, v.79, p.1737-1756.

Anderson, R.N., E. Bagdonas, A. Boulanger, L. Xu, and W. He, 1995a, 4-D seismic interpretation techniques for the detection of drainage and migration in oil and gas reservoirs: US. Letters Patent Pending.

Anderson, R.N., A. Boulanger, W. He, Y.F. Sun, L. Xu, 1995b, 4-D seismic imaging of drainage and pressure compartmentalization in the Gulf of Mexico, Oil and Gas Journal, part 1, March 28, part 2, April 4.

Anderson, R.N., P.B. Flemings, and S. Losh, 199Sc, The GBRN/DOE Eugene Island Dynamic Enhanced Recovery Project, CD-ROM, Lamont Press.

Breitenbach, E.A., G.A. King, and K.N.B. Dunlop, 1989, The Range of Applications of Reservoir Monitoring, Society of Petroleum Engineers Paper 19853.

Domenico, S.N., 1976, Effect of brine-gas mixture on velocity in an unconsolidated sand reservoir, *Geophysics*, v.41, p.882-894.

Dunlop, K.N.B., G.A. King, and E.A. Breitenbach, 1988, Monitoring of oil/water fronts by direct measurement, Society of Petroleum Engineers Paper 18271.

Gregory, A.R., 1976, Fluid saturation effects on dynamic elastic properties of sedimentary rocks: *Geophysics*, v.41, p. 895-921.

He, W., R.N. Anderson, and X. Wang, 1994, Constructing 3-D porosity and fluid pressure models in the Eugene Island Block 330 Area offshore Louisiana: American Association of Petroleum Geologists, Annual Convention Official Program, v.3, p.167.

He, W., and R.N. Anderson, 1995a, Seismic Attribute mapping of the geopressure surface in the Gulf of Mexico, *Journal of Geophysical Research*, submitted.

He, W., R.N. Anderson, X. Wang, and Y.-C. Teng, 1995b, Application of finite element seismic modeling in the Eugene Island Block 330 Field offshore Louisiana, Gulf of Mexico: American Association of Petroleum Geologists, Annual Convention Official Program, v.4, p. 41A.

Holland, D.S., LB. Leedy, and D.R. Lammlein, 1990, Eugene Island Block 330 Field-U.S.A. Offshore Louisiana: in *Structural traps III: Tectonic fold and fault traps: Treatise of Petroleum Geology, Atlas of Oil and Gas Fields*, E.A Beaumont and N.H. Foster, compilers, American Association of Petroleum Geologists, Tulsa, p.103-143.

Lumbly, D., 1995, Seismic monitoring of oil production: a feasibility study: presented at the 1994 Society of Exploration Geophysicist Annual Conference, Los Angeles.

King, M.S., 1965, Wave velocities in rocks as a function of changes in overburden pressure and pore fluid saturants: *Geophysics*, v.31, p. 50-73.

Nur, A.M., 1982, Seismic Imaging in Enhanced Recovery, Society of Petroleum Engineers Paper 10680.

Nur, A.M., 1989, Four dimensional seismology and (true) direct detection of hydrocarbons: the petrophysical basis: *The Leading Edge of Geophysics*, v.9, p.30-36.

Sun, Y.F., 1994, On the foundations of the dynamical theory of fractured porous media and the gravity variations caused by dilatancy, Ph.D. Dissertation, Columbia University.

Taner, M.T., F Koehler, and R.E. Sheriff, 1979, Complex seismic trace analysis: Geophysics, v.44, p.1041-1063.

Wang, Z., and A.M. Nur, 1988, Effect of temperature on wave velocities in sands and sandstones with heavy hydrocarbons: Reservoir Engineering, v.3, p.158-164.

Wang, Z., and A.M. Nur, 1992, Aspects of rock physics in seismic reservoir surveillance: in Reservoir Geophysics, R.E. Sheriff, Editor, Society of Exploration Geophysics, p.285-300.

Wyllie, M.R.J., A.R. Gregory, and G.H.F. Gardner, 1958, An experimental investigation of factors affecting elastic wave velocities in porous media: Geophysics, v.23, p.459-493.

Task Three - Field Demonstration Experiment

Roger N. Anderson - Task Manager

OBJECTIVE:

The objective of task three was to drill one Well extension to test the Dynamic Enhanced Recovery Technologies objectives of this project. In November and December, 1993, we drilled into the fault zone in Eugene Island Block 330 (A20-ST) and performed the following experiments: whole coring, wireline logging, sidewall coring, formation pressure tests, stress tests, completion with frac-pack, flow test, and pressure transient test.

SUMMARY:

Interpretation of Results of Well Experiments:

The A-2OST "Pathfinder" well was drilled by Pennzoil Exploration and Production Co., on behalf of partners Exxon, Mobil and Cockrell, into the 01-4 reservoir just above the "Red" growth fault zone that forms the northern boundary of the Eugene Island 330 minibasin. The well was then extended across the fault zone and into the footwall with DOE funding. The GBRN Field Demonstration Project consisted of three phases: whole coring, extensive logging, and stress and production testing in the Pathfinder extension. Measurements were made to determine in-situ conditions within and surrounding the fault zone and to test the hypothesis that hydrocarbons could be produced from a fault zone.

We found and sampled oil and gas from silty shales within the fault zone and discovered that the oils have similar chemistry to those being produced from the reservoirs directly above the fault zone. Whole coring revealed that faulting and fracturing extended at least 350 feet into the shales of the upthrown block. Many of the faults and fractures contained oil. Hydrocarbons would not flow at economically viable rates during drill-stem tests. The larger the drawdown pressure applied across the perforations, the lower the permeability of the fault zone became.

Where the A-2OST crossed the fault zone, the horizontal closure stress was found to be 500 psi greater than the fluid pressure. An increase in the pore pressure of 500 psi was then found to induce significant permeability within the fault zone.

A related well, the A-IOST, was drilled into the fault zone in El 330 in October, 1993, in anticipation of the Pathfinder well, completely with industry funds. In contrast to the "tight" fault encountered in the Pathfinder well, fluids flowed strongly when the fault zone was penetrated by the shallower A-IOST well. Fluid flow within the high-pressured fault zone was sufficient to cause differential sticking and the loss of two bottom-hole assemblies in the well. A pulsed-neutron, Thermal Decay Time log run through the stuck drillpipe recorded increased gamma ray radiation from oxygen activation indicating that water was flowing at rates of up to 700 barrels/day within the fault zone.

Introduction

The Global Basins Research Network (GBRN) is an electronic "Internet" organization that was formed to solve two very specific fluid flow problems: 1) the identification of expulsion mechanisms by which hydrocarbons migrate up fault zones from deep, geopressured strata into shallower reservoirs, and 2) the imaging of these hydrocarbon migration pathways so that wells can be drilled into these "streams" located within fault zones. As part of a GBRN/Department of Energy/oil industry cost-sharing project, we are experimenting with methodologies by which hydrocarbons can be economically produced from these natural conduits into deeper, as yet unexploited reservoirs. These deep reservoirs are targets of the sub-salt play currently receiving so much attention in the exploration community.

The specific hypothesis we are testing is that fluid pressures periodically exceed rock failure strength within the geopressured zone, reopening fault zones, which become transient conduits for fluids to rapidly exit the pressure chambers. The shallower reservoirs are filled by hydrocarbons that have migrated up these fault zones, but the timing, migration pathways, and rates of migration remain poorly understood. To address this hypothesis, we integrated a wide variety of geophysical, geochemical, geological and reservoir engineering technologies in order to image these ongoing fluid-flow processes in the Eugene Island 330 Field, and to site the test wells in Block 330 itself. In cooperation with the operator Pennzoil and partners Exxon, Mobil and Cockrell, we drilled, logged, sampled, Frac-Packed, and drill-stem tested a 700 foot extension of a development well into the deep fault zone (the A-20ST) in November-December, 1993, and logged an earlier extension of the A-IOST into the fault zone at a shallower level.

The Eugene Island 330 Field

We chose the Eugene Island 330 field for our oil migration study because it is the largest Pleistocene oil field in the world, it is geologically well-characterized, and most importantly, it shows a variety of indications of geologically recent hydrocarbon migration (Holland et al, 1990 and Whelan et al, 1994). The Eugene Island 330 Field is a typical Gulf of Mexico mini-basin (Alexander and Flemings, 1994). Structurally, a regional growth-fault system (the "Red Fault Zone") forms the northern boundary of alternating sequences of Plio-Pleistocene sands and shales overlying deep-water turbidities and basin-floor fan deposits from the ancestral Mississippi River delta. As the Red Fault Zone accommodated extension toward the deep-water Gulf of Mexico, the sediments in the depobasin formed rollover anticlines that are now filled with oil and gas. Extension was caused by withdrawal to the south of an extensive salt sill initially present near the surface of the mini-basin from 6 to at least 2.2 Ma (Rowan, Weimer and Flemings 1994). A counter-regional, down-to-the-north fault zone forms the southern boundary of the mini-basin. A thick shale sequence separates the shallow-water shelf sands from geopressured, deep-water deposits (Alexander and Flemings, 1994). Remnant salt feeder stocks and remobilized salt diapirs bound the mini-basin, exclusively upthrown to the bounding fault system. The deep turbidities are still geopressured (He and Anderson, 1994), even after the removal of the impermeable salt seal, because high sedimentation rates combined with the thick, deepwater shale accumulations in the Pliocene resulted in rapid burial and permeabilities too low for the excess pore fluids to escape (Mello, et al, 1994).

Migration of hydrocarbons is occurring today in the Eugene Island 330 Field (Anderson, et al, 1993). Seeps are active at the sea floor outcrop of the Red Fault Zone system. Oil and gas are being produced in reservoirs as young as 400,000-years-old beneath these seeps. Geochemical monitoring over the last twenty years has recorded temporal changes in the composition of the oils being produced from the shallow reservoirs; these changes may reflect recent injection of wet gas and gasolines (Whelan, et al, 1994). Also, biodegraded oils have been replaced by less biodegraded oils over time in the shallowest reservoirs.

Locations of the A-2OST Pathfinder and A-IOST Wells

Migration pathways of hydrocarbons can be imaged within the 3-D seismic surveys in the Eugene Island 330 Field by mapping high amplitude connectivity throughout the volume (Anderson, et al, 1993). The northern growth fault system is particularly involved in the migration of hydrocarbons, although the conduits are convoluted and more like 3-D "streams" than uniform, permeable, 2-D fault zone flow planes.

The GBRN focused on a strategy of testing the fault zone play concept by deepening appropriate development wells being drilled during the normal ongoing operations of the Eugene Island 330 Field. This strategy, though far more economical than drilling dedicated research wells, places practical limits to the targets available to the GBRN. In the A-2OST Pathfinder well, we penetrated the tightest, most shale-prone portion of the fault zone just beneath the deepest known reservoirs trapped against the Red Fault Zone in EI 330 (the 01-4 and 5 sands). In this location, the stress field was predicted to be the most constrictive to fluid migration (Flemings, et al, 1994). and by testing the fluid flow properties here, we could better understand the migration process itself

In addition, we were able to participate in the logging of the A-IOST well that Pennzoil and partners drilled into the fault zone to the southeast of the A-2OST. At this location, the fault zone was intersected at a shallower depth, and the seismic signature was of two splays 180 feet apart with a high seismic amplitude anomaly trapped in-between.

The Field Demonstration Experiments in the A-20 ST Pathfinder Well Pennzoil and partners primary economic target in the A-205T well was the 014 sand located between the "D" and "A" fault splays of the Red Fault Zone. The well was spudded on November 2, 1993, and Pennzoil, as operator, drilled to 7035' Total Vertical Depth (TVD) and set 9 5/8" casing. They then drilled-out and penetrated a section of the 01-4 pay that was 50 feet thicker than the downdip section of this sand that is currently on-production in the A-23 well. Pennzoil and partners agreed to log-while-drilling the well extension from the 9 5/8" casing point through their 01-4 and 01-5 pay zones to the point where the GBRN began to core the fault zone. The GBRN/DOE extension was begun on November 23, at 7300'TVD, and ended at 8075' TVD on December 25, 1993. Experiments were carried out in three stages.

Stage I: Whole Coring

We cored the next 350 feet of the well below the 01-5 pay, and though the upper 60 feet of the cored interval was dominated by down-to-the-southwest, slickensided faults. The major deformation zone imaged by the logging tools (see below) was just above this interval. We used

an experimental anti-whirl PDC bit developed by Baker Hughes Inteq. and Amoco Production Co. that had not yet been used in a well. We coupled this new coring bit with a full-closure core catcher, and a water-based polymer mud containing a 3% synthetic, non-fluorescing oil additive developed by M-I Drilling Fluids Co. to prevent adhesion of clays to the bit (balling). A 60' core barrel with a 4" aluminum inner tube was chosen over the usual 30' barrel normally used in the Gull. We obtained a total of 343' of 4 1/4" diameter core from an attempted interval thickness of 360', a 95% recovery rate. The cutting rates averaged better than 70'/hour and at times exceeded 150'/hour in these "gumbo" shales, and the entire coring operation took less than three days. The core was split into alternating 3' chilled and frozen sections, and is available for further study at the GBRN Core Repository at the Pennsylvania State University.

The cored interval was from 7330' to 7680'TVD, and overall, the rock consisted primarily of silty shale with minor sand beds. The Formation MicroImager (FMI) log indicates the cored interval begins just below the deformation zone mapped as the Red Fault Zone, and extends across a second, minor fault not imaged by the seismic surveys. Beds in the cored interval dip between 20 and 30 degrees to the north-northwest. The core sampled three primary structural domains. An upper faulted zone extends from 7330' to 7490', and containing slickensided faults at moderate to high angles. Many are filled with drilling mud, indicating fracture permeability. A middle zone from 7490' to 7560' is relatively unfaulted, and consists of silty shale, shaly silt, and thin, yellow fluorescing sand beds, the thickest measuring 9". Much of this interval corresponds with a slight increase in resistivity, and may be low resistivity pay. Finally, a lower fault zone was encountered from 7560' to 7680'TVD, consisting of silty shales with gouge zones that intersect the well at high angles. Slickensided faults are also present, and dip at a variety of angles. Much more fluorescence is apparent in both low- and high-angle structures in the lower fault than in the upper fault zone. The lowermost faulted zone in the core may reflect deformation associated with a fault beneath the Red Fault Zone.

The planning and execution of the coring stage of the project was a collaborative effort involving not only the GBRN scientists, but also many supporting oil and service companies, and the success was directly attributable to this collaboration. For example, an Exxon coring specialist, Mike Wooten, oversaw the on-site coring effort while Texaco, Chevron, Conoco, and M-I Drilling Fluids provided mud composition advice, CoreLabs processed and archived the core, a Chevron scientist collected gases, Shell and Exxon provided CAT-scanning of the core and other analyses, GERGI Texas A&M and Woods Hole, the organic geochemistry, Cornell, the structural and fracture mapping, Penn State, the acoustic correlation with seismic, Schlumberger, major element chemistry, the University of Michigan and Michigan Tech, the pore water chemistry of wells near the A-2OST, the University of Rochester, age dating of the pore fluids, Pennzoil, the paleontology and biostratigraphy, Woods Hole and Chevron, Mobil, Exxon and the University of Virginia, gas source and maturity analyses.

Stage II: Wireline Logging

The GBRN then logged from TD at 8010' to casing at 7046' TVD with a full suite of acoustic, nuclear and electrical "imaging" logs from Schlumberger to obtain as complete a picture of the fault zone as possible. The acoustic measurements made in the wellbore were from the dipole sonic log, which recorded compressional, shear, and stoneley waveforms throughout

the open-hole portion of the well. The fault zone was distinguished by a marked decrease in sonic velocities from the downthrown (shallower) to the upthrown (deeper) blocks. While compressional velocities decreased by 10% across the fault zone, the shear velocity decreased by more than 20%. The dipole shear source excited a shear wave only slightly faster than the stoneley wave. Fracturing, observed in the core, is thought to be the cause of the low shear velocities, and extensive acoustic measurements are planned at in situ conditions for the core samples.

An experimental nuclear geochemical logging tool developed by Schlumberger was then lowered across the fault zone. Using a controlled source of neutrons, this logging tool measures the elemental composition of the rock by neutron activation, in real time. The distribution of elemental abundances into a normative mineralogy model verifies that the rocks both above and below the fault zone are shales (quartz contents are less than 20% and clay mineral contents are greater than 40% in a rock with 25% porosity). The fault zone itself appears to be somewhat more silty with quartz contents of slightly more than 25%. This logging tool also recorded neutron porosity and gamma ray density.

The electrical logs obtained were array induction and Formation MicroImager (FMI); the latter measures resistivity variations with resolution down to mm-scale along four orthogonal swaths along the wellbore wall. A fluxgate magnetometer orients the four pads relative to true north. Possible pay was indicated within the Red Fault Zone by the induction log, and the FMI showed that a considerable part of the 01-5 pay, thought to be above the fault zone, was in fact, significantly disrupted by movement downthrown to the fault zone. As indicated by dip "tadpoles", the 01-4 sand has normal, 10-20 degree regional dips to the north. Below this, the 01-5 dips first steeply to the west, then steeply to the east before the fault zone top is encountered at 7270' TVD. The fault zone is deformed by 40' of southwest-dipping faults imaged by the FMI. Below 7310', footwall deformation is seen to 7350', below which 20-30 degree dips to the north are the norm. No further southwest-dipping fractures are imaged by the FMI until the small fault zone, seen in the lower two cores, is encountered at 7560-7680' TVD. However, the core revealed that many such small faults exist throughout the footwall section.

In fact, the first core was repeatedly cut by down-to-the-southwest, slickensided faults that were too small to be imaged by the FMI. The FMI revealed that the lower half of the 01-5 target was within the fault zone itself, and consequently, we had begun our coring program about 10' BELOW the deepest down-to-the-southwest fracture within the fault zone imaged by the FMI.

From the bottom of the Red Fault Zone upward, the FMI revealed a zone of interbedded shales and silts with gentle dip, but cut by southwest dipping faults with increasingly more throw until a distinct surface dipping 55 degrees to the southwest was mapped at 7280' TVD. Above this discontinuity, highly deformed silty shale is found, cut by and rotated along an antithetic fault. Three large vertical fractures were mapped above this deformation zone, and each was found to have high electrical resistivity, possibly indicative of hydrocarbon charge. These natural fractures strike in the orientation of the fault zone, and may connect the fault zone hydraulically with the overlying 01-4 and 5 pay zones in the downthrown block. The composition of the oils recovered from the fault zone is identical to the 01-4 oils currently being produced in the A-23 well (see below).

The modular dynamics formation tester (MDT) was next run in the well. We intended to

use this tool to obtain at least 12 pressures throughout the well extension, but because of the hole conditions, the MDT was stuck obtaining the first pressure measurement. Pennzoil then acquired 75 sidewall cores from 7157'-7661' TVD in three coring runs in the hole, including valuable samples from within the major deformation zone of the fault zone.

Stage III: Stress and Production Testing

On December 2, 1993, we ran a 7 5/8" liner into the well extension. As a result of an incomplete cement job, we were required to squeeze cement through casing into the intervals directly above and below our test zone to insure isolation. Stress tests were performed below the fault at 7380-7384', within the fault at 7270-7310', and above the fault at 7240-7244' to obtain pore pressures and tectonic stress magnitude variations across the fault zone.

The difference between the minimum compressional stress (S3) and the fluid pressure (P) controls the hydraulic conductivity of the fault zone. As the fluid pressure converges upon the minimum horizontal stress, significant fracture permeability may be created. Our stress and pore pressure experiments allowed us to measure these in situ conditions above, below, and within the fault zone. We measured pore pressures that were 0.8 of the vertical stress (S1) above and 0.95 of S1 below the fault zone. Direct measurements of the stress field using hydraulic fracturing experiments show that fluid pressures of an additional 500 psi would be required to reopen fracture permeability and allow significant fluid flow within this segment of the fault zone.

It is also interesting to note that the maximum hydrocarbon columns in the OI reservoirs result in buoyant pressures of approximately 500 psi. Thus, it is possible that these large OI columns are in dynamic equilibrium with the closure stresses along the fault. This, in turn, implies that any new hydrocarbons migrating up the fault from depth would be able to naturally hydrofracture into lower pressured reservoirs. We believe the natural vertical fractures imaged just above the fault zone by the FMI log reflect this migration pathway. A fundamental question we continue to address is whether this process of ongoing vertical migration is presently occurring.

Drill-Stem Tests in the Fault Zone

We then perforated, frac-packed and flow tested a 40' interval within the fault zone. On December 14, 1993, the tubing conveyed perforating gun was fired at 7270-7310'. Since only a trickle of flow-back was seen at the surface, low permeability of the formation was assumed. We then hydraulically fractured the perforated interval using Dowell's new telemetry capability in which the test was monitored in real-time in the Dowell offices in Lafayette, Louisiana. The procedures followed were: a) an acid job was performed to clean the perforations and formation near the wellbore, b) a minifracture was created using stepped-rate injection into the formation, and several constant rate stress tests followed (essential for the final design of the frac-pack), then c) the well was shut-in to retrieve the downhole data recorded on the Schlumberger DataLink system. The fracture design was then finalized, and the hydraulic fracture completed. However, the fracture pumps stalled-out at the beginning of the final injection stage, preventing the downhole completion of the fracture job. Although a tip screen-out was thought to be observed at the surface, later retrieval of the downhole DataLink recorders showed that the

increased surface pressure was from frictional loss and not from fracture completion in the formation. Although the highest permeability recorded after the fracture was only 120 md, fluids began immediately to flow to the surface at a rate of 2 bbl/hr at 400 psi against a 16.3 lb/gal zinc bromide completion fluid.

Then the drill-stem testing assembly was tripped into the hole to flow test the fault zone interval. The flow test began with flow to the surface at a rate of 8 bbl/hr but within two hours, the rate had dropped to less than 2 bbl/hr. Pennzoil then used a coiled tubing unit to "jet-in" the well with nitrogen. Once this procedure began, the flow rate increased to 8 bbl/hr again but would not sustain itself, dropping within 24 hours to zero net flow. We did, however, recover several barrels of oil at the surface: hydrocarbons that came from within the fault zone. Fifteen gallons of this fault zone oil were collected for geochemical analysis, and samples are available through GERG/TAMU or WHOI.

As the nitrogen jetting drew higher and higher differential pressures against the formation, the well flowed at smaller and smaller rates, until it completely stopped at more than 5000 psi of drawdown differential. In other words, the more underbalanced we were, the less the formation flowed. At the end of each drawdown experiment, we shut-in the well to measure the permeability of the formation from the pressure rebound.

The fracture permeability in the fault zone is strongly pressure dependent, and as we drew-down the pressure in the wellbore, the fracture network supplying the permeability within the fault zone closed tighter and tighter. This observation was verified on the rig when we shut down the jetting, re-equilibrated the wellbore, then pumped fluid into the formation through the perforations to verify that they were not plugged-off. The fault zone took fluid easily at about 500 psi over ambient fluid pressures.

Pennzoil then plugged the fault zone interval on December 25, 1993, and will complete in their economic target, the 01-4 formation in 1994.

The Logging of the A-IOST Well

In preparation for the A-2OST well, and to examine targets on the upthrown side of the Red Fault, Pennzoil and partners extended the AIO-ST well through the fault zone in October 1993. The A-IOST well is located approximately 1300 feet shallower and 1000 feet to the southeast from the A-2OST.

In the A-IOST well, the first splay of fault zone was encountered at 7500' MD (6000 ft TVD), and a clear fault break was observed by the mudlogger. Significant shows of oil and gas (2000 units, with C1 through C4 components present) soon followed. The volumes of oil that flowed into the mud pits were estimated by the mud engineer to be 1% of 730 bbl of 14.2 LB/gal mud being cut by gas to 12.5 LB/gal in one 12 hour interval, and 2% of 530 bbl of 15.8 LB/gal mud cut to 13.5 LB/gal in 14 hours of circulation. An oil chromatogram of fault zone oil recovered from the mud pits was measured at GERG/TAMU, and it shows that the oil is unbiodegraded and does not have the light n-alkanes or gasolines stripped-off (as do the Pathfinder oils). The A-IOST oils are as complete, chromatographically, as any found in the producing reservoirs of EI-330.

The drillpipe became stuck as the second splay was being encountered 180 feet into the fault zone. Pennzoil backed off and whip stocked, re-entering the fault zone with significantly

heavier mud (16.2 LB/gal). Again, oil and gas (3000 units) shows were reported at the surface, this time against mud weights up to 16.5 LB/gal mud.

An open hole Array Induction resistivity log was then attempted, but was stopped by a borehole bridge 50 feet beneath the first splay of the fault zone. However, a clear fault zone break was observed at 7500' MD, (6010' TVD), in the Gamma Ray and Spontaneous Potential logs, with an oil show in shaley sand indicated by the resistivity log at the top of the fault zone.

While trying to clear this bridge, the drillpipe became stuck again at 7650' MD (6200' TVD), within 8 feet of the previous event. We believe the sharp lithologic break encountered at 7500' MD (6010' TVD) is the first splay of the fault zone, with porous and permeable, hydrostatically pressured IC sands of the downthrown block juxtaposed against low permeability shale or shale gouge. The resistivity log indicates high resistivity in the shale just below the fault break. Beneath this first splay, a slightly sandier zone was encountered at 7550-7570' MD (6060-6080' TVD). The second splay of the fault zone could be indicated by the low Sigma and low porosity logged from 7630-7660' MD (6140 to 6170' TVD).

A dual-burst, Thermal Decay Time (TDT) log was then run through the stuck drillpipe to TDT. Lithologies determined from gamma ray and neutron capture cross-section (Sigma) measurements indicate that the fault zone consists of shaly sand interbedded with shale streaks near the top and bottom of the fault zone. Gas (Neutron Porosity, NPHI <10% porosity) and possible oil shows were indicated by the minima in the Sigma capture cross-section log at 7550-7570' MD (6060'-6080' TVD) and 7630-7660' MD (6140-6170' TVD). A water-wet, shaly sand was found at the base of this upper show at the center of the fault zone, with possible gas and oil shows measured both above and below. Gas continued to cut the mud from 16 to 13 lb/gal while the pipe was stuck. The oil-finding capability of the thru-pipe TDT was then verified by successfully logging the IC pay shallower in the well -- thru pipe, mud, casing, and cement.

Transient Fluid Flow from within the Fault Zone

In the most significant finding from the A-IOST, active, transient, fluid flow was recorded during four repeated TDT logging runs and subsequent station measurements within the fault zone. Water flow was detected by means of neutron activation of oxygen nuclei to produce the radioactive isotope ¹⁶Nitrogen (Schnorr, 1993). The use of the oxygen activation technique to measure water flow in boreholes has been known since 1967 (Wichmann, et al, 1967), and an impulse-activation technique for the TDT log has been applied successfully in Alaska (Scott, et al, 1993, McKeon, et al, 1993). Water contains abundant oxygen atoms, but no oxygen atoms reside within the structure of hydrocarbons, so any possible oil/gas mix traveling with the flowing water was not determined by the following observations.

Gamma ray counts recorded by the natural gamma ray logging tool (NGT) in the TDT were routine during the lowering of the logging tool to the bottom of the well. Shales were emitting about 80 api units of natural radiation, as expected, and sands were recorded at about 60 api units. Then, at the bottom of the well, the neutron generator was activated and began to pulse neutrons into the formation as the logging tool was pulled up the hole at 12 feet per minute. A 10-millisecond burst of 10^8 neutrons was followed by a 100-millisecond quiescence as the photoelectric accumulator was counting gamma rays returning to the logging tool. The total capture cross-section (Sigma) of the formation is the intended measurement of the TDT tool.

As the TDT was logging Pass 1 across the fault zone, gamma ray counts quickly jumped to >200 api units above background, and steadily increased until at 7580' MD (6095' TVD), a maximum radiation level of 290 api units was recorded--far in excess of the natural radiation level of any sedimentary rock. The gamma ray count then slowly decreased to 200 api units at 6030' TYD (7520' MD), then dropped to 60 api units at 7470' MD (5980' TVD), and remained near these background values that had been recorded on the trip into the hole for the rest of Pass 1. The minitron was then turned off, and the TDT logging tool lowered back to the bottom of the well. Normal gamma ray counts of 60-80 api units were recorded again on the trip back to the bottom of the hole with the neutron source turned off. Passes 2 and 3 repeated the cycle of logging up the hole with the pulsed neutron source activated. Pass 2 recorded the highest gamma ray counts from the bottom of the hole to the most radioactive depth at 7580' MD (6095' TVD), but then the count rate dropped more precipitously from there to the top of the fault zone at 7500' MD (6010' TVD), where this time normal gamma ray counts were recorded by the TDT even with the minitron still pulsing neutrons. Pass 3 resulted in gamma ray counts that fall between those of Passes 1 and 2. Pass 4 was then recorded without turning the neutron source on, and only normal gamma ray counts were recorded by the tool. Clearly, some transient fluid flow phenomenon was being observed.

We believe this to be the first recorded case in which the TDT log measured water flow by oxygen activation while the tool was moving upward during a logging operation. The previous water flow studies reported in the literature (c.f., McKeon, et al. 1991, Scott, et al. 1993, Schnoor, 1993) all utilized the tool in stationary locations within the Wilber.

In our case, the TDT was activating oxygen nuclei within flowing water, sending radioactive ^{16}N isotopes streaming uphole. The water must have been flowing at much faster rates than the logging tool was moving (12-17 ft/min) in order for the gamma rays emitted by the decay of the ^{16}N isotopes, which have a half-life of 7.13 seconds, to overtake and be recorded by the gamma ray detector which was 14.5 feet above the neutron source (McKeon, et al, 1991, Scott, et al, 1993, Schnoor, 1993).

The flux of gamma rays counted by the detector within the TDT logging tool quantitatively recorded the variations in water flow within the fault zone between the three activation passes logged in the well. That is, the number of oxygen nuclei streaming past the detector during the passes varied, and was measured directly by the TDT log.

As shown by McKeon, et al. 1991, fast neutrons generated by the neutron generator have energies of approximately 14 MeV, high enough to activate oxygen nuclei to produce radioactive ^{16}N isotopes. ^{16}N decays by beta emission, emitting a 6.13 MeV gamma ray. In most cases (69% of the time). Because of its high energy, the 6.13 MeV gamma rays penetrate several inches of borehole fluid, casing, drillpipe, and cement. However, these gamma rays are not ordinarily recorded by the natural gamma ray detector, because it is 14.5 feet above the minitron source, and logging is done while moving the tool uphole at 12-17 feet/minute. Water must be flowing at faster than the logging speed for the gamma ray detector to record the gamma rays emitted by this decay of ^{16}N .

McKeon, et al, (1991) report the development of a Monte Carlo neutron transport code that can be used to estimate the velocity and volume of the water flowing outside the drillpipe. Assumptions are that the 111/16" TDT logging tool is centered in the 5 1/2", 15.5 lbm/ft drillpipe, and stationary. The formation is assumed to be 30 porosity units of sandstone with water in the

pore spaces. The flow channel is a 2" thick annulus immediately outside the drillpipe.

The total number of activated oxygen nuclii passing the detector is proportional to a scaling factor and Avogadro's Number (there are 6.03×10^{23} oxygen nuclii in each gram molecular weight of water). Thus, the measurement appears, at first glance, to be independent of the flow velocity. However, the time that each activated nuclii remains in the vicinity of the detector is inversely proportional to the flow velocity, and since the activated ^{16}N signal decays exponentially after activation and before gamma rays reach the detector, the flow velocity can be estimated from the gamma ray detector count rate. The specific geometry of the flow pathway itself is irrelevant to the velocity calculation. The gamma ray count rate above background (C_t) is proportional to water flow velocity (v) by $e^{(-L/v)} / v$, where A is the ^{16}N decay constant, and L is the distance from source to counter.

Thirteen station measurements were made after pass 4, and after a 17.5 lb/gal "kill-slug" was circulated to the bottom of the hole. In this mode, the TDT tool is held stationary in the Wilber while the minitron bursts neutrons for 10 msec, then passively counts for 100 msec, then the cycle is repeated many times (see Schnorr, 1993). Much slower flow rates were encountered overall after the kill-slug, but "bursts" of radioactive fluid were periodically encountered in 4 stations adjacent to the fault top. In these bursts, radioactivity first increases dramatically, then decays exponentially as the ^{16}N flu is dissipated across the stationary detector.

These velocity-versus-gamma-ray-count ratios were used to approximate the flow velocities logged by the moving TDT tool, although the gamma ray counts recorded by the moving tool were considerably higher than those recorded during the stations (because of the different mud weights in the wellbore). The assumption made is that the fluid flow was all in the same direction as the tool was moving. In fact, the tool velocity was added to the calculated flow velocity. Variations in water flow velocities are predicted for the gamma ray variations logged by the TDT to have been up to 160 ft/minute.

The variations in volume flux up the hole versus depth are interesting. The flux increases from about 150 bbl/day at in to a peak at 7580' MD (6095' 'ND). The maximum flow was encountered in all three activation passes at this depth, which is also the minimum Sigma "peak" within the fault zone. flow up the wellbore then steadily decreases between there and the top boundary of the fault zone. Very little flow is observed from the fault zone into the hydrostatically pressured IC sands above the fault zone (less than 50 bbl/day). The differential sticking of the drillpipe seems likely to have occurred where fluid was exiting the wellbore as the flow rate decreased within the wellbore from 7500' to 7680' MD (6010' to 6200' 'ND). Variations in the water flow were monitored by three separate repeat logging runs, and each time the maximum upward flow rate was encountered where the minimum neutron capture cross-section (Sigma) was found in the fault zone. However, the flow rate was variable, with the maximum flux encountered during the first pass, but the minimum measured by the second pass. By the time of the third pass, the flow rate had increased again.

An 18 lb/gal kill slug was then pumped downhole, and verification that flow had stopped was made by active TDT logging that reproduced the normal gamma ray values recorded from the fault zone and by several stations. The drillpipe was then severed, and the bottom of the well cemented-off.

In summary, what we believe happened in the bottom of the A-IOST well is that, after crossing the first fault splay a very large pressure increase was encountered (8.8 to 16 lb/gal

equivalent). Then as the well penetrated deeper into the second bounding splay of the fault zone, strong fluid flow began with water entering the wellbore from below the fault zone sand and moving uphole to exit the wellbore between the sand and the top-bounding fault splay. Interestingly, little of the flow appears to have gone into the overlying hydropressured sands, but instead was confirmed to the interval between the fault splays. This fault zone is clearly capable of producing fluids at high rates, especially if it were part of an interconnected fluid migration network.

Geochemistry of Hydrocarbons Recovered from El 330 Reservoirs and the Red Fault Zone

All of the biomarker and aromatic hydrocarbon maturation parameters measured to date in the Eugene Island 330 reservoir oils are consistent with these oils having been generated and expelled approximately from the beginning to the middle of the oil generation window, equivalent to a vitrinite reflectance, R_{o1} of about 0.75w 0.8%, depending on the exact type of kerogen present. However, gases from the same GOR mixes in wells have much higher maturity (1.1% to 1.2% R_o equivalent vitrinite reflectances, Whelan et al, 1994), suggesting a much deeper source for the gases. The biomarker maturation values from the A-2OST Pathfinder well's fault zone oils are also very constant and the same as those for the deeper "standard" EI reservoir oils from the KE, LF, MG, and OI reservoirs.

The ratio of $(nC3 + nC4) / nC17$ was used by Whelan et al. (1994) to represent ratios of wet gas to oil. High wet gas to oil ratios may be diagnostic of recent hydrocarbon reinjection into reservoirs in El 330, since the lighter hydrocarbons are also more prone to escape from a reservoir undergoing leakage. In addition, in any reservoir undergoing active biodegradation which produces "humpane" type baselines, such as those observed for the GA and HB reservoirs, it would be expected that $nC3$ and $nC4$ should also be absent. These low molecular weight compounds are easily and preferentially lost by biodegradation, as well as by a number of other processes, including water washing and evaporative fractionation (Thompson, 1983; 1987; 1988). Therefore, high $(nC3+nC4)/nC17$ ratios observed in the GA and HB oils of Eugene Island 330 are consistent with recent active oil migration and/or remigration.

Changes are noticeable over time as well, particularly in the ratios of light ($C3-C5$) to heavier ($C7-C8$) components among samples taken in 1984, 1988, and 1992, with an ever higher proportion of lighter components being present in 1994. Ratios of B (toluene to n-heptane), F (n-heptane to methylcyclohexane), H (a maturity ratio based on the ratio n-heptane to the sum of branched and cyclo to n-alkanes), and I (ratio of branched $C7$ compounds to the sum of cyclic $C7$ dimethylcyclopentanes) also show systematic changes over the 6 year period indicative of changes in reservoir hydrocarbon composition and possibly of dynamic injection of hydrocarbons from deeper sources into the reservoirs over this interval time, Q. Whelan et al, 1994).

The whole oil chromatograms of the A-2OST Pathfinder fault zone oils are identical to those of the deeper KE through OI oils recovered from other "A" platform wells, and particularly the A-23 oils from the nearest reservoir "updip" to the fault zone, the OI-4. However, the Pathfinder oils from the fault zone show very low wet gas to oil ratios, suggesting no recent hydrocarbon injection of light hydrocarbons in this particular fault zone interval. In contrast, the A-1OST oils are from an interval of the fault zone with higher seismic amplitudes than are

present in the Pathfinder fault zone penetration, implying higher gas contents. Indeed, analyses of the A- IOST oils show them to have higher wet gas to oil ratios than do the Pathfinder oils. Perhaps the A-IOST oils are closer to a light hydrocarbon migration pathway within the fault zone than the A-20ST Pathfinder oils, or the Pathfinder oils have been stationary for long enough to lose their light components.

During drilling of the A-2OST Pathfinder well, gas samples were obtained by Martin Schoell, Chevron, using a new gas sampler technology. Initial molecular and isotopic compositions for these gases show that the gases from the cored interval beneath the fault zone contain a progressively higher biogenic versus thermogenic component with increasing depth. The biogenic gas represents that generated in organic rich sediments of the footwall at much shallower depth which was then carried down and buried. DLFflisive mixing is indicated, with more thermogenic gas entering the sediments through the fault zone at the top of the cored interval and mixing with biogenic gases in the shales from the upthrown block. Thus, the d13C methane values for the Pathfinder well show that no significant fluid flow is occurring from the high-pressure footwall to the lower pressure reservoirs of the hanging wall sediments. Also, the source of the thermogenic gases found within the fault zone appears to be from deeper along the fault zone trajectory.

How to Produce Oil and Gas from a Fault Zone Conduit

Our current working hypothesis for hydrocarbon migration in the El 330 area is that deep in the geopressed turbidities, formation pressures periodically increase until fracture-reopening stresses are overcome in the fault zones that connect into these "chambers". At such times, large volumes of hydrocarbons are released rapidly in transient bursts up the fault zones towards the surface. and then the faults close back up. Put another way, with added pressure. oil is expelled up the fault zones, but then the very act of releasing the fluids drops the pressure and the faults become tight again. Over and over, the cycle repeats. Evidence from the Pathfinder well to support this hypothesis is that the fracture permeability within the fault zone is strongly pressure dependent. We have shown that oil and gas are present even in the tightest portion of the Red Fault Zone in Eugene Island 330, and that these would flow under fluid pressures 500 psi higher than those measured within the fault zone today. We have demonstrated that such pressurization increases the permeability of the fault zone to Darcy values. However, we have also found that the fluid-release from such a pressurized fault zone immediately lowers the permeability by several orders-of-magnitude. In addition, the A- IOST well provides strong evidence that once fluid flow is established within the fault zone, transient behavior can be expected.

The GBRN/DOE Field Demonstration Experiments have provided tests of likely strategies for future production:

- 1) Locate wells into high permeability pathways within the fault zones that have high-seismic amplitudes,
- 2) Change the angle of penetration from perpendicular to parallel to the fault zone in order to expose more surface area, such as drilling along a fault isolated sand lobe. Such strategies are likely to be profitable, since they increase permeability by drilling higher seismic amplitudes and

increase thickness by drilling along the plane of the fault zone.

We believe that technology transfer of the GB RN/DOE methodology of integrating geophysical and geochemical dynamics with the more traditional stratigraphic and structural techniques will lead to a more complete hydrocarbon-system view of the deep subsurface. In addition, these technologies led to a new play concept that could help locate and exploit large volumes of deep, geopressured reserves not only in the Gulf of Mexico, but also in other sedimentary basins where hydrocarbons are currently migrating out of deep geopressured chambers, such as in Nigeria, the North Sea, Indonesia and the Caspian Sea.

Task Four - Reservoir Characterization **Peter Flenning - Task Manager**

OBJECTIVE:

The purpose of this task was to integrate the geological and geophysical data to construct the minibasin and reservoir models in the SEI 330 Area in order to understand the hydrodynamics of the minibasins. The minibasins are analyzed through stratigraphic interpretation, salt analysis, pressure and temperature mapping. Temporal seismic amplitude analysis is to monitor the dynamic changes occurred in the reservoir

SUMMARY:

Through the final year of the project we continued to acquire important data for the 330 field. These included: 1) complete wire- line data for Blocks 338 and 339 (donated by Texaco), 2) fracture completion data, and leak off data for Blocks 330, 338, and 339. and 3) the entire 316 A-12 core (now housed in the Penn State Core Repository) which was recently drilled by Pennzoil. Throughout the year, Beth Bishop and Amanda Sbaw have continually updated the Landmark Openworks project and distributed data to all of our colleagues in this DOE-funded project.

The following work was performed by Parvel Peska of Stanford University as consulting services to Columbia's Lamont-Doherty Earth Observatory from April 1, 1994 through July 31, 1995:

CONSTRAINING IN SITU STRESS IN THE SOUTH EUGENE ISLAND FIELD, GULF OF MEXICO

Pathfinder well

We analyzed data from the GB RN/DOE Pathfinder well, block 330 of the South Eugene Island field (extension of the Pennzoil A-20ST production well, offshore Louisiana). The data include: 4-arm caliper leak-off/minifrac, pore pressure, FMI and hole orientation data.

Four-arm caliper measurements associated with an FMI log run in the Pathfinder well indicated systematic borehole enlargements from a depth interval 2158-2180m, about 150 m above the main growth fault. The breakouts occur at an azimuth of N550E LF projected onto a horizontal plane. At these depths, the wellbore deviates 320 from the vertical at an azimuth

N350K

A leak-off test from a depth of 2148 m provides an estimate of the minimum principal stress. The corresponding vertical stress was computed from average density given by the density log, and the estimated formation pore pressure. These observations represent information that is typically available in many offshore reservoirs. The occurrence of naturally-occurring vertical extension fractures on the FMI log near the depth of interest indicates that S_V is a principal stress. Thus, to fully determine the stress state, two stress components are still unknown: the magnitude and azimuth of SH_{max} (or azimuth of Sh_{min}).

The subsequent analysis revealed that the azimuth of Sh_{min} must be between N37°E and N49°E and the corresponding values of SH_{max} must be between 39.5 MPa and 43 MPa. No other values satisfy the observed wellbore breakouts. Although it is commonly assumed that in the Gulf Coast, the SH_{max} value determined in this case departs significantly from Sh_{min} . The computed azimuth of Sh_{min} deviates from the azimuth of observed breakouts (whereas in a vertical well the breakouts are at the same azimuth of Sh_{min} , and it appears to be quite reasonable as it is orthogonal to strike of the major growth fault passing through the hole just below the measurement depth. No knowledge of either rock strength or elastic moduli was necessary in these computations.

Once the range of allowable magnitudes of SH_{max} and azimuths of Sh_{min} is computed, the uniaxial rock strength necessary to prevent borehole failure can be estimated. The occurrence of breakouts implies a strength less than about 22 MPa. If $SH_{max} = 39.5$ MPa and less than ≈ 32 MPa if $SH_{max} = 43$ MPa. These are reasonable values considering the sediments in question are poorly-indurated and clay-rich (Anderson et al. 1994).

The results of the study were presented in the paper "In situ stress and rock strength in the GBRN/DOE Pathfinder well, South Eugene Island, Gulf of Mexico" (Zoback and Peska 1995).

Surrounding well

Analysis of borehole breakouts detected in deviated wells by caliper logs was extended from the Pathfinder well to other wells in the South Eugene Island field where the logs were available. Borehole enlargements at azimuths, which do not correlate with the hole inclination, were detected in the wells at depths of 6000'-8000'. The caliper difference was relatively small and subsequent stress analysis revealed that either the breakouts are not stress-induced or the stress state is highly heterogeneous in the region of interest.

Miscellaneous

As a part of the stress studies in the South Eugene Island field, we also performed compilations on stress magnitudes in the Gulf Coast particularly on fracture gradients and pore pressures as a function of depth. This revealed that the Mohr-Coulomb frictional model controlling stress magnitudes in crystalline rocks in many parts of the world (e.g. Zoback and Healy 1984) is not working for overpressured formations in the Gulf Coast unless the coefficient of friction is extremely low. A theoretical model of stress distribution in overpressured sedimentary basins was developed to demonstrate changes in stress magnitude and orientation with depth in areas where gravitational sliding controls the extensional faulting. Also, a FORTRAN code was written for inverting breakout orientation data from deviated boreholes based on the method proposed by Qian and Pedersen (1991).

ANALYSIS OF THE RELATIONSHIP BETWEEN IN SITU STRESS AND BOREHOLE FAILURE FOR STRESS DETERMINATION AND

BOREHOLE STABILIZATION

An integrated methodology was developed to analyze the relationship between the in situ stress and failure of inclined boreholes. We have conducted a comprehensive series of calculations of the occurrence of borehole breakouts and drilling-induced tensile wall-fractures in arbitrarily inclined boreholes and showed how such observations can be used to determine stress orientation and magnitude, effective rock strength and the optimal mud weight for borehole stability. The results are summarized in the paper Compressive and tensile failure of inclined wellbores and direct determination of in situ stress and rock strength, Peska and Zoback 1995).

Optimally, there is a two-step procedure how to apply this methodology in practice:

1. Utilize observations of wall failures in inclined holes to constrain the in situ stress and effective rock strength assuming that independent information such as on the least principal stress, pore pressure and overburden is available.
2. Utilize the knowledge on the stress field from the previous step to predict optimal wellbore trajectories and mud weights to stabilize the wellbore.

Computer codes were written in Matlab programming environment to implement the methodology. The computations are based on the assumption that the rock is isotropic and it behaves elastically to the point of failure, which is controlled by the Mohr-Coulomb criterion.

The *GetStress* program computes the orientation and magnitude of the stress tensor (principal stresses are assumed to act vertically or horizontally) from the azimuth of borehole breakouts observed in an inclined borehole and from other a priori information. The program *may* be also used to constrain the rock strength as the conditions for failure are expressed by means of the critical strength and also the breakout width may be taken into account. The in situ stress may be also computed by the *BreakoutRotation* program, which is an improved version of the Barton and Zoback [1994] technique for stress magnitude measurement using observations of rotations in borehole breakout orientation in the vicinity of an active fault, penetrated by the borehole.

Once the stress state is known, the *GetFailure* program computes orientations of compressive and tensile failures in an arbitrarily oriented borehole and constrains mud weight or effective rock strength required stabilizing the wellbore. Directions of potential breakouts and tensile wall-fractures around holes of various inclinations and azimuths are shown using the "looking down the hole" convention, i.e. as if the reader is viewing the hole by looking down its axis and the breakout azimuth is displayed with respect to the bottom Side of the deviated borehole (the *FailureOrientation* program gives even a more detailed look at the stress concentration around an arbitrarily oriented borehole and makes it easier to understand the "looking down the hole" convention). The *Wellbore Trajectory* program also computes orientation and tendency to fail by compressive or tensile failure for the given stress field and borehole orientation but now the stress and hole orientation are functions of depth which makes possible to analyze stability along the whole borehole. Both programs are optimal to design a stable wellbore trajectory from the platform to the target under the assumption that the stress state was determined from observations in the surrounding wells.

REFERENCES

Anderson, R. N., P. Flemings, S. Losh, J. Austin, and R. Woodhams, In situ properties of a major Gulf of Mexico growth fault: Implications for behavior as a hydrocarbon migration pathway, *Oil*

Gas J., 92(23), 97-104, 1994.

Barton, C., and M.D. Zoback, Stress perturbations associated with active faults penetrated by boreholes: Possible evidence for nearcomplete stress drop and a new technique for stress magnitude measurements, *J. Geophys. Res.*, 99, 9373-9390, 1994.

Hart, B. S., P. B. Flemings, and A. Deshpande, Porosity and pressure: Role of compaction disequilibrium in the development of geopressures in a Gulf Coast Pleistocene Basin, *Geology*, 23(1), 4548, 1995.

Peska, P., and M.D. Zoback, Compressive and tensile failure of inclined wellbores and direct determination of in situ stress and rock strength, *J. Geophys. Res.*, in press. 1995. Qian, W., and L. B. Pedersen, Inversion of borehole breakout orientation data, *J. Geophys. Res.*, 96, 20093-20107, 1991.

Zoback, M.D., and J. H. Healy, Friction, faulting and in situ stress, *Ann. Geophys.*, 2, 689-698, 1984.

Zoback M.D., and P. Peska, In situ stress and rock strength in the GBRN/DOE Pathfinder well, South Eugene Island, Gulf of Mexico, *J. Pet. Technol.*, July 1995.

Temperature Mapping (G. Guerin, LDEO)

The mapping of the present day temperature distribution around Block 330 is now complete, and after 3-D numerical modeling of the conductive regime in this area, a 5-10 C° anomaly following the strike of the Red Fault can be observed in the depth range of the most productive sands. This observation is interpreted as the influence of warm hydrocarbon-bearing fluids migrating up along the fault, and will be used as a constraint for the 3-D numerical modelling of these circulations, under development.

Amplitude Mapping Analysis (R. Anderson, Wel He, LDEO)

This sub-task is now completed, with a patent filed and granted for geopressure mapping using seismic amplitude changes. In addition, considerable bypassed pay has been identified along the property line between Eugene Island blocks 330 and 338. New Wells to test the validity of the ~D analysis are in the planning stages by Pennzoil and Texaco for 1996 to be paid for entirely with industry funds. The A-8St continues to produce at about 1400 bbl/day, with total production now exceeding 800,000 bbl. At a royalty percentage of 18% and assuming oil prices of \$20/bbl this entire Class I Oils study will be paid for in an additional 3 years through the royalties paid to the US Treasury on oil from just this one successful well, located in no small part through the use of 4-D technologies.

Predicting the geopressure transition zone in the Plio-Pleistocene of offshore Louisiana,

Gulf of Mexico

Geopressure or overpressure is abnormally high pore fluid pressure. This condition occurs when the formation pressure exceeds the hydrostatic pressure. The surface that marks the first occurrence of geopressure in a sedimentary basin is termed the top-of-geopressure surface. Geopressure is common in sedimentary basins of all ages (Ferti 1976 and Anderson et al., 1991). These abnormally high fluid pressures are an extreme hazard to drilling, since the undercompensation for borehole pressures results in blowouts. The top-of-geopressure is a hydrodynamic subsurface. The topography and dynamics of the geopressure surface are closely related to thermal-chemical and dynamic evolution of the basin. An accurately determined top-of-geopressure surface and a quantitatively evaluated geopressed transition zone is of great significance in studying the fluid dynamics and thermal maturation of the basin, because hydrocarbon generation and migration are usually controlled by the pressure distribution.

Geopressure can be caused by many different physical, chemical, or tectonic factors. Aquifer head (Levorsen, 1954), tectonic compression (Finch, 1969 and Hubbert et al, 1959), sediment loading, compaction, and the absence of drainage systems (Dickinson, 1953; Hubbert et al, 1959; Jones, 1969 and Harkins et al., 1969), phase changes, or diagenesis, such as the water release from the phase change of montmorillonite to illite (Powers, 1967 and Burst, 1969), smectite dehydration (Bruce, 1984), gypsum to anhydrite (Heard et al., 1966), organic material maturation (Hedberg, 1974), aquathermal expansion of water due to the temperature variations (Levorsen, 1954), osmotic membrane phenomena (Hanshaw et al, 1965), and thick shale-sand sequences with the sand to shale ratio less than 15% (Harkins et al, 1969) have all been cited as causes of geopressure.

In the offshore basins of Gulf of Mexico, geopressure is caused by continuous sediment loading at fast sedimentation rates and to a lesser extent by clay phase changes (Jones, 1969). The excessive pore fluid pressure built up in such a short geological time frame (<2.5 ma) dissipates at an extremely slow rate due to the permeability bottle necks developed in interbedded sand and shale stratigraphic sequences (Mello et al, 1993).

The geopressure transition zone is the depth interval within which the hydrostatic pore fluid pressure gradually increases with depth to approach lithostatic pressure. The geopressure transition zone occurs at the permeability bottleneck. The bottom of the geopressed formation has not yet been reached by any wells drilled in the Gulf Coast region.

Acoustic velocity and bulk density are greatly effected by geopressure. Because the excessive pore fluid pressure partially supports the weight of rock column, the effective pressure exerted on the rocks is dramatically decreased. As a result the acoustic velocity and bulk density of geopressure formations are usually much lower than those of normally compacted formations at the same depth. For the same reason, a velocity inversion (from high to low) usually occur at the geopressure transition zone because velocity is proportional to the effective pressure. The decrease in velocity and density can be further enhanced by under-compaction of the rocks.

The original depositional porosity of sediments (often 65%) is partially preserved by under-compaction of sediments due to the geopressure. Under continuous loading at fast sedimentation rate, pore fluids of previously deposited sediments can not escape fast enough because of low vertical permeability, which effectively prevents further mechanical compaction of these sediments. With further burial, more fluids are generated from clay diagenesis and the

pore fluid pressure increases (Powers, 1967 and Spencer, 1987). We believe that the remarkable decrease in compressional-wave velocity and bulk density across the geopressure transition zone in the Gulf of Mexico is due to coupling of pore fluid pressure and porosity preservation.

The geopressure transition zone is also characterized by abnormally low vertical permeability, high salinity, and high temperature gradients (Dickinson, 1953; Bredeheft et al., 1968; Burst 1969; Jones, 1975; Hunter, 1990 and Tigert et al., 1990). In a geopressure transition zone with fixed thickness, the higher the pore fluid pressure, the lower the acoustic velocity and density. A large negative seismic amplitude is expected. On the other hand, the thicker the geopressure transition zone, the lower the frequency of the seismic reflection.

In this chapter, we present a method that uses reflection strength of real seismic data to predict the top-of-geopressure surface. We use forward seismic modeling and cross-correlation to quantitatively estimate the thickness of the geo pressure transition zone. Once validated, these methods are applied to a 2D seismic survey acquired in the South Eugene Island Area offshore Louisiana Gulf of Mexico.

The acoustic velocity transition observed in sonic logs suggests that the geopressure transition zone can be quantified in terms of two variables: pore fluid pressure gradient and the transition zone thickness. The well data also suggest that the formations below the bottom of the geopressure transition zone are highly overpressured. The well data also indicate that the velocity changes are significant only when the pressure gradient ranges from 13.6 to 18.1 Mpa/Km (0.6 to 0.8 psi/ft). As the pore fluid pressure approaches the overburden pressure, no further decrease in velocity occurs. Our prediction technique is reliable only in defining the top portion of the geopressured zone.

Background of geopressure prediction techniques

Geophysical methods for detecting and predicting the top-of-geopressure surface can be classified into drilling methods, wireline logging methods, reflection seismic methods, and gravity or electric-magnetic potential field methods. The first two methods can only be performed when wells penetrate the top-of-geopressure surface. Seismic and potential field methods require only surface measurement. Potential field methods suffer from the limitation of being unable to distinguish overpressured formations from massive shale formations. The efficiency of reflection seismic methods are addressed in this chapter.

Many attempts to identify reflectors from the top-of-geopressure fail because the thickness of the transition zone can vary greatly over short distances (Anderson et al., 1992). Seismic interval velocity analysis (Pennebakker, 1968 and Reynolds et al., 1971) and inverted pseudo velocity or acoustic impedance analysis Musgrave et al., 1965 and Martinez et al., 1991) attempt to detect interval velocity or impedance changes across the top-of-geopressure surface. Using velocity techniques, the top-of-geopressure surface is interpreted as the depth where the internal velocity trend departs from the velocity trend expected under normal compaction conditions. The velocity technique works well on sonic logging data, which have high resolution, but fails for lower resolution velocities determined by stacking and migration. The pseudo velocity and impedance derived from seismic inversion, although have higher resolution, fails due to its lack of low frequency information (He et al., 1995). Missing the onset of geopressure can cause inconsistency in the predicted top-of-geopressure surfaces even within a single vintage of seismic data, this scenario deteriorates in areas where geopressure pressure transition zones

are thick or highly variable.

Changes in seismic reflection strength (instantaneous amplitude) of reflection seismic data can be used to detect geopressures as long as a sound relationship between the velocity transition and geopressure transition can be established. Our approach is to develop techniques that can distinguish seismic amplitude anomalies caused by geopressure transition zones from other reflections. We detect reflections from acoustic transition zones. Because reflection strength measurements contain low-frequency energy contained in original seismic traces, the reflections from acoustic transition zones can be enhanced and separated from other reflections by low-pass filtering. Reflection strength estimates derived from velocity transition models are used in the design of these filters. Top-of-geopressure can be directly detected as the uppermost boundary reflector between the high and low amplitude regimes in the reflection strength cross-sections (Anderson et al., 1992 and He et al., 1992 and 1994). The geopressure transition zone can also be imaged.

Characteristics of seismic reflections from geopressure transition zones

The appearance of geopressure on seismic data

In the Plio-Pleistocene basin of the Gulf of Mexico such as the South Eugene Island area geopressured formations produce observable features on reflection seismogram and wireline logging records. Substantial weakening of seismic amplitude is observable in time windows between about 1,500 ms and 3,000 ms on the eastern and western footwalls of the central Eugene Island basin and between 2,800 ms and 4,000 ms on the hanging wall. This weakening is caused by strata with less internal acoustic impedance contrast than normally pressured strata. Deepwater turbidities have reflectors of normal amplitudes; they are located beneath the weakening zones in the center of the basin. Salt diapir structures are seen beneath both footwalls. The boundaries of the weak reflection regions do not necessarily follow stratigraphic sequence boundaries.

Distinct features of the geopressure transition zone in seismic data

The generalized reflection coefficient of a transition zone in a laterally homogeneous acoustic medium has the form of a superposition integral (Wolf, 1937). The maximum amplitude is proportional to the ratio between the velocities at the top and bottom of the transition layer. The cut-off frequency (the highest frequency preserved) is inversely proportional to the thickness of the transition layer (Seo, 1978). An acoustic medium with a transition zone not only attenuates reflected seismic energy, but also greatly changes the phase of the reflected seismic waveforms (Bortfeld, 1960 and Gupta, 1965). We have generated two groups of seismic models to illustrate the seismic reflection effects of changing the velocity and thickness of the transition zones. Group I models have a transition zone with constant thickness and varying velocities of the underlying layer Group II models have a transition zone that varies in thickness with a constant velocities of the top and bottom layers. The cut-off frequencies are dramatically reduced as the transition thickness increases. The reflection energy increases with the velocity contrast. Small

increases of cut-off frequency are also observed for Group I models. These basic seismic characteristics of the geopressure transition zone are the main features on which our geopressure predicting technique is based.

In practice, the post-stack seismic data are usually treated as zero-offset seismic reflections. A seismic trace observed in an area with geopressured formations consists of reflections from both discrete geological events and the transitional zone. These seismic traces can be modeled as the convolution of a reflection coefficient function and a seismic source function. Using seismic data processing techniques, it is possible to separate the transitional events from the discrete events in an observed seismic trace.

Predicting top-of-geopressure surfaces using our seismic amplitude technique

We constructed a geological model consisting of an acoustic transition layer with varying thickness and several discrete layers with constant velocities. Using the first derivative of a 35 Hz, zero-phase, Ricker wavelet as seismic source, a synthetic seismic section was generated using a finite element seismic modeling algorithm (Teng, 1989).

Because our prediction technique is to detect the top-of-geopressure surface in two-way traveltimes domain in which the convolution forward model is used in data processing, a synthetic model generated from a forward model other than convolution is necessary to test our prediction technique independently.

Our first step is to detect the low-frequency seismic reflections in the synthetic section. Using complex seismic trace analysis (Taner et al., 1979). The algorithm treats a real seismic trace as the real part of a complex signal. with an imaginary part is equal to Hilbert transform of the real part. The reflection strength is quantified by the envelope (magnitude) of this complex function. The complex seismic trace analysis was applied to compute the reflection strength of our test model. The reflection strength section is composed only of low frequency reflections.

Thick geopressure transition zones only contribute to low frequency contents in reflection seismic data, whereas large velocity contrasts between the top and the bottom of transition zone only contributes to large amplitudes. Therefore, our second step is to distinguish the reflections contributed by the transition layer from those contributed by discrete layers. Since the generalized reflection coefficient of typical transition zones contains mostly low frequencies, we designed a lowpass filter than enhance those frequencies. We took this filter to be simply the low-frequency part of the amplitude spectrum of the generalized reflection, up to the first zero. We then apply this filtered to the reflection strength. The bandwidth of the lowpass filter depends on the thickness of the velocity transition zone, which is unknown. We use a filter with an intermediate bandwidth (estimated from assumption), which is effective enough to enhance the majority of transition zone reflections. On the filtered reflection strength section, the top-of-geopressure surface can be interpreted as the uppermost boundary between the high (shallow) and low (deep) amplitude regimes. The top of the transition zone is interpreted as the enhanced (or unchanged) reflectors. The estimated top and bottom of the transition zone is almost identical to that of the true velocity model. Our processing technique can be visualized more clearly using a single seismic trace extracted from the synthetic section.

Verification of the prediction technique

We apply the technique to a synthetic trace generated from sonic and bulk density logs from Eugene Island well 331-SH-1. Both sonic and density logs show a transition from high values to low values across the geopressure transition zone.

The top of sonic velocity transition is at 2,460 ms (2,621 m), and the measured pressure gradient is 13.6 Mpa/Km (equivalent to mud weight of 1,400 Kg/m³). The bottom is at 2,600 ms (2,792 m), and it corresponds to a 18.1 Mpa/Km gradient (1,800 Kg/m³). Acoustic velocity at the top and bottom of the geopressure transition zone are 2.772 m/s and 2.242 m/s, respectively (a 19% decrease).

The reflection strength derived from the complex seismic trace analysis is lowpassed compared with data. The highest frequency preserved in both traces is less than 30 Hz. A velocity transition model with thickness of 140 ms was constructed. The filter is obtained and applied to the reflection strength traces. The reflections from the geopressure transition zone are clearly seen at 2,460 ms on both filtered traces.

These results suggest that our geopressure prediction technique can be used to identify the top-of-geopressure surface using seismic amplitudes. However, the nonuniqueness introduced by the low frequency cyclicity of the sedimentary sequences may sometime affect the interpretation of the top-of-geopressure. Constraints from well logs are required for two reasons: 1) a well must be used to provide a *priori* knowledge of the geopressure transition zone at one location to construct the low-pass filter; and 2) the pressure detected in the well must be used to calibrate the occurrence and depth of the top-of-geopressure surface.

Prediction of the top-of-geopressure surface in the Plio-Pleistocene basin in offshore Louisiana Gulf of Mexico

We use a 2D seismic survey acquired in 1983 in the Eugene Island Area of offshore Louisiana to examine the feasibility and accuracy of our geopressure predicting technique. The survey area is about 90 Km (east-west) by 41 Km (north-south) with approximately 3.2 Km spacing between north-south "inlines" and 6.4 Km spacing between east-west "crosslines". There are 110 seismic lines contained in this survey. The survey covers the entire Eugene Island South Addition Area Block 330 minibasin, and its vicinity. The stacked and migrated seismic data of relative seismic amplitude ("true" amplitude) have a frequency range from 6 to 60 Hz.

Regional geology

The sedimentation history of the offshore Louisiana sub-basin is well studied by numerous authors (e.g., Galloway et al., 1991). Significant sedimentation in the offshore Louisiana did not occur until the Jurassic rifting of the Gulf of Mexico and the subsequent Laramide Orogeny and its uplift of the Rocky Mountains. Abundant terrigenous materials from erosion of the Rocky Mountains were delivered into the Northern Gulf of Mexico Basin, but were delayed by a lower Cretaceous barrier reef system that developed along the hinge zone of the Gulf. The Laramide erosional products finally breached the reef in the Tertiary, and the ancestral Mississippi River delta system rapidly dumped an enormous thickness of sediments

into the Gulf Coast basin. The thickness of progradationally deposited sand and shale sequences in the Cenozoic reached at least 12,000 m, and the thickness of the Pleistocene alone reached more than 3,000 m. This deposition took place in only about 5.3 ma (Galloway et al., 1991). The Pre-Tertiary sediments were buried, loaded, and heated with unusual rapidity. This rapid loading triggered the massive migration of the Louann salt toward the surface and to the south into the deepwater continental slopes. Pore pressures within the deeper sediments increased above hydrostatic, and large volumes of hydrocarbons were generated and migrated to shallow traps. These processes continue to this day (Anderson et al., 1991).

Large-scale hydrodynamic processes are coupled with the ongoing deposition of the massive sedimentary load. Convection is occurring in all three of the major hydrological regimes active in the Louisiana Gulf Coast. At shallow depths, meteoric flow, controlled by topography and directed towards the shelf, mixes with upward moving connate water and diagenetic fluids from deeper in the basin. At mid-depths, considerable dissolution of salt occurs producing an unstable layer of heavy, dense, and highly saline pore fluids.

Salinities in Pleistocene sediments are often found to be more than 4 times greater than sea water. In the deepest portion of the basin, metamorphism and hydrocarbon maturation reactions release large volumes of high-temperature, gas-charged and extremely buoyant fluids. Thermal build-up and restricted fluid flow are associated with this geopressured zone which dominates the deeper compressional system within the basin. Hydrothermal fluids migrate both laterally and vertically for considerable distances (Anderson et al., 1991).

Several minibasins were formed in the survey area by the withdrawal of a salt canopy approximately 2 ma ago. These minibasins are situated on the major shelf-margin deltaic depocenters of Plio-Pleistocene age and are bounded by regional and counter-regional growth faulting systems. Their evolution is characterized by three sedimentary phases: prodelta, proximal deltaic, and fluvial (Alexander et al., 1995). In the prodelta phase, bathymal and outer neritic shales and turbidities loaded and mobilized an underlying salt sheet. During the proximal deltaic phase, salt continued to withdraw from beneath the minibasin and low stand shelf margin deltas deposited across a regional growth fault zone system, which grew along the northern margin of the minibasin. Sediment accumulation and fault slip rates were high as thick sequences of deltaic sands were deposited on the footwall of the fault system. During the final fluvial phase, salt withdrawal waned and the creation of accommodation space within the minibasins ceased. The Eugene Island minibasin was filled less than 500,000 years ago and the lowstand deltaic system prograded southward (Alexander et al., 1995). Many hydrocarbon reservoirs discovered in the study area were formed during the second and third phases. Continuous sediment loading at fast sedimentation rates and clay diagenesis caused geopressures to occur widely.

Velocity characteristics of geopressure transition zone

Well logs provide the starting point for understanding the behavior of acoustic velocity in the geopressure transition zone. More than 500 wells have been logged in this area. Among them, 107 wells penetrated the to-of-geopressure surface. A 19% velocity decrease is observed in the geopressure transition, which has a pressure gradient that varies from 13.6 to 18.1 Mpa/Km within a 140 ms time window. We use one well to design the lowpass filter for the entire seismic survey.

The pore fluid pressure gradient measured at the bottom of the well is 19.7 MPa/Km,

well above the 10.5 Mpa/Km hydrostatic pressure gradient. Nevertheless, the sonic log does not show any transition at that depth, because only pressure gradients in between 13.6 Mpa/Km and 18.1 Mpa/Km can produce an observable velocity transition. The filter design for the velocity transition use a 30 Hz, zero-phase Ricker wavelet. This filter is applied to all the reflection strength traces computed for the entire 2D seismic survey in the next section.

Seismic data analysis to predict the top-of-geopressure surface

The top-of-geopressure surface is interpreted as the uppermost reflector that separates high amplitude region above from the low amplitude regions below, using the top-of-geopressure surface in the test well as reference. The geopressure surface is depressed in the center of the EI-330 minibasin due to the thick sediment load. The surface rises near bounding faults on both sides of the minibasin. It intersects stratigraphic and lithologic interfaces. Our results agree well with the top-of-geopressure surface detected in the another well.

Our technique allows the top-of-geopressure surface to be systematically interpreted across faults and other structural boundaries. The spatial consistency between stratigraphic horizons, faults, and the to-of-geopressure surface can be achieved. Such consistency is essential to integrate geopressure interpretations with other geological and geophysical data successfully.

By applying the same procedure to the other 109 seismic lines, we are able to predict the top-of-geopressure surface consistently with respect to faulting and stratigraphic configuration in these minibasins. The interpreted top-of-geopressure surface is then converted from two-way travel time to depth using the interval velocity derived from the corresponding stacking velocity of each seismic line. The compartmentalization of the predicted geopressure surface shows individual pressure chambers being bounded by major growth faults.

Accuracy and reliability of the predicted top-of-geopressure surface

The accuracy and reliability of the predicted depth to top-of-geopressure surface is investigated by comparing it with that detected by well logs and mud weights. Major discrepancies as well as some other subtle differences are present in a few places. The map based on seismic data includes faults, and thus it has much higher lateral resolution than the map based on wells. The agreement is better at the well locations themselves. The root-mean-square error is about ± 107 m. The largest errors are introduced from eighteen wells, which are located in areas with complex geological structures, such as shallow salt diapirs. If we exclude these 18 wells, the root-mean-square error is reduced to ± 46 m.

Quantitative evaluation of geopressure transition zone

If the geopressed formations share the same hydrodynamics, pressure differential between the top and bottom of the transition zone should be the same everywhere, regardless of the thickness of the transition zone. Quantitatively estimates of the geopressure transition zones can be obtained through the correlation of pressure gradients and acoustic velocities. The thickness of the geopressure transition zones in the wells is not constant, but the measured pressure gradients tend to linearly correlate with velocity contrasts across the geopressure transition zones. This correlation is used to define an empirical, linear relationship between pressure gradient and velocity.

We develop a suite of velocity transition models with fixed velocity contrast (22.7%) and

varying thickness of the velocity transition. Thirty models were generated with thickness increments of 5 ms, up to a maximum thickness of 240 ms. Using a 30 Hz, zero-phase Ricker wavelet as the source function, synthetic seismograms were computed for each of the thirty velocity models. Reflection strength tracts were then computed.

Using the previously interpreted top-of-geopressure surface, we can compute cross-correlation functions between the modeled and observed reflection strength functions. The velocity model corresponding to the maximum correlation among the thirty cross-correlation functions is then chosen as the best velocity transition model for that trace. The time lag of the maximum cross-correlation function is used to precisely locate the final, predicted top-of-geopressure surface. This technique produced an improved top-of-geopressure surface, an estimate of the thickness, as well as estimate of the thickness of the velocity transition and associated geopressure transition zone.

Minor time shifts are observed between the newly obtained and previously predicted top-of-geopressure surfaces. The topographic variations of the predicted bottom of geopressure transition zone are different from those of the top-of-geopressure surface. The largest deviations are observed near the large growth fault systems.

Using the interval velocity derived from the stacking seismic velocity, the final, predicted top-of-geopressure surface and the bottom-of-geopressure surface are converted from time to depth. The actual pore fluid pressure is computed from the predicted pressure gradients in the geopressure transition zone. The pore fluid pressures above the top-of-geopressure surface are at hydrostatic pressures. Pore fluid pressures below the bottom of geopressure transition zone are not estimated, because the pressure gradients are greater than 18.1 Mpa/Km in the study area and can not produce enough velocity contrast to be observable by our analysis. Two wells penetrating the top-of-geopressure surface are also projected onto the quantitatively predicted geopressure transition zone. The agreement between wells and prediction is good.

Geological significance of the predicted geopressure transition zone

The geopressures were developed in the early Cenozoic, when large amounts of clastic sediments were rapidly deposited. Subsequently, they have evolved along with the structural, stratigraphic, and thermal conditions. Large amounts of heat are trapped within the geopressed formations because no advective heat transport occurs across the top-of-geopressure. The effects of heat insulation on thermal evolution are two fold. On one hand, the heat transport to the hydrostatic zone is reduced, causing much lower formation temperatures in the hydrostatic zone than average temperatures observed in Tertiary basins without geopressing. On the other hand, the trapped heat may have significant impact on the maturation of the deep Cenozoic organic source rocks. Strong thermal anomalies in the hydrostatic zone are observed along the red fault in the study area. They are caused by heat carried by transient fluids expelled from the overpressured formations along these faults (Anderson et al., 1991). These thermal anomalies indicate that many of the regional growth faults in the study area are still active at the present time. When pore fluid pressures within the geopressed formation continuously built up to exceed the minimum horizontal stress, periodic reopening of these faults occurs usually parallel to the regional faults. Consequently, the reopening releases tremendous amounts of fluid from the overpressured formations into the reservoirs in the hydrostatic zone.

The periodic reopening of growth faults every two thousand years is the mechanism for

present-day fluid migration. The pressurized fluid mixtures with high temperatures migrate from the geopressed formations to fill reservoirs in the hydrostatic zone and balance the pressure and temperature differences. Overproduction of some shallow reservoirs (Anderson, 1993) may be associated with this active fluid flow. To prove and quantify such a fluid recharging process, much work is still left to be done.

There is a good correlation between the locations of some large oil fields and areas with large horizontal pressure gradient. The horizontal pressures are highest near the top-of-geopressure surface, in regions where the topography of the surface is steep. The oil fields tend to occur in these areas. Since steep topographic gradients are probably associated with faults, we propose that the correlation is due to oil being forced up from greater depths along these faults by geopressure.

Conclusion

Geopressure transition zones are characterized by monotonically decreasing acoustic velocities in our study area. In our method, reflection strength is successfully used to extract the low-frequency content of seismic reflections needed to define acoustic transition zones. The top-of-geopressure surface, associated thickness and gradients of geopressure transition zones are obtained deterministically. Good agreement between the predicted results and measured results in wells is observed. Our prediction method is robust and effective. The accuracy of the seismically predicted regional geopressure surface is within ± 46 m, using only one well as control, which is more accurate than the results obtained from other seismic methods.

The cross-correlation technique has several advantages over the seismic inversion technique. Accurate phase information is not required, because the technique uses phase-free reflection strength information. The implementation of our technique does not suffer from numerical instability. The cross-correlation technique is a deterministic method, of which all possible models are already generated from the well logs. The results obtained can be directly used to other geological analysis.

Missing the onset of the geopressure is avoided in our geopressure prediction method even in areas with highly variable geopressure topography. The predicted and characterized geopressure transition zones are reliable and accurate. We have successfully tested our method in other basins besides the Gulf of Mexico.

References

Alexander, L., and P.B. Flemings, 1995, Geologic evolution of a Plio-Pleistocene salt-withdrawal minibasin: Eugene Island Block 330, Offshore Louisiana: American Association of Petroleum Geologists Bulletin, v.79, p.1737-1756.

Anderson, R.N., 1993, Recovering dynamic Gulf of Mexico reserves and the US. Energy future: Oil & Gas Journal, week of April 26, PennWell Publication.

Anderson, R.N., W. He, M.A. Hobart, C.R. Wilkinson, H.R. Nelson, 1991, Active fluid flow in the Eugene Island area, offshore Louisiana: The Leading Edge of Geophysics, v.10., p.12-17.

Anderson, R.N., and W. He, 1992. Method and apparatus for petroleum and gas exploration: US.

Patent No.5,311,484.

Bracewell, R.. 1965. The Fourier transform and its applications: M~raw-Hill Book Co.

Bredehoeft, LD., and B.B. Hanshaw, 1968, On the maintenance of anomalous fluid pressures. I. Thick sedimentary sequences: Geological Society of America Bulletin, v.79, p.1087-1106.

Bordeld, R., 1960, Seismic waves in transition layers: Geophysical Prospecting, v.8, p. 178-217.

Bruce, C.H., 1984, Smectite dehydration-Its relation to structural development and hydrocarbon accumulation in Northern Gulf of Mexico Basin: American Association of Petroleum Geologists Bulletin, v. 68, p.673-683.

Burst, J.F., 1969, Diagenesis of Gulf Coast clayey sediments and its possible relation to petroleum migration: American Association of Petroleum Geologists Bulletin, v.53. p.73-93.

Claerbout, J.F., 1985, Fundamentals of geophysical data processing with applications to petroleum prospecting: Mcciraw-Hill Book Co.

Dickinson, G., 1953, Reservoir pressures in Gulf Coast Louisiana: American Association of Petroleum Geologists Bulletin, v.37, p. 410A32.

Fertl, W.H., 1976. Abnormal formation pressures-Implications to exploration, drilling, and production of oil and gas resources: Elsevier Scientific Publishing Company, Amsterdam-Oxford-New York.

Finch, W.C., 1969, Abnormal pressure in the Antelope field, North Dakota: Journal of Petroleum Technology, v.21, p.821-826.

Galloway, W.E., D.G. Bebout, J.B. Fisher, J.B. Dunlap Jr, R. Cabrera-Castro, J.E. Lugo-Rivera, and T.M. Scott, 1991, Cenozoic in The Gulf of Mexico Basin: Geology of North America, A. Salvador, Editor, v. J, p.245-324.

Gupta, R.N., 1965, Reflection of plane waves from a linear transition layer in liquid media: Geophysics, v.30, p.122-132.

Hanshaw, B.B. and E-an Zen, 1965, Osmotic equilibrium and over-thrust faulting: Geological Society of America Bulletin; v.76, p.1379-1386.

Harkins, K.L. and W. Baugher III, 1969, Geological significance of abnormal formation pressures: Journal of Petroleum Technology, August, p.961-966.

He, W. and R.N. Anderson, 1992, A seismic amplitude analysis approach for mapping the top-of-geopressure surface in the Pleistocene, Offshore Louisiana: EOS Transactions, American

Geophysical Union, v.73, p.304.

He, W., 1994, Mapping the top-of-geopressure surface in the Pleistocene, offshore Louisiana, Gulf of Mexico: M. Phil. thesis, Columbia University.

He, W., R.N. Anderson, and Y.& Teng, 1995, Application of seismic inversion to quantitative mapping geopressure transition zones in the Pleistocene, offshore Louisiana, Gulf of Mexico: The 2nd International Conference on Theoretical and Computational Acoustics, Honolulu, Hawaii.

Hedberg, H.D., 1974, Relation of methane generation to undercompacted shales, shale diapirs, and mud volcanoes: American Association of Petroleum Geologists Bulletin, V.58, p.661-673.

Heard, H.C., and W.W. Rubey, 1966, Tectonic implications of gypsum dehydration: American Association of Petroleum Geologists Bulletin, v.77, p.741-760.

Hubbert, M.K., 1940, The theory of ground-water motion: Geology, v.48, Part 1, p. 785-944.

Hubbert, M.K., and W.W. Rubey, 1959, Role of fluid pressure in mechanics of overthrust faulting. I. Mechanics of fluid-filled porous solids and its application to overthrust faulting: Geological Society of America Bulletin, v.70, p.115-166.

Hunt, J.M., 1990, Generation and migration of petroleum from abnormally pressured fluid compartments, American Association of Petroleum Geologists Bulletin, v.74, p.1-12. Jones, P.H., 1969, Hydrodynamics of geopressure in the northern Gulf of Mexico Basin: Journal of Petroleum Technology, July, p.803-810.

Levorsen A.I., 1954, Geology of Petroleum: W.H. Freeman, San Francisco, 703 p.

Martinez, R.D., J.D. Schroeder, and G.A. King, 1991, Formation pressure prediction with seismic data from the Gulf of Mexico: Society of Petroleum Engineers, Formation Evaluation, no.3, p.27-32.

Mello, U.T., G.D. Karner, and R.N. Anderson, 1994, A physical explanation for the positioning of the top of overpressure in shale-dominated sequences in the Gulf Coast Basin: Journal of Geophysical Research, v.99, p.2775-2789.

Musgrave, A.W., and W.G. Hicks, 1965, Outlining shale masses by geophysical methods: American Association of Petroleum Geologists Bulletin, Memoir no.8, p.112-136.

Pennebaker, E.S., 1968, Seismic data indicate depth, magnitude of abnormal pressures: World Oil, v.166, p.73-78.

Powers, M.C., 1977, Fluid-release mechanisms in compacting marine mudrocks and their importance in oil exploration: American Association of Petroleum Geologists Bulletin, v. 51, p.1240-1254.

Reynolds, E.B., J.E. May, and A. Klaveness, 1971, The geophysical aspects of abnormal fluid pressures: Abnormal subsurface pressure, Houston Geological Society Study Group Report p.31-47.

Seo, J.H., 1978, Detection of abnormal geopressure using seismic reflectivity: M.A. thesis, University of Texas at Austin.

Spencer, C.W., 1987, Hydrocarbon generation as the mechanism for overpressuring in the Rocky Mountain region: American Association of Petroleum Geologists Bulletin, v.77, p. 2006-2010.

Taner, M.T., F. Koehler, and R.E. Sheriff, 1979, Complex seismic trace analysis: Geophysics, v.44, p.1041-1063.

Tigert, V., and Z. Al-Shaieb, 1990, Pressure seals: their diagenetic banding patterns: Earth Science Reviews, v.29, p.227-240.

Teng, Yu-Chiung, 1989, Three-dimensional finite element analysis of waves in an acoustic medium with inclusion: Journal of Acoustic Society of America, v.86, p.4144-22.

Wolf, K. 1937, The reflection of elastic waves from transition layers of variable velocity: Geophysics, v.2, p.357-363.

Wyllie, M.R.J., A.R. Gregory, and G.H.F. Gardner, 1958, An experimental investigation of factors affecting elastic wave velocities in porous media: Geophysics, v.23, p.459-493.

Task Five - Modeling
Larry Cathies - Task Manager

OBJECTIVE:

The objectives of the modeling task as set forth in the DOE proposal were to address:

- The cause of pressure, temperature, fluid chemical, and porosity anomalies near the Red Fault,
- The possible sources of oil and gas moving up the fault, and
- The causes of organic and inorganic chemical alteration near the fault

This was to be done realistically and with the aim of facilitating the interpretation of data collected in the study area. Particular attention was to be focused on: (1) porosity and excess pressure development in the RVE, (2) hydrocarbon maturation in the RVE, (3) detailed fluid flow near the fault focusing on the detailed distribution of high permeability sands, (4) the effects of salt diapirism on subsurface temperatures, (5) the effects of fault movement on fault permeability and fluid venting out of the fault, (6) the effects of gas venting on oil migration, (7) the transport of oil as a separate phase up the fault, and (8) the effects of fluid flow (water, gas, and oil) on rock chemistry and mineralogy. The modeling was to be carried out in 3D as well as 2D.

No computer software existed that was adequate to these tasks. To even attempt to interpret specific geologic data, the models needed to couple disparate phenomena such as faulting, salt diapirism, sealing and overpressure development, temperature and fluid flow. The software needed to do so realistically, specifically for the configuration of faults and salt domes in the South Eugene Island Block 330 area and in three dimensions. To fill these needs we have (in collaboration with a finite element modeling company, the Computational Mechanics Corp. of Knoxville, Tennessee) developed a basin modeling system capable of investigating the highly coupled phenomena associated with hydrocarbon migration up the Red Fault of the South Eugene Island Minibasin. The modeling system has been applied to the geologic data collected under other tasks of the DOE project.

The AKCESS.BASIN Modeling System we developed and applied to the SEI Block 330 region is described in full in this final report. Because there is a great deal of material to report, the report is organized hierarchically: Section II gives an executive summary of the principle accomplishments of Modeling Task 5. Section III reviews the plans and performance in each sub-task. References are given there to the detailed reports given in the various subsections of Sections IV. In this way it is hoped that an interested reader can both rapidly obtain an overview of what has been done and also rapidly find parts of the work of specific interest.

It is probably natural that not all of the work proposed has been accomplished in exactly the fashion proposed three years ago. Preparation of the geologic data in a fashion that takes account of diapirism, overpressuring, and faulting in three dimensions proved far more difficult and time consuming than we had anticipated. Substantial effort was also devoted to developing algorithms that accurately describe critical parameters such as thermal conductivity and permeability in the data cube. However some areas proceeded far better than originally envisioned, and many new results have been obtained. All the important principal subtasks will

be fully accomplished by the time the students involved in this project complete their Ph.D. theses. Furthermore, a powerful modeling capability has been created that is supported by a private company and a growing group of academics spread over five separate institutions. This is certain to impact basin studies for years to come.

SUMMARY:

The principal accomplishments to date under this proposal and the matching projects it encompasses are:

1. Development of a 3-D finite element basin modeling system with sound and fully articulated fundamentals and accurate algorithms for thermal conductivity and sand permeability. This provides for easy input of highly detailed three dimensional geologic data with options to infer salt diapirism from the surface pattern of sedimentation and sea level takes into account all major physical and chemical phenomena: (e.g., isostasy, salt diapirism, faulting, overpressuring, seals, hydrocarbon maturation, fluid flow driven by haline or thermal convection, water table topography, or overpressuring, salt dissolution and transport, etc.). It solves the coupled equations with an easy to use but versatile and controllable finite element solver, which can execute rapidly on parallel machines, and has convenient and easy to use visualization tools at all stages.
2. Distribution of that modeling system across 5 institutions (Cornell, LSU, Michigan Tech., and Bowling Green) with appropriate training of professionals and students at each.
3. Extensive benchmarking demonstrate the validity of various aspects of the modeling system (Section IV).
4. Application of the Modeling System to eight - 100 km long 2D seismic lines centered on the South Eugene Island Block 330 area of the Gulf of Mexico and one 1200 km interpreted N-S section. The modeling shows that the flexural rigidity of the Gulf lithosphere is less than about 10^{23} M-m. The history of salt movement over the last 20 Ma inferred directly from sedimentation shows evolution from a salt sheet to multiple minibasins and domes. The domes have a major impact on subsurface temperature ($\pm 70^{\circ}\text{C}$ temperature anomalies above and below the salt domes) (Section II and V.)
5. Construction of a highly detailed 3-D data cube in the SEI 330 area resolving all principal sands and their displacement across four NE-SW faults over the last 3.4 Ma. The salt movement inferred from the pattern of sedimentation shows the burial of a local salt sill, and its remobilization into the South Eugene Island Block 330 Minibasin with the Red Fault at its northern margin.
6. Detailed analysis of bottom hole temperature data shows a positive temperature anomaly of about 5°C below the Pennzoil oil and gas fields roughly along the Red Fault and a negative (-5°C) temperature anomaly above the oil reservoirs. Modeling shows that temperature anomalies of this magnitude or greater will be produced by the insulating hydrocarbon-filled sand reservoirs. fluid flow could produce the positive anomaly below the reservoirs along the

Red Fault, but not the negative anomaly above the reservoirs. This suggests that the present day temperature field in the South Eugene Island Block 330 minibasin is due to thermal conductivity anomalies associated with hydrocarbon reservoirs and not rapid fluid flow (Section V).

7. Fluid flow modeling shows that pulses of overpressured fluid through the Red Fault can expel large quantities of water (and hydrocarbons), and produce significant temperature anomalies provided the permeability of the overpressured zone is on average more than -0.05 md. Sand units below, in, and above the transition from hard overpressure to hydrostatic fluid pressures were found to be very important in controlling fluid flow and temperature anomalies associated with rapid venting. Clear vitrinite reflectance and isotopic anomalies in the A6 sidetrack (but not in the Pathfinder well 1000 ft away) suggest pulses of fluid have been expelled up the Red Fault, but that the flow channels are highly localized. (Section V).

8.. Under a matching grant from the Gas Research Institute a new concept for sealing in which the flow of water (and other phases) is inhibited where there are multiple sand-shale (coarse-fine) interfaces and a non-aqueous (especially gas) phase present was conceived, tested in the laboratory, and shown to be applicable to the pressure transition drilled and cored by the Pathfinder well. (Section I).

9. The discovery that the part of the Red Fault penetrated by the Pathfinder well had a Poisson's ratio very close to that of a fluid led to the conception and quantification of a new hypothesis that significant fluid (water and hydrocarbons) migration may take place through propagating fractures. (Section V.)

By
Roger N. Anderson

Work Performed Under Contract No. DE-FC22-93BC14961

Prepared for
U.S. Department of Energy
Assistant Secretary for Fossil Energy

Chandra Nautiyal, Technology Manager
National Petroleum Technology Office
P.O. Box 3528
Tulsa, OK 74101

Prepared by:
Columbia University
New York, NY 10021

Application of Akcess.Basin to SEI Block 330 Area

INTRODUCTION

The AKCESS.Basin Modeling System was developed to investigate phenomena associated with hydrocarbon migration up the Red Fault of the South Eugene Island Minibasin. It is thought that hydrocarbons moved up this fault to charge Pennzoil's Block 330 oil and gas fields, which are among the largest accumulations of oil and gas in the Gulf of Mexico. Because the strata that host the oil and gas reservoirs are less than 1.5 ma old, and some only -0.46 ma, because there are temperature anomalies along the Red Fault that are of the form that pulses of fluid flow up the fault might produce, and because some of the Pennzoil Reservoirs have produced more oil than is conventionally thought possible (up to and perhaps more than 100% of the oil originally in place), it is thought that hydrocarbon migration up the Red Fault may have occurred very recently taking place at the present day. As part of this project the Red Fault was drilled to investigate these possibilities. The fault was drilled at the transition zone between soft and hard overpressure; massive amounts of data were collected and analyzed.

The part of the project reported here is concerned with modeling. Our charge was to develop a modeling methodology capable of realistically addressing temperatures and fluid flow in a data cube centered on the drilled portions of the Red Fault. The modeling was to be of large enough scale to encompass phenomena associated with and recent hydrocarbon migration up the Red Fault. The models were to address: (1) the cause of pressure, temperature, fluid chemical, and porosity anomalies near the Red Fault, (2) the possible sources of oil and gas moving up the fault, and (3) the causes of organic and inorganic chemical alteration near the fault. Specific attention was to be taken of: (1) porosity and excess pressure development, (2) hydrocarbon maturation, (3) detailed fluid flow near the fault focusing especially where high permeability sands were juxtaposed, (4) the effects of salt diapirism on subsurface temperatures, (5) the effects of fault movement on fault permeability and fluid venting out of the fault, (6) the effects of gas venting on oil migration, and (7) the effects of fluid flow (water, gas, and oil) on sediment mineralogy. The modeling was to be carried out in 3D as well as 2D.

These objectives, as reported below, have been largely met. Several new concepts of potential significance have emerged from the modeling. In particular it has been found that:

- (1) Temperature anomalies may be caused by the low thermal conductivity of the hydrocarbon reservoirs.
- (2) Hydrocarbons may migrate up faults as propagating fluid filled cracks.
- (3) Hydrocarbon gas may cause sealing and fundamentally control the pattern of fluid flow.
- (4) The porosity distribution in the study area is most compatible with a seal (pressure transition zone) that migrates upward through the section as sedimentation takes place.

THE GEOGRAPHIC CONTEXT OF THE MODELING

A critical question from the onset of the project was the size of the model volume required to capture the processes that drove and are driving fluid and hydrocarbon venting in up the Red Fault. Almost certainly the process scale is larger than the ~20 km dimensions South Eugene Island Block 330 Minibasin. Modeling was carried out on a range of scales to assure capture of the relevant processes: The largest scale was a 1200-km section running from the Arkansas-Louisiana boundary to the Sigsbee knolls. This line was used to constrain the flexural rigidity of the lithosphere and to show that salt diapirism is required to provide accommodation space for sediments deposited at the scales of the higher resolution modeling. Modeling on this scale was based on six interpreted seismic lines contributed by Arco, and two 2D seismic lines that were interpreted as part of this project by Mark Rowan and Colorado University.

The highest resolution modeling was carried out on a -30 x 30km scale. It focused on temperature the South Eugene Island Block 330 Minibasin. The geology up (n which the modeling is based was derived from the interpretation of well logs, 2D (Alexander, 1994 Cornell PhD thesis) and 3D (Coehlo, Cornell PhD thesis) seismic surveys, and well logs The detailed 3D modeling is based on nine NE-SW sections mapped across Pennzoil's 3D seismic survey. The sections capture all the major sand units in the cube.

REGIONAL MODELING

1200km Scale

100 km Scale Modeling

Modeling on this scale simulates the southward migration of the shelf edge and Modeling was carried out utilizing a method by which the modeler could specify the position of the shelf margin as a function of time. The oceanward increase of water depth on the continental shelf and slope, and the maximum water depth in the oceanic parts of the Gulf Basin were assumed to be the same in the past as today. With this assumption the paleo-ocean depth profile can be specified by tabulating the position of the shelf break at all modeling timesteps. Estimates of the shelf break position were made from the thickness and character of the sediments, and the position and geometry of salt domes.

The results of the modeling are described here for a single case. This case is known as Arco Line 10, and it is located to the west of the Eugene Island study area. The total length of the line is 199.54km. It extends from near the shoreline due south along the boundary between East Cameron/Vermillion and East Cameron South/Vermillion South. It extends slightly basinward of the latter boundary.

This model was constructed using 27 vertical pseudowells placed appropriately to capture the basic characteristics of the subsurface. Refinement of the model is possible and desirable in areas where this first pass does not accurately reflect the subsurface geology. The base of the salt section was assumed to be absent beneath minibasins, and to have a thickness below domes or walls so that its base was no deeper than the depth of the surrounding minibasin and the salt thickness was minimized. It seems likely, in light of subsalt imaging that is now appearing in vendor's displays at technical conventions, that the salt beneath domes and walls may actually be even thinner in some areas. We did not, however have extensive subsalt information so the estimates were made consistently. They can be modified in the future if necessary.

Temperature at the present time, after the basin is fully developed through forward modeling, shows that temperature increases with depth from a minimum of 3.9 degrees to a maximum of 412.6 degrees. The isotherms are elevated by up to 60⁰C beneath minibasins and depressed up to 80⁰C beneath salt domes. This is a result of the contrast in thermal conductivity between salt and sediment. Again, the anomalies may be somewhat exaggerated if the salt thickness in the model is larger than it should be. However similar magnitude temperature anomalies were computed by an extensive independent modeling study that was also part of this DOE project (Mello, 1994).

An important feature noticed by the simulations of compactive fluid flow is that fluid flow is significantly concentrated at the margins of the northernmost salt structure. This pattern of fluid flow out of minibasins and up along the margins of salt structures is observed for all of the modeled minibasins at various stages in their evolution. Most hydrocarbon migration occurs in conjunction (and possibly assisted by) connate water flow. The natural concentration of compactive flow at salt dome margins may in part account for the occurrence of hydrocarbon reservoirs above and along the margins of salt domes. It should be emphasized that the concentration of flow at the salt margins was not due to the margins having a greater than typical permeability. The permeability of the sediments adjacent of the domes in the models was the same as the permeability of the sediments elsewhere.

The modeling is described in more detail in Huntoon, et. al. (in preparation). The calculations reported there will include estimates of the regional hydrocarbon maturation and the fluid flow driven by maturation reactions as well as compaction.

SEI BLOCK 330 AREA MODELING

The most intensive modeling addressed processes on a 30 x 30 km scale in the main SEI study area. A three dimensional data cube was assembled and analyzed through modeling. Modeling requires a computational grid, material properties, and heat, fluid flow, and chemical computation. Below we first describe the construction and geometric analysis of the computational grid, then we describe the determination of the proper material properties and the thermal state of the data cube, and finally we describe the modeling and conclusions reached from it.

1. The 3D Modeling Grid (L. M. Cathles, Cornell)

The 9 NE-SW sections³ were processed to obtain the evolution of the SEI Block 330 area over the last 3.4 Ma. The grid consists of time horizons and appropriately-selected "pseudo-wells". Salt was redistributed in 3D by processing each section twice and solving a set of equations to make the salt redistribution as uniform as possible in 3D. The thickness of the present (0 ma) section is 8.5 km, and each section is about 12 km long. At 3.4 Ma the area that now holds the South Eugene Island minibasin and the Pennzoil oil and gas reservoirs was covered by a salt sheet about 2 km thick. Over the next 0.8 Ma this salt sheet was rapidly buried by thick shales. The sheet remobilized into a large dome at the right hand side (southern margin) of the data cube, in the area that is now the SEI minibasin. The salt dome was not uniform. It was large in the west, thinner in the middle, and very large on the far eastern side of the data cube. A salt ridge remains to this day on the eastern side of the data cube. Over the next 2.15 Ma this salt dome was itself loaded with sediments and remobilized. Its collapse provided the accommodation space for the SEI Block 330 minibasin. Starting about 1.5 Ma and continuing to the present, thin sands were periodically deposited over the whole area. Many of these sands are now filled with hydrocarbons.

The juxtaposition of sands across these faults is of interest, as many oil companies believe that fluids migrate up section by crossing the fault where a lower stratigraphic sand is juxtaposed against one higher in the stratigraphy. In this fashion fluids step up through the section. Fault plane (Allan-type) maps showing the juxtaposition of sands are often prepared from 3D seismic surveys, and the maps are then used to infer what connections there might have been at past times. The AGEOHIST pre-processor provides a way to automatically generate Allan-type sections over the full span of the basin's history, explicitly taking into account decompaction and eliminating the need for inference. Decompaction can be significant and can make a significant difference when specific sand-sand connections occur across the faults.

Sands on the upthrown (northern) side of the faults cut across the sands in the downthrown minibasin which block. There is a break in sand continuity in most of the faults about a third of the way across all the sections. This offset represents throw on the NE-SW trending fault captured between Lines 4 and 5. The fault plane sand connections captured by the grid allows Allan-type fluid flow to be calculated in our 3D basin simulations.

Present day temperature in South Eugene Island Block 330 is a particularly critical parameter for modeling. A principal hypothesis of this project, founded in geological/ geochemical reasoning most recently discussed by Whelan (1995), as well as in the geometry of the anomalies with respect to the main fault system (known as the "Red Fault System"), was that the migration of hot fluids along the fault planes could be responsible for a positive temperature anomaly observed there (Holland et al, 1990). Evidence for localized fluid migration through seepages along the fault system exists at the sea bottom in the South Eugene Island area (Holland et al, 1990). However, rapid fluid migration would be necessary to produce the observed anomalies.

Guerin (1995), using bottom-hole temperature data and a steady-state finite difference heat conduction model, concluded that if the temperature field is corrected for the effect of the salt domes a positive residue is left which is probably due to fluid advection. His model assumes the thermal conductivities are constant for each layer. By comparing the pure conductive heat transfer and pure advective one, Guerin conclude that the difference is due to fluid flow along the fault system.

McKenna (1994), did a similar study in the same area and, after recognizing the impossibility of resolving the spatially restricted thermal anomaly along fault planes, concluded that the thermal anomaly in the area could be explained by sedimentation differences between the downthrown and upthrown sides of the Red Fault System. Contrary to Guerin, McKenna concluded the same temperature anomalies attributed by Guerin to fluid flow were due to differential sedimentation across the Red Fault system.

Losh et al. (1994) observed that the well 330-PZ-6ST shows geochemical evidence of significant fluid flow but the Pathfinder Well located only 1000 ft away, does not. This suggests that the pathways for fluids along the Red Fault could be highly localized.

We followed the same steps as the previous authors, and compiled a database of bottom-hole temperatures. Our data set consists of approximately 400 measurements taken in vertical and inclined wells, as well as in exploratory and production wells. The information compiled was the depth of the temperature measurements, the temperatures and the time after stopping the mud circulation. Unfortunately, there is no data on the duration of mud circulation.

In the wells with more than one measurement at a single depth we applied the Homer plot technique as described in Dowdle and Cobb (1975) to correct for the cooling effect due to the mud circulation. The Homer method requires the mud circulation time as well as the time since the end of circulation at which multiple temperature measurements were made. Because the circulation time was not available, a sensitivity analysis was done to determine the impact of the mud circulation time on the magnitude of the Homer plot temperature correction. The Homer method gives similar corrected temperatures provided the circulation time is relatively short. The corrected temperatures shift significantly in the cases only when the circulation time exceeds about 14 hours. Dowdle and Cobb (op. cit.) pointed out that the Homer plot method is most reliable for short circulation times, basically for this reason. Common industry practice in the Gulf of Mexico makes it unlikely that circulation times exceeded 10 hours. Provided this is the case. It suggests it is possible to correct bottom hole temperatures to $t + 2^{\circ}\text{F}$ by assuming a circulation time of 6 hours. The time of circulation could be a few hours or as much as 10 hours and the correction would still be accurate to $\pm 2^{\circ}\text{F}$ (1.1°C).

There is, however, another potentially larger source of error that must be assessed. Because of the difference in mud temperature compared to local ambient, differences in diffusivity etc., it is possible that the slope for 6 hours circulation line used in the Homer plot correction may not be the same for all depths in all wells. Data from different Blocks in South Eugene Island show the gradients for a 6 hours circulation time obtained from the Homer plots versus depth. The average gradient is 9.0°F^{-1} with a standard deviation of $\pm 4.8^{\circ}\text{F}^{-1}$.

Because most of the wells in the SEI 330 area are inclined, all the temperature measurements were located at their proper spatial position. Then, using a 3D Krigging algorithm from Spyglass with 500 meters cells, we built a 3D data cube with the interpolated observed temperatures. Slices through this data cube show the same basic features observed by the authors cited above: temperature anomalies follow the strike of the Red Fault System and change with depth.

Bottom Water Temperature (by L. M. Cathles)

The temperature of the top surface in *AKCESS. BASIN* calculations is controlled by water depth, the water temperature above the thermocline, and the depth to the top and bottom of the thermocline.

For the South Eugene Island data cube, excellent data is available on the position of the thermocline (see Cathles, et. al, 1991). We assume the thermocline was in this same position over the last 3.4 ma of basin history.

Material Properties of SEI Block 330 Sediments (by D. Coehlo, Cornell)

Material properties such as thermal conductivity and permeability, and chemical parameters characterizing the rates of organic and inorganic reactions are needed for modeling. This section briefly summarizes the parameters used in the SEI Block 330 modeling.

Long Term Sediment Compressibility

Under a matching grant from the Gas Research Institute and this DOE grant all available porosity logs in the SEI study area were obtained and interpreted. Density logs were found to give the most reliable estimates. Six wells on the hanging wall of the Red Fault, and six on the footwall were selected for analysis.

The wells nearest the Red Fault typically show an increase in porosity below the top of overpressure, whereas the wells more distant from the Red Fault show a flat porosity profile below the seal. From 200-m depth to 1500 to 2000 m depth porosity decreases linearly with depth. Porosities above 200 m decrease more rapidly with depth and were not addressed in the modeling.

Depth was converted to effective stress in the hydrostatic interval above the top of overpressure and porosity regressed linearly against effective stress.

Thermal Conductivity (M. Luo and J. Wood. MTU: L. Cathles. Cornell) Thermal conductivity is a particularly critical parameter for this study. Thermal conductivity is a strong function of temperature, sediment porosity, and pore fluid composition. The temperature dependent media conductivity was obtained by: (1) obtaining the temperature-dependence of the grain, water, oil, and gas thermal conductivities, and (2) then combining them in an appropriate fabric mixture:

A paper showing that a scheme very similar to the above replicates thermal conductivities of water-saturated sediments to within *10% has been published by Luo et. al. (1995) as part of this DOE project. The difference between the Luo et al. scheme and the one given above is that the parallel and series grain thermal conductivities are constructed from sums of the mineral grain thermal conductivities, rather than from sums of the grain thermal conductivities lumped into sand, shale, carbonate sand, etc., end members, where the end members are calculated from their average mineral grain compositions. We have shown that the difference between these two schemes is at most about 1.5%. The lumped approach is geological, simple, flexible (the lumped end members are easily modified), and easy to use. The errors associated with the lumping in to lithologic types are much less than the 10% uncertainty in the mineral composition estimates and thus insignificant.

The parameters used in our thermal conductivity model, plus some other parameters discussed above and below, are:

Permeability in Block 330 Data Cube (By D. Coeblo, Cornell)

An extensive database on sand permeabilities in the SEI Block 330 study area was obtained from Pennzoil. It consisted of porosity and permeability measurements from core wall samples in many reservoirs in Block 330. This database was used to develop an empirical model that describes permeability in terms of porosity and sand-shale ratio. The model fits the observed data very well and will

allow, since our model calculations predict porosity changes appropriate sand permeabilities to be ascribed at past geologic times.

Our log model was found to fit the observed relations between porosity and permeability much better than the Karmen-Kozeny relation. The quality of the log model fit can be appreciated if $\log k$ is plotted versus porosity. The base permeability of sediments is a function mainly of the size of the mineral grains that comprise the sediment and the lithology of those sediments. The effects of porosity are added to this reference value with the amplitude of the porosity dependence modified by the fraction -of coarse sediment component. The sand permeabilities fit those observed in South Eugene Island Block 330 very well. The shale permeabilities are reasonable. The precise value of the shale permeability is not too critical as long as it is substantially smaller than the sand permeability, as is the case in our lithology-porosity model for permeability. The permeability model is a smooth function of porosity.

TTI and R Indices (M. Luo and J Wood, MTU; P. Meulbroek, Cornell)

TTI, a Lopatin-type time temperature index and vitrinite reflectance, R_0 , are two measures of sediment maturity that are used in our modeling. 'TI is calculated as described in Waples (1985,1990) by summing the products of the time in millions of years a sediment has spent in each 10^0C temperature interval and a temperature factor. For example a temperature just above 10^0C would have a temperature factor of 2, and a temperature just below 100^0C would have a temperature factor of 0.5.

A Sweeny and Burnham (1990) model for the R_0 measure of vitrinite reflectance is incorporated in Akcess.Basin. In this model:

These models have both been implemented in Akcess.Basin.

The chemistry of the light hydrocarbon gas and heavy oil can be specified in the program. The reactions have first order kinetics with the kinetic parameters as in Burnham and Braun.

The volume change associated with the hydrocarbon maturation reactions is calculated:

- (1)The specific volumes of type I kerogen is 0.83 cc/g.
- (2)The specific volumes of type II kerogen is 0.74 calg
- (3)The specific volume of bitumen and all chars is 0.83 cclg
- (4)The volume of hydrocarbon fluids is detenmined from an equation of state.

Hydrocarbon maturation is of interest in its own right because we need to know how much oil and gas could have been generated in the SEI minibasin. Hydrocarbon maturation is also important because the positive volume maturation reactions produce overpressures

With the bottom water temperature defined as a function of water depth, the material propensities of thermal conductivity, porosity, and sediment permeability defined in terms of calculable parameters, and a realistic evolution of the SEI minibasin defined from seismic data and well logs, we are in a position top model the SEI minibasin and interpret observations made there. In what follows we first discuss porosity modeling, then temperature modeling including the effects of episodic venting, and finally chemical modeling including hydrocarbon generation and maturity indicators.

Porosity Modeling (L. Cathles, Cornell; Matching funded by GRI)

Porosity depends on effective stress, but the porosity profile in a basin also

depends on whether there is relative movement of the pressure transition zone (seal) and the basin sediments. The Pathfinder well was logged from 6950 to 8300 ft depth in an interval where the pressure transitioned from soft (13.6 pound mud weight) to hard (16.3 pound mud) overpressure in two roughly equal steps. Below each of the major jumps in pore fluid pressure is a gas-filled sand. The gamma log indicates there are 40 to 50 transitions from sand to shale in the shale intervals above these gas sands. Shosa and Cathles (in preparation) have shown in laboratory experiments that under basin conditions of pressure and temperature and in the presence of a gas phase, an exit pressure of a few bars can be expected at each sand-shale interface within a basin. Since free gas is clearly present, and since the gamma logs show that there are enough sand-shale interfaces in both pressure transition zones to account for the increase in pressure by gas capillary exit pressure effects discussed by Shosa et. al., the pressure transition zones in the pathfinder well could be gas capillary exit pressure seals. If so, because gas exsolution is controlled by pressure and there is no lack of sand-shale interfaces in the upper part of the SEI minibasin, the position of the pressure transition zone there could have maintained a relatively constant depth, with sediments moving through the seal with time.

The porosity profile in a basin depends strongly on whether the seal is fixed to a particular strata or migrates through the sedimentary layers as sedimentation progresses. If there is no seal, compaction is linear until the minimum porosity of 0.1 is attained. If there is a seal overpressuring below the seal decreases the effective stress and inhibits compaction. If the seal is fixed to a particular strata, porosity increases under the seal. Compaction is arrested from shallow depths, and, since the pressure under the seal is limited to 0.8 times the reduced lithostatic load at the seal (e.g., the lithostatic load just under the seal minus the cold-water hydrostatic head there), compaction resumes once a certain amount of burial takes place. For a fixed seal the porosity under the seal is greater than the porosity just above the seal.

If the seal migrates through the stratigraphy so as to maintain a constant depth (e.g., the "migrating" seal), the porosity is arrested at the value just above the seal when the sediments move into the seal. The result is a constant porosity to depths at which the effective stress again attains the values it had just above the seal.

Porosity profiles of both the fixed and migrating style are observed in the Gulf Coast. However, it is clear that the porosity profiles in the SEI 330 study area are most similar to the migrating seal profiles. Porosity profiles near the Red Fault show a minor increase in porosity below the top of overpressure in most cases. Thus there is a tendency for seal migration to be more fixed near the Red Fault than further from it. The reasons for this are not clear, but it may be that shearing has disturbed the contiguity of sand-shale interfaces and made it more difficult for the gas-capillary seal to smoothly migrate upward through the section.

The porosities are calculated for the material properties calibrated to the SEI 330 area are slightly different for sands and shales. Thus the sands show up as relatively uncompacted (white) layers on the cross sections. Note that the porosities are calculated for the mid-point of each sedimentary layer.

Comparing the porosity-depth profiles and the observed profiles we conclude that at least since 1.5 ma it is likely that the pressure transition in the SEI 330 area maintained a relatively constant depth and thus the pressure transition zone migrated steadily upward through the sedimentary section as sedimentation took place.

Temperature Modeling (D. Coehlo, Cornell)

Introduction

A large number of 2D temperature simulations have been run for the. Most runs were made for Line 6, the line that passes through the center of the minibasin and passed directly under Pennzoil's Block 330 reservoirs. Several 3D simulations have also been made, and results from these runs are presently being analyzed. The thermal modeling proceeded in stages. First sensitivity analyses were carried out to

assess the relative importance of variable sedimentation, thermal conductivity, sea level variations, heat generation in the sediments by radioactive decay, etc., and to determine the best base case model. These studies revealed the importance of hydrocarbon-related temperature anomalies and radiogenic heat generation. Consequently hydrocarbons and radioactive heat generation were present in the base-case model.

Temperature in the base-case model was then calibrated to the present day temperatures by varying heat flow. Heat flow was not previously known in the SEI study site. Our calibration indicates that the heat flow at 8.5 km depth is be about 1.05×10^{-6} cal/cm²-sec. This is about the value one might have estimated by interpolation from locations in the region where heat flow has been determined.

With the basal heat flow defined, we then calculated the thermal effects of hydrocarbon emplacement between 0.709 and 0.46 ma, and the consequences of this on vitrinite reflectance and other maturity indicators. The emplacement of hydrocarbons produces a thermal blanketing and heating, and this produces a small but potentially measurable vitrinite reflectance anomaly. The anomaly is small compared to that observed in the A6-sidetrack, however.

Table V 2 The impact of various parameter changes on subsurface basin temperature at the level of the Pennzoil reservoirs, ranked in order of magnitude.

	Variable Changed In Test Case	Nature of comparison	Maximum AT in Wells 6 and 17
Hydrocarbons	Hydroc. on reservoirs- dipole above reserve. no hydrocarbons in reservoirs		+15° below
Paleobathymetry	max: always very shallow very deep probable: always present depth-variable		+12 ⁰ C +2 ⁰ C
Salt	No salt under line 6 reservoirs - obsv sale		3 ⁰ C
Timing of HC emplacmt	Hydrocarbons from deposition-base case Early plausible emplacement - base case		3 ⁰ C 1.7 ⁰ C
Heat Generation	Reasonable maximum - reasonable minimum		+2 ⁰ C
Solid Advection	Building with hydroc. - steady state w. HC		2 ⁰ C
Fluid Advection	no flow - steady compactive <i>flow</i>		1.5 ⁰ C
Thermal Conductivity	all sand - all shale stratigraphy realistic lithologic variations sand best HF changed from 1.05 to 1.25 RFU		- 1.4 ⁰ C ±0.2 ⁰ C from 9.5 to 11.5 TCU shale from 7.4 to 8 TCU
Seal Position	reasonable high - reasonable low seal		+0.08 ⁰ C

Hydrocarbon maturation calculations show that significant oil is matured only below the salt weld at the base of the SEI minibasin. Thus the oil in the SEI minibasin cannot have been sourced from within the minibasin, and must have been supplied from greater depths either locally or regionally.

Temperature perturbations produced by rupture of the seal were computed for the models and parameters described above, and much more intensively with a very refined grid and very high temporal resolution in an extensive series of calculations. This modeling shows that thermal anomalies of up to

30°C can be produced by episodic rapid fluid venting. The critical parameter controlling the initial thermal anomalies (first - 100 years of venting) is the fault and sand permeability. The shale permeability is not important at these short time scales.

Temperature Sensitivity Analysis

Sensitivity analyses were carried out to assess the relative importance of the various factors that affect subsurface temperature. The impact of variable changes was generally assessed by calculating the difference in temperature between the test calculation and a reference calculation along pseudo wells 6 and 17 of Line 6 located in the upthrown and downthrown blocks respectively. Table V.2 lists the maximum temperature difference between the test and base models and the parameter varied.

Table V.2 shows that after hydrocarbons, which will be discussed below, the next most important factor is historical variations in water depth in the study, and the position of the sediment-water interface relative to the thermocline that this variation dictates. The water depths assumed for the study area are shown in TableV.3. The depths are constrained by paleontologic data reported in Alexander(1994) and Rowan (1994).

TableV3 Water depths used in the SEI Block 330 modeling as a function of time.

<u>Depth (m)</u>	<u>Time (ma)</u>	<u>Water Depth (m)</u>	<u>Time (ma)</u> <u>Water</u>
	0	762.2	100
	0.46	152.6	338
	0.65	372.7	381
	0.9	913.4	495
	1.1	914	495
	1.27	100	10
	610		
	1.5	91	

Other variables affecting temperature have minor impact for various reasons. As can be seen from Table 3, only extreme variations in salt distribution significance affect subsurface temperatures at 1.5 to 4km depth. Heat generation is an important effect, but errors here will be transferred to errors in the inferred heat flow. Solid advection affects subsurface temperature but the differences across the faults are negligible at the depths of interest. This contrasts with McKenna's (1994) conclusion that the "Red Fault" temperature anomalies could have been caused by differences in sedimentation on the two sides of the fault. We find no such effect. Steady fluid advection produces no significant anomalies along the faults. Reasonable variations in the other variables in the Table have a negligible impact on subsurface temperatures.

The sensitivity analysis identified heat generation and hydrocarbons as important variables. Consequently a base case incorporating these variables was established. The base case model is described in Table V.4.

Table V.4. The Base Case Model for the SEI 330 Study Area.

Thermal Conductivity	K(T, f, So, Sg)
Compaction	Linear function of effective stress
Bottom Water T	Function of thermocline and paleodepth
Hydrocarbons	0.709 into GA and HB; 0.65 into OI-JD, 0.46 into
DA	
Permeability	Function of lithology and porosity
Heat Generation	Values determined by McKenna
Sedimentation History	Inferred from 3D seismic interpretation

Basal heat flux	1.05 x 10 ⁻⁶ call cm ² -sec
Hydrocarbon Generation	Modified Burnham and Sweeney
Maturity Indicators	Burnham and Sweeney, Luo

Basal Heat Flow

The basal heat flow in the SEI 330 area was unknown at the start of this study. It was determined by varying heat flow in the base model (Table V.4) and determining the base heat flow that produces present-day temperatures in closest agreement with those observed. In Line 6 the present subsurface temperatures are best matched with a heat flow of 1.0 cal/cm²-sec. in the downthrown block and a heat flow of 1.1 cal/cm²-sec in the upthrown block. In our base case we use a compromise heat flow of 1.05 x 10⁻⁶ call cm²-sec. These heat flow values are compatible with the regional pattern of heat flow as inferred from measurements at other sites.

Subsurface T Anomalies produced by Hydrocarbons

The sensitivity analysis shows that the distribution of hydrocarbons is the most important factor affecting subsurface temperatures at 1.5 to 4km depths in the SEI 330 area. Even the timing Hydrocarbon emplacement can affect subsurface temperatures significantly.

The temperature pattern along line 6 with and without hydrocarbons in the Pennzoil reservoirs. When hydrocarbons are added to the appropriate sands and the impact of these hydrocarbons on thermal conductivity is considered, the subsurface temperature pattern changes significantly. Because the hydrocarbons make the sediments much more thermally insulating, their presence in reservoirs produces a steep temperature gradient in the reservoirs, a negative temperature anomaly (isotherm syncline) above the oil fields and a positive anomaly (isotherm anticline) below them. From the perturbation of the isotherms above and below the hydrocarbon reservoirs it can be seen that the positive anomaly below the reservoirs is about 15⁰C in magnitude, and the negative anomaly above the reservoirs about 5⁰C in magnitude.

The calculated and observed temperature anomalies are compared. The form of the temperature distribution is very similar. In both calculated and observed cases the temperature in the upper salt sill is 75⁰C. The observed positive temperature anomaly along the Red Fault is 15⁰C, the same magnitude as the calculated, and the negative anomaly above the reservoirs is 5⁰C in both cases. The observed temperature distribution does not show the strong steepening in temperature gradient in the reservoirs that the calculated pattern shows so clearly. However, This we attribute to the 500 m cell size of the Krigging that was used to interpret the temperature data in three dimensions. When the 3D temperature simulations are run we will be able to compare the observed and calculated data without interpolation of the observed temperature data and make a much better comparison of the two. At this stage of the analysis we conclude that the present subsurface temperature field appears to be well explained by the thermal conductivity effects of the subsurface hydrocarbon distribution. Rapid fluid venting up the Red Fault is not required to explain present day subsurface temperatures.

Maturity Indicators

Vitrinite reflectance, illite-smectite, and TTI indices of maturity were calculated. Vitrinite reflectance was measured in the Pathfinder and A6 sidetrack wells. The Pathfinder vitrinite reflectance agree extremely well with the values calculated for our base case model. The effect of the differential movement on the Red Fault is clearly reflected in the reflectance Ro, mainly because of the shorter time sediments take to reach equal depths on the high sedimentation side of the fault.

Additional Maturity Caused by Introduction of Hydrocarbons

The thermal blanketing initiated with the introduction of hydrocarbons increased temperatures below the Pennzoil reservoirs. Over time this increased temperature can be expected to produce higher vitrinite reflectance in organic material under the reservoirs. The increased vitrinite reflectance due to the introduction of hydrocarbons was calculated. The increase is about 0.07%. This is not large enough to account for the 0.3% Ro anomaly observed in the A6 sidetrack. Thermal blanketing by hydrocarbons

cannot explain the A6 sidetrack anomaly. However, the maturity anomalies produced by hydrocarbon blanketing are large enough that there is some hope that their accurate definition might constrain the time of emplacement of hydrocarbons in some instances.

Hydrocarbon Maturation

Calculation of hydrocarbon maturation in the SEI data cube shows clearly that there is no hydrocarbon maturation in the minibasin itself. Oil is being generated below the salt weld at the base of the minibasin, but not in the minibasin itself. This is an important result. It shows that the hydrocarbons in Pennzoil's Block 330 fields cannot have been produced in the SEI Block 330 minibasin that hosts them, but must have been produced below the minibasin and introduced when the salt weld opened.

Steady Fluid Flow in the SEI Minibasin

The permeability of the seal is adjusted in nature and in our calculations such that the excess fluid pressures under the seal do not exceed 0.8 reduced lithostatic (lithostatic minus hydrostatic). Fluids leak through the seal where it is topographically highest because it is there that fluid pressures first exceed this fraction of lithostatic. Calculated subsurface fluid pressures agree well with the pressures inferred from mudweights.

Because of the interaction of the migrating seal with low permeability faults and salt, there are several fluid compartments in our simulations of the South Eugene island subsurface. The most interesting case is shown in Line 4 where the Red Fault is a nexus of 4 parallel faults. Flow is occurring into the horse between the two of the faults, and that this focussed leakage is producing a very localized finger of overpressure at shallow depths. Such a finger of overpressure is not observed in the study area, probably because flow leaks across the faults where sands are juxtaposed. However, narrow fingers of overpressure are known in the Gulf Coast. Another feature observed in the simulations is important. Fluids were observed to move horizontally through the sands both to the east and to the west. We are currently addressing this pattern and seeking to simulate Allen-type flow across the faults where sands are juxtaposed. The important point to be made at this stage is that these horizontal fluid flow through sands is intense and the pattern of flow is complex. It is therefore perhaps no surprise that the kinds of rock alteration that depend on fluid flow is complex and difficult to interpret. We hope that despite the complexities modeling can identify the robust aspects of the flow pattern and that these can be verified by alteration data.

T Anomalies Produced by Pukes of Fluid Flow

The temperature pattern 400 years after the seal on both sides of the Red Fault was ruptured, rapidly venting fluids through the permeable sand network in the section. The sides of the fault were given 5.2 Darcy permeabilities, and the sand network had the realistic permeabilities assigned by the porosity-dependent permeability model.

Sudden venting is one possible explanation for the temperature anomalies observed along the Red Fault. However the pattern is not as good a match as the hydrocarbon-generated anomaly pattern. The rapid venting anomaly is not as broad as the observed anomaly, and fluid flow could account for the positive temperature anomaly under the reservoirs and along the Red Fault, but not the negative temperature anomaly above the reservoirs. The temperature pattern produced by hydrocarbons produces the dipolar anomaly pattern observed; rapid fluid venting cannot produce this dipolar pattern.

Analysis of Highly Episodic Fluid Flow (Roberts, Boling Green, Nunn, LSU)

A great deal of modeling attention has been devoted to assessing the magnitude of thermal anomalies that could be produced by episodic rapid venting through ruptured portions of the seal in the Block 330 study area.

The studies that are reported there found that venting from the Red Fault can produce temperature anomalies up to 30°C in magnitude 350 years after a 10 millidarcy fault is opened. The anomalies are localized within 0.5 km of the Red Fault and do not extend more than 0.75 km above the seal because flow is effectively diverted by the overlying sands. The depth extent of those parts of the fault that

become permeable during a rupture event is important. If the permeable part of the fault extends 0.5 km rather than 1.5 km below the seal, the maximum temperature anomaly after 100 years of venting is reduced from 24 to 15°C. The permeability of the shale units in the basin does not significantly impact the temperature anomalies produced in the first few hundred years of venting. The permeability of the sands and fault are the important controls. For example, the maximum temperature anomalies calculated for cases where the permeability of the fault is a time-dependent function of fluid pressure (not a constant 10 millidarcies) is 7°C at 100 years after the start of fluid expulsion. All sands were taken to have 1 millidarcy permeability in the simulations. This value is conservatively low.

These simulations show that temperature anomalies up to 30°C can be produced along the ruptured parts of a fault in and below the seal. With higher sand and fault permeabilities the episodic flow events could be of very short duration and the temperature anomalies produced along the fault could be extremely local. Very short and intense rupture appear the best candidate to account for the elevated vitrinite reflectance R_o anomalies observed in the A6 sidetrack and the lack of any such anomalies in the Pathfinder 1000 ft away.

Vitrinite Reflectance Anomalies in the A6 Sidetrack

Highly episodic fluid venting can account for the vitrinite reflectance R_o anomalies observed in the A6 sidetrack and the curious feature that the same anomalies are not observed in the Pathfinder well only 300 m from the A6. We have calculated the effects of subjecting fault sediments near where the A6 intersects the Red Fault to temperatures to temperatures 10°C and 30°C above present ambient for 150 years. These temperature perturbations cause an increase in vitrinite R_o of 0.14 and 0.21%, respectively. This level of additional maturation can easily account for the vitrinite anomaly observed in the A6 sidetrack. In addition, a thermal perturbation lasting 150 years will only propagate about 140 m on either side of the fault. Thus the lack of a vitrinite reflectance in the Pathfinder well 300 m distant from the A6 sidetrack can be explained providing the duration of the fluid venting episode was short.

Fluid Transport in Migrating Fluid-Filled Fractures (Nunn, LSU)

The conclusions of the previous section are very close to a new idea that came out of the DOE project: that upward propagation of water- and hydrocarbon-filled fractures could be a significant mechanism of fluid transport in the overpressured sediments below seals in the Gulf of Mexico and elsewhere. Analysis shows that such fractures could propagate at 1000 m/yr and could cumulatively accommodate mass flux rates of @100 kg / m²-yr. This idea is described in Nunn (in press).

Thermohaline Convection, Salinity Distribution, and Salt Dissolution

Pore water salinity varies in the SEI 330 study area in ways that suggest fluid movement. Pore water salinities of reservoir sands were estimated from about 50 SP logs. Reservoirs in the SEI study area at <1600 m depth have higher salinities than reservoirs at >2000 m depth. The salinity of the shallower reservoirs has decreased significantly since the 1970's whereas the salinity of the deeper reservoirs has not changed. This may suggest that recent expulsion of low salinity waters from the overpressured zone that have diluted the deeper reservoirs in the recent past are only now diluting the higher reservoirs.

Calculations (Sakar et. al., 1995) show that thermohaline convection can be a significant mechanism of salt dissolution even in sediments with permeabilities as low as 0.01 md. This shows that the high salinities in the upper Block 330 reservoirs could have been produced by convective dissolution of salt domes in the area.

CONCLUSIONS

Major conclusions from the modeling are:

(1) The present-day temperature distribution, contrary to the perceptions at the start of the project, is a steady state distribution. Thermal anomalies along the Red Fault are due to the blanketing effects of overlying hydrocarbons, not bursts of rapid fluid venting from the overpressured zone.

(2) Vitrinite reflectance and other maturity indicators in the Pathfinder drill hole are well matched by calculated maturity parameters assuming no rapid fluid venting.

(3) No hydrocarbons have matured in the SEI Block 330 minibasin. However kerogen has matured to oil below the salt weld at the base of the Miocene section. Oils and gases in the Block 330 reservoirs must have come from sources below the minibasin, perhaps when the salt weld opened.

(4) The blanketing effect of oil and gas in the Block 330 reservoirs causes the vitrinite reflectance of organic matter along the red fault to increase about 0.07%. This is a potentially observable increase and suggests that the time of hydrocarbon emplacement might be constrained by maturity anomalies. However the maturity increase by hydrocarbon blanketing is much smaller than the 0.3% anomaly observed in the part of the fault penetrated by the A6 sidetrack, a mere 1000 ft from the Pathfinder well. The Ro anomaly in the A6 is corroborated by conodont color changes and fluorescence data and thus the maturity anomaly thus appears to be real.

(5) The maturity anomaly in the AE sidetrack could potentially be caused by rapid episodic fluid venting. Very localized venting up the Red Fault is indicated by the lack of vitrinite anomalies in the Pathfinder well only 1000 ft from the A6 sidetrack. Calculations show that a short-lived (few hundred year) pulse of fluid up Red Fault could produce a localized temperature anomaly in the fault up to and perhaps somewhat greater than 30°C in magnitude. This magnitude and duration of thermal pulse would be sufficient to produce an Ro anomaly of 0.2%, nearly the 0.3% recorded by the A6 sidetrack measurements.

E. REFERENCES

Alexander, L. (1995). Geologic Evolution and Stratigraphic Controls on Fluid Flow of the Eugene Island Block 330 Mini-basin, Offshore Louisiana. Gulf of Mexico. Cornell PhD Thesis, 250p.

Dowdie, W. L. and W. M. Cobb (1975). "Static Formation Temperature from Well Logs -An Empirical Method. Journal of Petroleum Technology' 27:1326-1330.

Guerin, G., Anderson, R. N., He, W. (1994). "3D Temperature Distribution and Heat Flow Analysis for the Eugene Island 330 Area, Offshore Louisiana AAPG Abstract

Holland, D. S., W. E. Nunan, et al. (1980). "Eugene Island Block 330 Field - USA. Offshore Louisiana." in Halbouty. . ed.. Giant oil and gas fields of the decade:1968-1978 AAPG Memoir #30: 253-280.

Losh, S., L. Eglinton, et al. (1994). "Report on Geologic and Geochemical studies on rocks collected from the Pathfinder well and elsewhere in SEI Block 330 DOE annual report.

Luo, M., J. R. Wood, et al. (1994). "Prediction of Thermal Conductivity in Reservoir Rocks Using Fabric Theory." Journal of Applied Geophysics 32: 321-334.

McKenna, T. E (1994) Evaluation of Subsurface Temperature in Eugene Island Block 330 and Vicinity. AAPG Abstracts

McKenna, T. B. and J. M. Sharp (1995). "Thermal Conductivity and Radiogenic Heat Production from South Texas (Gulf of Mexico Basin)."GSA Abstracts 27(6):

McKenna, T E 3 M Sharp, et al. (1996). 'Thermal Conductivity of Wilcox and Frio Sandstones in South Texas (Gulf of Mexico Basin)."Submitted to AAPG Bulletin:

Mello, U. (1994). Thermal and Mechanical History of Sediments in Extensional Basins, Columbia University PhD thesis, 350p.

Meulbroek, P. and L. M. Cathles (in Preparation). "Modeling the Effects of Evaporative Fractionation on Bulk Composition."

Nunn, 3. A. (1996). "Buoyancy-Driven Propagation of Isolated Fluid-Filled Fractures: Implications for Fluid Transport in Gulf of Mexico Sediments."Journal of Geophysical Research In Press:

Nunn, J. A., 5.3. Roberts, et al. (1995). Fluid Migration in Eugene Island Block 330 Area of Offshore Louisiana Archie Visualization Technology Conference, Woodlands, Texas,

Roberts, S.J. and J. A. Nunn (1995). "Episodic Fluid Expulsion From Geopressed Sediments." Marine and Petroleum Geology 12: 195-204.

Roberts, S. J., J. A. Nunn, et al. (1996). "Expulsion of Abnormally Pressured Fluids Along Faults." Journal of Geophysical Research In Revision:

Sarkar, A., J. A. Nunn, et al. (1995). "Free Thermohaline Convection Beneath Allocthonous Salt Sheets: An Agent For Salt Dissolution and Fluid Flow in Gulf Coast Sediments." Journal of Geophysical Research 100:18085-18092.

Shosa, S.D. and L. M. Cathles (in Preparation). "A Direct Investigation of Capillary Exit Pressure as a Basin Sealing Mechanism"

Whelan, 3. K., L. B. Eglinton, et al. (1994). "Organic Geochemistry of fluids and Kerogens from DOE Drilling in Eugene Island 330 Reservoirs Indicators of Fluid Flow Pathways." AAPG Abstracts:

Task Six - Geochemistry
Steven Losh - Task Manager

OBJECTIVE:

The purpose of the geochemical phase of this project was to analyze rock, brine, oil, and gas samples in order to test the hypothesis that oil and gas have recently migrated and are still migrating from depth, along growth faults, into the currently-producing reservoirs in the SEI Block 330 field. To accomplish this, analyses were performed on samples from the Pathfinder well, within and adjacent to the main growth fault abutting the Block 330 field, and compared with data obtained from samples from the reservoirs. For organizational purposes, the data so obtained are divided into two categories and are presented in this order in the report: 1) inorganic geochemistry, which includes: a) geology of the core, b) petrographic, mineralogic, whole rock geochemical, and stable isotopic investigations of rock samples, and a) brine chemistry; and 2) organic geochemistry, which includes a) hydrous pyrolysis experiments in order to evaluate controls on and kinetics of gas generation from sediments, and b) a wealth of analyses (many published separately) pertaining to whole oil, gas, and condensate compositions, compound-specific isotopic composition, and biomarkers. An on-line database (c) has been constructed to allow public access to the data collected as a part of the inorganic and organic geochemical investigations. The inorganic geochemical report summarizes the work carried out over the duration of the project, whereas the organic geochemical report summarizes the work accomplished over the past year.

SUMMARY:

Some of the main findings of the geochemical investigation regarding fluid ascent via the growth fault system in SEI Block 330 are:

- Although there is a considerable degree of compositional heterogeneity between reservoirs, the oils, gases, and condensates in SEI 330 appear to have a single source in Mesozoic rocks. The presently-observed variations in composition have resulted from processes that affected the oil and gas during and after migration, such as evaporative fractionation and biodegradation. Gas is characterized via higher thermal maturity than oil, suggesting that the oil is "swept up" by vertically migrating gas. Brine composition, specifically ^{129}I and $^{87}\text{Sr}/^{86}\text{Sr}$, supports the interpretation of large-scale vertical migration of fluid into the reservoirs. Systematic variations in major element, specifically chlorine, composition of brine between reservoirs indicate that brine entered the reservoirs at different times and/or from different directions.
- A variety of data support ongoing filling of the GA sand via rapid injection, and high fluid flux in the fault zone in the past. Repeated sampling of wells over a period of 10 years has led to the finding that unbiodegraded oils are injected into the GA sand on the time scale of years or less. Biodegradation occurs rapidly there, and the presence of unaltered oil is interpreted to reflect rapid influx from depths at which biodegradation does not take place. A variety of other organic geochemical data corroborate this conclusion. In the A6ST well, which penetrates the main growth fault a point 1000 feet from the fault intercept in the Pathfinder well, sediments from within the growth fault are characterized by anomalously high vitrinite reflectances relative to sediments outside the fault, indicating that the fault is locally a paleothermal anomaly. Combined with stable isotopic composition of minerals from the fault in that well, these data support the conclusion that the fault, at least at some locations, acted as a conduit of relatively high-temperature fluids.
- The Pathfinder core contains three structurally - distinct fault domains, only the deepest of which contains oil. Based on structural and geologic data, this deepest domain is concluded to have been most recently active. Structural and geochemical data indicate the other two fault domains were active prior to oil migration. The oil-barren domains contain fractures that are favorably oriented to transmit oil. Oil is furthermore present in sands in these domains. It is evident that fault zone oil migration took place only within that part of the fault that was active during the time migratable oil was available to the fault. Despite the variability of hydrogeologic characteristics of faults as evident in the core, the geochemical data indicate that none of these cored faults transmitted significant amounts of fluid in the Pathfinder well, indicating the operation of a higher-order control on fluid flow in the growth fault. The same fault in the A6ST well has apparently acted as a fluid conduit, indicating relatively short-range lateral variability in fluid flow behavior in the fault.

Tasks include:

- Development of protocol for acquisition, preservation, and complete analysis of core, involving research and meetings in Houston with oil company and service company personnel. The coring procedure was highly successful and has been adopted by Pennzoil and other operators in the Gulf.
- Overseeing coring while on rig. Funds were also redirected to cover cost overruns for core acquisition.
- Logging core in detail while Pathfinder was being drilled.
- Structural interpretation of core.
- Core preservation and curation.

SUBTASK 6.2
ORGANIC GEOCHEMISTRY
Sean Whelan, WHOI
October 9.1995

SUMMARY OF TECHNICAL PROGRESS:

Organic Geochemistry, Hydrous pyrolysis:

Introduction

Thermal maturation of sedimentary organic matter involves numerous chemical transformations that result in the production of hydrocarbon and non-hydrocarbon gaseous alteration products. These products play a critical role in the development of overpressure, the transport of petroleum, and sediment diagenesis in sedimentary basins (Hunt *et al.*, 1995; Price *et al.*, 1983; Whelan *et al.*, 1994a,b). Understanding fundamental processes that regulate the generation of gaseous products is essential to constrain factors influencing the accumulation of hydrocarbons in the Gulf Coast, USA. Owing to the extreme complexity of natural systems, key processes that regulate the timing, amounts, and composition of organic alteration products are often obscured. Laboratory heating experiments have proven to be an effective tool for constraining physical and chemical processes associated with the generation of hydrocarbons. In particular, the role of water during organic reactions in geologic environments has received much attention in recent years (Helgeson *et al.*, 1993; Hoering 1984, Lewan 1991, 1993; Seewald 1994; Shock 1988; Siskin and Katritzky, 1991; Stalker *et al.*, 1994). Laboratory experiments have demonstrated that the presence of water during the maturation of sedimentary organic matter significantly influences the amounts and composition of liquid hydrocarbons. It is likely that water may also play an integral role in the generation of volatile hydrocarbons and non hydrocarbon such as carbon dioxide. Except for a few notable exceptions (Lewan 1992; Tannenbaum and Kaplan 1985; Seewald 1994) laboratory studies focusing on the generation and stability of hydrocarbon and non-hydrocarbon gases have been conducted in the absence of added water.

The experiments presented here were conducted to constrain factors influencing the generation of natural gas and carbon dioxide during the thermal maturation of sedimentary organic matter from the Monterey, Smackover, and Eutaw formations. The experimental design reflects our attempts to duplicate natural conditions in the laboratory. Water is ubiquitously present in most sedimentary basins. Accordingly, our experiments involved heating bulk sediments in the presence of liquid water. Experiments were conducted at temperatures ranging from 125 to 360°C at 350 bars pressure, conditions that are similar to those in most sedimentary basins during gas generation.

Methods

Sample Description and Preparation.

Samples of the Monterey, Smackover, and Eutaw Shale were used for the experiments presented here. These samples allow comparison of the gas generation characteristics of a sediment containing sulfur-rich organic matter primarily of marine origin (Monterey

Shale), with two sediment samples containing relatively sulfur-poor organic matter primarily of terrestrial origin (Eutaw and Smackover Shale).

The Monterey Shale is a thermally immature (bituminite reflectance = 0.25% expressed as R_0) consolidated sediment sample from the Miocene Monterey Fm. (ML9I-17). It was obtained from an outcrop at Naples Beach, CA. The sample was removed from a 10cm interval at the base of Unit 315, approximately 9 m below the lowest phosphorite horizon (M.D. Lewan, personal communication). The sample comprised a lenticularly laminated claystone and visually appeared fresh (i.e. unweathered) and blocky. The surfaces of the sample were scraped to expose pristine material and remove possible contaminants. This sample is organic rich (20.6 wt. % TOC) and based on petrographic observations and elemental analyses can be classified as a type II-S kerogen.

The Eutaw Shale is a Cretaceous consolidated sediment obtained from core cuttings recovered at a depth interval of 3011 to 320 m from the Hampton/Nelson Ball well in Pike County, Mississippi. It is a relatively organic lean shale (0.97 wt. % TOC) and contains abundant quartz. A measured vitrinite reflectance value of 0.45% R_0 indicates that the kerogen has not yet reached the oil window. Petrographic observations indicate that this sediment contains mostly terrestrial derived organic matter that can be classified as type-III kerogen.

The third shale is a sample from the Upper Smackover formation (Jurassic). It is a consolidated sediment obtained from core cuttings recovered at a depth of 3260 m from the Amareda Scotch Well #1 in Clark County, Alabama. This shale is relatively organic-lean (0.917 wt. % TOC), contains abundant quartz, and has a measured vitrinite reflectance value of 0.52% R_0 . Petrographic observations indicate that the kerogen in this sample is type-III and characterized by a similar maceral type distribution as the Eutaw Shale.

During this study our primary goal was to constrain chemical processes that regulate the rate and extent of chemical reactions responsible for the generation of gaseous products. Accordingly, to minimize physical processes associated with expulsion of produced gases. The starting sediments were pulverized in a disc mill until the entire sample passed through a <125- μ m sieve. In addition, existing hydrocarbons were removed prior to heating. This was achieved for the Eutaw and Smackover Shale by Soxhlet extraction in a 93:7 $\text{CH}_2\text{Cl}_2/\text{CH}_3\text{OH}$ mixture for 48 h. The Monterey was sequentially extracted by sonic disruption for 9 minutes in CH_2Cl_2 , a 1:1 mixture of $\text{CH}_2\text{Cl}_2/\text{CH}_3\text{OH}$, and CH_3OH . Because we were concerned only with carbon dioxide generated from sedimentary organic matter, the starting sediments were treated with 10% HCl at 4) $^\circ\text{C}$ for 2 h to remove sedimentary inorganic carbonate minerals that could dissolve during an experiment. For the Monterey Shale experiments at 225 and 275) $^\circ\text{C}$, the sediment was not treated with HCl. Thus, generated carbon dioxide for these two experiments almost certainly includes a contribution from inorganic carbonate.

Experimental Apparatus and Conditions

The experiments were conducted in 316 stainless steel tubing reactors with a 20 cm^3 internal volume. The experiments described here are in many ways similar to the hydrous pyrolysis experiments described by Lewan (1991) in that bulk sediments are heated in the presence of excess liquid water, but there are important differences. For example, in our experiments the reactor vessel is filled completely with liquid water precluding the existence of a vapor head space during an experiment. This may be particularly significant for studying volatile products since they effectively partition into a vapor head space at the conditions of an experiment removing them from intimate contact with the water and sedimentary components. In addition the apparatus utilized for this study allows fluid samples to be withdrawn from the pipe-bomb at the temperature and pressure of an individual experiment avoiding potentially ambiguous reactions during a prolonged quench process. Moreover, because the experiments do not need to be cooled to determine the amounts of generated gases, fluid chemistry can be monitored as a function of time during an individual experiment.

During this investigation, it was assumed that all generated gases dissolved into the aqueous phase at the conditions of these experiments. To avoid the formation of a separate gas or oil phase, which might represent a sink for gaseous alteration products, relatively high water/sediment mass ratios were used. For each experiment 1.0 g of bulk sediment was loaded into the tubing reactor before sealing. Prior to heating, the air in the tubing reactor was evacuated and partially filled with argon-purged distilled water to ensure that the sediment was in contact with liquid water during heating. The entire reactor was heated to the experimental temperature in a horizontal tube furnace in approximately 30 minutes. Once at the desired temperature, the tubing reactor was completely filled with distilled water and pressurized to 350 bars so that only a single liquid phase was present (i.e., no head-space). Temperature was monitored ($\pm 2^{\circ}\text{C}$) with a thermocouple at each end of the tubing reactor to ensure there were no thermal gradients. Experiments utilizing the Monterey and Smackover Shale were conducted isothermally for approximately 170 h. In contrast, the Eutaw Shale investigation was conducted by maintaining the tubing reactor at a constant temperature for a selected period of time before rapidly increasing the temperature to a new value. At each temperature condition gas generation was monitored as a function of time.

During the course of an experiment fluid samples were withdrawn into glass gas-tight syringes and monitored for the concentration of dissolved species. An internal 10 μm steel mesh filter ensured particle free fluids. Pressure was maintained during the sampling process by pumping argon-purged distilled water into one end of the tubing reactor with an HPLC pump while the fluid sample was removed from the other. The sampling process was performed rapidly (1 to 2 minutes) to avoid dilution of the fluid samples with the freshly injected water. All subsequent concentrations of dissolved gases were corrected for the amount of water injected on each sampling occasion.

Analytical Procedures

Fluid samples were analyzed for the dissolved concentrations of CO_2 , $\text{C}_1\text{-C}_4$ hydrocarbons, and for selected samples dissolved organic acid anions, H_2 , and H_2S . The first aliquot of fluid (0.5 ml) withdrawn from the tubing reactor on any sampling occasion was discarded and served only to flush the sampling valve and stainless steel lines. Dissolved CO_2 and $\text{C}_1\text{-C}_4$ hydrocarbons were analyzed in duplicate in subsequent aliquots (0.5 ml) by injecting the sample into a purge and trap apparatus interfaced directly to a gas chromatograph equipped with a flame ionization and thermal conductivity detector connected in series. The fluid samples were acidified with 1 ml of 25 % phosphoric acid in the purge cell to ensure complete evolution of dissolved CO_2 . Separation of gases in the gas chromatograph was achieved with either a porapak-Q packed column or a poraplot Q megabore capillary column. Authentic standards were used to establish a three level calibration curve for CO_2 and each hydrocarbon. Analytical uncertainties are estimated to be $<5\%$ for these species.

The concentrations of aqueous organic acid anions generated during the experiments were analyzed by ion chromatography on a Dionex DX-300 ion chromatograph equipped with an AS II column and a conductivity detector. Samples were preserved with 200 ppm mercuric chloride and stored in a refrigerator prior to analysis. Authentic standards were used to establish a three level calibration curve for all acids reported.

Dissolved H_2 concentrations were determined by gas chromatography (thermal conductivity detector and a SA molecular sieve packed column) following a headspace extraction. Dissolved H_2O was determined gravimetrically by acidifying the fluid sample with 25 % phosphoric acid and precipitating the evolved H_2S as Ag_2S in a 3 wt. % AgNO_3 solution. Estimated uncertainties for the H_2 and H_2S analyses are $<5\%$.

Careful accounting of all fluid removed and added to the tubing reactor allowed the absolute amounts of generated products to be calculated from the dissolved concentrations, tubing reactor volume, and the mass of sediment in each experiment. The specific volumes of water at the temperature and pressure conditions of each experiment were calculated from the equation of state for water of Haar *et al.*, (1980).

Elemental analyses (CRNSO) of the starting sediments and solid alteration products were conducted on either a Leco 932 or Fisons EAl 108 elemental analyzer. Inorganic carbonate (IC) was determined on a Coulometrics carbon analyzer. Total organic carbon (TOC) was determined by difference. The starting sediment and solid alteration products for the Monterey Shale experiments were demineralized by HCl and Hf acid digestions (Eglinton and Douglas, 1988) to isolate the kerogen. Iron sulfides were removed from the kerogen by treatment with CrCl_2 and HCl (Canfield *et al.*, 1986; Acholla and Orr, 1993). The relatively pure kerogen isolate was analyzed for its elemental composition. Similar kerogen isolations for the Eutaw and Smackover Shale were not possible owing to the low organic matter content of these sediments.

Results

Volatile Products

Thermal maturation of organic-bearing sedimentary rocks is characterized by (1) generation of gaseous alteration products, the extent and rate, which are strongly dependent on time and temperature. For example, during the Monterey and Smackover experiments, methane generation increased by more than three orders of magnitude during heating at 360°C relative to 125°C , while methane generation was almost 3 orders of magnitude greater at 360°C relative to 225°C for similar reaction times during maturation of the Eutaw Shale. The concentrations of ethane and propane showed similar temperature trends although the absolute abundance of these hydrocarbons were substantially less than that of methane. Although, methane is the dominant hydrocarbon gas generated at all conditions during these experiments, its relative abundance shows a clear trend as a function of temperature. At 125°C methane constitutes approximately 90% of the generated hydrocarbon gas while at 360°C its relative abundance has decreased to approximately 40 %. Increasing maturation time results in decreasing relative abundance of methane on the time scale of these experiments.

In addition to alkanes significant quantities of alkenes were generated at all temperature for all sediments. In general the abundance of alkenes increased with increasing temperature. In contrast to the saturated hydrocarbons, however, the abundance of alkenes decreased with continued reaction at constant temperature, except during the 125°C experiments in which their abundance remained effectively constant. These results indicate that ethene, propene, and *n* butene are unstable at temperatures $> 150^\circ\text{C}$. That the alkene abundance at 125°C remained constant while the abundance of alkanes increased may suggest that alkenes were being generated but degradation reactions were occurring at a similar rate. These results confirm the hypothesis of Tannenbaum and Kaplan (1985) who suggested that alkenes are initially produced in small quantities under dry or hydrous conditions but represent an unstable intermediate during the formation of petroleum.

Although the thermal maturation of sedimentary organic matter results in the production of substantial hydrocarbon gases, carbon dioxide was unequivocally the dominant gaseous alteration product. During thermal maturation at 360°C 312, 337, and 194 mg/g TOC carbon dioxide were produced from the Monterey, Smackover, and Eutaw Shale, respectively, and was still increasing in all experiments, even after heating the Eutaw Shale for 2716 h at 360°C . These quantities are at least an order of magnitude greater than the total amount of hydrocarbon gases produced from each sediment. Carbon dioxide generation increased with increasing temperature, similar to the hydrocarbon generation trends.

Owing to the possibility that carbonate minerals such as calcite or siderite can precipitate during hydrous pyrolysis experiments, carbon dioxide values represent absolute minimums. Evidence for calcite precipitation is provided by the Monterey experiments MS5 and MS 13. In contrast to the other Monterey experiments in which the rate of release of carbon dioxide to solution showed continuously

decreasing rates with increasing reaction time, MS5 and MS 13 were characterized by initially rapid carbon dioxide increases in solution followed by relatively minor increases between the samples at 25 and 70 h. A subsequent rapid release of carbon dioxide was observed between 70 and 170 h. This trend suggests that carbon dioxide may have been precipitating as a carbonate mineral suppressing the amount observed in solution. The non-systematic increases in carbon dioxide released to solution as a function of temperature during the Smackover Shale experiments may also suggest carbonate mineral precipitation, since the solubility of carbonate minerals is particularly sensitive to pH and dissolved Ca or Fe concentration in addition to temperature, pressure, and dissolved carbon dioxide concentration. Requisite Ca and Fe for the formation of calcite and/or siderite was likely derived from feldspars, clays, and/or iron sulfides present in the sediment. Carbonate minerals were not observed petrographically at the termination of each experiment. Although mass balance calculations indicate that only trace amounts of carbonate minerals would form unless the majority of carbon dioxide precipitated. Immersion of some of the alteration products in dilute HCl resulted in minor effervescence suggesting the presence of a minor carbonate phase.

Determination of total dissolved H_2S concentrations in the Monterey Shale experiments revealed increasing abundance in solution with increasing temperature in the range 250 to 360°C. At temperatures <225°C dissolved H_2S concentrations were too low for gravimetric determination, but H_2S was detectable by odor in all experiments. No attempt was made to determine H_2S abundance in the Eutaw and Smackover Shale experiments but a strong Pr_2S odor in all fluid samples indicated its presence. The absolute abundance of total dissolved H_2S was likely regulated by the solubility of iron sulfides such as pyrite and/or pyrrhotite owing to the rapid dissolution precipitation kinetics for these minerals under hydrothermal conditions (Seewald and Seyfried, 1990). Pyrite was abundant in the unheated Monterey Shale and persisted along with newly formed pyrrhotite in the thermally altered sediments. Sources of sulfur during these experiments include diagenetic pyrite and organic matter. Although it is not possible to quantitatively determine the relative contributions from these two sources, the amounts of H_2S released to solution at 350 and 360°C, 12.7 and 18.8 mg/g sediment, respectively, exceed the amount of sulfur present as diagenetic pyrite in the starting sediment (10.5 mg/g sediment as H_2S). Thus, these data indicate the release of organically bound sulfur to solution. Because sulfide is likely cycled through the solution into iron sulfide minerals, the amounts of organically bound sulfur indicated here represent minimum values.

Dissolved H_2 concentrations were determined in the final fluid samples from the Monterey Shale experiments at 200,300, 325,350, and 360°C and in samples from the 325 and 360°C phase of the Eutaw Shale experiment. During the Monterey Shale experiments the dissolved H_2 concentrations showed a systematic increase with increasing temperature, except for experiment MS5 at 325°C. Experiment MS5 was the first experiment conducted in a new tubing reactor and the relatively high dissolved H_2 concentrations may reflect R_2 released as a result of water disproportionation associated with oxidation of the stainless steel tubing reactor. Similarly, the Eutaw Shale experiment was also conducted in a new tubing reactor. Thus, the relatively high dissolved H_2 concentrations observed at 325°C may reflect oxidation of the reactor walls. Continued reaction at constant temperature resulted in decreasing dissolved H_2 concentrations.

Organic Acids

The abundance of organic acid anions were determined in fluid samples from the Monterey and Smackover Shale experiments. Acetate was the most abundant organic acid anion in all samples. Thermal maturation of Monterey Shale also resulted in the production of formate and propionate and trace amounts of valerate, oxalate, and succinate. In contrast, thermal maturation of the Smackover produced significant formate but did not generate detectable quantities of propionate, valerate, oxalate, and succinate, except for experiments SM6 and SM1 in which trace amounts of oxalate were detected. There is some indication that the abundance of acetate and propionate increased with increasing temperature

during Monterey Shale maturation. Continued reaction at constant temperature in the relatively high temperature experiments ($>225^{\circ}\text{C}$) resulted in decreasing acid concentrations, most likely the result of decarboxylation reactions (Kharaka *et al.*, 1983; Palmer and Drummond, 1986). The abundance of organic acids during the Smackover Shale experiments showed no clear trends with temperature.

Solid Alteration Products

In general, the bulk sediments were characterized by decreases in TOC contents consistent with the generation of hydrocarbons. The N and S content of the Monterey bulk sediment also decreased. Analyses of the Monterey Shale isolated kerogen, however, reveals chemical changes directly associated with kerogen maturation. For example, increasing C accompanied by decreasing O and H contents with increasing temperature indicates the residual kerogen was becoming more C-rich, a likely result of the generation of hydrocarbons and carbon dioxide.

Examination the data reveals a minor initial increase in the TOC content of the solid products during low temperature maturation. Because the sediment represents the only source of C present during the experiments, this increase likely reflects dissolution of the inorganic sediment components. Quantitative determination of the extent of inorganic mineral dissolution is not possible with the data available. However, to produce an increase from 20.6 wt. % TOC in the initial sediment to a value of 23.5 wt % in the alteration products from experiment MS 10 at 150°C requires dissolution of 12.3 wt. % of the inorganic minerals present. This value is an absolute minimum because generation of liquid and gaseous C-bearing alteration products would result in decreasing TOC contents for the solid alteration products. If the amount of liquid and gaseous C-bearing products are accounted for, dissolution of approximately 15.0 wt. % of the inorganic minerals present is required.

Discussion

Generation of gas during the thermal maturation of kerogen involves a diverse and large set of reactions. Formation of low molecular weight hydrocarbons and carbon dioxide can occur as a result of the direct cleavage of functional groups from the kerogen macromolecule and/or secondary reactions involving generated long chain hydrocarbons that compose bitumen. The latter process is commonly referred to as "oil cracking". Current models that constrain the timing and amounts of carbon dioxide and hydrocarbon generation are to a large extent based on compositional trends observed for the maturation of kerogen in response to increased time and temperature. Examination of the data reveals that early stage maturation results in the loss of oxygen, a likely result of the cleavage of carboxyl, carbonyl, and methoxy functional groups, and little decrease in the hydrogen content of kerogen. Continued heating results in exhaustion of kerogen oxygen and decreases in the hydrogen content of kerogen. It is generally assumed that kerogen represents the only source of oxygen and hydrogen available for carbon dioxide and hydrocarbon generation involving organically derived carbon (Tissot and Welte, 1984; Ungerer 1990; Cooles *et al.*, 1985; Barker, 1990). Accordingly, peak carbon dioxide generation is generally viewed as an early-stage phenomenon that precedes peak hydrocarbon formation (Tissot and Welte, 1984). The results of this study, however, suggest that carbon dioxide generation may be substantially more pervasive. Although, significant quantities of carbon dioxide were generated during sediment maturation at low temperatures, carbon dioxide continued to be the dominant gaseous alteration product at 360°C in all experiments. For the Monterey experiments, carbon dioxide production continued at temperatures significantly higher than those associated with peak bitumen formation which occurs during hydrous pyrolysis experiments at approximately 275°C (Baskin and Peters, 1992; Nelson *et al.*, 1995). Thus, based on experimental evidence carbon dioxide generation occurs before, during, and after peak hydrocarbon generation.

Variations in the compositional evolution of kerogen during the Monterey Shale experiments are consistent with maturation trends observed in nature. Large decreases in the oxygen kerogen content were observed in the relatively low temperature experiments with only a minor decrease

in the hydrogen content while maturation at relatively high temperatures resulted in only minor decreases in oxygen content and substantially greater decreases in the hydrogen content.

Possible sources of oxygen during these experiments include H₂O and oxygen bound in inorganic minerals. Considering the low ferric iron content of the Monterey Shale and thermodynamic barriers to reducing ferrous iron and aluminosilicate minerals, oxygen directly from these sources is not available for the formation of oxygen-bearing organic alteration products. Thus kerogen and H₂O represent the only additional source of oxygen during these experiments. H₂O has been implicated as a source of oxygen in other hydrous pyrolysis experiments at temperatures ~300°C (Lewan 1992; Stalker et al., 1993). Thus, H₂O may represent an important source of oxygen during kerogen maturation in these experiments and in natural systems.

Consumption of H₂O-derived oxygen during the production of oxygen-rich alteration products would necessarily result in the release of hydrogen. Hydrocarbon formation represents a likely sink for excess-hydrogen during the thermal maturation of sedimentary organic matter. Results of redox-buffered hydrothermal experiments have demonstrated the incorporation of water-derived hydrogen during the saturation of ethene to form ethane at 325°C (Seewald 1994). These experiments demonstrated that the relative abundance of ethene and ethane are controlled by a state of metastable redox dependent thermodynamic equilibrium that directly involves water. Similar reactions are likely during the present experiments. Alkenes which are a known product during the pyrolysis of sedimentary organic matter under dry and aqueous conditions (Tannenbaum and Kaplan, 1985; Esser and Schwochau 1991) were abundantly present in the early stages of these experiments and showed decreasing abundance with increasing time, even at temperatures as low as 150°C. This trend is consistent with saturation of alkenes with H₂O derived hydrogen to form alkanes. Alkenes did not completely disappear during any of these experiments even after reaction 2716 h at 360°C suggesting they were likely approaching a state of metastable thermodynamic equilibrium in response to the redox state of the chemical system.

The possibility that H₂O may represent a source of oxygen and hydrogen for the formation of carbon dioxide and hydrocarbons has important implications for the generation of oil and natural gas in sedimentary basins. Presently, most models that predict maximum oil and gas yields during from kerogen assume that requisite hydrogen and oxygen are only derived from kerogen only. Owing to the ubiquity of water in most sedimentary basins, these models may underestimate the oil and gas potential of sedimentary organic matter. Predicting maximum yields of organic-derived alteration products is a complicated and difficult task since the reactions involved are a function of numerous parameters including organic matter composition, temperature, pressure, and the chemical environment at the site of generation. It is unlikely that hydrogen availability represents the limiting factor during the initial generation of liquid hydrocarbons since it is generally believed that these products are produced to varying extents by the cleavage of intact fragments of kerogen which retain many of the compositional characteristics of the source kerogen. In addition, because early generated oil is composed of relatively long chain hydrocarbons only minor amounts of hydrogen are required to produce saturated products. With increasing thermal maturation, however, hydrogen demands increase as organic transformations result in a decrease in the average carbon chain length of hydrocarbons and associated increases in the H/C ratio. Thus, it is likely that H₂O-derived hydrogen may represent an important contributor to the overall hydrogen budget under high temperature conditions that result in the extensive cracking of oil to form natural gas.

Catalytic Processes

Reactions responsible for the production of natural gas via the cracking of long-chain hydrocarbons have been viewed as purely thermal processes during which sufficient thermal energy is available to result in cleavage of carbon-carbon bonds (Tissot and Welte, 1984; Barker 1990; Ungerer 1990) or as thermocatalytic processes in which the energy required to break carbon-carbon bonds is substantially lowered due to the presence of a catalyst (Mango et al., 1993). Mango et al. (1993) argues that a purely thermal model for the production of natural gas requires temperatures in excess of those

found to exist during natural gas production in natural systems and produces a gas that is compositionally distinct. In general, natural gas is composed predominantly of 50 to 100 wt. % methane with lesser amounts of ethane and propane. In contrast, laboratory experiments have demonstrated that thermal cracking of petroleum and pure hydrocarbons produces a hydrocarbon assemblage that contains significantly lower amounts of methane (Horsfield et al., 1992; McNab *et al.*, 1952; Fabuss et al., 1962; Appleby et al., 1947). Mango (1993) demonstrated in the laboratory the catalytic activity of the Monterey Shale by producing a gas product via the thermocatalytic cracking of n-octadecene-1 in a hydrogen at 1 atm total pressure at 190 to 220°C under anhydrous conditions to produce a gas product with a strikingly similar composition to that of natural gas. He suggests that transition metals present in the sediment represent the catalytically active species.

Reactions occurring during laboratory heating of the Monterey, Smackover, and Eutaw shale results in the production of low molecular weight hydrocarbons whose relative abundance is consistent with those observed in nature. In all the experiments, methane constituted approximately 40 to 90 % of the generated hydrocarbon gas suggesting catalytic activity may be important. The relative abundance of methane varied systematically with temperature and time. Increasing temperature resulted in decreases in the relative abundance of methane. A possible explanation for this trend is that the selectivity of the operant catalyst varies with temperature. Alternatively, the temperature dependence may reflect a systematic shift in the individual reactions responsible for the production of methane. For example, methane generation at low temperature may reflect production directly from kerogen while high temperature generation may be the result of oil cracking reactions. Regardless of the reactions responsible, the rates of methane production observed during these experiments are sufficiently rapid to produce substantial accumulations of natural gas on a geologic time scale (see below).

Although the results of these experiments appear consistent with those of Mango et al. (1993), there are some important differences related to the experimental conditions. The experiments presented here were conducted at 350 bars in the presence of liquid water while those of Mango et al. (1993) were at 1 atm in a dry system. Mango et al. (1993) observed decreasing selectivity towards methane upon addition of high amounts of water. Perhaps more importantly, however, is the presence of abundant dissolved sulfur species in our experiments, which were essentially absent in the Mango et al. (1993) study. Sulfur is well known poison for the catalytic activity of transition metals due to the formation of transition metal sulfides. The presence of sulfur notwithstanding, the apparent catalytic activity in our experiments suggests that sediment components other than transition metals may represent the catalytically active species. Possibilities include dissolved sulfur species, inorganic minerals, and organic compounds such as NSO-rich asphaltene.

Kinetic Modeling

Numerous models have been developed to predict the extent and timing of hydrocarbon generation in sedimentary basins (Sweeney et al., 1995; Hunt et al., 1991; Ungerer 1990; Braun and Bumham, 1990; Lewan 1985; Lopatin 1971, 1976; Karweil 1956; Waples 1980). In general, these models are based on reactions that are governed by first order reaction kinetics and the Arrhenius equation, but vary significantly with respect to the number of reactions that are used to describe the process of hydrocarbon generation. The thermal maturation of kerogen to produce oil and gas is an inherently complex process involving numerous sequential and parallel reactions. Accordingly, even the most complex kinetic models represent gross simplifications of naturally occurring processes. Nonetheless, they represent effective tools for petroleum exploration and predicting the geochemical evolution of sedimentary basins, provided of course that reliable data for activation energies and pre-exponential factors are available.

Laboratory experiments represent a unique opportunity to calibrate kinetic models under controlled conditions of time and temperature. Data from the present experiments are ideally suited to provide kinetic data for the generation of light hydrocarbons and carbon dioxide since gas generation was monitored as a function of time over a wide range of isothermal conditions. For this purpose we used computer code KINETICS (Braun and Burnham, 1990) to analyze the data from the experiments. This code fits an average pre-exponential frequency factor (A_0) and the relative fractions associated with a given activation energy (E_a) for by up to 25 first order parallel reactions. For the present analyses, the absolute amounts of gases generated were converted to fractions reacted relative to the maximum generated at 360°C. A 2-kcal/mole spacing between consecutive values of E_a was used for all calculations.

Results of the kinetic analyses indicate that the generation of carbon dioxide and methane are characterized by different pre-exponential frequency factors and activation energy distributions that are also dependent on the composition of the source kerogen. Methane production from the Eutaw and Smackover Shale (type-III kerogen) is best accounted for by E_a values in the narrow range of 70 to 74 kcal/mole and A_0 values of $1.15 \times 10^{19} \text{ s}^{-1}$ and $3.74 \times 10^{19} \text{ s}^{-1}$ respectively while production from the Monterey shale (type II-s) requires E_a values in the range 66 to 68 kcal/mole and a an A_0 value of $6.37 \times 10^{18} \text{ s}^{-1}$.

In contrast to low molecular weight hydrocarbon generation, the E_a distributions for carbon dioxide production are characterized by a wide range of energies that vary from approximately 40 to 64 kcal/mole for both the Monterey and Eutaw shale. This distribution may suggest that a more diverse set of reactions is responsible for the generation of carbon dioxide. For example, it is likely that carbon dioxide production associated with low values of E_a is the result of the cleavage of oxygen-bearing functional groups directly from the kerogen macromolecule while that associated with high values of E_a may reflect reaction of organic compounds with water.

Application of the kinetic parameters retrieved from the experimental data to temperature and time conditions typical of petroleum producing sedimentary basins allows predictions to be made regarding the timing of gas generation. Gas generation curves for a hypothetical basin with a geothermal gradient of 25°C/km that is subsiding at a rate of 2 km/My. The bulk of methane generation is restricted to a relatively narrow temperature range of 170 to 220°C for the Monterey Shale while generation from the Eutaw and Smackover Shale is shifted to temperatures approximately 20°C higher. Carbon dioxide generation from organic matter, however, is predicted to occur continuously from low temperatures that characterize early diagenesis to temperatures as high as 220°C reflecting the wide range of activation energies associated with its production. Thus, extrapolation of the experimental results to natural conditions indicates that carbon dioxide production is not restricted to diagenetic processes that proceed peak hydrocarbon generation but can be expected to occur during all phases of kerogen maturation including natural gas formation deep within a sedimentary basin.

Comparison of the kinetic parameters derived here with previous studies shows both agreement and disagreement. Horsfield et al. (1992) used the results of confined anhydrous pyrolysis experiments to derive an E_a distribution that ranged from 66 to 70 kcal/mole and a A_0 value of $1.1 \times 10^{16} \text{ s}^{-1}$ for the cracking of a relatively immature crude oil from the North Sea to form C_1 - C_4 hydrocarbons. These values correspond to the bulk of natural gas formation at temperatures of approximately 170 to 220°C in the hypothetical basin described above, consistent with the results of our experiments. Generation of gas during our experiments is a two step process involving the initial generation of bitumen followed by thermocatalytic cracking to produce gaseous products. The striking similarity of E_a and A_0 values determined here with those Horsfield et al. (1992) for petroleum cracking suggest that generation of bitumen may be a relatively rapid process occurring at relatively low temperatures while the cracking of bitumen represents the rate limiting step that dominates the timing and extent of gas generation in our experiments.

Knaus et al. (1992) derived individual Gaussian distributions of activation energies for the generation of methane, ethane propane and butane from hydrous pyrolysis experiments examining the

New Albany Shale. Their results indicate Ea distributions centered on a value 55 kcal/mole for the generation of all gases. The significantly lower Ea values may be due to the fact that they assumed an A₀ value determined using a Pyromat II instrument applied to their hydrous pyrolysis experiments. There is no obvious reason to support such an assumption, however, since reactions occurring during open-system anhydrous, high temperature and low pressure pyrolysis are not likely to resemble those during closed system, hydrous, relatively low temperature and high pressure pyrolysis experiments. Alternatively, the discrepancy between Ea values determined by Knaus *et al* (1992) may be due to compositional differences between the New Albany Shale and the sediments examined here.

Summary

Laboratory experiments represent an effective means to constrain processes responsible for organic transformations that occur in sedimentary basins. Results of hydrous pyrolysis experiments conducted as part of this project indicate that carbon dioxide is the dominant volatile alteration products generated during thermal maturation of the Monterey, Smackover, and Eutaw Shale. Carbon dioxide formation is not limited to early diagenesis but continues during and after peak hydrocarbon formation. Methane constitutes 40 to 90 % of the generated hydrocarbon gases. This distribution of hydrocarbon gases is consistent with those observed in nature and suggests that thermocatalytic cracking controls the generation of natural gas. Low molecular weight alkenes are generated but rapidly decrease in abundance with continued maturation to a level that may be controlled by metastable thermodynamic equilibrium.

Results of kinetic modeling indicate that Ea for the generation of methane range from approximately 66 to 74 kcal/mole while A₀ values vary from 6.37×10^{18} to $3.74 \times 10^{19} \text{ s}^{-1}$. Calculated Ea and A₀ values for carbon dioxide generation show a much wider range of values varying from 40 to 64 kcal/mole and 1.98×10^{14} to $2.95 \times 10^{17} \text{ s}^{-1}$. Predictions based on these kinetic parameters suggest peak methane and carbon dioxide generation in the range of 200°C, while carbon dioxide generation is predicted to occur continuously at both low and high temperatures in a typical sedimentary basin.

Organic Geochemistry, petrography, isotopes:

Summary of biomarker work

All analyses have been completed, and data is in process of being entered into an on-line data base which will be accessible through the Ethernet. Two papers have already been published on this work, Whelan *et al*, 1994 and 1995. A summary paper is also planned describing a plausible overall plumbing system for rapid injection of hydrocarbons into EI-330 reservoirs, as outlined below.

On the basis of biomarkers, all EI-330 oils have a common (Jurassic to Early Cretaceous marine) source. The Jurassic is currently estimated to be deeper than 30,000 ft. It is assumed to be directly beneath EI-330 or to the south because continental shelf oils to the north are compositionally different. The organic geochemistry is most consistent with the oils from the stacked faulted EI-330 reservoir system having been generated fairly early and then having been expelled into overlying reservoir rocks (Cretaceous or other rocks which currently lie at 20,000 to 25,000 ft or somewhat deeper). These, in turn, were buried further under impermeable cap rocks, possibly under salt. Later, as the salt receded, the oil remained trapped beneath overpressure until very recently when further gas formation and pressurization either in situ or from deeper formations caused ejection of the deep reservoir oil into modern Pleistocene reservoirs, in some cases through overpressure. This scenario fits the relative oil and gas maturities, with gases in all reservoirs being much more mature than the oil ($R_o = 1.5$ to 1.7% for gas compared to 0.7 to 0.8% for oil, Whelan *et al* 1994a, 1995). The depths corresponding to these maturities at the present time is coupled with current best estimates on the limits on the oil and gas generation zones

beneath EI-330. We assume that the gases were generated in deeper, more mature formations and have subsequently moved upward to solubilize and pressurize the oil, although a combined marine source/reservoir facies below 25,000 ft is also a possibility. The gas/oil phase is envisioned as episodically having sufficient pressure to break through the overpressure in order to flow upward into the overlying Pleistocene reservoirs. From an exploration standpoint, this hypothesis is important because it implies deeper reservoirs, below overpressure and below reservoirs, which are producing and actively filling today.

This scenario is supported by ages of the inorganic fluids in EI-330 reservoirs. The ^{129}I ages are fairly uniform and are in the range of 35 to 58 Ma. The ^{129}I originates during kerogen maturation and, therefore, roughly reflects the age of sediments from which the oil was generated. These ages are minimum because of potential for contamination with younger fluids during upward migration. It is interesting that ^{129}I ages agree fairly well with those calculated by Qian et al, (1996) based on calculations or Younger et al, (1977) using ratios of gasoline range hydrocarbons. The ages calculated from the oil compositions are 2 to 59 million years at 100°C , or 4 to 20 million years at 150°C . The lower temperature gives ages closest to those measured by the ^{129}I data. Considering the numerous processes other than maturity are known to affect the hydrocarbon compositions, the agreement between the two ages is remarkable, particularly when one is made using the oils and the other on the aqueous fluids.

Whatever the exact age, all of the estimations above are consistent in suggesting that EI-330 fluids, both aqueous and organic, have spent considerable time in reservoirs much hotter than the EI-330 reservoirs are today, consistent with contemporary oil/gas migration from much deeper reservoirs.

Reproducibility of gas and oil compositions over time.

The manuscript by Qian et al, also presents additional evidence regarding the temporal changes in oil and gas described previously for EI-330 oils (Schumacher, 1992, Whelan et al, 1994). The new analyses are most consistent with these temporal changes being caused by recent migration for a deeper reservoir or source. Artifacts produced by sampling or storage or the analytical procedures have been pretty well ruled out. Evidence is presented against an alternative hypothesis of lateral migration as the cause of these temporal changes in composition.

TLC-FID (Iatroscan) results

Introduction

Petroleum migration conduits and reservoirs contain molecular records of petroleum as it migrates from source to trap. Compositional changes associated with increasing maturities of the sourcing kerogens and chemical interactions that occur along the migration pathways affect the bulk and molecular compositions of petroleum and rock extracts. Therefore, vertical and lateral differences in the molecular composition of petroleum streams can help identification of migration pathways and field filling directions (Karlsen and Larter, 1991). Bulk compositions of petroleum and the organic fingerprints left behind in the regional rocks through which petroleum has flowed can be used to interpret heterogeneities in reservoir sands and migration pathways (Karlsen and Larter, 1991). Comparison of the compositions of petroleum flowing through more permeable sand vein networks and/or fractured host-rock, in association with biomarker and phenol data (Taylor, 1994) from oils and fluids may provide further information relating migration pathways and field filling history (Karlsen and Larter, 1999).

Our goal was to reveal compositional information to predict whether migrated hydrocarbons have penetrated host-rock, rock fractures and sandstone veinlets. Host-rock and rock fracture enrichment with saturated hydrocarbons may indicate the presence of lower molecular weight compounds which have faster diffusion coefficients, according to estimations by England et al., (1987) for oil migrating in tortuous media. This diffusion may be further enhanced by the degree of fracturing in the host-rock.

Methods

An Iatroscan TH-10 MK-III, equipped with a flame ionization detector was used to quantify the bulk compositions of oils and core extracts separated by thin layer chromatography on Chromarod-S III silica rods. The solvent system used for separation into saturated hydrocarbons, mono- and di-aromatic hydrocarbons, poly-aromatic hydrocarbons, resins and asphaltenes was as follows:

Compound groups	Elution time		Solvent mixture	Solvent
1). Saturates	27 mins	100%	Hexane	
2). Mono-, di- and poly-aromatics	10 mins	100%	Toluene	
3). Resins and asphaltenes	3 mins	95:5%	Dichloromethane: Methanol	

External standard quantification was performed using a calibration mixture containing known amounts of:

<u>Surrogate standard</u>	<u>Compound group</u>
n-Eicosane	Saturate response
n-Undecylbenzene	Mono-, di-aromatic response
Phenanthrene	Poly-aromatic response
2,6,-Dimethoxyphenol	Resins and asphaltene response

Samples

The Eugene Island Block-330 Pathfinder (A-20SJT) core provided high quality, contamination free core material ideal for detailed geochemical analysis. Core plugs were collected from the slabbed core, which had been stored in a frozen state, two weeks after core recovery.

To monitor detailed compositional heterogeneities throughout the Pathfinder cored interval, the dominant silty shale lithology was sampled in relation to a number of sand and silty laminae and thin-bedded sandstones. The Pathfinder core logging revealed three distinct major structural zones (Anderson et al, 1994). An upper faulted zone exists between 7670 - 7848' m.d. This zone contains slickensided faults at moderate to high angles. A middle structural zone between 7848-7923' m.d. is relatively unfaulted and unfractured but contains several thin, yellow fluorescing sand beds and laminae. The lower zone between 7923-8053' m.d. is faulted. Silty shales have gouge zones that intersect the well at both low and high angles. Fractures in this zone are fairly persistent and thin hairline faults are often slickensided and occasionally show fluorescence (Anderson et al., 1994).

Samples from all three structural zones were collected from the dominant medium-dark grey silty-shale, termed host-rock, and thin sand laminae and sandstone veins, termed vein-rock. The latter invariably showed fluorescence properties under blue-light excitation. Frozen core sub-samples were defrosted and carefully sectioned to collect vein-rock without interference from host-rock and vice-versa. The vein- and host-rock samples were Soxhlet extracted for 48 hours using a 93:7 azeotroph of dichloromethane and methanol. The extracts were all reduced and diluted to a set volume ready for separation by TLC-FID (Iatroscan). Eight rods were spotted and eluted with 2 external standard rods loaded per rack of 10 rods. Data was acquired and quantified using Rainin Dynamax® software. Each

sample was analyzed in triplicate and relative abundances calculated. Relative abundance is used in preference to absolute concentrations to counter the effects of porosity changes (Karlsen and Larter, 1989).

Results and discussion

The sandy and silty vein-rock extracts bulk compositions show a fairly constant predominance (50%) of saturated hydrocarbons. Poly-aromatic hydrocarbons are the second most dominant compound group in these extracts with average abundances of 28%. The polar resins and asphaltenes are present in lower abundances, averaging 14% and 3.5% respectively. The resins show a small increase in abundance with depth below 7858.5' m.d., which lies within the middle, relatively unfaulted structural zone.

Polar compounds are enriched in the deeper pans of the host extracts averaging about 75%. There is <5% relative abundance of poly-aromatics and less than 2% of mono- and di-aromatic hydrocarbons which remains fairly constant vertically. However, the saturates show a striking trend. There is a greater relative abundance of saturates (-40%) between 7678.8'm.d. and 7815.5'm.d. in the shallowest, more faulted structural zone followed by a sharp decrease (~8%) to 7893.70'm.d. within a polar enriched zone (89%), with the exception of one sample near 7846.4'm.d. which contains about 60% saturated hydrocarbons. Comparison of the compositions of the faulted host-rock extract and the adjacent vein-rock extract at 7846.4' m.d. show similar relative abundances of saturates (59% and 62% respectively). Most variance occurs in the amounts of poly-aromatics, which are more dominant in the vein-rock extract (18% vein-rock, 2% host-rock). This host-rock (7846.4'm.d.) was sampled from a small sub-vertical, sinistral fault zone that had no fluorescence properties, unlike adjacent thin, strongly fluorescing sand laminae. Since contamination can be ruled out, we conclude that detectable volumes of more volatile, saturated hydrocarbons have infiltrated the silty shale along this vertical fault plane. The host extract from 7894.5' m.d. contains -80% of saturated hydrocarbons and very few resins and aromatics but 16% asphaltenes. This sample was taken from a non-fluorescing zone within a section of core that had several thin fluorescing sand laminae and may indicate minor migration or diffusive action. The high abundance of polar compounds in most of the host-rock extracts is consistent with other immature rock extracts (bitumens) which tend to be dominated by polar compounds (particularly asphaltenes) (Tissot and Welte, 1978). Figures II-B-iii-6-10 show comparison relative abundances between host and vein samples for each compound group separated.

Summary and conclusions

TLC-FID has shown that vein extracts are compositionally quite distinct from the host-rock extracts in the Pathfinder core. The vein-rock extracts indicate petroleum is present in the sandy migration conduits and that petroleum composition is dominated by saturated hydrocarbons and relatively small abundances of polar compounds and is similar in composition to oils from producing reservoirs. Ternary plots were made of the summed aromatics, polars (NSO's) and saturated hydrocarbons for 47 reservoir and fault zone oils from Eugene Island Block 330 and vein-rock extracts, respectively. These data show a good correlation between the bulk compositions of vein-rock extracts and oils. It is reasonable to conclude that these thin sand and silty laminae form part of complex distributary migration networks, channeling petroleum to shallower, more extensive reservoir sandstones. The ternary plot shows the distribution of host-rock extracts from fractured and unfractured sections and shows that although, saturated hydrocarbons are enriched in some fractured samples, aromatic compounds remain in low relative abundance. One possibility to explain the low abundance of aromatics in host-extracts may reflect water-washing of the host rock. Since, aromatic hydrocarbons are more water soluble than saturated hydrocarbons they may be preferentially removed by water. Polar compounds are also water soluble but since they are so predominant in immature sediments they may not show such a

pronounced loss. However, host-rock samples that transect a fracture or small faulted zone do show evidence for the presence of migrated hydrocarbons. The relative intensity of the compound groups is also higher in fractured and faulted host-rock extracts relative to unfractured and faulted host-rock extracts. Phenol analysis may help to clarify some of these observations.

Phenol analysis

Twenty three representative EI-330 oil and their associated aqueous fluids from each of the stacked reservoirs described in Whelan et al., 1994 and from the Pathfinder well have been sent to Dr Steve Larter at the University of Newcastle for analysis of phenols. If successful, this analysis can potentially distinguish between rapid oil migration up faults versus slower migration through pore spaces. The analysis uses compositional changes in phenols, polar fractions of oil, which partitions between the moving oil and water migrating phases and the solid immobile mineral phase. The partition coefficients for phenol between the three phases are well known from the environmental literature. Measurement of the distributions of phenols between the three phases can then be combined with calculations for partitioning between the various possible phases and reservoirs, developed by Larter. The calculations place limits on the amount of time the oil has "seen" the walls of the migration conduit (Larter and Aplin, 1995; Taylor et al., submitted). Dr Steve Larter from Newcastle University in the U.K., who developed these procedures on fluids from North Sea reservoirs, spent the summer of 1995 at Woods Hole. He has agreed to collaborate with us in applying these procedures to Gulf Coast reservoirs, particularly EI-330. We hope this analysis will allow a distinction between fault-associated migration (fast migration; predicted for some GA and RB and SD and LF reservoirs) versus (predicted) slower migration through the capillary pore system (predicted for many of the shale associated OI oils from the Pathfinder well).

These procedures will also allow us to address several important questions regarding migration in EI-330 - is the migration occurring up fault or through pore space? A 3-D seismic profile of migration of a gas plume in S. South Marsh Island from underneath salt goes all the way to the surface and appears to be bypassing faults. Such plumes are evidently common in this area of the Gulf Coast

An alternative migration scenario also consistent with the EI-330 organic geochemical data is that oil is currently being generated and expelled from early Cretaceous (marine) rock already saturated with more mature gas derived from the underlying Jurassic rocks. The additional on-going gas generated from a marine Early-Cretaceous marine source rock is sufficient to move indigenous gas plus oil upward into Pleistocene reservoirs. In this case, the Lower Cretaceous marine oil source and reservoir rocks are the same. In marine carbonate and siliceous formations, source and reservoir rocks are commonly very closely associated, often being the same rock, (e.g. Hunt and McNichol, 1984). In this case, the whole source/reservoir rock system is carried downward, with efficient oil expulsion being impossible until a depth is reached where sufficient gas can be generated to aid in the expulsion and migration process.

The distinction between these two scenarios is important from an exploration point of view -the first implies deeper conventional reservoirs which could be produced; the other implies a lower porosity marine source/reservoir rock where the producing permeable zones might be much patchier and harder to find.

Limited data suggests that year time scales of oil/gas injection into reservoirs, which appears to be occurring at EI-330, is extremely fast on the scale of normal reservoir mixing processes. Therefore, it seems unlikely that rapid time scale injection could be occurring from a source rock. However, because marine rocks can act simultaneously as both a source and reservoir, it is possible that some sort of combined deeper source/reservoir rock could be providing the "deep holding tank" required for rapid oil injection into shallower reservoirs.

Organic geochemistry, Modeling and technology transfer:

Description of data base

A data base has been created for all of the geochemical data gathered during the course of this project using commercially available "4D Database" on the MacIntosh. Entry into a CERN database folder allows access to other parts of the program. The data base has input sheets for data as well as for sample inventories. Data sheets and plots can be inserted into the "CERN share" files for transfer by ftp to any other organization. Currently, CERN members can access these files via the World Wide Web. This version of 4D replaces an earlier attempt using the same program designed by Chancy Rego and Mary Zawoysky.

For plotting, macros are utilized to export the data from the 4D data sheets to Excel, which has much more sophisticated plotting routines than are available within the 4D program. This has proved to be very advantageous in plotting the very complex data sets generated by the high resolution gas chromatograph mass spectrometer data (HRGCMS) of the biomarkers in the EI-330 oils. At the present time, loading of the most complex HRCCMS data set is complete.

**Oil Migration in a Major Growth Fault:
Structural Analysis of the Pathfinder Core,
South Eugene Island Block 330, Offshore Louisiana**

Steven Losh
Dept. of Geological Sciences, Cornell University

ABSTRACT

The Pathfinder core taken in the South Eugene Island field, offshore Louisiana, provides an outstanding sample of structures associated with a major growth fault that abuts a giant oilfield and which is thought to have acted as a conduit for hydrocarbon migration into the producing reservoirs. Where cored, the growth fault zone cuts semi-consolidated Plio-Pleistocene mudstone and is over 100 meters wide. The fault zone in the core consists of three structural domains, each characterized by distinct rock type, distribution of fault dips and dip azimuths, and distribution of spacing between adjacent faults and fractures. Although, all of the domains contain oil-bearing sands only faults and fractures in the deepest domain contain oil even though the oil-barren fault domains contain numerous faults and fractures that are parallel to those, which contain oil in the deepest domain, and are thus favorably oriented for transmitting oil. This deepest domain is also distinguished from the other two by a greater degree of structural complexity and by a well-defined power-law distribution of fracture spacings. The departure of the fault spacings in the upper two domains from a power-law distribution, combined with stable isotope data that points to low-temperature water-rock interaction within a gouge zone that separates these two fault domains, indicates that the faults in those domains may have been active only in the early stages of the growth fault zone. These faults may thus predate oil migration. In contrast the faults in the oil-bearing domain may have been active later in the fault zone's history, when geologic and organic geochemical investigations indicate oil migrated into the Block 330 reservoirs. Even though oil was present in sands throughout the core, its restriction to faults in the probably-youngest portion of the fault zone implies that oil migrated only through that part of the fault that was active during the time when oil was available. The absence of oil in favorably-

oriented fractures in the other, probably-older fault domains indicates that the oil was never sufficiently - pressured to hydraulically fracture its way up the fault zone, and instead migrated along faults and fractures that were opened primarily by tectonic stresses.

Introduction

High-angle faults in sedimentary basins should logically play a significant role in hydrocarbon migration from deep, overpressured reservoirs and "kitchens" to shallower reservoirs from which they can be economically produced. A number of studies have documented indirect and direct evidence of large-scale cross-formation fluid flow along growth faults (Jones and Wallace 1974; Weber et al. 1978; Hippler, 1993; Galloway et al, 1982, review of Hooper, 1991). While these examples provide valuable information about processes that affect such flow and also give permissive evidence that large volumes of hydrocarbons may migrate in such a fashion. There has remained a large uncertainty as to the actual connections between fault-conduit fluid flow and the filling of economically-producible oil and gas reservoirs. A clear understanding of fault charging could be extremely valuable as a prospect evaluation criterion. Although many reservoirs are spatially associated with faults, what role do the faults really play in charging of the reservoirs? Do some faults, or portions of faults, act as hydrocarbon migration conduits, while others do not? If fault charging does occur, what controls fluid migration up such faults and into the reservoirs?

In order to develop and test answers to these questions, the Global Basins Research Network, a consortium of universities and industry affiliates, undertook a multifaceted U. S. Department of Energy - funded project in South Eugene Island Block 330, offshore Louisiana. The goal was for simultaneously drilling and sampling a large, active growth fault and carrying out a variety of analyses of rocks, brines, and oil and gas from reservoirs adjacent to the fault. This particular location was selected because of a variety of evidence supportive of recent (even ongoing) reservoir filling linked to the bounding fault system (Anderson, 1993; Anderson et al, 1994). The fault was drilled and cored as an extension of a Pennzoil development well (the MO sidetrack) in the fall of 1993, a variety of logs were run and measurements made, and the fault was drill-stem tested as a potential reservoir (Anderson et al, 1994).

The purpose of this paper is to present a structural description of the core that was taken from the well. Particular attention is paid in this study to understanding why, although a wide fault zone was cored, only a discrete portion of it contained oil.

Core acquisition and processing

Because of the need to continuously sample the fault zone in order to fully characterize it, we utilized a whole-coring system designed to maximize recovery in the semi-consolidated sediments typical of the SEI Block 330 field. The bottom-hole assembly (BHA) consisted of the following:

Bit: Baker-Hughes INTEQ prototype RC 425 anti - whirl PDC bit The cutters were asymmetrically placed around the bit in order to minimize "walking" of the bit in the hole.

Core barrel: 18.3 meter x 0.1 meter (6(3-foot x 4 - inch) barrel with 6 - millimeter (1/4 inch) aluminum liner, with pressure release valves. Barrel was equipped with full-closure "clamshell" type doors just above the bit. Closure of these was activated from the surface before pulling out of the hole.

Coring was done at a mudweight of 1.97 kg/liter (16.3 pounds per gallon). There was no appreciable fluid pressure gradient associated with the fault in this well.

We anticipated that the core would be taken primarily in semi-consolidated smectite-mudstone. Industry experience with whole coring in this type of sediment led us to use an experimental mud formulation in order to stave off "balling", or adhesion of clay to the bit, which typically slows penetration rates to 60 centimeters an hour or, usually less. The requirement that we use a water-based mud constrained us to utilize an environmentally safe synthetic additive: we used a poly alpha olefin (Friedheim et al, 1991), such that it constituted 3% of the mud. This substance does not fluoresce. It is chemically distinct from nearly all of the organic compounds we anticipated finding in the core, and, at the low concentrations used, it did not interfere with sensitive electrical resistivity measurements required for the Formation MicroImager (FMI) log. We also used an additive to inhibit clay swelling which could have led to jamming in the core barrel.

The combination of the above enabled us to obtain unprecedented penetration rates with the core bit in the semi-consolidated mudstones, averaging 21 meters/hour, ranging as high as 52 meters/hour. We retrieved 104.6 meters of core out of 109.8 meters attempted for a recovery rate of 95%.

Because we initially anticipated slow (30 to 60 cm/hour) penetration rates during curing, we expected to retrieve perhaps 25 meters of core in the time available to us. Thus, we opted not to put on the coring BHA until we had drilled to within 12 meters of the fault, as determined from seismic data. Unfortunately, the uncertainty in picking the fault and converting time to depth for the seismic data resulted in our drilling through the upper bounding fault of the growth fault zone, which was marked by a gas show of 360 units (compared to a background of about 75 units), before changing to the coring RHA. This fault zone later produced several barrels of oil in a drill stem test (Anderson et al, 1994). The top of the core is thus about 8 meters below the first main fault in the growth fault zone.

On the rig, the core was marked with orientation stripes as it was pulled out of the core shuttle, then cut into 91-cm (three-foot) sections, or tubes. Every other tube, beginning with the second one, was placed in dry ice on the rig, and has been continuously frozen since in order to preserve organic compounds for geochemical analysis. The unfrozen tubes were placed on a tilted table in order to drain the drilling mud, and then capped and filled with non-fluorescing epoxy in order to stabilize the core in the liner and thus prevent damage during transport and storage.

In Houston, the cores were logged for spectral gamma radiation, oriented for slabbing by means of X-ray radiography, and logged on site at a scale of 1:5 as soon as they were slabbed. Wherever possible, tubes were slabbed perpendicular to the predominant set of fractures in order to facilitate sampling of them; where no fractures were present, tubes were cut perpendicular to bedding. The cores are presently stored at Pennsylvania State University. Frozen cores are kept at -15 C, the unfrozen ones are waxed and stored in a humidified room at 3 C.

Methods

All observed faults and fractures were recorded on the core logs, and their geometries in three dimensions were verified using X-ray fluoroscopy. A feature was considered a fault if it displayed gouge, breccia, pervasive slickensides, or offset beyond that which accompanied breakage of core in the inner tube. A disproportionately large share of faults are perpendicular to the long axis of the core, and at least some could represent breakage and rotation of core in the barrel as it was drilled (Kulander et al, 1990). However, many of these faults experienced only transnational offset, with no evidence of rotation either in the form of differences in apparent bedding dip across the fault s)r of circular grooves or slickensides on the fault surface. Where such evidence of coring-induced faulting was lacking, the fault was recorded as a natural feature. In contrast to faults, a fracture was indicated by a planar break across which no offset was observable, or which did not display any other fault characteristics.

Except for the fault at 2325 meters DD, faults and fractures were generally not detectable in the FMI log, perhaps owing to their tightness, so their orientations in real space had to be obtained indirectly. Structures in the core were oriented by the following procedure: 1) the core was co-registered with the FMI log by comparing the core gamma log with the downhole gamma ray log that was run with the FMI, as well as utilizing log header information. The depths recorded on the core (driller's depths) are 4.6 meters less than those recorded on the FMI log (logger's depths); this magnitude of discrepancy is not unexpected. 2) Places were identified where the bedding dip in the core matched the apparent bedding dip in the Formation MicroImager log. In those instances, the apparent azimuth of the bedding dip in the FMI and that of the slabbed face of the core were identical. 3) The apparent orientation of the stripes on the core inner tube was computed. It is assumed that this orientation does not vary over the length of a given 9.1 - meter (3- foot) core, as care was taken to maintain the core orientation when pulling it out of the shuttle on the rig. 4) The apparent azimuth of the slab face for each section was then computed, according to the angle between the orientation lines on the inner tube and the slab face. The azimuth was uniquely constrained by the direction of bedding dip in the core. 5) Apparent dip and dip azimuth were measured for all faults whose dip azimuth lay in the plane of the slab face. Because the slab faces were oriented to be cut parallel to the apparent dip azimuth of the majority of faults in a given section, the overwhelming majority of faults in the core were measured. However, the dataset of oriented faults and fractures does not contain planes that were oblique, rather than perpendicular, to the slab face: these account for about 20% of all observed planar features. 6) The apparent dip and dip azimuth data so obtained were then

rotated to account for the hole deviation, which in the cored interval was 22 degrees to the vertical in the 038 direction. Over four hundred data points were obtained in this fashion.

GEOLOGIC SETTING AND DESCRIPTION OF FAULTS

Geologic setting of the Pathfinder Well

The DOE-Pennzoil. well in SEI Block 330, the Pathfinder, was drilled in a fault-bounded salt withdrawal minibasin of Plio-Pleistocene age (Holland et al, 1990; Alexander and Flemings, 1995). This minibasin hosts the giant South Eugene Island field, presently the largest producing field in offshore Gulf of Mexico and the largest Pleistocene oil field in the world. Production is primarily from rollover anticlines in a section of deltaic and fluvial sands, and the reservoirs are segmented into a number of fault blocks (op cit). This sequence of sands, interbedded with mudstones overlies a thick (600-meter) mudstone and below that, turbidite/slope fan deposits (Alexander and Flemings, 1995).

The main growth fault zone penetrated by the Pathfinder well (the 'A' fault zone) is seismically imaged from > 5 seconds to approximately 0.4 seconds; at shallower depths, it is not resolvable in the data. The 'A' fault zone has a throw of approximately 600 meters at the level of the OI sand, just above where the Pathfinder intersected it, and displacement decreases approaching the surface. Based on stratigraphic evidence, the fault experienced its highest slip rate during deposition of the deltaic sand - shale sequence between 1.8 and 1.2 Ma (Alexander and Flemings, 1995). Current activity of the fault is implied by its presence at the shallowest resolvable depths in seismic data and by oil seeps along its trace on the seafloor. The geometry of the fault and hangingwall deformation in SEI Block 330 are consistent with dip-slip normal movement. Preliminary data on well-bore breakouts from the Pathfinder well indicate a minimum horizontal compressive stress direction nearly perpendicular to the fault trace (Peter Flemings, Penn State Univ., 1995, oral comm.), again consistent with normal faulting with no discernible strike-slip component.

Fault zone geometry and displacement in the Pathfinder well

In the Pathfinder well, the upper bounding fault for the A fault zone was intersected at 2325 meters driller's depth (DD), just below the 01-5 sand and 23 meters below the first appearance of the foraminifera Robulus 64 (1.8 Ma). This bounding fault has a dip of 53 degrees in the 213 (southwest) direction, according to the Formation MicroImager, and is about one meter thick in the well. Below this fault is a thick (>244 meters. to the bottom of the well at 2563 meters) section of variably faulted calcareous and non-calcareous silty mudstone, shaly silt, and rare sand, mostly as laminae but also, in one instance, in beds up to 25 cm thick. Using the paleontological picks and assuming a sedimentation rate of 1.3 mm/year for the D. brouweri - Robulus 64 interval (cf. Alexander and Flemings 1995), an omission of about 67 meters of section across the upper bounding fault at 2325 meters DD can be calculated taking true bed thickness into account. The first appearance of G. miocenica (2.0 my.) at 2476 meters DD. below the bottom of the core, is consistent with an apparent sedimentation rate of 1.04 mm/yr in the D. brouweri - G. miocenica interval. This is within the range of expected sedimentation rates, thus implying a small net throw on all of the cored faults. In contrast, D. pentaradiatus (2.2 my.) appears at 2503 meters DD. consistent with an omission of about 240 meters of section between that marker and the G. miocenica marker just 27 meters higher in the well, again assuming that a sedimentation rate of 1.3 mm/year applies to this interval. Additional faults may lie below this depth, but are not discernible from the paleontological, FMI, or seismic data.

In contrast to the gentle northeast bedding dips determined from seismic data and well intercepts for strata above the main fault zone, the FMI log shows consistent moderate (20-40 degrees) north to northwest bedding dips below the main fault. Seismic and well top data from the upthrown block to the northeast of the fault zone indicate horizontal to gentle southwest dips. The cored portion of the Pathfinder well is best interpreted as a rotated horst between two or more faults, only the top one of which is evident on the seismic section. The northwest component of dip azimuth observed on the FMI in the cored interval can be accounted for by a modest counterclockwise rotation (looking northeast) about an

axis perpendicular to the plane of the upper bounding fault at 2325 meters. The northerly dips may be the result of rotation related to cross-faults that may lie within the faulted rock below the fault .

Nature of faults in core

Although we had drilled past the upper bounding fault before beginning to core, the core contains over 500 faults and provides much information about the nature and geometry of faults in the growth fault zone. In terms of physical appearance, there are two main types of faults logged in the core. The predominant type is a very thin to hairline slickensided fault across which displacement or truncation of beds can be observed in many cases. The slickensided fault surface is polished, and the slickenlines are very fine parallel grooves. Much less abundant than the "hairline" faults are gouge/breccia zones, which are up to 15 centimeters across in the core. In these, mudstone has been reconstituted into slickensided gouge that is slightly lighter colored than the adjacent mudstone and supports clasts of relatively undeformed mudstone up to 1.5 cm across, typically elongated parallel to the gouge foliation. A number of faults comprise zones up to 1 cm wide, mainly containing brecciated mudstone clasts with minor clay gouge infilling the interstices; these faults may represent a gradation between the two types above. No consistent cross-cutting relationships between sets of "hairline" faults was observed. Shallowly-dipping faults cut steeply-dipping ones and vice versa, although the former situation is more common. However, the gouge zones, which typically dip shallowly to moderately to the southwest are almost never cut by any later structures in the core and in fact truncate more steeply-dipping faults and fractures.

Several faults and fractures in the core are mud-filled, but no natural fracture fillings or mineralized fault breccia were observed, and few open fractures or faults were detected in situ on the FMI log. However, about 25 faults and fractures in the core fluoresced strong gold, indicating the presence of oil, and will be described later. In addition, a weak gas show (increase of 70 units above background) was recorded in faulted mudstone at the bottom of the core.

Orientation of faults in core

Three structural "domains" can be identified in the core on the basis of plots of depth vs. fault dip and dip azimuth. The upper and lower thirds (more or less) of the core contain faults having a wide range of dips, and their dip azimuths nearly span the compass. The middle third, in contrast lacks shallow-dipping faults and faults whose dips lie in the northeast quadrant; southeast-dipping faults are present but rare. The boundary between domains 1 and 2 in the core corresponds to a 15-cm wide gouge zone that dips shallowly to the southwest and separates calcareous mudstones above from non-calcareous mudstones below. This fault zone is also marked by a high density of fractures and faults. Within domain 2 faults are scarcer and the rocks are siltier progressing downhole: the few notable sand beds in the core lie in the interval of minimal fault/fracture density. Although no distinct fault boundary was observed between domains 2 and 3, the rocks of domain 3 are much shalier than those immediately above, the faults typically contain more gouges than those in domains 1 and 2, and the fault+fracture density is also much higher. All but one of the 25 oil-bearing faults and fractures lie in domain 3.

Utilizing the above breaks, the fault data were analyzed separately for each domain. Dip/dip azimuth lines were plotted on an equal-area lower hemisphere stereographic projection. The number of lines per 1% area was then corrected for the angle between the line and the borehole orientation (Terzaghi, 1965; Barton and Zoback, 1992), and the resultant dip-corrected dataset was contoured using spherical Gaussian statistics (Kamb, 1959). Each domain is characterized by a distinctive concentration of fault orientations. The faults in domain 1 are predominantly shallow to moderately southwest dipping, although a weakly-developed set of east-dipping faults is also present. Domain 2 consists predominantly of moderately- west to west-northwest-dipping faults. Domain 3 contains two well-developed populations of faults, one moderately to steeply west-dipping, the other shallowly dipping to the southwest. A lesser population of northeast-dipping faults is also present. The dip/dip azimuths of oil-bearing faults are also plotted individually. They do not appear to have an affinity for any particular population.

In contrast to the fault domains, fracture orientations do not appear to show systematic variations with depth. A stereographic projection of the total population of fracture dip/dip azimuth data, corrected for the angle between the dipline and the drillhole, as done for the fault data above, shows a single broad maximum dipping steeply to the west-northwest (figure 6b).

Geometric distribution of fault/fracture spacing

As a way of evaluating each domain with respect to its propensity to act as a fluid conduit, some simple analyses of fracture/ fault spacing in each domain were carried out. The depth of every planar discontinuity that intersected the centerline of the core was recorded, including those for which orientations were not derived; spacings between immediately adjacent structures were figured directly from these depths. Log-log plots of fracture/fault spacing vs. the cumulative frequency of fractures/faults at or greater than a given spacing are, like the stereonet plots, distinctive for each domain. A plot of data using this transformation would be expected to yield a straight line for a power-law distribution of fracture/fault spacings (Gillespie et al, 1993). The data from domain 1 cannot be well fitted with a straight line over any significant range of spacings. Domain 2 spacings can be fitted with a straight line if the spacings below 10 centimeters are considered to be under-sampled and thus dropped from the dataset; the correlation coefficient (r^2) for the remaining data is then 0.96, with a slope of 1.00. The validity of considering fracture/fault spacings under 10 centimeters to be under-represented is questionable. However, as the practice during logging of this core was to record all distinguishable fractures and faults. Even in massive mudstones, fractures or faults 10 centimeters apart are readily distinguishable from one another. The lower threshold of spacing resolution for the core as a whole is on the order of 5 cm in well-laminated intervals. Fractures and faults as closely spaced as 5 mm were mapped as separate features. Including fractures and faults as closely-spaced as 5 cm in the domain 2 dataset results in a poorer straight-line fit to the data with a correlation coefficient of .926. Thus, the data for domain 2 do not appear to be well characterized by a power-law distribution or the closely-spaced fractures and faults are characterized by much different statistics than are the more widely-spaced ones.

Fracture/fault spacing data from domain 3 are well-fit by a straight line on a log-log cumulative frequency plot, using a lower spacing cutoff of 3 cm. The correlation coefficient for a straight line of slope 1.59 is 0.98, over a range of 1-1/2 orders of magnitude. The fracture/fault spacings in domain 3 clearly follow a power-law distribution.

The same data were also analyzed using an interval counting method. Intervals of varying sizes (d) were imposed on the core log. and the number of intervals (N) containing at least one fracture or fault was counted. Plots of log N vs. log (1/d) yield linear slopes for power-law distributions (Barton, 1995). The data for domains 1 and 2 are moderately characterized by such a distribution, having correlation coefficients of 0.98 and 0.97. respectively for interval sizes greater than 30 cm; however, the data also show a weak but continuous curvature. The data for domains 1 and 2 depart significantly from a power-law distribution at sampling intervals less than 30 cm. This departure is not believed to be an indication of a lower limit of perceptibility, as fractures much closer than 30 cm apart were logged routinely, as noted above. Thus, the fracture spacing data from these two domains are not characterized by a power-law distribution. In contrast to domains 1 and 2, and consistent with conclusions drawn from the cumulative frequency vs. spacing plots above, data for domain 3 are well-fit by a straight line on a plot of log N vs. log (1/d), yielding a slope of 0.88, with r^2 equal to 0.995 over 1-1/2 orders of magnitude of interval sizes. Analysis of residuals (Brooks, 1995) and incremental slopes between adjacent data points (Gillespie et al, 1993; Walsh and Watterson, 1993; Manning, 1995) corroborate the validity of a straight line fit to the domain 3 data.

Discussion

The above data demonstrate the structural complexity of a typical young growth fault zone in a mudstone-dominated section offshore Louisiana. Any conclusive interpretation for the cause of the uneven distribution of oil within the cored faults, as envisaged in the introduction to this paper is greatly hindered by the fact that the drill hole is a one-dimensional sample of what is clearly a three-dimensional system. For instance the presence of oil within domain 3 faults could be simply due to the proximity of an oil-charged sand in or adjacent to that particular fault zone near the Pathfinder well or to a locally complex fault pattern related to a nearby subsidiary fault. In fact, the structural data for domain 3 demonstrate the presence of two distinct fault sets, one of which is oblique to the main growth fault trend.

The interaction of these fault sets would be expected to result in an interconnected set of fractures that could constitute a permeable pathway for fluid flow.

Overlaid on the structural complexity, however, the analysis of fault spacing data indicates there may also be intrinsic differences in fault mechanics between the three structural domains in the core. The oil-barren domains are also characterized by a "deficiency" of closely-spaced faults and fractures relative to a power-law distribution, in contrast to domain 3. Because it is unlikely that this behavior is an artifact of a lower limit of perceptibility, this geometric difference may in fact reflect a difference in the mechanics of faulting. As shown above, fault/fracture spacings of domain 3 are well characterized by a power-law distribution, typical of "tectonic" faults/fractures documented elsewhere in consolidated rocks (Velde et al. 1991; Barton and Zoback. 1992; Gillespie et al, 1993; Barton. 1995). Departure from this behavior in domains 1 and 2 may reflect deformation of sediments whose material properties during faulting differed from those of consolidated rock, as suggested by Gillespie et al (1993). In this case, the faults in domains 1 and 2 may have been active earlier in the consolidation history of the sediment than were the faults of domain 3; the domain 3 faults could even be presently active.

Oxygen isotope data from which one may derive temperature and thus depths at which water-rock interaction took place were collected for calcite from two faults, including the low-angle gouge zone that separates domains 1 and 2. This gouge zone contains an unusually high amount of calcite (up to 9 weight %, determined by X ray diffraction (Losh et al, 1994), which is primarily diagenetic in origin. The ^{18}O values of this calcite are consistent with isotopic exchange with pore fluid having oxygen isotopic composition of 0 permil SMOW at temperatures of 14 to 22 C (fractionation equation of O'Neil et al, 1969). The fluid that circulated through the gouge zone precipitated calcite at temperatures not much higher than those that probably prevailed at the seafloor at the time. Thus indicating isotopic exchange took place at shallow burial depth, early in the fault's history. Oxygen isotopic equilibration between calcite and fluid at present day temperatures in the cored portion of the fault zone (about 65 C) would have produced

Distinctly different calcite $\delta^{18}\text{O}$ values on the order of 2‰ permil, which are nowhere in evidence in the sampled faults in the core. Thus, the sampled faults in domains 1 and 2 have served as fluid conduits only early in the history of the growth fault zone, a finding consistent with the above interpretation of fault spacing data.

The coupling of relative timing of fault movement with the distribution of oil in faults, fractures, and sands in the core provides some insight into the timing and controls of oil migration relative to faulting. As was noted earlier, oil is present in all sands in the core, regardless of structural domain, but is (with one exception) present only in faults and fractures in domain 3. Furthermore, the stereograms illustrate the presence, in all three domains, of faults having "favorable" orientations for being oil-filled. The attitudes of faults that contain oil, a *de facto* indicator of favorable orientation, in domain 3 generally lie well within the population of fault orientations deduced for domains 1 and 2, but these features are barren of oil in those domains. Taken together, the above observations and interpretations indicate that: 1) faulting in domains 1 and 2 took place before the sands in those domains were charged with oil, 2) faults in domain 3 have been active more recently than those in domains 1 or 2 and may be active now, and 3) oil migration in the fault zone took place relatively late in the evolution of the growth fault, and may be occurring now. The relatively recent timing of oil migration into Block 330 reservoirs is indicated by organic geochemical and geologic studies (Whelan et al, 1994; Alexander, 1995). Thus, oil migration appears to have taken place within the same time interval as activity of faults in domain 3. The mere presence of favorably-oriented breaks, as defined above, did not appear to have enhanced oil migration in the upper two domains (Barton and Zoback, 1995). Rather, oil and gas migration in the fault zone probably took place only in those faults that were active when migratable hydrocarbons were available.

If fault-hosted oil migration was in fact restricted to the active part of the fault, some inferences may be made with respect to mechanisms of fluid migration within the fault zone. In particular, Anderson et al (1994) hypothesized that fluid ascent within the fault zone was described in terms of cycles of fluid pressure build-up followed by hydraulic fracturing, rapid fluid migration, fluid pressure dissipation, and ultimate closure of the fracture. In this interpretation, fluid migration up the fault is not directly linked to fault active. However, the temporal linkage between oil migration and tectonic activity as described above, and the lack of migration via faults that were evidently inactive when oil flushed through the sediments, implies that deviatoric tectonic stress sufficient to produce failure was a major control on

fracture and fault permeability in the Pathfinder core, and that fluid pressures alone were never sufficient to hydraulically open fractures.

Conclusions

The Pathfinder core provides a detailed traverse through much of a major growth fault, which is believed to have played a significant role in migration of hydrocarbons from deep to shallower levels. Detailed logging of the core shows that this growth "fault" is a zone at least 100 meters thick and that it consists in the core of three distinct domains, each characterized by its own distribution of fault orientations and fault/fracture spacings. Except for the upper bounding fault, only the faults in the lowest of the domains are known to contain oil. This domain is also characterized by a more complex fault pattern and is well described by a power-law distribution of fault/fracture spacings, in contrast to the other domains whose faults contain no oil. Both faulting and oil migration appear to have taken place in the same relatively recent time interval in domain 3, whereas faulting probably preceded oil charging of sands in the other two domains. The restriction of oil-bearing faults to the youngest portion of the fault zone, and their absence from portions of the fault that were active before migration, points toward fault activity as a major controlling factor on oil migration in the faults sampled by the Pathfinder core.

Acknowledgements

Funding for this work was provided by the Global Basins Research Network and Dept. of Energy grant DC-FC22-93BC14961 to Roger Anderson, Lamont-Doherty Earth Observatory. I especially thank Pennzoil Exploration and Production Co, without whose involvement the Pathfinder Well would not have been drilled. Paleontological analysis was carried out by Ardy Callender and Bernie Shaffer. Applied Biostratigraphix, Houston, and elucidated by Denise Butlen Pennzoil. Formation MicroImager interpretation was performed by Laura Foulk, Schlumberger, and Bruce Hart assisted with core logging. I thank Bruce Malamud, Ben Brooks and Prof. Don Turcotte for assistance with statistical analysis. Any shortcomings in interpretation are my own.

REFERENCES

- Alexander, L. 1995, Ph.D. thesis, Cornell University
- Alexander, L., Flemings, P.. 1995. Geologic evolution of a Plio-Pleistocene silt withdrawal mini-basin, Eugene Island South Addition, Block 330, offshore Louisiana; Amer. Assoc. Petrol. Geol. Bull.
- Anderson, R., 1993, Recovering dynamic Gulf of Mexico reserves and the U.S. energy future; Oil and Gas Jour., April 26, p.85-91
- Anderson, R., Flemings, P., Losh, S., Austin, J., Woodhams. R., 1994, Gulf of Mexico growth fault drilled, seen as oil, gas migration pathway; oil and Gas Jour., June 6, pp.97-103
- Barton, C.C., 1995. Fractal analysis of scaling and spatial clustering of fractures, in Barton, C.C., and LaPointe, P.. eds., Fractals in the Earth Sciences, Plenum Press, New York, pp.141-178
- Barton, C.A., Zoback, M.D., 1992, Self-similar distribution and properties of macroscopic fractures at depth in crystalline rock in the Cajon Pass scientific drill hole.; Jour. Geop. Res., vol. 97, pp.5181-5200
- Barton, C.A., Zoback, M.D., Moos. D., 1995, Fluid flow along potentially active faults in crystalline rock; Geology vol.23, pp. 683-386
- Brooks, B., 1994, Fractal clustering of metamorphic veins: Comment; Geology, v. pp. 1147-1148
- Friedheim, 3., Hans, O., Park, A., Ray, C.. 1991. An environmentally superior replacement for mineral-oil drilling fluids; Soc. Petrol. Eng. preprint SPE 23062. pp.299-312
- Galloway, W., Henry, C., Smith, O.. 1982, Depositional. framework, hydrostratigraphy. and uranium mineralization of the Oakville Sandstone (Miocene), Texas Coastal Plain. Univ. of Texas at Austin Bur. of Econ. Geol. Rept. of Investigations 113, 51 pp.
- Gillespie, P, Howard. C., Walsh, 3., Watterson, 3.1993, Measurement and characterization of spatial distributions of fractures; Tectonophysics. vol. 226, pp. 113-141

- Hippler, S., 1993, Deformation microstructures and diagenesis in sandstone adjacent to an extensional fault: Implications for the flow and entrapment of hydrocarbons; Amer. Assoc. Petrol. Geol. Bull., vol.77, pp.625-637.
- Holland, D., Leedy, 3., Lammlein, D., 1990, Eugene Island Block 330 field - U.S. A., offshore Louisiana; in Beaumont, F., and Foster, N., eds., Structural Traps III: Tectonic Fold and Fault Traps; Amer. Assoc. Petrol. Geol. Treatise of Petroleum Geology, pp.103-143
- Hooper, E. C. D., 1991. fluid migration along growth faults in compacting sediments; Jour. Petrol. Geol. vol. 14. pp.161-180
- Jones, P., Wallace, R., Jr., 1974. Hydrogeologic aspects of structural deformation in the northern Gulf of Mexico basin; Jour. Res. U.S. Geol. Surv., vol. 2, pp.511-517
- Kamb, W., 1959, Ice petrofabric observations from Blue Glacier, Washington, in relation to theory and experiment, Jour. Geop. Res.. vol.64, pp.1891 - 1910
- Kulander, B., Dean, S., Ward, B., Jr., 1990, Fractured Core Analysis: Interpretation, Logging, and Use of Natural and Induced Fractures in Core; Amer. Assoc. Petrol. Geol. Methods in Explor. Series. vol.8,88 pp.
- Losh, S., Eglinton, L., Wood, 3., 1994, Coring and inorganic geochemistry in the Pathfinder Well, in Anderson, R., Billeaud, L., Flemings. P., Losh, S., and Whelan, 3.. Results of the Pathfinder Drilling Program into a Major Growth Fault: Part of the GBRN/DOE Dynamic Enhanced Recovery Project in Eugene Island 330 Field, Gulf of Mexico; Annual Report (CD-ROM) to DOE. contract no. DE-FC22-93BC14961, pp.183-249.
- Manning, C., 1994, Fractal clustering of metamorphic veins: Reply; Geology. vol. - pp. 1148-1149
- O'Neil, 3., Clayton, R., Mayeda, T., 1969. Oxygen isotope fractionation in divalent metal carbonates; Jour. Chem. Phys., v.51, pp.5547-5558
- Terzaghi, R., 1965. Sources of error in joint surveys: Geotechnique, vol.15, pp. 287-304
- Velde, B., Dubois, J., Moore, D., Touchard, G., 1991, Fractal patterns of fractures in granites: Earth Planet. Sci. Lett., vol.104, pp 25-35
- Walsh, 3., Watterson, J., 1993, Fractal analysis of fracture patterns using the standard box-counting technique: Valid and invalid methodologies: Jour. Struc. Geol.v.. 15. pp. 1509-1512
- Weber, K., Mandl, G., Pilaar, W., Lehner, F., Precious, R.. 1978, The role of faults in hydrocarbon migration and trapping in Nigerian growth fault structures; Tenth Annual Offshore Technology Conference Proc., vol. 4, pp.2643-2653 (OTC 3356)
- Whelan, 3., Eglinton, L., Requejo, R., Kennicut, M., 1994, Pathfinder Well organic geochemistry: Indicators of oil source and maturity and fluid flow mechanisms, in Anderson, R., Billeaud, L., Flemings. P., Losh, S., and Whelan, 3., Results of the Pathfinder Drilling Program into a Major Growth Fault: Part of the GBRN/DOE Dynamic Enhanced Recovery Project in Eugene Island 330 Field, Gulf of Mexico, Annual Report (CD-ROM) to DOE. contract no. DE-FC22-93BC14961, pp.616-662.

Water - Rock Interaction in a Large Growth Fault, South Eugene Island Block 330 Field, Offshore Louisiana

Steven Losh

Dept. of Geological Sciences, Cornell University, Ithaca, NY

Lorraine Eglinton
Dept of Chemistry, Woods Hole Oceanographic Institution, Woods Hole, MA

James Wood
Dept. of Geological Sciences, Michigan Technological University, Houghton, MI

ABSTRACT

We examined whole core, sidewall core, and cuttings from seven wells that penetrated a large growth fault abutting the Plio-Pleistocene South Eugene Island Block 330 field, offshore Louisiana, for evidence that the fault acted as a conduit for fluid flow into the prolific reservoirs. The analytical program was designed to deduce mass and heat flux within the fault zone, and focused on comparing a variety of measurements on faulted and unfaulted rocks. Data include vitrinite reflectance and spore fluorescence measurements, standard petrographic and cathodoluminescence techniques, Rock-Eval pyrolysis, oxygen and carbon isotopic analysis, determination of bulk mineralogy and illite/smectite ratio by X-ray diffraction, and whole-rock major element and trace element geochemical determinations.

Rocks within and adjacent to the fault zone in the D.O.E.-Pennzoil Pathfinder well, taken at about 2226 - 2317 meters (7300 - 7600 feet) TVD, were characterized by low vitrinite reflectances, averaging 0.3%Ro, yellow to yellow-green spore fluorescence colors, moderate to high $\delta^{18}\text{O}$ and $\delta^{13}\text{C}$ values ($\delta^{18}\text{O}$ of calcite in faulted rocks ranged from 28 to 31 permil SMOW with $\delta^{13}\text{C}$ from 0.8 to -3.1 permil PDB), and, except for slight increases in K_2O , CaCO_3 , and Zn in some faulted samples, no differences in major or trace element composition between deformed and undeformed sediments. The lowest $\delta^{18}\text{O}$ value, 21.8 permil, was from a calcite-cemented siltstone 11 meters above the fault. The rocks were characterized by illite/illite+smectite ratios between 40% and 60%, unexpectedly high considering the low maturity of organic matter, and in most cases, there is no distinction between faulted and unfaulted rocks in terms of mineral assemblage or relative abundance. One gouge zone contained calcite in excess of that in the average mudstone, but oxygen and carbon isotopic data, noted above, indicate the calcite precipitated at shallow burial depth.

Rocks from the A6ST Well, which intersects the 'A' fault about 300 meters northwest of the Pathfinder at 1980 meters (6500 feet) TVD, exhibit higher vitrinite reflectances, averaging 0.55% Ro in the 'A' fault decreasing to 0.4% Ro at a distance of 50 meters (160 feet) feet above the top of the

fault, yellow-orange to orange spore fluorescence colors, a distinct $\delta^{18}\text{O}$ and $\delta^{13}\text{C}$ shift to lower values (22.4 and -9 permil, respectively) at the top of the fault, and, like the Pathfinder, little evidence of mass influx into the sampled fault rocks. There are no observed mineralogical differences between faulted and unfaulted rocks, and the illite/illite+smectite ratios are a subject of dispute: one laboratory obtained a range of 40-55%, averaging 44%, whereas another obtained a range of 23-35%, averaging 27%, from samples from the same interval within the fault zone.

Based on the existing data, the 'A' fault in the Pathfinder is concluded to have transmitted little fluid from depth, whereas the same fault in the A6ST well appears to have been a conduit for ascent of a substantial amount of fluid.

Introduction

High-angle faults in sedimentary basins may be expected to play a significant role in hydrocarbon migration from deep, overpressured reservoirs and "kitchens" to shallower reservoirs from

which they can be economically produced. A number of studies have documented indirect and direct evidence of large scale, cross-formation fluid flow along growth faults (Jones and Wallace, 1974; Weber et al. 1978; Hippler, 1993; Galloway et al. 1982, review of Hooper, 1991). While these examples provide valuable information about processes that affect such flow and also give permissive evidence that large volumes of hydrocarbons may migrate in such a fashion, there has remained a large uncertainty as to the actual connections between fault-conduit fluid flow and the filling of economically producible oil and gas reservoirs. A clear understanding of fault charging could be extremely valuable as a prospect evaluation criterion. Although many reservoirs are spatially associated with faults, what role do the faults really play in charging of the reservoirs? Do some faults, or portions of faults, act as hydrocarbon migration conduits, while others do not? If fault charging does occur, what controls fluid migration up such faults and into the reservoirs?

In order to develop and test answers to these questions, the Global Basins Research Network, a consortium of universities and industry affiliates, undertook a multifaceted U. S. Department of Energy - funded project in South Eugene Island Block 330, offshore Louisiana, having the twin goals of simultaneously drilling and sampling a large, active growth fault and carrying out a variety of analyses of rocks, brines, and oil and gas from reservoirs adjacent to the fault. The centerpiece of this project was the Pathfinder well, drilled into the main fault bounding a salt withdrawal minibasin of Plio-Pleistocene age (Holland et al, 1990; Alexander and Flemings, in press). This minibasin hosts the giant South Eugene Island field, presently the largest producing field in offshore Gulf of Mexico and the largest Pleistocene oil field in the world. Production is primarily from rollover anticlines in a section of deltaic and fluvial sands, and the reservoirs are segmented into a number of fault blocks (op cit). This sequence of sands, interbedded with shales, overlies a thick (600 meter) shale, and below that turbidite/slope fan deposits (Alexander and Flemings, in press). This particular location was selected because of a variety of evidence supportive of recent (even ongoing) reservoir filling linked to the bounding fault system (Anderson, 1993). The fault was drilled and cored as an extension of a Pennzoil infill development well (the A20 sidetrack) in the fall of 1993, a variety of logs were run and measurements made, and the fault was drill-stern tested as a potential reservoir (Anderson et al, 1994, 1995).

Geochemical research on rocks from Block 330 has focused on ascertaining chemical and thermal signatures of fluid thought to have ascended the main growth fault (the 'A' fault) and flowed into reservoir sands. This paper presents petrographic, mineralogic, stable isotopic, and bulk geochemical data from fault zone Samples from the Pathfinder well, the A6ST well, which also penetrated the 'A' fault, and several other wells along the 'A' fault. Whole coring was carried out in the Pathfinder well in order to continuously sample a major growth fault abutting the Block 330 reservoirs. Continuous sampling, as opposed to sidewall coring, across the fault zone was considered important in that many features related to fluid flow in fault zones typically vary greatly over distances of centimeters. Thus, we attempted to obtain as much whole core as was practical, and recovered 109 meters (343 feet) of 10.2-cm (4-inch) diameter core in unfaulted to highly faulted rock, primarily mudstone. Sidewall cores were taken above the cored interval in order to evaluate evidence for fluid flux within the main 'A' fault, which was not cored, as well as in the downthrown block to the fault zone.

Analytical procedures

Vitrinite reflectance measurements were carried out on three different types of samples: 1) kerogen concentrate samples, cold set in epoxy resin and polished in accordance with ICCP protocol (1963, 1971); 2) thin sections, prepared in accordance with the methods of Stach (1982), and 3) polished blocks of sediment. In whole-rock samples an "operator selective approach" (European method of Mukhopadhyay, 1992) is used, whereby morphology, color, relief quality, internal structure and other characteristics are used to identify vitrinite particles indigenous to the sediment. The whole rock approach is preferred for Gulf Coast sediments since one can distinguish autochthonous vs. allochthonous vitrinite, bitumen populations, cavings, and drilling contaminants. Rather than measuring a wide range of reflectances on a variety of macerals and then selecting the dominant or lowest-reflectance population as indicative of vitrinite maturity, as is frequently done for kerogen concentrates, we believe that more-reliable results can be obtained from these organic-lean, immature sediments by measuring fewer, but better characterized vitrinite particles in whole-rock mounts (Barker and Pawlewicz, 1993).

Vitrinite reflectance was measured using a Zeiss standard universal research microscope-photometer system (MPMO1K) equipped with a tungsten-halogen lamp (12V, 100W), a x40 Epiplan oil immersion objective, filtered 546 nm incident light, and Zeiss immersion oil (n_c 1.517 @ 23C). Three standards are measured in triplicate before analysis and every 30 minutes once analysis commences. Blue light fluorescence observations on spores (Mukhopadhyay, 1992) was performed on the same microscope fitted with a high-pressure mercury lamp (HBO100) for autofluorescence and an LP520, BP450-490 filter system.

Illite/smectite ratios were determined at Michigan Technological University on the $<2 \mu\text{m}$ fraction with selected samples further separated to $<1 \mu\text{m}$. Samples from each size fraction were mounted on ceramic plates using a vacuum pump apparatus with XRD analysis carried out on an automated Dapplr/Noreko machine using $\text{CuK}\alpha$ and 1 degree slit size at a counting time of 2 seconds per step. Samples were then solvated with ethylene glycol in a desiccator for 24 hours at room temperature. Identification of I/S and estimation of percent expandables were made from techniques described by Moore and Reynolds (1989). A similar procedure was followed at Exxon Production Research for samples analyzed there.

Sample preparation and analysis for carbon and oxygen isotopic analysis of whole-rock carbonate was carried out by Krueger Enterprises, Cambridge, Mass. Carbon dioxide was liberated from the calcite by reaction with phosphoric acid at 90 C. Several calcite+dolomite samples were analyzed by timed extraction: a CO_2 sample was taken from the reaction vessel at 20 minutes, and is taken as representative of the isotopic composition of calcite, and a second sample was collected at 3 hours after initiation of reaction, and is taken to represent dolomite.

Whole - rock multielement geochemical analyses of whole core and sidewall core samples were obtained by X Ray Assay Labs. in Don Mills, Ontario. Major elements, Cl, Cr, Sn, Rb, Sr, Y, Zr, Nb, Ba, and LOI were analyzed by X-ray fluorescence, rare earths by neutron activation. S by LECO, and Li, Be, B, V, Co, Ni, Cu, Zn, Ge, Mo, Ag, Cd, Pb, and Bi by ICP spectroscopy. Gold, platinum, and palladium were analyzed by fire assay with DCP spectroscopy finish, but were found to be below the detection limits of 1, 1, and 10 ppb respectively. Major element oxides are computed without consideration of LOI or $\text{H}_2\text{O}^+/\text{H}_2\text{O}^-$. For all plots BaSC_4 , taken as a tracer of drilling mud, is corrected for in samples having greater than 10,000 ppm Ba.

THE PATHFINDER WELL

General geology

In the Pathfinder well, the first detectable fault in the 'A' fault zone was intersected at a measured driller's depth (DD) of 2325 meters (7625 feet), after drilling through a 15-meter thick section of tilted sands and shales of the OI-5 sand. According to the Formation MicroImager, the main fault has a dip of 53 degrees in the 213 (southwest) direction, and is about 120 centimeters thick in the well. Below this fault is a thick (>245 meters, to the bottom of the well at 2563 meters (8405 feet) DD) section of faulted and unfaulted calcareous and non-calcareous silty mudstone, shaly silt, and rare sand. In contrast to the gentle northeast bedding dips determined from seismic data and well intercepts for strata above the main fault zone, the FMI log shows consistent moderate (2040 degrees) north to northwest bedding dips below the main fault. Seismic and well top data from the upthrown block northeast of the fault zone indicate horizontal to gentle southwest bedding dips. Thus, the cored portion of the Pathfinder well is best interpreted as a rotated horst between two or more major faults, only the top one of which is evident on the seismic section.

The core was taken from 2332 - 2442 meters (7650-8012 feet) DD, within the interval defined by Robulus 64(1.8 Ma), first encountered at 2303 meters DD, and Globorotalia miocenica (about 2 Ma), first encountered at 2476 meters. The average sedimentation rate of 0.7 mm/yr calculated for the above faulted interval is about half the 1.3 mm/yr rate calculated by Alexander and Flemings (in press) for unfaulted shales of this age elsewhere nearby in the minibasin, and is consistent with a stratigraphic omission on the order of 120 meters due to faulting in this interval.

Lithology and structure

The core consists of three lithologic "domains" that correspond to structural domains in the core. The uppermost 26.2 meters of core consists primarily of slightly to moderately calcareous, predominantly medium gray laminated to massive silty shale (mudstone) to shaly silt, also sampled by sidewall cores above the fault. The next 47 meters of core are significantly siltier but non-calcareous, and the thickest sand beds, up to 22 centimeters, are found in this interval. The bottom 36.6 meters comprise laminated, non-calcareous silty shale with only a paucity of sand. Siderite concretions to 4 cm in diameter are common. The boundary between domains 1 and 2 is a low-angle gouge zone at 2358.5 meters (7736 feet) DD that was sampled as part of this study. Oil was found almost exclusively in faults and fractures in the deepest structural/lithologic domain in the core.

The fault zone partly sampled by the core is believed to have a total throw on the order of 600 meters at the depth of the core (Alexander and Flemings, in press). The FMI log shows faults both above and below the cored interval, and paleontological data suggest that the cumulative throw on faults in the core is relatively minor. Nonetheless, the core contains over 500 faults and fractures, which are of two types: very thin slickensided, polished "hairline" faults that display mm to tens of cm of offset in the core and that have a range of orientations, and slickensided gouge/breccia zones to 15 cm thick that are of indeterminate offset and that have low to moderate dips to the southwest.

Petrography, Mineralogy, and Vitrinite Reflectance

Petrographic examination of faulted shale from the whole core and sidewall cores shows a variety of structures: microshears defined by bands of rotated clay from tens to a couple of hundred microns wide, rotated blocks bounded by microshears, and microduplex structures. In terms of cathodoluminescence, calcite/dolomite in these rocks comprises two populations: angular, bright red-orange luminescing calcite and redder dolomite grains that appear to be detrital, and subangular to subhedral dull red-orange luminescent ferroan calcite grains that are disseminated throughout the rock and in some instances lie in fractures. This latter type of calcite is believed to be authigenic. Foraminiferal calcite tends to be non-luminescent.

X-ray diffraction of shales from the core and sidewall cores was carried out at Exxon Production Research and Shell's Bellaire Laboratory, with one sample analyzed by Fourier Transform Infrared spectroscopy (FTIR) at Core Labs. The eleven shales consist primarily of clay (42 to 71%) and quartz (21 to 37%), and contain between 6 and 17% combined feldspars and a few percent calcite (0-9%). Clay and K-feldspar are negatively correlated. Only one sample had detectable dolomite, and one had detectable pyrite. Samples from within or near fault zones (7631, 7635-7636.1, 7734.9) tended to have more calcite than samples farther than a few feet from a known fault (7612, 7657), although the sidewall core at 2317.4 meters (7601 feet) consists largely of authigenic calcite. The fault at 2358.5 meters (77.36 feet) separates calcareous rocks above from noncalcareous ones below, and no sample below 2358.5 meters has more than trace amounts of calcite, regardless of position with respect to faults.

Clay mineralogy has been determined for a number of samples, both in terms of bulk mineralogy and smectite-illite ratios in the mixed-layer clays. The former was primarily performed at Exxon Production Research, Houston, with one sample analyzed at Shell Bellaire Labs, Houston. Smectite-illite ratios (Table. 1) were determined primarily at Michigan Technological University, with four samples analyzed at Exxon Production Research. Clays are predominantly mixed-layer smectite-illite (60-69%: four samples), with lesser detrital illite (16-22%), kaolinite ((14-17%), and chlorite (1-2%). Overall, smectite/(smectite+illite) ratios in the <2micron glycolated fraction from cuttings, sidewall cores, and the whole core show an gradual increase in I/S from about 30-40% at depths of 1200-1500 meters (4000 to 5000 feet) to 45-60% deeper in the hole. The shift to intermediate I/S ratios at depth is permissible given the bottom-hole temperature on the order of 70 to 75 degrees C (Abercrombie et al. 1994; J. Boles, oral comm., 1994)), although these ratios are not normally observed in rocks below temperatures on the order of 100 C (Hower et al. 1976; Milliken, 1985). However, the relatively high I/S ratios higher in the well (most published profiles for Plio-Pleistocene rocks show I/S ratios on the order of 20-30% at the depths of the Pathfinder well) suggest the initial composition of the smectite may favor transformation at lower temperature than usually observed. The elevated I/S ratio is probably not an effect of pore fluid chemistry, if the brine samples (Losh and Wood. 1995) are representative of fluids that interacted with the fault rocks, if anything, the potassium concentration is low (on the order of 300 mg/L), and the Na and Mg

concentrations are high (ca 40,000 and 1500 mg/L. respectively), which should suppress the smectite to illite transformation rather than enhance it (Huang et al. 1993).

Vitrinite reflectance measurements were made at Woods Hole Oceanographic Institute (WHOI). Reflectance measurements were made on a variety of macerals, allowing distinction to be made between reworked and "indigenous vitrinite, with indigenous vitrinite reflectance measured on telocollinite.

In the Pathfinder well, indigenous vitrinite reflectance ranged from 0.25%Ro to 0.47%Ro (figure 5). The highest-reflectance sample comprised 2 readings: excluding this sample, the maximum reflectance was 0.37% Ro. Reflectance increases slightly with depth, and shows no increase relative to known faults at 2325 meters (7625 feet DD) (A fault) and 2055 meters (6741 feet) (B fault). In addition, no petrographic evidence of oxidation or bitumen impregnation was observed. The vitrinite reflectance values are in accord with burial along a normal (20-25 C/km) geothermal gradient and do not allow for anomalous heating related to the fault zones. Yellow and yellow-green spore fluorescence colors corroborate the low thermal maturity of the sediments indicated by the vitrinite reflectance data.

Pyrolysis

Pyrolysis Tmax data were also obtained at Woods Hole on some of the same samples analyzed for vitrinite reflectance, using a Chemical Data Systems pyroprobe system interfaced for computer data acquisition and processing. Tmax data in general covaries with vitrinite reflectance, although they indicate a somewhat higher thermal maturity in terms of equivalent vitrinite reflectance than do the actual reflectance measurements. Elevated Tmax values for the Pathfinder well are commonly associated with organic assemblages containing greater than 60% reworked vitrinite and inertinite particles, and so may not be indicative of actual thermal maturity of the rocks themselves. In addition to providing evidence concerning thermal maturity, the pyrolysis measurements give evidence of migrated hydrocarbons in the form of P1 peaks or pyrograms from the sidewall and whole core samples. Nearly all sidewall cores from the reservoirs penetrated by the Pathfinder well show enhanced P1 peaks indicative of migrated hydrocarbon; however, the fault zone samples show no such peaks.

Stable isotopes

Oxygen and carbon isotope data have been obtained from whole-rock shale samples taken from fault zones and undeformed shales near the faults. As expected, the $\delta^{18}\text{O}$ values of dolomite and calcite from the same samples differ by several permil, but the

minimum $\delta^{18}\text{O}$ value of the calcite obtained in this manner is virtually the same as that of the lowest - $\delta^{18}\text{O}$ calcite + dolomite sample, indicating that the $\delta^{18}\text{O}$ values of the; calcite + dolomite mixtures are reasonably representative of the calcite $\delta^{18}\text{O}$. Because of the extremely fine-grained, disseminated nature of the calcite, separate samples of distinct cathodoluminescent character cannot be made. However, the isotopic composition of a shale containing both types of calcite and dolomite must be a mixture of the two end-point compositions of detrital and diagenetic carbonate, and thus useful information about the isotopic composition of diagenetic calcite + dolomite, which is of the greatest interest can be obtained from the presence or absence of an isotope shift from values in equilibrium with seawater at seafloor temperatures. Re-equilibration with higher-temperature fluid during burial would produce a shift to lower $\delta^{18}\text{O}$ values, which, even in a mixed sample, will be observable in the data.

In the case of samples from the Pathfinder whole core and sidewall cores, oxygen isotopic composition of calcite and calcite + dolomite mixtures ranges from 21.8 to 31.1

permil relative to SMOW, with no observable distinction in calcite $\delta^{18}\text{O}$ between undeformed and highly sheared samples at a given location. Calcite from sidewall cores near or in the 'A' fault at 2325 meters (7625 feet) DD yield $\delta^{18}\text{O}$ values between 26.3 and 28.2 permil, slightly shifted to lower $\delta^{18}\text{O}$ values relative to the deeper fault zone and to undeformed shales above and below the fault. Calcite from undeformed calcite-cemented shale around 2317 meters (7600 feet) (logger's depth) yields the lowest $\delta^{18}\text{O}$ values of all, at 21.8 permil. Calcite-cemented intervals are commonly known above fault zones in the Gulf of Mexico, and these samples probably represent such an occurrence. Carbon isotopic composition of calcite ranged from -0.7 to -9.5 permil relative to PDB; the low $\delta^{13}\text{C}$ value for the sample having 3180 of 31.1 permil may reflect contamination from epoxy, owing to the non-reproducibility of

the value (a second analysis of this sample gave $\delta^{13}\text{C}$ value of -8.2 permil), or less likely, it may indicate some of the calcite in that sample was precipitated from water containing oxidized methane or "kerogenic" CO_2 at or near the seafloor. Generally, the carbon isotopic composition of the calcite is typical of normal marine shell and foraminiferal material, and is largely independent of $\delta^{18}\text{O}$. On average, calcite $\delta^{13}\text{C}$ in faulted rocks is slightly higher than in undeformed ones (-1.7 permil vs. -2.5 permil).

In a well-developed gouge zone at 2358.5 meters (7736 feet). Both $\delta^{18}\text{O}$ and $\delta^{13}\text{C}$ of calcite are typical of values in equilibrium with seawater at seafloor (10-20 C) temperatures, and, particularly in the case of the oxygen isotope data, do not reflect re-equilibration with, or precipitation from higher-temperature fluids during burial. Even if the sediment were buried as a closed system, with only pore fluid available to exchange with calcite as temperature increased, an $\delta^{18}\text{O}$ shift would be observed as a result of moderate to high water-rock ratio: volumetrically, pore fluid occupies about 25% of the rock, whereas calcite + dolomite, considered to be the only phases to exchange significantly (by recrystallization) with fluid at these low temperatures, comprise only 2 to 3% of the rock, leading to a volumetric water/rock ratio (W/R) on the order of 10, or an oxygen water/rock ratio of about 7. Even if clays were considered to exchange freely with water, the W/R would be on the order of 0.5, still sufficient to produce a significant shift in calcite $\delta^{18}\text{O}$ during closed-system exchange during burial. At 70 C and W/R of 0.5, equal to an oxygen W/R of 0.35, calcite initially at 30 permil in the closed system described above would exchange with pore fluid and equilibrate to $\delta^{18}\text{O}$ value of 27.4 permil (fractionation of 0'Neil et al. 1969). As the calcite $\delta^{18}\text{O}$ values from the fault at 2358.5 meters show no shift away from pristine, seawater-equilibrated values, even resulting from closed-system exchange with pore fluid, they are interpreted to have been precipitated at low temperature, thus, at shallow burial depth. Since calcite is easily exchanged under ambient conditions by recrystallization, its high $\delta^{18}\text{O}$ indicates a lack of influx of even locally-derived fluid, which implies inactivity, in this fault during most of its burial history.

Along similar lines, calcite in the sidewall cores taken near the 'A' fault is only weakly shifted in $\delta^{18}\text{O}$ from unexchanged values of about 30 permil, and reflects minor interaction with fluid during burial and/or faulting. The lowest $\delta^{18}\text{O}$ samples from 2317.4 meters (7601 feet), reflect interaction with aqueous fluid at or near present-day temperatures, as indicated by their near-agreement with the modeled $\delta^{18}\text{O}$ equilibrium trend for burial diagenesis at a geothermal gradient of 22 C/km, comparable with that observed presently in the Pathfinder well.

The calcite $\delta^{18}\text{O}$ values appear to correlate with sandiness of the sediment rather than with proximity to shear zones. In no case do the oxygen isotopic data reflect equilibration with ambient pore fluid at temperatures higher than those attributable to a normal geothermal gradient; if that were the case, the $\delta^{18}\text{O}$ values would lie to the left of the "equilibrium line". However, it is possible that, because the isotopic values were measured on whole-rock samples that include a mixture of detrital and diagenetic carbonate, a low $\delta^{18}\text{O}$ authigenic population exists and that it is masked by the presumably higher $\delta^{18}\text{O}$ detrital component. It is also possible that a fluid ascending rapidly from depth would have a $\delta^{18}\text{O}$ value higher than the ambient static values assumed in calculating the equilibrium curve, resulting in anomalously high-temperature calcite lying on the high $\delta^{18}\text{O}$ side of the curve. The data are insufficient to address these possibilities, and the simpler interpretation - that of an absence of thermally anomalous fluids affecting the oxygen isotopic composition of calcite in the Pathfinder well samples - remains.

Bulk Chemistry

Bulk chemical analysis was performed on 69 samples from the core, including all samples for which stable isotope data were obtained. Samples were collected every 60 centimeters (two feet) over a 3-meter (100-foot) interval in the relatively unfaulted middle of the core. Samples were also collected from gouge, fault breccia, sidewall con-as within and above the 'A' fault at 2325 meters (7625 feet) DD, and nearby undeformed rocks elsewhere in the core for the purpose of evaluating element flux in the fault zones.

Crossplots of typically immobile phases and elements, such as Al_2O_3 , Zr, and Sc show high correlation coefficients, indicating their usefulness as monitors of element flux in fault zones sampled in the Pathfinder well. Zirconium and Al_2O_3 are inversely correlated: Zr (from zircon) tracks the sand

fraction, as indicated by the strong, positive correlation between Zr and SiO₂, whereas Al₂O₃ tracks the clay fraction determined by XRD. These elements are less well correlated with other elements considered to be immobile in the sedimentary environment, but the correlations are sufficient to warrant the conclusion that these elements are immobile as a group. For the purposes of gauging mobility of other elements such as potassium, silica, and sodium, Al₂O₃ and Zr are used as references.

The bulk geochemical data indicate little or no difference in chemical composition between faulted and unfaulted rocks in the Pathfinder well. Furthermore, the data indicate that many normally-mobile components, such as K₂O, SiO₂, Zn, and Cu, are largely immobile in these rocks, even in samples characterized by a pronounced ¹⁸O shift. Sample 7593, Zn shows a slight increase in gouge samples from the lowest of the three fault domains in the core. A plot of K₂O vs. Al₂O₃ shows a strong correlation ($r^2=0.85$) and a trend having a slope of 0.15, dominated by the stoichiometry of mixed layer smectite-illite clays. Potassium content in the samples is consistent with XRD data indicating the shales consist of approximately 30 to 45 weight percent I/S clay, compared with at most 11 percent K-feldspar in addition to kaolinite and detrital illite. However, a small group of samples from the fault zone at 2358.5 meters (7736 feet) DD plots at slightly elevated K₂O/Al₂O₃ ratio. XRD analysis of one of these samples (7736.4) shows a relatively high I/S ratio of 57% implying that the increase in K₂O content could be due to illitization of I/S clays. Addition of pure illite (K_{0.5}Al₃Si_{3.5}O₁₀(OH)₂) would produce a trend having a slope of 0.3 on this plot, and addition of 11 weight percent illite to the I/S phase of these shales, which average 40% I/S clay by weight, could account for the observed departure from a linear trend; as noted, one gouge sample shows an elevated I/S ratio. Growth of potassic feldspar would be represented as a line having a slope of 1.7 on this plot, and addition of 0.7 weight percent K-spar could also account for the observed slight K₂O increase; this increase would not be resolvable by XRD and would barely be perceptible by petrographic analysis.

Other frequently mobile components show strong correlation to immobile components in the Pathfinder rocks. SiO₂ shows no departure from immobility in faulted samples, and FeO and MgO correlate well with Zr. Similarly, zinc and copper, both soluble as chloride complexes at pressure and temperature conditions prevailing in the cored interval, show surprisingly good correlation with alumina, implying that even these elements were not introduced into the Pathfinder rocks by throughgoing fluids. In contrast $\delta^{18}\text{O}$ of whole-rock calcite is positively correlated with percent clay (3 data points) and negatively correlated with Zr, which tracks sand content. This relationship is interpreted to reflect the control of bulk permeability of rocks in and near the fault zone on calcite $\delta^{18}\text{O}$.

Na₂O in both faulted and unfaulted rocks is essentially independent of K₂O and Al₂O₃, implying that variations in sodium concentration in these samples is not due to mineralogy, but rather may be due to contamination. Assuming a pore fluid having 50,000 mg/l Na, similar to brines taken from the OI sands nearby, and a shale porosity of 25%, the deposition of salt in pore spaces due to evaporation is calculated to increase Na₂O by as much as 0.9% of the total rock mass, or equivalently, by as much as 40% over the Na₂O content of the rock itself. A number of samples were washed prior to analysis in order to circumvent this source of contamination, and generally show lower Na₂O content than do unwashed samples. No quality control was carried out at the lab in order to ascertain that all of the salt had indeed been washed away. Thus, none of the Na₂O values should be considered accurate.

Some of the above samples show elevated CaO content relative to Al₂O₃, indicating mobility, particularly in the fault zone at 2358.5 meters (7736 feet). Samples from that interval contain as much as 9% calcite, as determined by X-ray diffraction. As discussed above, the oxygen isotope data indicate that this calcite exchanged with fluid only at low temperature; thus, the calcite was precipitated at shallow burial depths.

Gas geochemistry

Martin Schoell, of Chevron Petroleum Technology Company, La Habra, California, collected 15 gas samples during drilling of the Pathfinder well by means of "...splicing a 'T' into the gas stream of the mudlogging unit and transferring the gases with a hand pump into aluminum-coated gas bags at ambient pressure. The samples were analyzed for ¹³C₁ and ¹³C₂ using the newly developed Rapid Gas Isotope Analyzer (RGIA). A temperature programmable GC (equipped with a 30 m GS-Q megabore column), is on-line connected with a mass spectrometer via a combustion furnace. The mud gases were sampled with a gas tight syringe from the gas bags that were filled at the mud logging unit. Every unknown and

standard (NGS-2) was injected at a 6:1 split ratio. The reproducibility of the NGS-2 values is ± 0.25 permil. Our values were on average 0.9 permil more positive than the accepted value of the standard. Daily correction factors determined from the gas standards were applied to the methane and ethane isotope values...

"The methane isotope values become increasingly more negative with depth. The value of 47.8 permil above the fault zone in reservoir sand that will be likely a producer is fairly typical for gases in the Gulf of Mexico. The systematic trend to more negative values in the fault zone indicates two interesting aspects: 1) gases in the fault zone are not homogeneous and 2) the gases are mixtures of bacterial gas and thermogenic gas. Taken at face value the data are in many aspects surprising. Firstly bacterial gas in the fault zone suggests that gases of thermogenic and bacterial origin migrate as mixtures in the migration conduits. Secondly, the systematic trend within the fault zone would suggest unmixed discrete zones of compositionally different gases within the fault. This is difficult to rationalize as one would assume that the fluids are homogeneous in an active feeder fault..." (taken from Schoell and Haught. 1994)

DISCUSSION: Implication of geochemistry for fluid flow in the Pathfinder fault zones

The evidence concerning fluid flow can be divided into two categories: that bearing on thermal imprint of fluids on rocks (smectite-illite ratio, oxygen isotopes, vitrinite reflectance), and that bearing on chemical imprint of fluid (also smectite-illite ratio, oxygen isotopes, mineralogy, bulk chemistry). The former type of data are useful only in determining whether fluid may have ascended the shear zone rapidly enough to produce thermal anomalies. Whereas, the latter type of data are sensitive to the passage of fluid from any source, at any flux, provided that major or trace elements are transported and precipitated. Thus, the first type of data may yield negative conclusions for the same rocks that are shown by the latter type to have hosted fluid flow. Such appears to be the case for the fault zone rocks studied in the Pathfinder core.

Vitrinite reflectance measurements indicate the fault zones in the Pathfinder well do not represent measurable thermal anomalies relative to unfaulted rocks or rocks at similar depths and geothermal gradients elsewhere in the region. These data yield a more definite insight into thermal maturity of fault rocks than do smectite-illite ratios in that the latter are highly susceptible to a variety of influences, such as fluid chemistry and initial clay composition. The smectite-illite data may equivocally be interpreted as reflecting unusually high temperatures (as discussed above). The vitrinite reflectance measurements, corroborated by spore fluorescence colors, preclude such a thermal anomaly in faults encountered in the Pathfinder well, including the main 'A' fault zone at 2325 meters (7625 feet) DD. Oxygen and carbon isotopic composition of calcite in and near fault zones in the Pathfinder well does not support throughgoing fluid flow in the sampled shale dominated portions of the faults. If anything calcite composition points to fluid focusing into sandier sediments adjacent to the main 'A' fault. These data are in accord with carbon isotopic composition of gas samples collected and analyzed by Martin Schoell of Chevron, which indicate that the biogenic component of the fault zone gases has not been swept out by migrating thermogenic gases during burial.

As noted, scant data indicate flux of some elements in some fault zones in the core. In particular, calcite has been precipitated and illite appears to have formed from smectite in a gouge zone at 2358.5 meters (7736 feet). Although this particular mass flux is interpreted on the basis of stable isotope compositions to have taken place early in the burial history. The main 'A' fault at 2325 meters (7625 feet) DD is inferred to have hosted fluids on the basis of a modest calcite ^{18}O shift from unexchanged shale values; however, there is no evidence of mass gain or loss in the sidewall cores taken within or near this fault. The strongest evidence for fluid influx in the form of an ^{18}O shift is from a calcareous shaly silt some 11 meters above the main fault zone. Indicating that, on the basis of the available samples, fault-related fluid flow at the location of the Pathfinder well may have been focused in permeable rocks adjacent to the fault rather than within shale gouge zones of the fault itself. The fluid responsible for the ^{18}O shift in calcite did not introduce or remove mass from the affected rocks, implying either that the actual volume of fluid was small or that it in any event was in chemical equilibrium with the bulk shale mineralogy. Much or all of the observed ^{18}O shift in mudstone calcite could have been produced by water-rock interaction in a closed system undergoing burial. This stands in marked contrast to fault rocks

from the A6ST well, which penetrates the same fault as does the Pathfinder about 300 meters to the northwest.

The A6ST Well

The AE sidetrack well was drilled in 1991 to test a target in the KE sand at a TVD of approximately 1890 meters (6200 feet). A rathole was drilled through the 'A' fault, and a pressure surge was encountered, with oil-cut mud coming to the shaker. Pennzoil shot about 45 sidewall cores in the fault, but cased it off as reservoir dimensions could not be assigned to it. The sidewall cores form the basis of this investigation, which consists of petrographic and cathodoluminescence observations, stable isotope analysis of calcite, X-ray diffraction analysis, smectite-illite ratio determinations, and vitrinite reflectance measurements.

Petrography, Mineralogy, and Vitrinite Reflectance

Petrographic observations indicate the rocks are pervasively faulted, displaying numerous microshears characterized by rotated clays. In some instances showing coarser grain size than in the matrix, as well as rotation of clasts, duplex structures, and drag folding. As with the sidewall cores from the Pathfinder well, these fault structures are believed to represent *in situ* deformation not associated with the process of collecting the cores. At the outer edge of most cores a band of clay on the order of 1/4 mm wide has been rotated into parallelism with the core margin. This deformation and associated fracturing near the core margin is related to the coring procedure. However, the penetrative structures listed above show consistent displacement sense throughout the entire sidewall core; this, coupled with the observation that measured displacement on some of the faults is greater than that which would be expected on faults produced during the coring operation, implies a tectonic origin for the structures.

The A6ST samples contained essentially the same mineral assemblage as reported for the Pathfinder well. As is the case for the Pathfinder samples, there are two general types of carbonate with respect to cathodoluminescence: a bright red-orange, angular population, and a dull orange-red to red, subrounded to subhedral group that in some instances occurs as isolated grains in fractures. Both types of grains are disseminated throughout the rocks, are between 10 to 20 microns across, and are not mechanically separable. Calcite comprises an estimated 3 to 5 percent of the shale. As was the case with the Pathfinder samples, dolomite is not detectable in XRD scans made at Cornell University, but was detected in trace amounts in samples analyzed at Exxon Production Research Co, Houston. Electron microprobe analysis indicates dully-luminescent calcite in these rocks contains 2 to 3 percent iron as FeCO_3 .

Smectite/illite ratios in rocks from the A6ST well varied considerably according to the laboratory carrying out the analyses. The first samples were analyzed at Michigan Technological University, and were concluded to have I/I+S ratios in rocks from within and just above the fault zone between 40% and 55%, averaging 44%. Significantly higher than "background" I/I+S ratios of 20-30% reported for Plio-Pleistocene rocks in the area by Milliken (1985). A second group of ten samples from the same interval was analyzed at Exxon Production Research (EPR) in Houston, and found to have I/I+S ratios between 23% and 35%, averaging 27%, lying within the "normal" range as defined above. All samples are characterized by $\text{Reichweite} = 0$. The difference in reported values from the two laboratories could simply be due to different methods of interpreting the X-ray spectra. It must be noted that the two laboratories did obtain similar I/S ratios for samples from the Pathfinder well, but also that the A6ST and Pathfinder I/S determinations at MTU were carried out by different researchers. They were carried out by the same personnel using the same techniques at EPR. In view of the above considerations, the lower EPR numbers are taken as accurate. Their I/S determinations show a modest correlation with semi-quantitative degree of deformation in the fault rocks. Application of illite-smectite data to paleothermometry of the fault rocks awaits resolution of two issues. 1) The I/S ratios in the Pathfinder well are significantly higher than expected given the low vitrinite reflectance values and spore fluorescence colors; they also show no relation to the fault. 2) If the EPR I/S determinations for the A6ST well are indeed accurate, and there is no known reason to believe otherwise, the I/S ratios there are significantly lower than expected when compared with the vitrinite reflectance values and spore fluorescence colors.

Vitrinite reflectance measurements were made on polished thin sections and whole-rock blocks from fault rocks in the AEST. Five epoxy mounts of kerogen from fault rocks yielded an average reflectance of indigenous telocollinite, using the same apparatus as described above, of 0.55%Ro. with a standard deviation of 0.08 (79 measurements). Other macerals were also measured; typically these were higher than those of the indigenous material and defined discrete populations on histograms. The relatively high reflectance of rocks from the fault zone in the A6ST well identifies that zone as a thermal anomaly with respect to rocks outside the fault zone, and to rocks elsewhere in the fault zone (i.e., the Pathfinder well). The relatively higher reflectance is corroborated by yellow-orange to mid-orange spore fluorescence colors in the same samples; these indicate higher thermal maturity than do the green-yellow, yellow, and yellow-orange colors observed in the Pathfinder samples.

Stable isotopes

As is the case with the Pathfinder samples, dolomite in the samples is volumetrically minor in comparison to calcite and its presence does not appear to affect the $\delta^{18}\text{O}$ of the calcite + dolomite mixture to any significant extent. Oxygen isotopic composition of calcite (+ dolomite) shows a pronounced shift to lower $\delta^{18}\text{O}$ values, as low as 23.4 permil. The $\delta^{18}\text{O}$ shift actually involves unfaulted rocks just above the fault zone: calcite in rocks at the "top" of the fault shows a reverse $\delta^{18}\text{O}$ shift, back to higher $\delta^{18}\text{O}$ values with depth. Faulted rocks well below the top of the fault (for example, Samples at 2269 meters (7443 feet) DD) lie at high, unexchanged $\delta^{18}\text{O}$ values. These data suggest that, if the observed $\delta^{18}\text{O}$ shift is related to fluid flow in the fault, that fluid preferentially flowed along the "top" of the fault.

As noted for the Pathfinder samples, the $\delta^{18}\text{O}$ shift observed in the data may represent a mixing trend between low- $\delta^{18}\text{O}$ diagenetic calcite and high - $\delta^{18}\text{O}$ detrital and foraminiferal calcite, present in samples above and within the fault zone, and the low- $\delta^{18}\text{O}$ endpoint may lie to the high-temperature (low- $\delta^{18}\text{O}$, or left) side of the "equilibrium line". However, there does not appear to be a relationship between abundance of dull-luminescent calcite and whole-rock calcite $\delta^{18}\text{O}$. Alternatively, the calcite $\delta^{18}\text{O}$ values may simply be partially "frozen in" by partial equilibration with pore water during burial. The data are inconclusive in this regard: they permit, but do not unequivocally support, the interpretation of thermally anomalous fluids in the fault zone.

Calcite $\delta^{13}\text{C}$ values are correlated with the $\delta^{18}\text{O}$ values, such that the lowest- $\delta^{18}\text{O}$ samples also have the lowest $\delta^{13}\text{C}$, between -4 and -9 permil, whereas the highest- $\delta^{18}\text{O}$ samples have normal marine foraminiferal $\delta^{13}\text{C}$ values of around 0 permil. The ^{13}C depletion in the lower- $\delta^{18}\text{O}$ calcites may be due to incorporation of some carbon related to hydrocarbon maturation and/or organic acid decarboxylation, supporting a relatively deep source for the diagenetic fluid.

Whole rock geochemistry

The combined vitrinite reflectance, stable isotopic, and initial smectite-illite data lead us to conclude that at least part of the 'A' fault encountered in the A6ST well acted as a fluid conduit, and that at least some of the fluids were hotter than ambient temperatures. We then sought to corroborate the above evidence for fluid flow with whole rock geochemistry, anticipating that we might be able to determine the flux of major and trace elements into fault rocks.

As in the case of the Pathfinder well, Zr, Al_2O_3 , and Sc are correlated with one another. Although the correlation coefficients are lower than for Pathfinder samples. Al_2O_3 was selected as a "reference" immobile component against which the behavior of other components can be measured. In terms of their geochemistry, the A6ST samples are nearly identical to the Pathfinder samples reported above, and can be plotted together with them. However, to facilitate analysis of the A6ST samples as a group, they are considered independently from the Pathfinder analyses.

Plots of normally mobile elements, such as SiO₂, K₂O, Zn, and CaO versus Al₂O₃ indicate little to no mass influx into the fault zone samples. SiO₂ shows a negative correlation with Al₂O₃ and K₂O is positively correlated with it. The former relationship indicating that SiO₂ content is controlled by abundance of detrital quartz (r^2 of SiO₂ vs. Zn which tracks zircon and thus tracks the coarser detrital fraction, is 0.75), and K₂O is controlled by abundance of clay. The slopes of the K₂O vs. Al₂O₃ plots for the A6ST and Pathfinder well samples are nearly the same, 0.13 and 0.15, indicating, as noted for the Pathfinder well samples, that K₂O occurrence is described by mixed-layer 1:1 stoichiometry. Unlike the Pathfinder samples, rocks from the A6ST well do not show even a weak relationship between K₂O content and extent of faulting. Zinc shows no enrichment in faulted versus unfaulted rocks. CaO does show possible weak enrichment in some weakly to moderately deformed rocks relative to undeformed ones, and the lack of correlation of CaO with Al₂O₃ indicates it is largely in the form of carbonate minerals rather than plagioclase or Ca-montmorillonite. $\delta^{18}\text{O}$ of calcite and mixed calcite+dolomite from these rocks is weakly inversely correlated with CaO content, suggesting that CaO, hence carbonate, in these rocks may be at least partly of diagenetic origin.

DISCUSSION: Thermal anomaly in the fault penetrated by the A6ST well

Modeling based on vitrinite maturation in the fault rocks, as described above, requires a significant thermal pulse in order to produce the average 0.55% Ro vitrinite reflectance at the depths from which these samples came. For this study, the first-order, distributed activation energy model of Burnham and Sweeney (1990) was used. In the simple situation rocks now in the fault zone are modeled as being buried along a constant, present-day, geothermal gradient of 30 C/km (present day temperature is about 80 C in the fault zone), with a pulse of instantaneous peak temperature of 120 C, or about 45 C above the ambient temperature, being required to produce the measured reflectance values. Longer-duration pulses (i.e., 20-30Kyr) need not have such high temperatures, but still are on the order of 35 degrees hotter than ambient temperature. The same burial history, without a temperature pulse, produces a calculated vitrinite reflectance of 0.27% Ro.

The combined vitrinite reflectance and stable isotope data support the interpretation of thermally anomalous fluid flow in the fault zone at the AEST well. Large volumes of fluid would be required in order to produce the interpreted thermal anomaly. Furthermore, if fluids are responsible for the thermal anomaly, they must have sourced below the massive shales that lie below the OI sands: only there are the temperatures sufficient to produce the thermal maturation recorded by the vitrinite. However, other interpretations for a temperature anomaly, such as influence of salt in the past are possible. Further study is required regarding the detailed history of salt movement in this area, as well as the distribution and nature of other thermal anomalies, if any, within and outside of the fault zone in Block 330.

Vitrinite reflectance measurements elsewhere in Block 330

Vitrinite reflectance was measured from cuttings from five other wells in Block 330. In most cases the samples were of only fair to poor quality, and yielded only a few measurements: thus any conclusions drawn from these data must be considered tentative. That said, the data taken at face value highlights the Pathfinder well as a "cold spot" in the 'A' fault zone. The data imply that the imprint of an anomalous heating event or events, perhaps related to ascent of fluid in the 'A' fault, decreases to the southeast. Additionally, Rock-Eval pyrolysis data were obtained from a suite of cuttings through the fault in the C-7 well, Block 330, in order to evaluate thermal maturity and evidence for migrated hydrocarbons. The data shows a migrated hydrocarbon peak (P1) in the 5650-5680 sample, which corresponds to the 'B' fault intercept at 1732 meters (5680 feet) DD. No P1 peak in the sample taken below that fault, and weak P1 peaks in the 5980-6010 and 6010-6040 intervals, corresponding to the 'A' fault intercept at 1828 meters (5997 feet). Fault picks were based on marked logs provided by Pennzoil Exploration and Production Co.

In order to address the question of whether the fault represents a paleothermal anomaly and thus may have acted as a conduit for hot fluids, vitrinite reflectance measurements were made on four samples from the KE sand (1.5 My), of approximately the same age and depth as the fault samples at varying

distances from the fault system. Thin sections from these samples yielded significantly lower average vitrinite (telocollinite) reflectance, between 0.25 and 0.3% Ro, than did most samples from the fault zone.

CONCLUSIONS: Comparison of fluid flow between the Pathfinder and A6ST wells

Data in hand indicate the main ("A") fault zone is heterogeneous with respect to fluid flow, as is typically the case with fault zones. The evidence is against significant throughgoing fluid in the fault zone encountered in the Pathfinder well, while it supports the interpretation of such flow in the fault drilled in A6ST well, only 300 meters away. Specifically, the elevated vitrinite reflectances and spore fluorescence colors in the A6ST fault rocks and the well-constrained extrapolation of vitrinite reflectances to "normal" values 100 meters above the fault identifies the fault as a paleothermal anomaly relative to rocks just above it. A thermal model for the vitrinite reflectance anomaly, while not a unique solution implicates fluids at temperatures compatible with oil generation.

Furthermore, the low $\delta^{13}\text{C}$ values, combined with low $\delta^{18}\text{O}$, of fault zone calcite combined with early- to mid-Tertiary brine iodine-129 ages (Losh and Wood, 1995) point to fluid that interacted with rocks at temperatures at which kerogen maturation was taking place (Udo Fehn, Univ. of Rochester, 1994, oral comm). As the maximum ambient temperature at the A6ST well fault intercept was probably no greater than its present-day value of 80 C (and even this value is unusually high for this depth in this area), fluids of these temperatures and/or from these sources must have ascended from depth. Extrapolation of the 30C/km geothermal gradient in the A6ST well indicates such fluids must have migrated a kilometer or more vertically: the brines have migrated considerably more than that since they first interacted with rocks undergoing kerogen maturation in the early to mid-Tertiary.

The lateral variability in fault-hosted fluid flow may result from lithologic and concomitant permeability variations along the fault zone: sandy intervals in the "massive shale" may have smeared out along the fault, providing channelways for fluid to ascend from depth. Along the same lines, structural anisotropies in the fault, such as dilatant bends acting in concert with oblique slip, may produce fractured channelways. In the Pathfinder well, the deepest of the three fault domains in the core is interpreted to be the best suited to have acted as a fluid conduit and, as stated above, is the only portion of the cored fault that contained oil. However, even samples of oil-bearing fault rocks from this domain did not yield geochemical or mineralogical evidence for significant mass influx, nor did samples taken in or near the main 'A' fault. Unlike the A6ST well samples, there is no mitigating evidence for fluid flow: vitrinite reflectance values are uniformly low, and calcite $\delta^{13}\text{C}$, which is unfortunately obtainable only in the upper, calcareous portion of the core, is almost uniformly unaffected by products of kerogen maturation. Thus, even though oil is present within some of these deeper faults, indicating that they were capable of transmitting fluid to some extent. It is evident that some factor beyond local fault complexity or geometry of fault/fracture spacings controls large-scale fluid ascent in the 'A' fault. Both the Pathfinder and A6ST wells are distant from intersections of the 'A' fault with subsidiary structures as shown on structure contour maps interpreted from seismic and well data, and the 'A' fault has approximately the same trend and, probably, relationship to the stress field at both locations. Thus, a complete answer to the question of which factors exert control on fluid flow in the fault zone does not present itself on the basis of the above data alone. The seismic data and maps derived from them may not be of sufficient resolution to allow distinction of features that could indicate the propensity of the fault to transmit fluid. Answers to this question will probably be best derived from integrated geologic and geochemical studies at a number of points along the fault.

Acknowledgements

Funding for this research was provided by the Global Basins Research Network and Department of Energy grant DC-FC22-93BC14961 to Roger Anderson, Lamont-Doherty Earth Observatory. We are deeply grateful to Pennzoil Exploration and Production Co. for their matchless cooperation and generous access to samples and data; without their support, this entire project would not have been possible. SL also acknowledges the valuable help of Peter Vrolijk and Michael Wooten, Exxon Production Research, and the participants in the coring strategy meetings. Mn smectite-illite analyses were performed by Ahn Tu (Pathfinder samples) and Kirsten Price (A6ST), with the knowledgeable help of Prof. Doug

McDowell. Biostratigraphic analysis was performed by Applied Biostratigraphix, Houston, and elucidated by Denise Butler, Pennzoil.

REFERENCES CITED

- Abercrombie, H., Hutcheon, I., Bloch, J. DeCaritat, P., 1994. Silica activity and the smectite-illite reaction; *Geology* vol. 22. p 539-542
- Alexander, L., Flemings, P., in press. Geologic evolution of a Plio-Pleistocene salt withdrawal mini-basin. Eugene Island South Addition. Block 330. offshore Louisiana; *Amer. Assoc. Petrol. Geol. Bull.*
- Anderson, R., 1993, Recovering dynamic Gulf of Mexico reserves and the U.S. energy future: *Oil and Gas Jour.*, April 26. p.85-91
- Anderson, R., Flemings, P., Losh, S., Austin, J. Woodhams, R., 1994, Gulf of Mexico growth fault drilled. seen as oil, gas migration pathway: *Oil and Gas Jour.*, June 6. pp.97-103
- Galloway, W., Henry, C., Smith, G., 1982, Depositional framework, hydrostraigraphy. and uranium mineralization of the Oakville Sandstone (Miocene), Texas Coastal Plain. *Univ. of Texas at Austin Bur. of Econ. Geol. Rept. of Investigations* 113. 51 pp.
- Hippler, S., 1993. Deformation microstructures and diagenesis in sandstone adjacent to an extensional fault: Implications for the flow and entrapment of hydrocarbons; *Amer. Assoc. Petrol. Geol. Bull.*, vol.77. pp.625-637.
- Holland, D., Leedy, J., Lammlein, D., 1990, Eugene Island Block 330 field - U. S. A., offshore Louisiana; in Beaumont, B., and Fosten, N., eds.. *Structural Traps III: Tectonic Fold and Fault Traps*; *Amer. Assoc. Petrol. Geol. Treatise of Petroleum Geology*, pp.103-143
- Hooper, E. C. D., 1991, Fluid migration along growth faults in compacting sediments; *Jour. Petrol. Geol.* vol 14, pp.161-180
- Hower, S., Eslinger, F., Hower, M., Perry, F. 1976, Mechanism of burial metamorphism of argillaceous sediment I: Mineralogical and chemical evidence; *Geol. Soc. Amer. Bull.*, vol. 87, p.725-737
- Huang, W.-L., Longo, S., Pevear, D., 1993, An experimentally-derived kinetic model for smectite-to-illite conversion and its use as a geothermometer; *Clays and Clay Minerals*, vol. 41, p.162-177
- International Committee for Coal Petrology (ICCP): *International handbook of coal petrology*. Centre Nat. Resch. Sci. (Paris), 2nd ed 1963, 164 pp. 1st suppl. 1971, 400 pp.; 2nd suppl. 1975, 68 pp.
- Jones, P., Wallace, R., Jr., 1974, Hydrogeologic aspects of structural deformation in the northern Gulf of Mexico basin: *Jour Res. U.S. Geol. Surv.*, vol 2, pp.511-517
- Land, L., MacPherson, O., 1989, Geochemistry of formation waters, Plio-Pleistocene reservoirs, offshore Louisiana; *Gulf Coast Assoc. Geol. Soc. Trans.* vol.39, p. 421-430
- Land, L., Lynch, F., Mack, L., Milliken, K.L., 1995, Regionally inhomogeneous potash metasomatism, Paleogene mudrocks, Texas Gulf Coast: *Amer. Assoc. Petrol. Geol. Abstr. W/Prog.*, vol 4, p. 53A
- Losh, S., Wood, S., 1995. Brine chemistry. SF1 Blocks 316 and 330; in Anderson, R., ed. *Results of the Pathfinder Drilling Program into a Major Growth Fault; Part of the GBRNIDOE Dynamic Enhanced Recovery Project in South Eugene island 330 Field, Gulf of Mexico*. CD-ROM available from Geosciences Dept., Lamont-Doherty Earth Observatory, Palisades, NY 10964
- Milliken, K., L., 1985. Petrology and burial diagenesis of Plio-Pleistocene sediments, northern Gulf of Mexico: unpub. PhD thesis, Univ. Texas at Austin. 112 pp
- Moore and Reynolds, 1989
- Mukhopadhyay, R., 1992: In *Diagenesis III Developments in Sedimentology*. 47: pp. 435-510. Eds. K. H. Wolf and G.V. Chillingarian. Elsevier Science Publishers
- O'Neil, J., Clayton, R., Mayeda, T., 1969, Oxygen isotope fractionation in divalent metal carbonates: *Jour. Chem. Phys.*, v.51.5547-5558

- Schoell, M., Hought, M., 1994. Preliminary report on mudgas isotope analyses. GBRN well E1330 A2OST; Chevron Petroleum Technology Company. La Habra. CA. internal report TM94000(5)1. 7 pp.
- Stach, E., Mackowsky, M-Th., Teichmüller, M., Taylor, G., Chandra, D., and Teichmüller, R.. 1982, Textbook of Coal Petrology, 3d ed. 536 pp. Gebrüder Borntraeger
- Sweeney, J., Burnham, A., 1990, Evaluation of a simple model of vitrinite reflectance based on chemical kinetics; Amer. Assoc. Petroleum Geol. Bull., vol 74, p.1559-1570.
- Weber, K., Mandl, G., Pilaar, W., Lehner, F. Precious, R., 1978, The role of faults in hydrocarbon migration and trapping in Nigerian growth fault structures; Tenth Annual Offshore Technology Conference Proc., vol 4, pp.2643-2653 (OTC 3356)

Brine Chemistry, Blocks 330 and 316

Steven Losh

Cornell University: Jim Wood, Michigan Technological University

Twenty-two samples of brine were collected from producing wells in South Eugene Island Blocks 330 and 316 by Dr. Lynn Walter and Anna Martini (University of Michigan) over a three-day period during January, 1994. Seventeen phases were analyzed at the University of Michigan in addition to temperature at the wellhead, pH, density, and Sr isotopic composition. Chemically, the brines are similar to those documented in nearby Plio-Pleistocene reservoirs by Land and MacPherson (1989). They are NaCl waters that exhibit a sizeable range of chloride content, from 19,900 to 103,100 mg/L (however, the 10W-salinity sample from the A10ST well is probably contaminated by completion fluid, as that well has only recently gone into production), but lie on a seawater-halite dissolution line. Calcium concentration is somewhat higher than would be expected from dissolution of halite, but may reflect dissolution of gypsum associated with salt. Sulfate concentration is unusually low, in most cases below the detection limit, and may reflect ongoing sulfate reduction. The brines appear to be seawater mixed with varying proportions of halite-saturated fluid, or seawater that has simply dissolved varying amounts of salt as it migrated. These fluids have been further modified by limited fluid-silicate interaction.

Iodine-129 dating has been carried out at the University of Rochester, under the direction of Dr. Udo Fehn, on nearly all brines collected during this study. This method yields apparent brine ages between 31 and 61 Ma considering only a cosmogenic source of ^{129}I . However, even when accounting for likely fissiogenic contributions, an early Cenozoic age of the brine is indicated, and significant vertical fluid flow is implied. It is not anticipated that dissolution of Gulf Coast evaporites would significantly affect the measured brine age, as these materials contain very low concentrations of iodine (U. Fehn, 1994. oral comm.); indeed, no correlation between iodine age and chloride concentration is present. The brine age is likely strongly affected by the age of maturing kerogen from which much of the brine's iodine was derived, but even so, the ages imply that at least a component of the brines was present in rocks of at least mid-Cenozoic age.

Chloride concentration of the brines shows no systematic variation with depth. Nor does it appear to vary with respect to distance from faults, with one notable exception; however, it does show sizeable differences between reservoirs. It is highest in the shallowest reservoir, the GA, about half as high in the underlying HB sand, and high but variable in the deeper sands. Chloride concentration also shows no noticeable change from upthrown to downthrown blocks. As noted, chloride concentration in brines near faults is similar to that in brines far from faults, with the exception of the sample from the A2 well (OI-5 sand), which is unusually dilute for waters at this depth. This fluid may represent incorporation of water from shales undergoing dewatering below the OI sands. However, other brines collected near faults (the A6ST sample, for example, was taken from the KE sand, immediately above the 'A' fault) show no such decrease in chloride concentration. In a manner analogous to the distribution of chloride concentrations, ^{129}I ages show no systematic variation with respect to faults (although the range of ^{129}I concentrations is small), nor do there appear to be significant age variations between reservoirs.

The pronounced variations in brine chemistry between reservoirs and the evident compositional homogeneity within a reservoir using chloride as a monitor, indicate that the brine entered the reservoirs at different times and/or from different directions. As opposed to a model in which a single stream of fluid migrated up the fault and leaked into each reservoir it passed by. For example, the GA2 sand contains the highest - salinity brines in the dataset, yet is the shallowest reservoir sampled. Brines that entered that reservoir necessarily bypassed the HB I sand, in which brines have only half the salinity of the GA2 sand a few hundred feet above it. If Sr^{87}/Sr^{86} ratios are interpreted as indicative of brine source (that is, neglecting water-rock interaction), comparison with the DSDP seawater Sr isotope curve implies that the least radiogenic brine with respect to Sr isotopes originated in 30 Ma sediments. This brine is also characterized by the lowest $1/Sr$ value in the dataset; other brines have higher Sr^{87}/Sr^{86} and lower $1/Sr$, and thus appear to have been contaminated by a radiogenic component of sediment-derived strontium. The mid-Tertiary age deduced from Sr isotope ratios is consistent with the above iodine-129 data, and points to large-scale vertical migration of brine to its present location in the Pleistocene reservoir sands.

REFERENCE CITED

Land, L., MacPherson. O, 1989, Geochemistry of formation water, Plio-Pleistocene reservoirs. offshore Louisiana: Gulf Coast Assoc. Geol. Socs. Trans. vol 39, p 421-430.

Reservoir Diagenesis, SEI Block 330

Steven Losh

Cornell University, with contribution from Jim Boles, Univ. California, Santa Barbara

The diagenesis of Pennzoil's Block 330 reservoir sediments has been studied in order to assess the possible relationship of cementation and alteration of these rocks to the fault that has presumably provided a conduit for diagenetic fluids. Approximately 200 thin sections from sidewall cores of reservoir rocks throughout Block 330 have been examined for diagenetic effects; the GA, 1413, JD, and OI reservoirs in particular have been studied in terms of cementation and grain alteration. In general, cement is sparse, less than 2 percent of the rock (in many cases, much less), and consists of calcite, ferroan dolomite, and siderite. Diagenetic pyrite, usually framboidal, is also present, whereas silica overgrowths are rare. Organic matter is scattered but ubiquitous, typically being found within foraminifera, as layer-parallel stringers in shale (especially in the KR sands), and as discrete bitumen "patches" in sands.

These observations were made as a complement to the petrographic analysis of sediments from the same reservoirs carried out by David K. Davies Associates for Pennzoil. It was originally anticipated that cementation or grain alteration may be more intense as the fault is approached, and this study focused on obtaining samples in traverses across faults and examining for grain alteration, specifically albitization and plagioclase dissolution. Diagenetic minerals as determined both by Davies Associates and in this study show no apparent relationship with distance from the fault in terms of their abundance or type.

GA sands

Most of the sections are of sandy or silty shale to shaly silt; clean sand are not well represented in this suite, probably in part because sidewall cores of sand disaggregate very easily. Calcite cement in silty rocks is sparse (up to 3%) and extremely fine-grained. Plagioclase commonly shows weak to moderate pitting, but in any given sample, most plagioclase grains show no albitization. It is likely that any albitized plagioclase in these sands has been reworked from an older sand. Detrital carbonate grains are common, in many cases comprising 5-20% of the grain population.

Dr. Jim Boles, University of California, Santa Barbara, concluded his examination of selected sidewall cores from the GA sand, Block 330, wells B16, A19ST, and B3ST. His report is as follows. Photographs are not included here.

"A petrographic study of 17 sidewall core samples of the "GA sand", Block 330 was undertaken to look for evidence of diagenesis resulting from fluid movement along faults. Results indicate that very little diagenesis has occurred.

The samples were received as loose particles and thus were prepared as grain mounts. Overall, samples are very fine to fine grain size sand with varying proportions of silt and clay matrix. Porosity could not be estimated from these samples due to their disaggregated condition.

The detrital components are quartz, K-feldspar, plagioclase, siliceous rock fragments, detrital carbonate shell material, micas, and trace minerals including glauconite, green hornblende, and garnet. A notable feature of some samples is the presence of zoned plagioclase feldspar indicating a hypabyssal or volcanic source component and rare volcanic rock fragments. No systematic changes in detrital or diagenetic mineralogy were noted with depth in the wells nor in comparison between wells.

Diagenetic smectite and illite are the most abundant authigenic phase but even these minerals do not exceed 10% by volume in the samples. The clays occur as thin rims on detrital grains and as pore-filling cement. In many cases diagenetic clay appears admixed with detrital clay matrix and it is difficult to distinguish the detrital from the authigenic phase. The samples with the most abundant, what is clearly authigenic clay, are B16@5074' which has up to 10% of small scattered lath-shaped birefringent illite clay particles. Curiously, these crystals are length fast, whereas typical illite is length slow. Other examples of diagenetic clay are in the A19ST well where a birefringent (illitic?) clay forms thin rims about detrital grains or in some cases, pores are partially filled with a yellowish-green to yellowish-brown clay.

Diagenetic carbonate occurs in trace amounts in some samples. Typically it occurs as scattered subeuhedral to euhedral grains or in some cases as grain coatings. In some cases, such as B3ST @5917' and 5930', the yellowish-brown color of the carbonate indicates it is probably siderite. Similar appearing siderite is found in Cretaceous sands from the Alaska North Slope and in this case they can be shown to have formed near the sediment-water interface.

Syntaxial quartz overgrowths are very rare in these samples, indicating that they have not undergone silica cementation due to upwelling hot fluids. The few samples with quartz overgrowths occur as incipient syntaxial overgrowths on a few grains in a few samples. The rarity of the overgrowths indicates that they could be reworked.

Feldspar diagenesis is a sensitive indicator of changing burial conditions. Neither dissolution of feldspar nor in situ albitization of detrital plagioclase can be demonstrated in these samples. Albitized feldspar occurs in the samples, but it is in a mixed population with fresh plagioclase. This suggests that albitization is not an in situ process. In addition, zoned plagioclase, typically some of the most unstable feldspar, appears unaltered.

In summary, these samples are not extensively cemented. Clay minerals, which appear to be the dominant diagenetic phase, appear similar to those found in incipient diagenesis. The most compelling evidence for upwelling hot fluids from deep in the basin would be the presence of abundant authigenic silica. Such evidence is not found in these "GA" sand samples."

HR sands

Most sections are of moderately sorted shaly silts and shaly sands. Detrital calcite is common, in many cases comprising 10-20% of the rock. Authigenic calcite and ferroan dolomite occurs as ragged overgrowths on the detrital grains, and is thus more abundant in rocks containing more detrital carbonate. Aggregates and disseminations of extremely finegrained siderite are common, comprising perhaps 2% of many sands. At most, diagenetic carbonate comprises 10% of the rock, and is always extremely fine-grained. Plagioclase dissolution is minor to non-existent in many of the silts, but is moderately advanced in others. Michel-Levy analysis of albite twin angles for unaltered plagioclase indicates the feldspars may be as calcic as An60.

Diagenesis of the 70 examined HR sand samples (wells B16, B3ST, A7ST, C15ST, C13, C11, C9, C21, C2, #3, #4 (A1), A23, A19ST, C20, A6ST, A13, B12, C3, #1, #6; is largely similar to that observed in the GA sand, except that carbonate (both detrital and authigenic) is slightly more abundant, and that dissolution of plagioclase, K feldspar, and in some cases quartz, is more common. In some cases involving all of the plagioclase and a significant percentage of other grains in a

sample (particularly samples from C2, C9, and C13). The dissolution is manifest both in the forms of uncommon skeletal grains and as microporosity, which may affect up to 15-20% of the quartz and feldspar grains in a sample. Skeletal grains are interpreted as reflecting in situ dissolution, whereas the intensely-pitted grains are similar in appearance to pitted grains described from the vadose zone (i.e., soil profiles) in humid regions. In at least one case (B 16,6144') dissolution is inversely correlated with carbonate cement.

Where cement is abundant, feldspars are fresh, whereas uncemented zones contain pitted and rare skeletal plagioclase and K feldspar. This type of relationship indicates the dissolution is at least partly in situ, and that the carbonate cement in this sample predates at least some of the dissolution. Pronounced variations in proportion of pitted grains to unpitted ones exist over short vertical distances in the wells. Intergrown fine-grained calcite and dolomite were noted in two samples from the B16 well; these were analyzed for carbon and oxygen isotopic composition

(dolomite: $\delta^{18}\text{O} = 26.0\text{-}26.6$ permil SMOW, $\delta^{13}\text{C} = 1$ to 1.9 permil PDB; calcite $\delta^{18}\text{O} = 23.1\text{-}23.4$ permil, $\delta^{13}\text{C} = 0.3$ to 0.5 permil). These diagenetic indicators show little to no apparent spatial relationship between the extent of diagenesis and proximity to faults. Samples above the oil/water contact on the north side of a nearly east-west fault traversing the southern part of Block 330 have more carbonate cement and a higher proportions of pitted to unpitted grains than do samples south of this fault or samples below the OPY contact. There does not appear to be any correlation between abundance of pitted grains or authigenic carbonate and stratigraphic position within the HB sand. More work is being done to assess the possibility of in situ dissolution: if such a process were occurring, it would be unusual given the relatively low temperature of the 1413 sand. In situ dissolution generally begins at about 80-100 C, whereas the HB sand is at temperatures closer to 60 C.

JD sands

These are mostly clean sands, with high porosity. Calcite cement is sparse, at most 3-4 modal percent in rocks containing detrital carbonate, and is absent in many cases. Plagioclase is pitted to a varying extent in the sections: nearly all rocks show some pitting, and in some cases, up to half of the plagioclase shows weak to moderate dissolution. Clay coatings on sand grains are very rare; no pore-filling, authigenic clay has been noted.

OI sands

Clean to shaly silt and sand. Calcite cement is absent in most rocks, and is scarce (1%) at best. Several of the sands have clay coatings on sand grains or rare pore filling "felted" clays. Plagioclase dissolution and pitting is weak, typically affecting 10 - 25% of the plagioclase grains in a given section.

Temporal Variability in the Composition of Some Petroleum Fluids from Eugene Island Field-330 Over Short Time Scales

Mahlon C. Kennicutt H, Yaorong Qian and Adolfo G. Requejo
Geochemical and Environmental Research Group
Texas A&M University
College of Geosciences and Maritime Studies
833 Graham Road
College Station, TX 77845

Jean Whelan and Lorraine Eglinton
Department of Chemistry
Woods Hole Oceanographic Institute
Woods Hole, MA 02543

Introduction

While petroleum is often perceived as a rather uniform fluid, its composition, even within a field, can be quite heterogeneous (Baily et al. 1973; Milner et al. 1977; Hunt 1979; Tissot and Welte 1984; Connan 1984; Leythaeuser and Ruckheim 1939). Variations in the composition of petroleum can occur due to many factors including, source rock composition, thermal maturity, migration alteration, in-reservoir alteration, and mixing of fluids from multiple sources. The chemical characteristics of petroleum often provide clues for deciphering the evolution of a fluid in regard to temperature history, age of source rock, migration pathways, and the effects of post-generation alteration processes such as biodegradation, evaporative fractionation, water washing, in-reservoir maturation and gravity segregation. It has also been demonstrated that low rates of in-reservoir mixing of multiple charges of petroleum can lead to inhomogeneities (England et al. 1987; England and Mackenzie 1989; Karlsen and Larter 1989; Larter et al. 1989). These variations can be assessed on a variety of vertical and horizontal spatial scales. Regional (kilometers) trends in petroleum compositions provide insight into variations in organic facies, thermal maturity, reservoir filling history, and viable source horizons (England and Mackenzie 1989). Observations within a field can provide insight into post-generation alteration as well as communication amongst reservoirs, sands, and/or across fault blocks.

In contrast to spatial variations, temporal changes in fluid compositions have received little attention. Recent observations have led to the hypothesis that in certain geologic settings oil and gas may be migrating into producing reservoirs relatively recently compared to geologic time scales (Anderson et al. 1991a,b; Anderson 1993; Schumacher 1993; Whelan et al. 1994). A variety of circumstantial geological, geophysical and geochemical evidence has been presented in support of the "dynamic fluid injection" hypothesis. The evidence includes slower than predicted rates of reservoir fluid depletion, coherence of pressure and temperature profiles, the existence of deep seated conduits for fluid migration, displacement of heat flow anomalies away from salt features, intense present-day surface hydrocarbon seepage, temporal changes in oil and gas compositions, and secondary injection of non-biodegraded fluids into biodegraded fluids (Whelan et al. 1994; Anderson 1993; Schumacher 1992, 1993; Holland et al. 1990; Barnard and Bastow 1991; Anderson et al. 1991a,b.). To further define the origins of temporal variations in fluid compositions, the present study compares and contrasts the composition of fluids collected over an eight-year period at the site where "dynamic fluid injection" was first suggested, the Eugene Island-330 Field in the northwestern Gulf of Mexico.

The geologic setting and chemistry of fluids recovered from the EI-330 field have been discussed in detail elsewhere (Holland et al. 1990; Kennicutt et al. 1992; Whelan et al. 1994). More than 25 Pleistocene sandstones are produced at depths from 701 to 3658 meters (Holland et al. 1990). The EI-330 field consists of more than 100 oil and gas reservoirs that are separated by faults and permeability barriers. The field is considered to be one of the giant oil and gas fields of the world (Carmalt and St. Johns 1986). Fluid compositions are highly variable and different sands produce a variety of admixtures of gas, condensate, and oil. Differences in oil compositions are apparent vertically within the section as well as between fault blocks and within single reservoirs (Schumacher 1993; Whelan et al. 1994, 1995). Despite these variations in composition it has been argued on the basis of biomarker data, that the majority of fluids at EI-330 are derived from the same or similar source facies (Whelan et al. 1994). However, it has been recognized that different molecular weight ranges (boiling points) exhibit characteristics typical of a range of thermal maturities suggesting more than one infusion of fluids (Thompson and Kennicutt 1990). Reservoired petroleum across the Gulf of Mexico exhibits a high incidence of alteration due to non-thermal processes such as biodegradation, evaporative fractionation, migration contamination, and extraction by water (Thompson and Kennicutt 1990).

The objective of this study was to evaluate intra-field fluid compositions to document changes in fluid compositions over short-time scales (months to years.). The first goal of the study was to minimize variations due to non-geochemical processes. Variations in fluid composition due to collection, storage and analytical methodologies must be carefully considered. Most surface collection techniques do not recover fluids in their natural state in the reservoir. Physical alterations due to depressurization and cooling are expected. Partitioning of compounds among phases upon depressurization has been

demonstrated in the laboratory Thompson 1987, 1988, 1990). Long-term storage of collected fluids can result in the loss of the more volatile fractions. Gas chromatographic data are strongly influenced by the conditions of the analysis. Operating conditions such as the gas stream split between the vent and the column can lead to significant fractionation of volatile compounds. Differences in the liquid phases of chromatographic columns determine the elution order and the degree of resolution of components in complex mixtures. Chromatographic temperature programs and column gas flows effect the detector response of analytes. Effects related to variations in apparent fluid composition due to analytical conditions, storage, and the method of sample collection must be clearly delineated if variations in reservoir fluid compositions are to be attributed to natural processes occurring over short-time scales (months to years).

Variability Due to Analysis, Storage, and Sampling Conditions

Oil (including condensate) samples were collected from the producing wells of EI330 in 1985, 1988, and 1993. Oil and condensate samples were analyzed by high resolution capillary gas chromatography (GC) to quantify the percent composition of each fluid from propane to n-C34 (Kennicutt et al. 1992). Samples were also analyzed using a second gas chromatographic column to provide confirmation of peak identities.

Comparison of the results for samples collected and analyzed in 1988 and re-analyzed in 1994 provide an assessment of storage effects on fluid compositions and a comparison of analytical methodologies. An oil sample was also analyzed six times and then re-analyzed six months later to assess the reproducibility of successive injections and the effects of storage.

Replicate analyses were highly reproducible from one injection to the next. For the majority of the compounds the integrated peak areas exhibited less than 5% coefficient variation for six replicates. As expected, the coefficient of variation is directly related to the concentration of the compound being analyzed. Compounds accounting for less than 0.5% of the mixture exhibited larger coefficients of variation due to the precision of integrating small chromatographic peaks. However, a coefficient of variation of less than $\pm 10\%$ was obtainable even for minor oil components. When the average results of six replicate analyses were compared to the results of an analysis conducted six months earlier, most compounds, with the exception of C3-C4 compounds, were within $\pm 5\%$ of the mean area of the later analyses. The C3 and C4 compounds were reduced by 20 to 30% in the later analyses. This suggests that under these storage conditions, gases dissolved in the oil were partially lost. However, for compounds with five or more carbons the reproducibility over time approached that of replicate injections.

Comparison of the analyses of forty-two EI-330 oil samples analyzed in 1988 and then re-analyzed in 1994 showed significant variations in composition. On average, the C3-C5 compounds had greater relative abundances in the 1994 analysis than in 1988. Intuitively, the C3 and C4 compounds might have been lost during storage as already demonstrated for a six-month storage period. On the contrary, the most volatile components accounted for more of the gas chromatographically resolvable compounds after storage for six years. Variations in compositions between the two analyses were also apparent as over- and under-estimated. The most likely explanation is that gasoline range compounds were significantly effected by the chromatographic conditions, especially the split ratio, which is known to fractionate compounds based on boiling point or volatility. The over- and under-estimates can be partially attributed to the improved resolution of components using later analytical methodologies. Peaks occurring as shoulders in the 1988 analysis were either merged or more completely separated depending on the particular analyte. These differences in compositions suggest that variations due to analytical technique must be minimized to ensure comparability of results. Therefore all samples were reanalyzed within as short a period of time as possible under nearly identical chromatographic conditions. The following comparisons only utilize the later analytical results thus minimizing variations due to analytical conditions.

The effect of sampling technique on fluid chemistries is uncertain. Sampling which involves depressurization and cooling is known to cause changes in fluid chemistry (Price et al. 1983). Single step depressurization experiments produced relatively small variations in composition, whereas multiple episodes of depressurization are believed to cause fairly dramatic shifts in chemical composition (Thompson 1987, 1988, 1990; Larter and Mills 1991; Whelan et al. 1994). However, changes due to sample collection in this study equally affect all samples and only one episode of depressurization

occurred during sampling. Larter and Mills (1991) reported little change in gasoline range hydrocarbon compositions during a since stage depressurization and phase separation at STF'.

Origins of Fluids in EI-330 Field

Identical biomarker distributions and stable carbon isotope values (Holland et al. 1990; Kennicutt et al. 1992; Whelan et al. 1994) indicate that the fluids in the various reservoirs of EI-330 field have a common source.

Even though hydrocarbons in the GA and HB sands are relatively depauperate of C₉+ n-alkanes, these fluids contain large amounts of hydrocarbons with three to eight carbons. The API gravities (2325° API) of the fluids from the GA and HB sands are in the range of a normal oil (Holland et al. 1990) despite the abundant light hydrocarbons. The co-occurrence of these light hydrocarbons with low API gravity fluids and the reduced C₉+ aliphatic hydrocarbons suggests that the light hydrocarbons were added to these reservoirs after biodegradation had proceeded to an advanced stage (Whelan et al. 1994). This process has also been described for Trinidad Basin and Ecuadorian.

Spatial Variations in Fluid Compositions

Vertical spatial variations in hydrocarbon compositions are significant amongst producing sands in the EI-330 field. The heterogeneity in fluid compositions among sands is believed to be primarily caused by post-generation alteration processes such as remigration, biodegradation, and phase separation (Whelan et al. 1994). Among these processes, biodegradation causes some of the most dramatic changes in fluid compositions.

Variability within a sand (GA-2) and a block (A) was compared. Variability within the sand and the block are similar and significantly greater than analytical variability. However increased variability in normal alkanes with 9 to 12 carbons, isoprenoids with 11 and 13 carbons, and the low molecular weight aromatics benzene and toluene in the GA-2 sand is apparent. It is known that in this shallow sand reservoir biodegradation is quite common. The observed lateral variability in the GA sand fluids is most likely the result of variations in the degree of degradation. Degradation has been observed to be most rapid in alkanes with 9-10 carbons (Thompson 19__). The variability in benzene and toluene content is most likely related to the intensity of water washing. These two aromatic compounds are more water soluble than aliphatic hydrocarbons of similar molecular weight. Individual locations within a sand have been subjected to differing intensities of biodegradation and water washing.

A more detailed look at variability between sands and between fault blocks confirms these interpretations. Deeper in the section degradation decreases and the fluids within a given sand are more uniform. Therefore spatial variability can be most closely linked to in-reservoir alteration processes. The greatest variability in a fluid is in the shallowest sand (GA-2) which also contains the most altered fluids. Samples from other sands are less degraded or undegraded. Variability within a fault block reflects vertical spatial variability in fluid compositions. The characteristics of fluids within a fault block are controlled by the distribution of samples among the producing sand, for example, the fault block B sample collection contains a large number of samples from the GA-2 sand and thus the observed variability is primarily related to shallow reservoir alteration processes. However, it should be noted that fluids from the same sand but from different wells show variations on the order of -25-50%.

Another cause of spatial heterogeneity of hydrocarbon compositions in reservoirs is differences in the permeability of the reservoir sands (England et al. 1987; Leythaeuser and Ruckheim, 1989; Horstad et al. 1990; Hillebrand and Leythaeuser, 1192). Low permeability can restrict the lateral diffusion and mixing of hydrocarbon fluids. The porosity and permeability of sands in the EI-330 field are high, with an average porosity of 30% (Holland Et al. 1990). Permeability is in the range of 6 md to 6 darcys, with 80% of the sands having permeability of greater than 100 md (Holland et al. 1990). The heterogeneity in compositions within sands may be partially the result of restricted diffusion and mixing however the difference between sands is most likely related to the history of hydrocarbon charge.

Temporal Variability in Fluid Compositions

The amount of low molecular weight to high molecular weight hydrocarbons in fluids from the same well and sand within the EI-330 field increased with time over an eight year period. Gasoline hydrocarbon concentrations were highest during the latest samplings in many samples. Specifically, examining the GA-2 sands between 1988 and 1993 an envelope of compounds is recognizable as an addition. The additions include cyclohexane and a range of hydrocarbons with 7 and 8 carbons. The normal alkanes are particularly enhanced. These differences are most clearly apparent in the GA sand since most of the compounds in this carbon range were greatly reduced in the original charge due to biodegradation and water washing. The additional fluid is of a composition typical of a condensate.

The hydrocarbon ratios proposed by Thompson (1983; 1987) varied consistently from 1985 to 1993). The H, I, and F parameters are believed to reflect fluid maturity (Thompson 1983; 1987). These ratios increased from mature in 1985 samples to super-mature for most of the samples in 1993. The presence of abundant light hydrocarbons in the biodegraded GA and HB sands, the increase in the amounts of light hydrocarbons relative to the higher molecular weight compounds in the later samplings, and the increase in the maturity of light hydrocarbons in the latest samplings all point to a systematic variation in the light hydrocarbon compositions over a period of years.

The Origins of "injected" Hydrocarbons

The variation in the chemical composition of fluids from the sands of the EI-330 field over short-time scales indicates an influx of fluid into these reservoirs in the past several years. The observed temporal changes could be explained by inducing localized and lateral migration, migration from deeper intervals, and/or production induced depletion of the reservoir.

An influx of fluids from adjacent less permeable sands to the primary reservoir bodies as the field was depleted has been suggested. The concept of "feeder pays" was suggested by Holland et al. (1990) to explain the overproduction for the GA sands. It was suggested that even though adjacent sandstones had little capacity for significant lateral flow they may recharge the more permeable productive zones. However, the temporal change in fluid chemistry on the EI-330 field was characterized as an increase in fluids of higher maturity. In contrast, Leythaeuser and Ruckheim (1989) observed that fluids in high porosity/high permeability sand intervals bear a higher proportion of saturated hydrocarbons and have a higher apparent maturity compared to fluids from lower porosity/lower permeability zones. Therefore it would appear that adjacent "feeder pays" cannot be attributed with recharging the adjacent high porosity zones since it would be hypothesized that less mature fluid would arise from the lower permeability zones with time. Another words, the initial maturity of the fluids charging the sands could not be exceeded and yet maturity increases far beyond that documented throughout the field.

If the change in fluid composition was due to injection from much deeper strata, the latest influx of hydrocarbons would be expected to have had a more advanced thermal history different than the fluids originally emplaced. As well, the apparent age of the latest arriving hydrocarbons would be different from those of the originally reservoir hydrocarbon. Young et al. (1977) used the relative molar concentrations of paraffins, naphthenes, and aromatics in the light hydrocarbon range (C₅-C₇) and the relative concentrations of the naphthenes with different numbers of rings in higher molecular weight (C₁₅+) hydrocarbons to calculate the ages of these hydrocarbons. The rationale was that the chemical composition of an oil from a single source is determined by the combined effects of time and temperature. With increased time and temperature, the chemical composition of the oil gradually shifts according to chemical kinetics. Based on this rationale the ages of several hundred oil samples were calculated.

Based on the equations and constants given by Young et al. (1977), the relative concentrations of naphthenes (C_n. relative to paraffins and aromatics) and the mean thermal history of light hydrocarbons in EI-330 field were calculated. Assuming that the thermal history during and after the generation of hydrocarbons is mostly responsible for the variation of the C_n values observed in the oils and assuming the temperatures of the reservoirs have not changed after the emplacement of oil in these sands, the apparent ages of the light hydrocarbons were calculated using the current reservoir temperatures and the C_n values.

The relative concentrations of naphthenes decreased uniformly from 0.35 in 1985 samples to about 0.25 in 1993 samples for all the reservoirs with the exception of GA-2 sand where the C_n value decreased from 0.4 to 0.34 over the same time period. This rapid diminishing of naphthenes might be the result of a temperature-time effect. With increased exposure to high temperature, the oil would become

more mature (more paraffinic). However, if the C_n values had decreased from 0.35 to 0.25 within only 8 years at the current reservoir temperatures (55 to 86°C) solely by the effect of temperature, then the C_n values of all of the fluids now in reservoirs should be much lower and the hydrocarbons should have been extensively cracked to gases. A more plausible explanation of the high C_n values of the hydrocarbon fluids at 1985 (0.35) and the rapid decrease to lower values (0.25) over the eight year period is that highly mature hydrocarbons have been added lowering the C_n values of the original hydrocarbon charge. Based on the analyses of several hundred different-aged oil samples a decrease in C_n value from 0.40 to 0.25 should be expected to take millions of years, depending on the temperatures experienced (Young et al. 1977).

The calculated ages of these oils lie between 8 and 133 million years. Given the age of the reservoir sands of 1 to 2 million years (Pleistocene), the calculated ages of the hydrocarbons are substantially older than the age of the reservoir sands. However, the age of the hydrocarbons was calculated based on current reservoir temperatures. Petroleum must have been generated at higher temperatures in deeper sources than the present day reservoirs of EI-330. Young et al. (1977) and Quigley and Mackenzie (1988) concluded that temperature is the most critical factor that influences the generation, maturity, and compositions of oils and time is believed to be less influential than temperature (Quigley and Mackenzie, 1988, Mango, 1990, 1991). If the hydrocarbons were indeed derived from deeper sources (either from source rocks or deeper reservoirs), then higher temperatures should be used in the age calculations. Using the minimum hydrocarbon formation temperatures of 100 C to 150°C (e.g. Quigley and Mackenzie, 1988) and assuming a constant thermal history, the calculated ages are substantially lower than the ages calculated. The ages range from 12 to 59 million at 100 C and 4 to 20 million years at 150 C, respectively. This wide variation in the calculated ages of the light hydrocarbons might indicate the presence of hydrocarbons of different ages in these reservoirs. The variation is most prominent among different sampling periods. The ages of the hydrocarbons at the same sampling times are similar between reservoirs. One exception is the GA sands where biodegradation may have obscured the age calculations. In addition, the ages of the hydrocarbons during the earlier sampling period, particularly 1985, are low ranging from 22 to 42 million years based on the current reservoir temperature. The ages are 15 to 21 millions years if 100 C is used in the calculation. These two groups of values are similar to the values reported by Young et al. (1977) for Eugene Island. The calculated ages of the light hydrocarbons are much older for samples from 1993 than those from 1988 and 1985 suggesting a further influx of highly mature (older age and/or higher temperature) hydrocarbons. The source of these hydrocarbons must be substantially deeper in the section and at much higher temperatures. If this is the case, the C_n values and their changes over the past several years in all the reservoirs (including GA-2 sand) could be explained by the ongoing process of "dynamic fluid injection".

Assuming the hydrocarbons were generated and emplaced in these reservoirs at similar time (i.e. the age of these fluids are similar), their thermal history should also be similar, or more precisely, the hydrocarbons in the shallow reservoirs should have experienced slightly less thermal stress than the deeper ones because the temperature of the shallow reservoirs are lower. The difference in the calculated mean thermal history (mean temperatures) between the shallow reservoirs at each using the OI from that time as a reference. For fluids in the OI sand, the deepest sand, secondary processes such as biodegradation are minimal. With the exception of the GA-2 sand and the HB sand, the difference in the temperatures between each reservoir and that in the OI sand at each sampling is small, suggesting that the thermal history of the fluids was similar. This conclusion agrees with oil maturities calculated from biomarkers and aromatic hydrocarbons (Whelan et al. 1994, 1995).

The calculated temperatures in GA and HB sands are substantially lower than the others. Several possible mechanisms can result in these lower calculated temperatures. The amounts of light hydrocarbons that were injected into the GA and HB sands might be small, whereas the amount of injection into the OI sand might be large. As a result, the calculated thermal histories of GA and H13 sands relative to the OI sand are low. Alternatively, light hydrocarbons in GA and HB sands have experienced biodegradation (Whelan et al. 1994) because of the lower reservoir temperatures and shallower depth. Biodegradation selectively removes n-alkanes leading to higher naphthene concentrations relative to paraffins and aromatics (higher C_n values). If this second interpretation is correct, the light hydrocarbons in GA and HB sands would appear to be less mature and have lower

apparent temperature histories. The calculated temperatures and ages would also be biased on the low side.

The ages of the hydrocarbons in all of the reservoirs are assumed to be similar and the average thermal history of the hydrocarbons in the OI sand over their life time is 86°C (the current reservoir temperature, the actual thermal history of the hydrocarbons in OI sand might be slightly higher than this value), then the mean temperatures of the hydrocarbons in other reservoirs at different sampling periods can be calculated based on the measured C_n values for each reservoir at each sampling. These calculated temperatures are substantially higher in the 1988 and 1993 samplings than temperatures during the 1985 sampling. In addition, the calculated temperatures are substantially higher than the current reservoir temperatures for all the samples collected in 1988 and 1993. This higher temperature (higher thermal history) indicates that the light hydrocarbons were injected into these reservoirs recently from a deep, high maturity sources. As a result, the calculated thermal history (time-temperature effect) is higher in 1988 and in 1993 due to a continuing input of highly mature fluids. The increased calculated temperatures of GA sand in 1988 and 1993 is consistent with the injection of high maturity (high temperature 017 old aged) fluid into the GA reservoir in recent years, in spite of biodegradation, which lowered the calculated apparent temperature. The calculated temperatures for the hydrocarbons in most of the reservoirs in 1988, and particularly in 1993, and close to the temperatures of the proposed source rock currently generating hydrocarbons (150 to 170°C; Holland et al. 1990).

The H (heptane ratio), I (isoheptane ratio), and F (paraffinity parameter) values in all the samples show a consistent increase from 1985 to 1993 sampling period for each reservoir. Thompson (1983; 1987) proposed that these parameters reflect the maturity levels of oils, although Mango (1990) disputed this interpretation by arguing that the ratios might be controlled by kinetic mechanisms during the formation of hydrocarbons.

With an increase in maturity, these parameters should increase (Thompson, 1983, 1987). The consistent large increase in these parameters from 1985 to 1993 in all samples is consistent with fluid injection during that period. Such an input of high maturity, low carbon-number hydrocarbons derived from deep sources into these reservoirs would cause a rapid and concordant increase in these parameters. The relatively low values of H, I, and F parameters in GA and HB sands as compared with those of deeper reservoirs are probably the result of incipient biodegradation (Thompson, 1983; 1987; Whelan et al. 1994).

In contrast to EI-330, the C_n values from nearby South Marsh Island Block 128 (SMI-128) are nearly constant for all the sands, ranging from 0.32 to 0.34. The calculated ages of the hydrocarbons are in the range of 40 to 50 million years using the current reservoir temperatures. The H, I, and F parameters are also constant for all producing sands, with values of 22 to 25, 0.4 to 0.6, and 0.6 to 0.8, respectively. However, the SMI-128 field was not sampled at different production periods, as was EI-330.

Conclusions

Systematic changes in fluid chemistry have occurred over the time-scales of years at the EI-330 field. The changes are consistent with an on-going infusion of a relatively high maturity condensate fluid. Most evidence suggests that this change is a direct result of the influx of mature fluid from deep in the subsurface. One unknown is whether continued production of a field over long periods of time is sufficient to deplete the reservoired fluid to a degree that a compositional shift is observed. The EI-330 field is a mature field and believed to be in its decline, however less than 50% of the estimated reserves will be produced over the life-time of the field. The large amounts of unrecoverable fluids might argue against a shift in composition due to production. Intuitively it might be argued if anything was depleted over the lifetime of a field it would be the most volatile gaseous compounds that would be preferentially removed. This trend is contrary to the observed compositional variations where apparent maturity increases with time.

A range of observations suggest that fluids are being injected into the petroleum system of the EI-330 field at the present day causing measurable changes in fluid composition. If production induced changes in fluid composition are negligible, additions of highly mature fluids must be moving into the shallower reservoir sands from deeply seated horizons that are generating hydrocarbon fluids today or in

the recent past. This dynamic injection has resulted in compositional variations in fluids reservoirs in the EI-330 field that occur on time-scales as short as months.

REFERENCES

- Anderson, R.N. 1993. Recovering dynamic Gulf of Mexico reserves and the U.S. energy future. *Oil and Gas Journal*, 26 April: 85-91.
- Anderson, R.N., M. A. Hobart, C.R. Wilkinson, and H.R. Nelson. 1991a. Active fluid flow in the Eugene Island area, offshore Louisiana. *Geophysics: the Leading Edge of Exploration*, April: 12-17.
- Baily, N.3.L., A.M. Jobson, and M. A. Rogers. 1973. Bacterial degradation of crude oil: comparison of field and experimental data. *Chem. Geol.* 11: 203-2:21.
- Barnard, P.C. and M. A. Bastow. 1991. Hydrocarbon generation, migration, alteration, entrapment and mixing in the Central and Northern North Sea. In: W. A. England and A.J. Fleet, eds., *Petroleum Migration*. Geological Society Special Publication No.59: 167-190.
- Carmalt, S.W. and B. St. John. 1986. Giant oil and gas fields. In: M.T. Halbouty, ed., *Future petroleum provinces of the world*. American Association of Petroleum Geologists Memoir 40:11-54.
- Connan, J. 1984. Biodegradation of Crude Oils in Reservoirs. In: J. Brooks and D.H. Welte, eds., *Advances in Petroleum Geochemistry*. Academic Press, London, pp. 299-335.
- England, W.A. and A.S. Mackenzie. 1989. Some aspects of the organic geochemistry of petroleum fluids. In: R. S. Poelchau and U. Mann, *Evolution of Sedimentary Basins*. *Geol. Research*.
- England, W.A., A.S. Mackenzie, D.U. Mann, and T.M. Quigley. 1987. The movement and entrapment of petroleum fluids in the subsurface. *J. Geol. Soc. London* 144: 327-347.
- Hillebrand, T. and D. Leythaeuser. 1992. Reservoir geochemistry of Stockstadt oilfield: Compositional heterogeneities reflecting accumulation history and multiple source input. *Advances in Organic Geochemistry* 19:119-131.
- Holland, D.S., J.E. Leedy, and D.R. Lammlein. 1990. Eugene Island Block 330 field-U.S.A., Offshore Louisiana. *APPG Treatise of Petroleum geology, Atlas of Oil and Gas Fields, Structural Traps III*, pp.103-143.
- Horstad, I., S.R. Larter, H. Dypvik, P. Aagaard, A.M. Bjornvik, P.E. Johansen, and S. Eriksen. Degradation and maturity controls on oil field petroleum column heterogeneity in the Gullfaks field, Norwegian North Sea. *Advances in Organic Geochemistry* 16: 497-510.
- Hunt, J.M. 1979. *Petroleum Geochemistry and Geology*. Freeman, San Francisco.
- Karlsen, D.A. and S. Larter. 1989. A rapid correlation method for petroleum population mapping within individual petroleum reservoirs-application to petroleum reservoir description. In: R. Steel, ed., *Correlation in Hydrocarbon Exploration*. Graham and Trotman, London.
- Kennicutt II, M.C., T.J. McDonald, P.A. Comet, G.3. Denoux, and J.M. Brooks. 1992. The origins of petroleum in the northern Gulf of Mexico. *Geochim. Cosmochim. Acta* 56:1259-1280.
- Larter, S.R., K.O. Borlykke, D.A. Karlsen, T. Nedkvittne, T. Eglinton, E. Johansen, D. Leythaeuser, P.C. Mason, A.W. Mitchell, and G.A. Newcombe. 1989. Determination of petroleum accumulation histories. Examples from the Ula field, Central Graben, Norwegian North Sea. In: A.T. Huller, ed., *North Sea Oil and Gas Reservoirs*. Graham and Trotman, London.
- Leythaeuser, D. and S. Ruckheim. 1989. Heterogeneity of oil composition within a reservoir as a reflection of accumulation history. *Geochim. Cosmochim. Acta* 53: 2119-2123.
- Mango, F.D. 1990. The origin of light hydrocarbons in petroleum: a kinetic test of the steady-state catalytic hypothesis. *Geochim. Cosmochim. Acta* 54: 1315-1323.
- Milner, C.W.D., M.A. Rogers, and C.R. Evans. 1977. Petroleum transformation in reservoirs. *J. Geochem. Explor.* 7:101-153.

- Quigley, T.M. and A.S. Mackenzie. 1988. The temperatures of oil and gas formation in the sub-surface. *Nature* 339: 549-552.
- Schumachen D. 1993. Eugene Island Block 330 Field, Offshore Louisiana: Geochemical Evidence for Active Hydrocarbon Recharging. AAPG Ann. Convention Abstracts. New Orleans. April.
- Thompson, K.F.M. 1983. Classification and thermal history of petroleum based on light hydrocarbons. *Geochim. Cosmochim. Acta* 47: 303-316.
- Thompson, K.F.M. 1987. Fractionated aromatic petroleums and the generation of gas-condensates. *Org. Geochem.* 11: 573-590.
- Thompson, K.F.M. 1988. Gas-condensate migration and oil fractionation in deltaic systems. *Marine Petrol. Geol.* 5: 237-246.
- Thompson, K.F.M. 1990. Contrasting characteristics attributed to migration in petroleums reservoired in clastic and carbonate sequences in the Gulf of Mexico region. *Petroleum Migration Symposium*, 1989. Special Publication. Geological Society of London.
- Thompson, K.M. and M.C. Kennicutt II. 1990. Nature and frequency of occurrence of non-thermal alteration processes in offshore Gulf of Mexico petroleums. In: D. Schumacher and B.F. Perkins, eds., *Gulf Coast Oils and Gases, Proc. Ninth Ann. Research Conf.*, pp.199-218. SEPM:.
- Tissot, B.P. and D.H. Welte. 1984. *Petroleum Formation and Occurrence*. SpringerVerlag, Berlin.
- Whelan. J.K., M.C. Kennicutt II, J.M. Brooks, D. Schumacher, and L.B. Eglinton. 1994. Organic geochemical indicators of dynamic fluid flow processes in petroleum basins. *Org. Geochem.* 22:: 587-615.
- Young, A., P.H. Monaghan, and R.T. Schweisberger. 1977. Calculation of Ages of Hydrocarbons in Oils-Physical Chemistry Applied to Petroleum Geochemistry. AAPG *Bull* 61:513-600.

Technology Transfer

Roger N. Anderson - Task Manager

OBJECTIVE:

The purpose of this task was to integrate all results into one comprehensive perspective of the project's objectives and to transfer the results to industry. This will involve the interactions between the various project task outputs and the transfer and dissemination of the major conclusions of the study. There were two main efforts related to technology transfer in the field demonstration project. First, we made special efforts to patent and license technology developed as part of this project so that it would become commercially available to the oil industry. Second, we commissioned a study using the United States Geological Survey's fractal oil and gas reserves techniques to identify whether we were dealing with an additional source of oil and gas in the Eugene island 330 field's recharge-along-faults.

SUMMARY:

The DOE field Demonstration Project "Dynamic Enhanced Recovery technologies" has been a resounding success by any gauge. It has spawned important new technologies such as 4D Seismic Monitoring, resulted in the placement of successful new wells to drain new and bypassed oil and gas in one of the most prolific oil fields in the U.S. Offshore, grown into industry-only funding consortia for all its major tasks, and promoted Internet collaboration across institutional boundaries at a time before Internet was such a household word. In addition, there is every prospect that the U.S. Treasury will be repaid many times over for the direct investment of funds into the future of the oil industry in America.

Patents and Licenses

Two patents and one license were developed during this project. Lamont; developed and filed U.S. letters patents for geopressure snapping and 4D Software technologies. These form the core of one of the outstanding accomplishments of the project--the development of 4D seismic monitoring techniques

to track the migration and drainage of oil and gas in reservoirs. Though not solely due to this Class project, 4D seismic technologies have become some of the newest and "hottest" in the industry. There are workshops, industry consortia, AAPG Distinguished lectures, the keynote address at the 1996 Offshore Technologies Conference, 4 separate symposia at the 1996 AAPG convention, all about 4D Seismic technologies. DOE is perceived to be one founder of the technology because of their support of this Class I project.

The 3D Finite Element Model the project developed for fluid flow was licensed to Computational mechanics, and a commercial version, ACCESS.BASIN is currently in the marketplace. ELF, Texaco and Phillips Petroleum are interested in buying it as of this writing.

A key determinant to whether a Class Program was successful might be whether its results were of sufficient interest to the oil industry for them to continue the funding of the Research and Development completely from industry funds. We are pleased to report that all 4 of the major tasks of the project have been continued by industry. Lamont and Penn State have formed a 4D seismic monitoring consortium with 7 oil company supporters. Penn State and Stanford have funded further stress analyses in fault zones through the Gas Research Institute, as have Cornell, Woods hole and LSU for the modeling. Oil companies are funding a continuation of the organic and inorganic geochemistry analyses in the Eugene Island 330 field through Cornell and Woods Hole.

In addition, the DOE funding of experiments in the Pathfinder well resulted in the subsequent placement of the A-SST by Texaco and partners along the boundary of El 330 and 338 blocks. That well is still producing at more than 1200 bbl/day, and has had cumulative production of over 800,000 bbl of oil. At the government's royalty rate of 18%, and assuming oil prices of \$20/bbl \$2.8 million of the DOE project's costs have already been returned to the U.S. Treasury, and the well is targeted to produce at least as much again over the net year or so. In addition, another horizontal well is being planned into 4D seismic targets to the west of the A-85T in 1996, again paid entirely by industry. The government should be "paid-back" for its direct investment in 2-4 years, and the long-term benefits from the use of 4D seismic technologies in old fields within the United States can hardly be underestimated.

Estimate of New Hydrocarbon Supplied

As part of the DOE project, we commissioned the University of South Florida, in cooperation with the United States geological Survey to conduct a "fractal" analysis of oil and gas reserves in the offshore Louisiana segment of the northern Gulf of Mexico. That report follows below, but the conclusions are that while substantial gas reserves might lie undiscovered in the currently-drilled portion of both the north and south additions of offshore Louisiana, no significant new oil reserves remain to be discovered. However, the report goes on to say that they do not detect possible new supplied remaining to be discovered at deeper depths--specifically, the sub-salt play.

At Lamont, we have analyzed the fractal distribution of the Eugene Island fields under study, and find that they depart from the fractal slopes detected for the overall offshore by the South Florida report. The oil and gas migrating up the Red Fault in El 330 appear to come from deeper, "sub-salt" sources. We believe there are substantial new reserves to be found in the sub-salt play of the South Additions. Our project began before the sub-salt play was initiated by the Mahogany discovery of Phillips, et al., in 1994. The industry as a whole now agrees that there are substantial new discoveries to be made deeper in the South Additions of the Gulf, as can be seen, from the increase in bidding prices and activity at recent MMS lease sales for the area.

Assessment of the Undiscovered Oil and Gas Potential, Offshore Louisiana in the South Marsh, Eugene Island, and Ship Shoal Areas

Sarah F. Tebbens

*University of South Florida, Department of Marine Science,
St. Petersburg, FL 33701*

*Christopher C. Barton
U-S. Geological Survey, 600 4th Street, South, St. Petersburg, FL 33701*

*Gary L. Lore
Minerals Management Service, MS 5100, 1201 Elmwood Park Boulevard,
New Orleans, LA 70123-2394*

ABSTRACT

For the South Marsh, Eugene Island and Ship Shoal areas of the U.S. Gulf of Mexico Outer Continental Shelf we calculate the size (volume) and number of undiscovered oil and gas fields. We use a new method (Barton and Scholz, 1995) to assess the size, number, and total volume of undiscovered, conventionally recoverable hydrocarbon fields based on fitting a truncated fractal (power-law) distribution to a log-log plot of the cumulative size-frequency distribution of discovered fields in these three geographically defined areas. The results indicate that there are very few undiscovered oil fields above 1.0 million barrels volume in any of these areas. However, the analysis indicates significant volumes of undiscovered gas. In particular, estimates of remaining undiscovered gas in South Marsh North Addition, Eugene Island Area, and Eugene Island South Addition are 553, 674 and 487 MMBOE, respectively.

Introduction

The Gulf of Mexico basin holds approximately 9% of the world's known recoverable petroleum liquids, and approximately 11% of the world's known recoverable natural gas [Nehring, 1991]. Only the Arabian-Iranian province (with nearly half the world's total) holds more petroleum liquids [Nehring, 1991] - Only the Arabian-Iranian and West Siberian provinces hold more natural gas [Nehring, 1991]. No other province contains even 5% of the world's known conventionally recoverable resources of petroleum liquids or natural gas [Nehring, 1991]. The Gulf of Mexico Outer Continental Shelf is a significant source of domestic hydrocarbon resources. Cumulative production in United States Federal waters (3-200 miles offshore) through 1993 was 9.0 billion barrels of oil (BBO) and 108 trillion cubic feet (TCF) of gas. Ultimate known recoverable reserves in Federal waters in the Gulf of Mexico are 11.2 BBO and 137 TCF of gas [Melcanon et al, 1994]. For the entire Gulf of Mexico Basin, including reserves from Mexico, as of 1987, the ultimate known recoverable reserves (oil and gas combined) are 222.5 billion barrels of oil equivalent (BBOE). This includes 136.6 BB of petroleum liquids and 523.8 TCF of gas [Nehring, 1991]. During 1989, 22% of domestic gas and 10% of domestic oil were produced from the Gulf of Mexico Outer Continental Shelf United States Federal Waters) [Lore, 1991].

The reserve values cited above are minimum estimates based on known (discovered) reserves. These values demonstrate the significance of the Gulf of Mexico as a petroleum resource. This report assesses the remaining undiscovered oil and gas in South Marsh, Eugene Island, and Ship Shoal areas of the Central Gulf of Mexico, offshore Louisiana. These areas lie within the "Gulf Coast Offshore" sub province of the Gulf of Mexico basin, as defined by Salvador [1991] and Nehring [1991]. The assessment method of Barton and Scholz (1995) fits the population of known field sizes (past production plus reserve estimates, not "grown" to their ultimate sizes) with a power law distribution which is, in this report, then extrapolated down to an field size of 1 MMBOE. The total area under the power law distribution is a measure of the ultimate resource and the difference between is a quantitative estimate of the undiscovered conventionally recoverable resource.

Gulf of Mexico Basin Historical Production

A remarkable feature of the exploration history of the Gulf of Mexico basin is the number of economically viable fields discovered annually. Unlike most other petroleum provinces, in which discoveries have been highly concentrated within a period of one to three decades, substantial numbers of new discoveries have been made in the Gulf of Mexico for the past seven decades [Nehring, 1991]. An explanation for this unusual development is that new exploration and development technologies have been developed to take exploration from onshore, to near shore, to progressively deeper waters [Lore, 1991] -This record of success is likely to continue through the 1990's [Nehring, 1991].

The first significant discovery of oil and gas in the Gulf of Mexico basin was made in 1895 at Corsicana, Mexico [Nehring, 1991]. The rate of discovery in the basin accelerated in the 1920's with new geophysical exploration methods.

Prior to 1959, exploration in the offshore Gulf of Mexico was focused on shallow, near shore waters, reflecting extension offshore of active on-shore drilling. South Marsh, Eugene Island and Ship Shoals Block development was active at this time, located near the center of the area, in waters offshore Louisiana, from West Cameron to Main Pass. The average size of fields discovered was 139 MMBOE [Lore, 1991].

Between 1960 and 1969, exploration began to step further offshore, but still on the shelf (<200 m water depth) [Lore, 1991]. A 5-fold increase in the total number of both exploratory and discovery wells resulted in a near doubling of recoverable proved reserves and a 170% increase in the number of fields. In that decade, the average size of fields discovered decreased to 77 MMBOE [Lore, 1991].

In the next decade (1970 to 1979), drilling off Louisiana continued to extend further offshore. Activity on the upper continental slope was at water depths, greater than 200 m. Additionally, exploration and development in the western Gulf of Mexico, resulted primarily in the discovery of gas. During the 1970's, the average size of fields discovered on the outer continental shelf decreased to 42 MMBOE, with most of the larger fields discovered further offshore on the upper slope (average field size on the upper slope was 63 MMBOE).

In 1971, the Eugene Island Block 330 Field was discovered. The field now includes Eugene Island blocks 313, southern half of blocks 314,330,331,332,337 and 338 [Holland et al, 1991]). From 1975 to 1980, the field was the largest producing field in United States Federal Outer Continental Shelf waters [Holland et al, 1991]. As of 1991, the field ranked second in annual hydrocarbon production (Minerals Management Service Data as reported in [Holland et al, 1991]) and fourth in cumulative hydrocarbon production (Dwight's Energy Data as reported in [Holland et al, 1991]). Estimated at 671 MMBOE of recoverable oil and gas [Melcanon: et al 1994] the Eugene Island field ranks 437th among the giant oil and gas fields of the world [Carmalt and John, 1986].

In the 1980s, there was scattered development across the Central and Western Gulf of Mexico Shelf (figure 3D). Exploratory drilling had reached water depths in excess of 7,000 feet. The Auger field, discovered in 1987 in 2,862 feet of water, is estimated to hold 220 MMBOE of recoverable oil and gas [Taylor, 1994; Shirley, 1995]. Even with a few large discoveries, by 1989 the average field size had decreased to only 14 MMBOE.

The 1990s have witnessed discovery of the Mars field in 2,933 feet of water, which is estimated to hold 770 MMBOE [Taylor 1994; Shirley, 1995], making it the largest discovery in the Gulf to date. For a list of deepwater reserves (holdings in water 1,000 deep or greater) see Taylor [1994]. Near to shore and in shallow water, Ship Shoal, Eugene Island and South Marsh have been extensively explored through conventional methods and are in the mature stages of exploration and development.

Assessment Methodology

The methodology used to estimate the undiscovered oil and gas fields in the Eugene Island, South Marsh and Ship Shoal Areas was developed by Barton and his colleagues [Barton et al, 1991; Barton and Scholz, 1995; Barton and Troussov, in press] Barton and Scholz [1995]. We have determined that hydrocarbon fields ranging in size from a single play (i.e. Frio Strand Plain Play, Gulf Coast of Texas, and Cardium Scour Play of western Canada) to individual basins (Permian Basin, 0-5000' depths) to giant fields of the world follow a fractal (power law) distribution. In the following section we provide a brief

introduction to fractals in nature and then we describe the methodology as applied to oil and gas resource assessment. In a later section, we discuss the results of this application to regions offshore Louisiana.

Background: Fractals in Nature

Objects in nature are commonly very irregular, such that, within the constraints of Euclidean geometry, one is forced to grossly approximate their shape. A rock fragment, for example, generally is treated as being spherical, and a coastline as straight or smoothly curved. Upon examination, however, these objects are found to be jagged over a wide range of length scales, and these irregularities do not diminish when viewed at ever finer scales. *Mandelbrot* (1982) developed fractal geometry, which is applicable to many irregular natural objects. Fractal objects have a number of definitive characteristics that are identifiable and described by the methods of fractal geometry. The analytical techniques for treating fractal geometry, and their interrelationships, have undergone rapid evolution and broad application (for example, *Feder*, 1988). Fractal geometry has been applied to a wide variety of geologic and geophysical objects and phenomena (for example, *Scholz and Mandelbrot*; 1989. *Turconne*, 1992; *Korvin*, 1993; *Turcone and Huang*, 1995; and *Barton and LaPointe*, 1995a,b).

Distribution Function of Hydrocarbon Fields

For the past forty years, the size-frequency distribution of mineral deposits, including oil fields, has been thought to be log-normal (for example, *Krige*, 1951; *Arps and Roberts*, 1958; *Kaufman*, 1962, 1983; *McCrossan*, 1968; *Barouch and Kaufman*, 1976; *Lee and Wang*, 1983a, b; *Forman and Hinde*, 1985; *Davis and Chang*, 1989; *Power*, 1992). The log normal distribution resembles a power-law, or fractal, distribution in the middle of its range but is truncated at the lower end. Unlike the scale-independent power-law distribution, it has a characteristic size (mode) at which the distribution peaks and rolls off and has values below the mode. At the upper end, the log normal distribution tends quickly to zero and therefore has a thin tail. In contrast, the upper end of the power-law or fractal distribution tends to zero slowly and therefore has a fat tail. Note that only the fractal (power-law) distribution plots as a straight line. For size versus cumulative frequency distributions, the term fractal is used only for power-law distributions with slope (a) less than 2. Over small ranges in size portions of the other distributions can be approximated by straight lines with either steep slopes for large sizes or zero slopes for small sizes. It therefore is important to have data over a sufficient range so that the true distribution is observed. The general rule of thumb for a power law fit is that the data should range over as many orders of magnitude as the absolute value of the scaling exponent (slope of the line in log-log space) (*Mandelbrot*, pers. Com., 1995).

A power-law data set containing a perceptibility limit (the smallest size for which we have a complete census of the population) commonly is well fit by a log normal distribution. Because all observed distributors will have perceptibility limits; this misidentification is not uncommon. For example, a perceptibility limit occurs in earthquake detection. Because seismometers have lower-magnitude thresholds for event detection this results in a low-side truncation in observed earthquake sizes. Observed earthquake distribution is a power law distribution above the perceptibility limit. Installation of instruments with higher magnification results in detection of a multitude of smaller earthquakes that continue to belong to a power-law size distribution (which is called the Gutenberg-Richter law in seismology).

As progressively smaller hydrocarbon fields are discovered through time, the associated perceptibility limit moves to smaller field sizes, thus extending the power-law size distribution to progressively smaller field sizes. Such temporal change should not occur if the underlying distribution had a characteristic size, such as log normal distribution. A power law distribution, which has no characteristic size, appears to be the correct distribution to describe the size distribution of hydrocarbon fields.

Recognition that the size-frequency distribution of hydrocarbon fields may be a power-law was made by L.J. Drew and his colleagues (*Drew and others*, 1982; *Schuenemeyer and Drew*, 1983; *Attanasi and Drew*, 1985; *Drew and others*, 1988; and *Drew*, 1990; *Baker and others*, 1984; *Houghton*, 1988; *Scholz and Barton*, 1991; *Brett and Feldcamp*, 1993; *Barton and Scholz*, 1995; and *Crovelli and Barton*,

1995). An example from *Drew* (1990) shows the size distribution of discovered fields in the Frio Strand Plain play (onshore Texas) as a function of time, and as replotted by *Barton and Troussov* [in press] as a cumulative frequency versus field-size distribution in log-log space (figure SB). At any given time, the distribution in this play looks like a log normal distribution, but, as exploration proceeds, more small fields are discovered, with associated progressive decreases in the mode. We observe a similar pattern through time for the 200 top discovered oil and gas fields in U.S. Gulf of Mexico waters (based on original reserve estimates).

Drew and his colleagues maintained that the parent distribution in the Frio Strand Plain play is a power-law (or Pareto) distribution that is gradually being revealed by exploration. The rollover at any given time is determined by economics since uneconomic smaller fields are either undiscovered or not developed. This rollover is shifted to smaller sizes as price increases and more small fields are discovered and developed. The largest fields are commonly found early in the exploration cycle, and through time the population fills in with progressively smaller sizes. From this understanding of the discovery process we can infer that in any region at a mature stage of exploration, the right tail in the distribution provides a good estimate of the parent distribution down to the perceptibility limit, which is commonly at or near the economic truncation. Thus, the population in the largest size classes remains stable in time. Therefore, in order to obtain an estimate of the true or parent population of hydrocarbon deposits, we fit the right side of the size distribution in regions in the mature stages of exploration.

The Pareto distribution has been used by the U.S. Geological Survey (USGS) in past assessments of the undiscovered conventionally recoverable hydrocarbon resources of the United States. *Houghton and others* (1993) described application of the truncated shifted Pareto distribution in the 1989 USGS national petroleum assessment to fit geologists' estimates of the size and number of undiscovered hydrocarbon fields. In contrast, in the method proposed by Barton and his colleagues, and used in this work, the size and number of undiscovered fields are forecast by fitting a power-law to the distribution of discovered fields larger than the perceptibility limit and then extrapolating to field sizes smaller than the perceptibility limit.

Fractal Size-Frequency Distributions and their Application to Hydrocarbon Fields

A variety of geologic objects having this type of distribution are described by *Turcone* (1992); *Turcone and Huang* (1995); and *Barton and LaPointe* (1995a, 1995b). These collections of objects must be defined within some region, which we will call the distribution space. For hydrocarbon accumulations, this space may be a geographical region, such as the world, a basin, a country, or a State, or it may have a geologic definition, such as an oil province or a play. Members of the distribution must also be defined; these may be the field, for example, or the pool. These various members and spaces may constitute different hierarchies nested within one another. For example, there may be a distribution of pools within a reservoir and, at higher hierarchical levels, a distribution of reservoirs within a field within a play, and plays within a basin or province. In this report, we consider the hydrocarbon field sizes, as defined by Minerals Management Service [*Melcanon et al*, 1994, for example].

As mathematical expressions are defined over infinite ranges, but in any finite application the range must be limited by lower and upper fractal limits. The upper fractal limit (UFL) is always defined by the distribution space and is usually observable. For example, the largest possible field in a basin is constrained by the size of the basin and its geology. One can always find or estimate this largest field; in regions of mature or semi-mature stages of exploration the largest deposit has probably been discovered, based on the discovery process (see *Drew*, 1990). On the other hand, the lower fractal limit (LFL) is arbitrarily defined. It may be the smallest structural trap within the basin or the smallest oil-filled pore space within the reservoir rock. In either case, we do not know its size. The lower fractal limit is not generally of practical importance because it is always well below a perceptibility limit (FL), the smallest size for which

For the Eugene Island South Addition oil fields, we predict that when all the oil is discovered, most of the total volume will be in the large fields. Because this convergence constraint is a general property of fractal distributions, it follows that, as exploration proceeds from development of large to small fields, the volume discovery rate decreases even though many more small than large fields are present.

If the fit to the data is a good representation of the parent population, the ultimate volume of hydrocarbons in the distribution space can be obtained by summing the discovered volumes greater than the perceptibility limit and adding to them the calculated undiscovered volume by evaluation. Using this method, the total residual volume of hydrocarbons can be calculated down to any lower threshold. The cumulative size-frequency distribution is used to calculate because this distribution smoothes out the noise that results from inaccuracies in determining the volume of each field in the data sets.

Barton and Scholz (1995) fit a power law cumulative size frequency distribution to hydrocarbon populations at different hierarchical levels, each of which exhibits approximate fractal distributions. which means tat these populations consist of many nested fractal distributions. Such nesting may persist continuously over a wide range of sizes, all the way down to the porosity of the reservoir rock, which has also been shown to have a fractal size distribution (Krohn, 1988).

For several regions within the study area, the cumulative size-frequency versus field-size distribution will be shown to be strongly curved, concave downward, over the higher size ranges, such that the slope increases with size. if the data are truncated to a size about one order of magnitude smaller than the maximum field size, a power law is fit down to the perceptibility limit. The power law should not be extrapolated to the far right end of the distribution because it predicts an unrealistic maximum field size many times larger than that observed.

Curvature near the upper fractal limit is a local feature, affecting only the last one or two data points, and is expected because of the natural truncation associated with the upper fractal limit. Cases where the curvature, or enhanced slope, extends well below the last one or two largest field sizes cannot be explained in this way. We propose, instead, that the observed curvature in the large field sizes results from constructing data sets defined by the artificial boundaries of geographic areas tat contain portions of geologically defined plays, thereby including a diverse a set of sub populations. Consider the hypothetical case of five sub populations as solid lines. Each of these has cumulative-frequency size distributions with the same a value but different upper fractal limits. When combined, these produce the population shown by the ten data points. The line has curvature in the upper size ranges, whereas below the upper fractal limit, the a value for the total population is the same as for each of its parts.

This observation underscores the conventional wisdom in discovery process modeling (for example, *Kaufman*, 1983; *Drew* 1990) that one must carefully select data sets for homogeneity of geology and source. Data sets for larger regions (*Barton and Scholz*, 1995) are, however, still approximately fractal, and useful analysis can be made of them. The total resource in such a region can be estimated by summing the volume in the larger fields and integrating the remainder in the smaller fields in the way described above, stating from the point at which a becomes representative of the population as a whole.

Results

The assessment methodology presented above was applied to determine the size and number, and total volume of undiscovered conventionally recoverable oil and gas fields for Ship Shoal, Eugene Island and South Marsh areas. Based on the above discussion, we assume that the underlying distribution of oil and gas fields in these areas is fractal (power law). Field sizes (the sum of cumulative production through 1993, and remaining ungrown recoverable reserves) were provided by Minerals Management Service. They are defined and discussed in *Melcanon et al* [1994]. The lower fractal limit for this assessment is 1 mm BOE.

Cumulative frequency versus field size plots for oil, and gas in each of the three areas are presented. The following points made in the methodology section are particularly important for interpretation. 1) To infer a fractal distribution (i.e. to fit a line to a log-log plot (a power law, the data should span as many orders of magnitude as the absolute value of the slope of the line fit. For this work, the slope is usually less than one so that we need data with a range of values spanning a minimum of roughly one order of magnitude). 2) Rollover at smaller field sizes. suggests undiscovered fields at the smaller field sizes. 3) Rollover at larger field sizes suggests that data from several populations, each with fractal distributions, have been combined. The rollover at larger field sizes is expected for this work since the available data combine all fields at each area; the data are not separated by, for instance. stratigraphic source levels. We observe rollover at smaller field sizes (a perceptibility limit) for all three areas.

Rollover at larger field sizes is observed for South Marsh South Addition Gas, Eugene Island Oil and Gas, and all Ship Shoal Oil and Gas distributions. We note that for four of the fourteen assessments (South Marsh Gas, South Marsh South Addition Gas, Ship Shoal Oil, and Ship Shoal South Addition Gas), the data are sparse and the results should be considered tentative.

A summary of the oil assessment, including the volume of remaining undiscovered oil in each region down to a field size of 1.0 million barrels oil equivalent (mm BOE) was made. The calculated fractal scaling exponent represents the volume of discovered hydrocarbons, and the predicted ultimate volume of hydrocarbons. The remaining undiscovered volumes are further subdivided into the number of fields remaining to be discovered in each field class in each region.

In the seven regions studied, the region with the largest total volume of discovered oil is Ship Shoal block (1029 mm BOE) with the next largest discovered volumes in Eugene Island and Eugene Island South Addition areas (697 and 695 mmBOE, respectively).

The predicted volume of oil remaining undiscovered in each region is small (less than 90 mmBOE) or none. The largest predicted volume of oil remaining undiscovered is also in Ship Shoal block. We note that the Ship Shoal block oil assessment is one of the four assessments for which the data are scarce, so the results are tentative. If correct, the results predict 87 mmBOE oil remaining undiscovered in Ship Shoal block. These reserves are predicted to be comprised of two class S fields (mean field size 5.7 mmBOE), 10 class 7 fields (mean size 2.8 mmBOE) and 23 class 6 fields (mean size 1.4 mmBOE). The next largest predicted volumes of undiscovered oil are in South Marsh Island South Addition Area and Eugene Island South Addition Area, with 20 mmBOE and 11 mmBOE, respectively, remaining undiscovered. There are no remaining undiscovered fields larger than one mmBOE predicted in the South Marsh Island North Addition and South Marsh Island regions.

In the seven regions studied, the region with the largest total volume of discovered gas is Eugene Island South Addition (1449 mmBOE) with the next largest discovered volumes in Ship Shoal block and Eugene Island Block (1315 and 1283 mmBOE, respectively). The regions with the largest volumes of gas predicted to be remaining undiscovered are Eugene Island Area, South Marsh North Addition, and Eugene Island South Addition, with 674, 553 and 487 mmBOE, respectively. In the region with the largest volume of undiscovered fields, Eugene Island Area, the reserves are predicted to be comprised of 172 class six fields, 73 class seven fields, 30 class eight fields, and 10 class nine fields. The largest fields predicted are two class 10 fields (mean field size 23 mmBOE) in the Eugene Island South Addition Area.

We note that this analysis cannot evaluate the undiscovered resources located in plays at depths greater than those currently included in our data sets (subsalt); additional oil and gas plays at deeper horizons cannot be ruled out.

The scaling exponent can be used to inter the relative abundance of small fields to large fields. The smaller the (absolute value of the) scaling exponent, the greater the ratio of the large fields to the small fields. For gas fields, as one moves offshore, the scaling exponent decreases indicating the ratio of larger fields to smaller fields increases one moves offshore. For oil fields, the opposite trend is weakly suggested with the scaling exponent increasing slightly offshore in the South Marsh and Eugene Island Areas and observed to be roughly constant across the Ship Shoal Area.

Summary

Populations of hydrocarbon fields can be described by the power-law size distribution characteristic of fractal sets. This is true for all hierarchies of populations examined by *Barton and Scholz* (1995), ranging from pools in a play to giant fields in the world. *Barton and Scholz* (1995) suggest that any population of hydrocarbon fields consists of the combination of many fractal sub populations at different hierarchical levels nested within one another. We find that for the U.S. Gulf of Mexico Outer Continental Shelf, the underlying distribution of oil and gas fields appears to be fractal. For the South Marsh, Eugene Island and Ship Shoal areas we assume the underlying distribution is fractal (as is observed by *Barton and Scholz* (1995) to be the case for regions worldwide) and calculate the size, volume and number of undiscovered fields.

Our results indicate that there are minimal (or no) remaining undiscovered oil reserves down to the 1.0 million barrel field size in the regions. However, the analysis indicates significant volumes of undiscovered gas. In particular, the gas remaining undiscovered is 674, 553 and 487 mmBOE, in Eugene

Island Blocks, South Marsh North Addition, and Eugene Island South Addition, respectively. These reserves are predicted to be contained within smaller size fields. The largest fields predicted are three class 10 gas fields (mean field size 23 mmBOE) in the Eugene Island South Addition area.

Acknowledgments: We are grateful to D. Gautier and D. Higley for critical reviews. We thank Roger Anderson and the Global Basins Research Network for encouragement and advice. This work was funded by the Department of Energy Cooperative Agreement DEFC22-93BC 14961 subcontract 1245-187-L3.

References

- Arps, J.J., and Roberts, T.G., 1958, Economics of drilling for Cretaceous oil on the east flank of the Denver-Julesburg Basin: American Association of Petroleum Geologists Bulletin, v.42, p. 2549-2:566.
- Attanasi, E.D., Drew, L.J., 1985, Lognormal field size distributions a consequence of economic truncation: Mathematical Geology, v.17, p.335-351.
- Baker, R.A., Gehman, H.M., James, W.R., and White, D.A., 1984, Geologic field number and size assessments of oil and gas plays: American Association of Petroleum Geologists Bulletin, v.68, p. 426-437.
- Barouch, E. and Kaufman, G.M., 1976, Oil and gas discovery modeled as sampling without replacement and proportional to random size: Sloan School Working Paper No.888-76.
- Barton, C.C., and La Pointe, P.R., eds., 1995a, Fractals in the earth sciences: New York, Plenum Press, 265 p.
- _____, 1995b, Fractals in petroleum geology and earth processes: New York, Plenum Press, 317 p.
- Barton, C.C., and Scholz, C.H., 1995, The fractal size and spatial distribution of hydrocarbon accumulations--implications for resource assessment and exploration strategy, in Barton, C.C., and La Pointe, P.R. Eds. Fractals in petroleum geology and earth processes: New York, Plenum Press, p.13-34.
- Barton, C.C., Scholz, C.H., Schutter, T.A., Herring, P.R., and Thomas, W.J., 1991, Fractal nature of hydrocarbon deposits--2, Spatial distribution: American Association of Petroleum Geologists Bulletin, v.75, no.3, p.539.
- Barton, C. C. and Troussov, G.L., Fractal methodology for petroleum resource assessment and FRA - A computer program that calculates the volume and number of undiscovered hydrocarbon accumulations: U.S. Geological Survey Circular 1128.23 p.
- Brett, J.F., and Feldcamp, L.D., 1993, The evidence for and implications of a fractal distribution of petroleum reserves: Society of Petroleum Engineers, SPE 25826, p. 73-84.
- Carmalt, S.W., and John, B. S., 1986, Giant Oil and Gas Fields of the World, in Halbouty, M.T., ed., 'Future petroleum Provinces of the World: American Association of Petroleum Geologists Memoir 40, p.11-S⁴.
- Crovelli, R.A., and Barton, C.C., 1995, Fractals and the Pareto distribution applied to petroleum field-size distributions, in Barton, C.C., and LaPointe, P.R., eds., Fractals in petroleum geology and earth processes: New York, Plenum Press. P. 59-72.
- Davis, J.C., and Chang, T., 1989, Estimating potential for small fields in mature petroleum province: American Association of Petroleum Geologists Bulletin, V. 73, p.967-976.
- Drew, L.J., 1990, Oil and gas forecasting: Oxford, England, Oxford University Press, 252 p.
- Drew, L.J., Attanasi, E.D., and Schuenemeyer, J.H., 1988, Observed oil and gas field size distributions--A consequence of the discovery process and prices of oil and gas: Mathematical Geology, v.20, p.939-953.
- Drew, L.J., Schuenemeyer, J.H., and Bawiek, W.J., 1982, Estimation of the future rates of oil and gas discoveries in the western Gulf of Mexico: U.S. Geological Survey Professional Paper 1252, 26 p.
- Feder, Jens, 1988, Fractals New York, Plenum Press, 283 p.

- Forman, D.3., and Hinde, A.L., 1985. Improved statistical method for assessment of undiscovered petroleum resources: American Association of Petroleum Geologists Bulletin, v.69, p.106-118.
- Holland, D. S., Leedy, 3. B., and Lammlein, D. R., 1991, Eugene Island Block 330 Field - USA Offshore Louisiana: American Association of Petroleum Geologists, Treatise of Petroleum Geology, p.10:3-143.
- Houghton, J.C., 1988. Use of the truncated shifted Pareto distribution in assessing size distribution of oil and gas fields: Mathematical Geology, v.20, no.8, p.907-937.
- Houghton, J.C., Dolton, G.L., Mast, R.F., Masters, C.D., and Root, D.H., 1993, U.S. Geological Survey estimation procedure for accumulation size distributions by play: American Association of Petroleum Geologists Bulletin, v.77, no.3, p. 454-466. Kaufman, G.M., 1962, Statistical decision and related techniques in oil and gas exploration: Englewood Cliffs, N.J., Prentice-Hall, 307 p.
- 1983, Discovery process models; *in* Adelman, M.A., Houghton, J.C., Kaufman, G.M., and Zimmerman, M.B., eds.: Energy resources in an uncertain future: Cambridge, Mass., Bailing Press, p.213-268.
- Korvin, Gabor, 1993, Fractal models in the earth sciences: Amsterdam, Elsevier, 396 p. Krige, D.G., 1951, A statistical approach to some basic mine valuation problems on the Witwatersrand: South Africa 52, no.6, p.119-139.
- Krohn, C.E., 1988, Sandstone fractal and Euclidean pore volume distributions: Journal of Geophysical Research 93, p.3286-3296.
- Lee, P.3., and Wang, P.C.C., 1983a, Probabilistic formulation of a method for the evaluation of petroleum resources: Mathematical Geology, v.15. no.1, p.163-181.
- 1983b. Conditional analysis for petroleum resource evaluation: Mathematical Geology, v.15, no.2, p.349-361.
- Lore, G. L., 1991, Exploration and discoveries, 1947-1989, Gulf of Mexico 0(5): An historical perspective: Minerals Management Report 91-0078.87 pp.
- Mandelbrot, B.B., 1982, The fractal geometry of nature: San Francisco, W.H. Freeman, 460 p.
- McCrossan, R.G., 1968, An analysis of size frequency distribution of oil and gas reserves of Western Canada: Canadian Journal of Earth Sciences, v.6, p.201-211.
- Melcanon, J. M., Bacigalupi, S. M., Kinler, C. J., Marin, D. A, and Prendergast, M. T., 1994, Outer continental shelf estimated proved oil and gas reserves, Gun? of Mexico, December 31, 1993: Minerals Management Service Report 94-(0)45. 49 pp.
- Middlebrooks, E. 3., 1976. Statistical calculations--How to solve statistical problems: Ann Arbor, Mich., Ann Arbor Science, 120 p.
- Nehring, R., 1991, Oil and Gas resources; *in* Salvador, A., ed., The Gulf of Mexico Basin: Boulder, Colorado, Geological Society of America, The Geology of North America, v.3, p.445-494.
- Power, M., 1992, Lognormality in the observed size distribution of oil and gas pools as a consequence of sampling bias; Mathematical Geology, v.24, no.8, p.929-945.
- Salvador, A., 1991, Introduction; *in* Salvador, A., ed., The Gulf of Mexico Basin: Boulder, Colorado, Geological Society of America, The Geology of North America, v.3, p.1-12.
- Scholz, C.H., and Barton, C.C., 1991, The fractal nature of hydrocarbon deposits--I. Size distributions: American Association of Petroleum Geologists Bulletin, v.75, no.3, p.668.
- Scholz, C.H., and Mandelbrot, B.B., eds., 1989, Fractals in geophysics: Basel, Birkhauser, 313 p.
- Schuenemeyer, J.H., and Drew, L.J., 1983, A procedure to estimate the parent population of the size of oil and gas fields as revealed by a study of economic truncation: Mathematical Geology, v.15, no.1, p.145-161.
- Schuenemeyer, J.H., and Drew, L.J., 1991, A forecast of undiscovered oil and gas in the Frio Strand Plain trend--The unfolding of a very large exploration play: American Association of Petroleum Geologists Bulletin, v.75, no.6, p. 1107-1115.
- Schuenemeyer, J.H., Drew, L.3., Root, D.H., and Attanasi, E.D., 1990, Estimating potential for small fields in mature petroleum provinces--Discussion: American Association of Petroleum Geologists Bulletin, v.74, no.11, p.176¹-1763.

- Schuster, H.G.. 1988, Deterministic Chaos: VCH. Weinheim, 270 p
- Shirley, Kathy, 1995, Modeling proved a profitable cost: ALAPO Explorer, American Association of Petroleum Geologists, May 1995, p.11-12.
- Taylor, O., 1994, Deep Risks Paying off: Successes Buoy Gulf Hopes: AAPG Explorer, American Association of Petroleum Geologists. September 1994, p.1 and 4.
- Turcotte, D. L., 1992, Fractals and chaos in geology and geophysics: Cambridge, Cambridge University Press, 221 p.
- Turcotte, D.L., and Huang. J., 1995, Fractal distributions in geology. scale invariance. and deterministic chaos; *in* Barton, C., and LaPointe, P.R., eds., Fractals in the earth sciences: New York, Plenum Press, p.1-40.

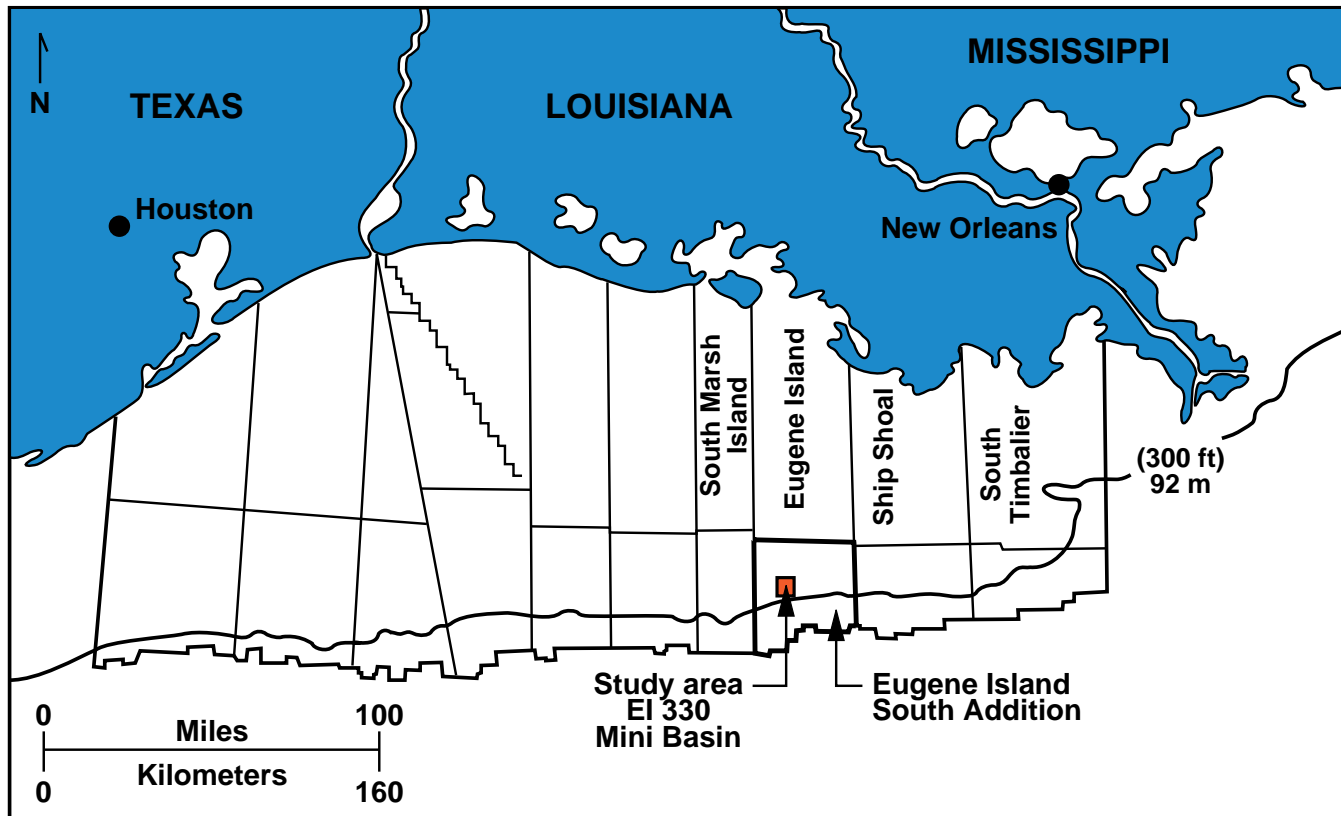


Figure I.i.1: Eugene Island 330, location of study area.

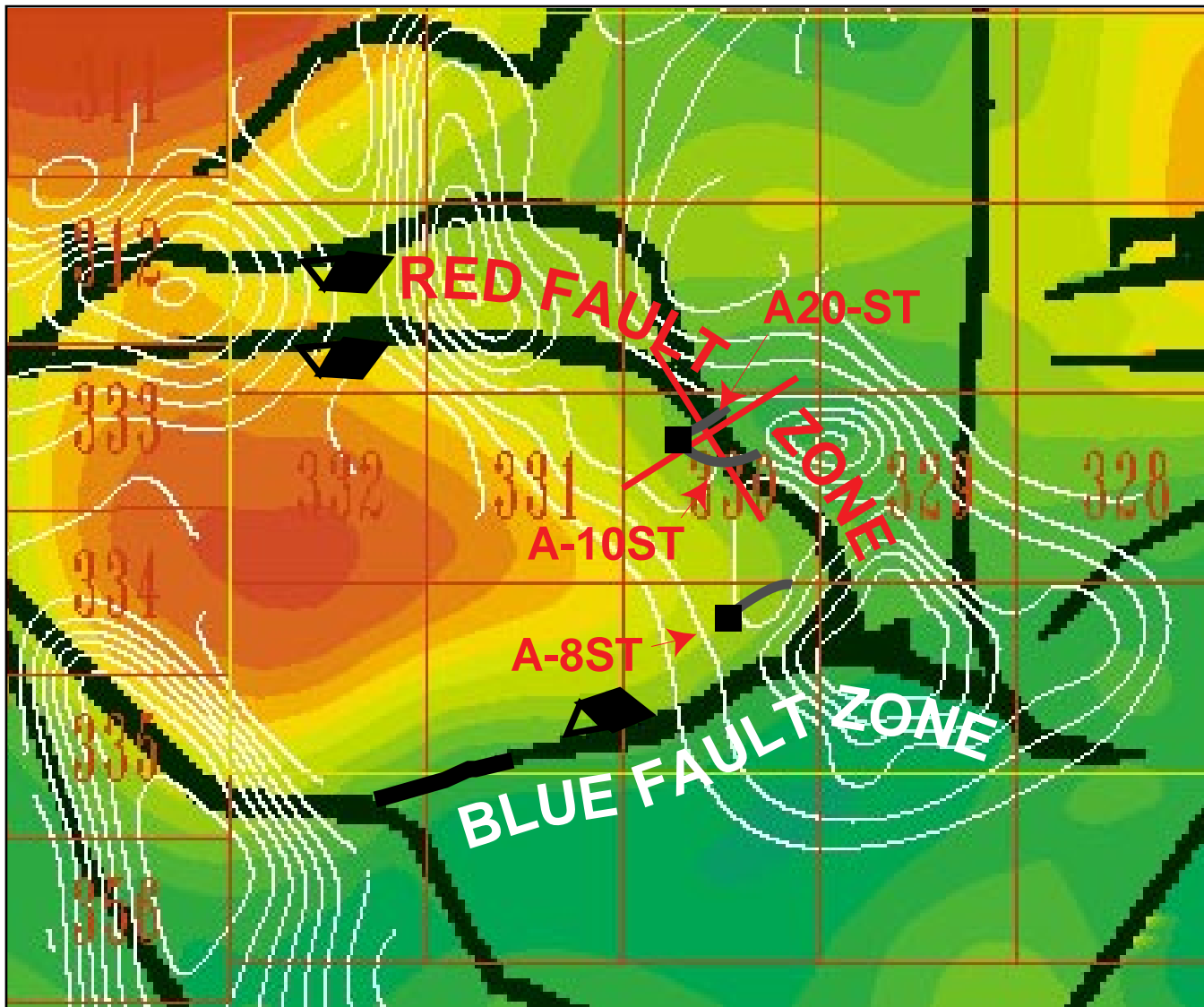


Figure 1i.2: The Eugene Island 330 minibasin is shown by depth to the top-of-geopressure surface (hot colors are deep, cold colors are shallow). White contours are top-of-salt, and black lines are faults. Pennzoil "A" platform and seismic profiles of [Figures 1i.3](#) and [1i.5](#) are located within block 330 (from He and Anderson, 1994).

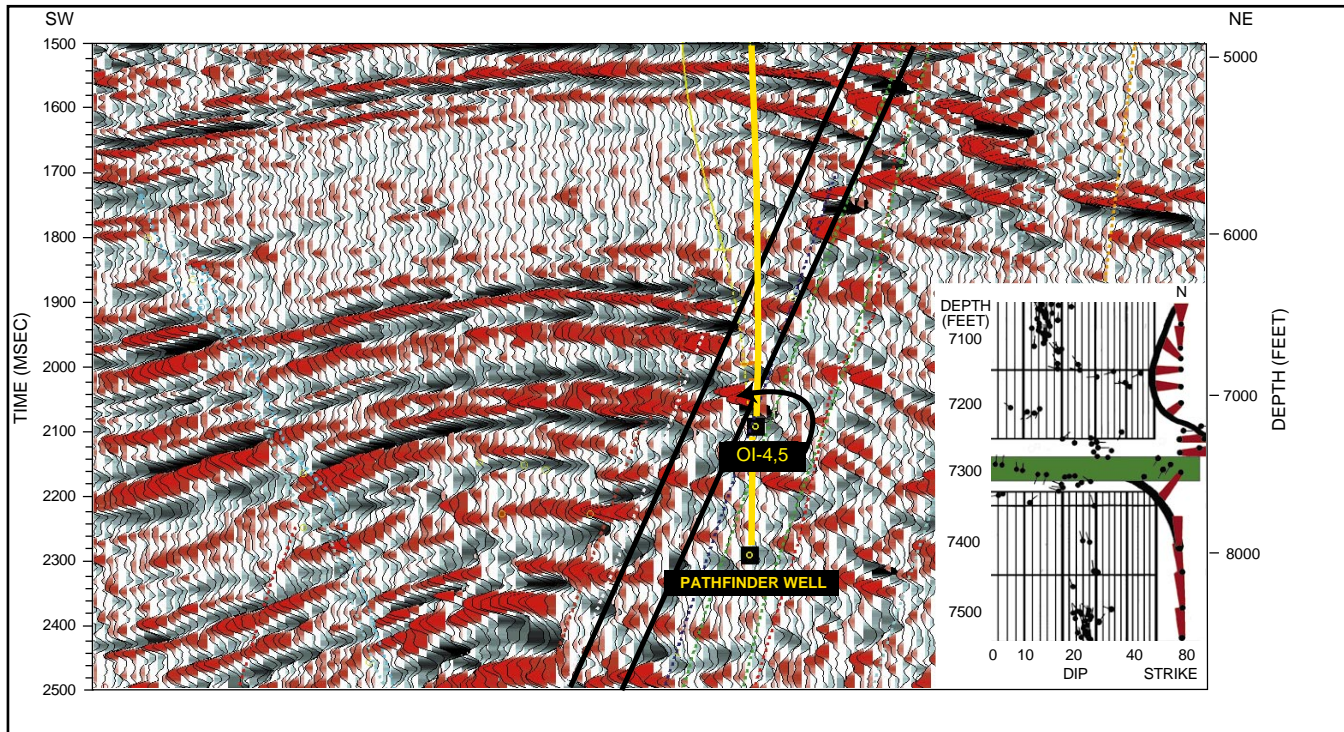


Figure I.i.3: Seismic reflection profile (courtesy Pennzoil, Exxon and Mobil) in-line to A-20ST "Pathfinder" well in Eugene Island block 330. Dipmeter "tadpoles" across fault zone shown in lower right. Note swing in strike of beds above, within, and below the fault zone.

WHITE LIGHT

FLUORESCENCE

7557.5'

7558.0'

7558.5'

TVD (FEET)

7559.0'

4"

Figure I.i.4: Core photos from 7557.5'-7559' showing hydrocarbon-charged fault connected to small sand lens.

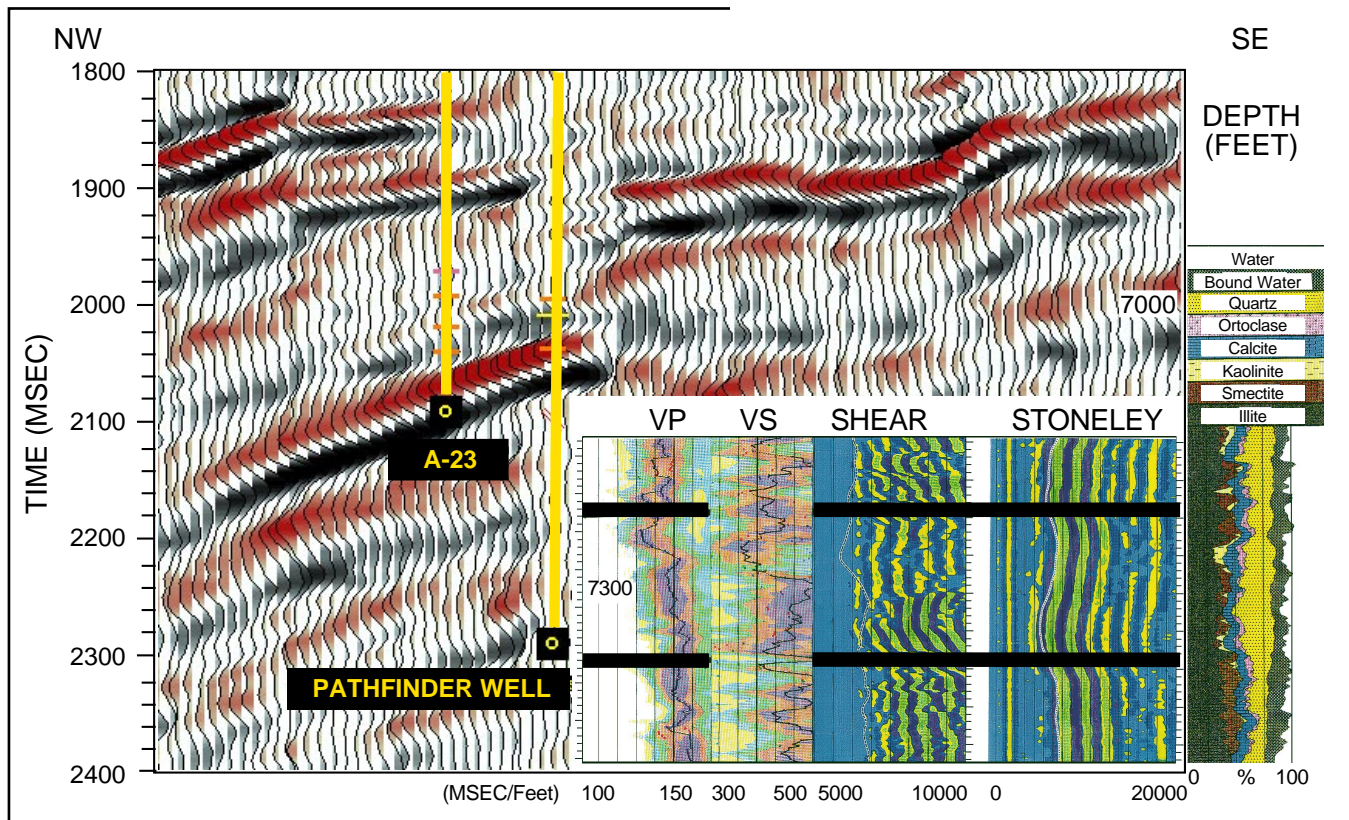


Figure I.i.5: Cross-line seismic reflection profile with dipole sonic and geochemical log inserts.

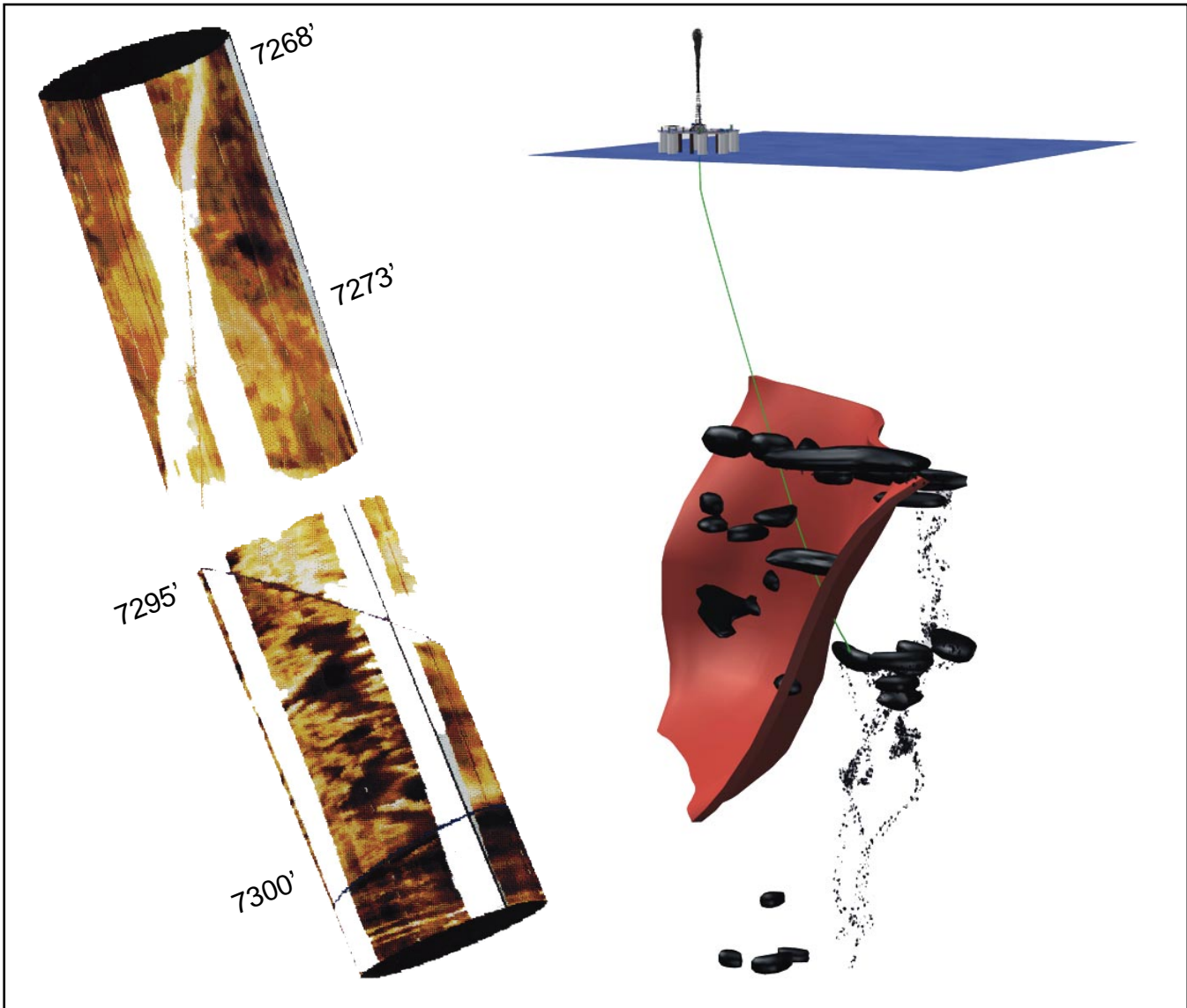


Figure I.i.6: Formation MicroImager of fault zone with well path image.

Red Fault: In-situ Conditions Pathfinder Well Path

Column Pressure =
~500-600psi

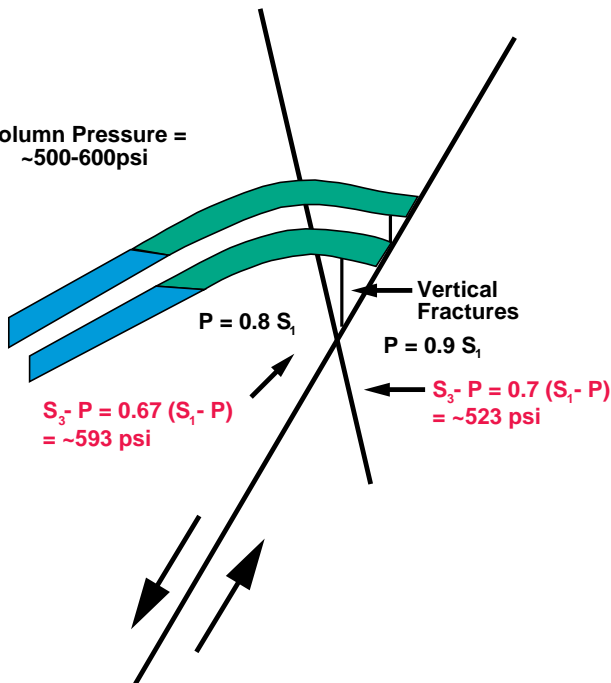


Figure I.i.7: In-situ stress and pressure measurements across fault zone.

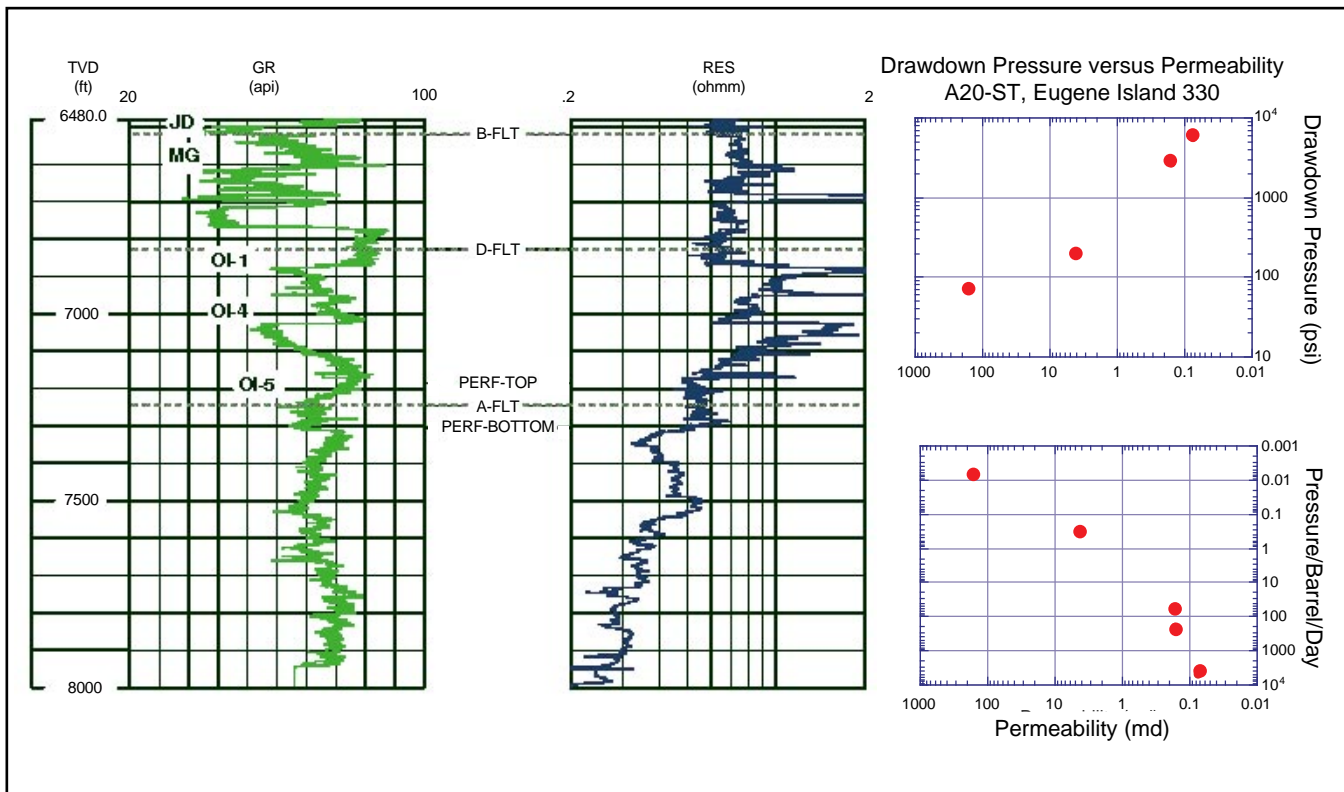


Figure I.i.8: Drill-stem test results.

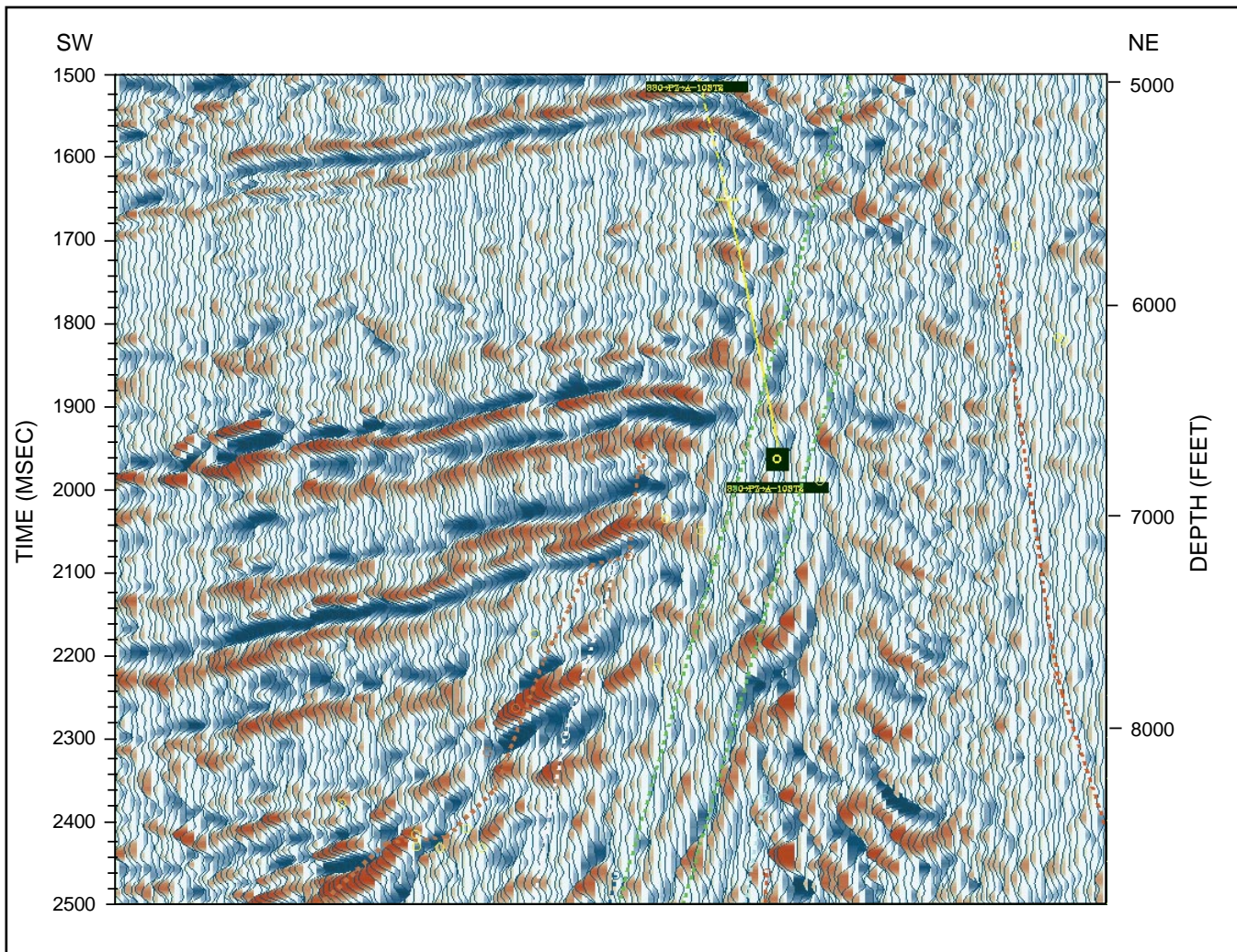


Figure I.i.9: Seismic profile along A-10ST wellpath.

7510' STATIONARY MEASUREMENT FROM TDT LOG

MINITRON

0

API

150

FAR DETECTOR GAMMA RAY GR

7510'

NEUTRON BURSTS

STATION

ON

TIME

TRANSIENT BURST

FAR COUNTER
1ST SEES
FLOW
81" ABOVE
MINITRON

THEN GR
14.5'
UP THE
HOLE
DETECTS
FLOW
FROM
SLUG

NO FLOW

Figure I.i.12: Flow detected across a stationary TDT tool from a slug of water moving across the upper fault zone boundary against a 17.5 lb/gal (kill-slug).

	Depth (ft)	Gamma Ray	Vel (ft/min)	Vel (bbl/day)
Logging	7450.0	8.0000	37.700	48.900
	7475.0	10.000	48.000	64.000
	7495.0	80.000	110.00	160.00
	7500.0	110.00	120.00	170.00
	7505.0	90.000	115.00	150.00
	7510.0	145.00	103.00	180.00
	7520.0	125.00	100.00	175.00
	7520.0	120.00	130.00	185.00
	7525.0	175.00	145.00	195.00
	7530.0	155.00	130.00	180.00
	7535.0	175.00	145.00	195.00
	7545.0	245.00	160.00	220.00
	7550.0	215.00	150.00	200.00
	7555.0	150.00	135.00	180.00
	7570.0	75.000	103.00	150.00
	7575.0	175.00	135.00	200.00
	7580.0	130.00	125.00	175.00
	7595.0	25.000	68.000	90.000
	7600.0	60.000	100.00	140.00
	7605.0	80.000	110.00	150.00
Stations	7625.0	15.000	52.000	70.000
	7630.0	30.000	85.000	115.00
	7635.0	30.000	85.000	115.00
	7045.0	2.0000	3.5000	12.000
	7055.0	4.0000	6.0000	14.700
	7100.0	4.1000	7.4000	23.700
	7110.0	3.5000	5.8000	34.300
	7135.0	6.3000	33.500	50.000
	7145.0	5.4000	19.100	28.500
	7150.0	66.900	53.700	81.000
	7190.0	38.100	50.000	75.000
	7200.0	6.0000	14.700	20.000
	7395.0	7.4000	23.700	35.500
	7400.0	3.5000	12.000	18.000
	7450.0	37.700	48.900	73.000
	7490.0	10.400	12.500	19.000
	7500.0	43.200	64.300	96.000
	7510.0	3.3000	18.200	27.000
	7560.0	4.5000	10.500	15.000
	7570.0	44.500	56.200	84.000

Table I.i.1: Gamma Ray counts and flow velocities calculated for TDT log of fault zone, Pass 1 (Figure I.i.11), and station measurements made subsequently in A-10ST well.

A-10ST WATER FLOW

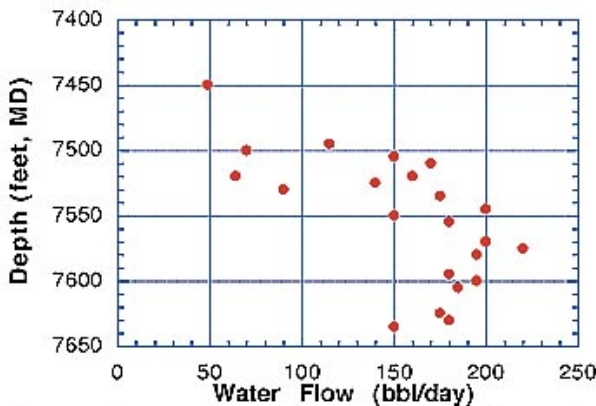
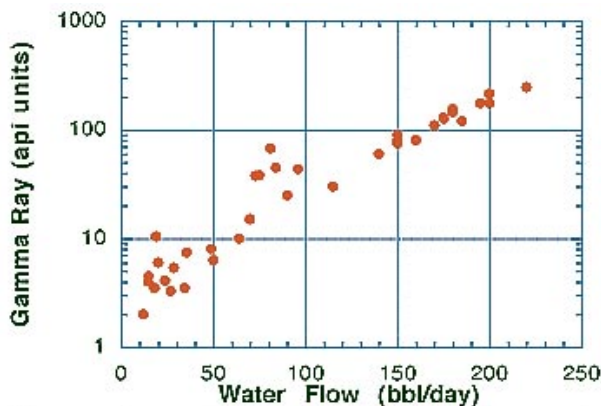
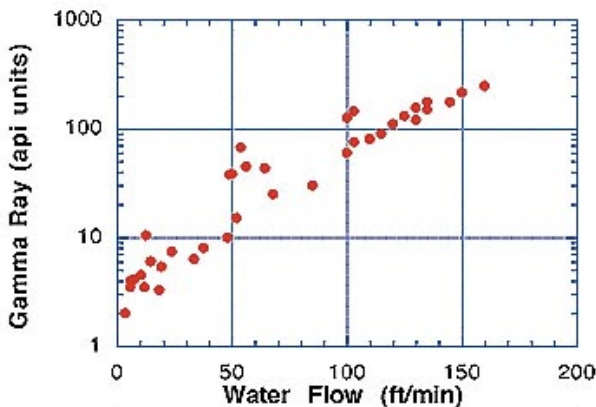


Figure I.i.13: Flow rates versus depth and gamma ray counts from TDT logs of fault zone in A-10ST.

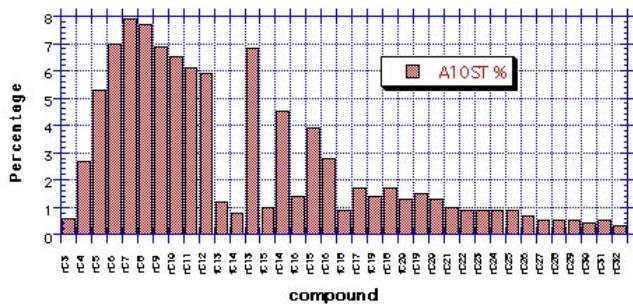
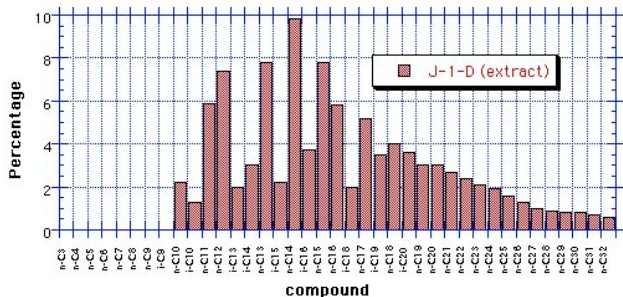
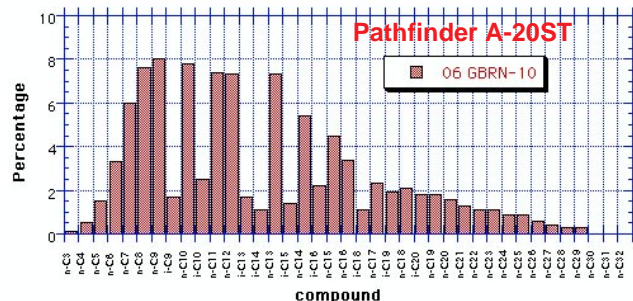
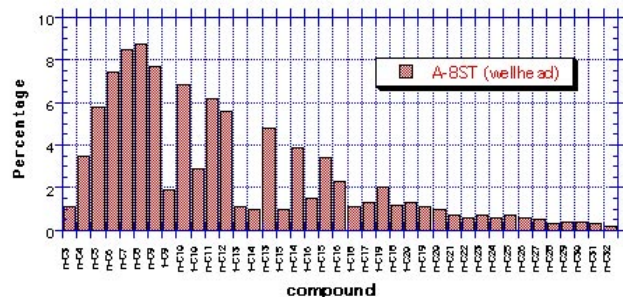
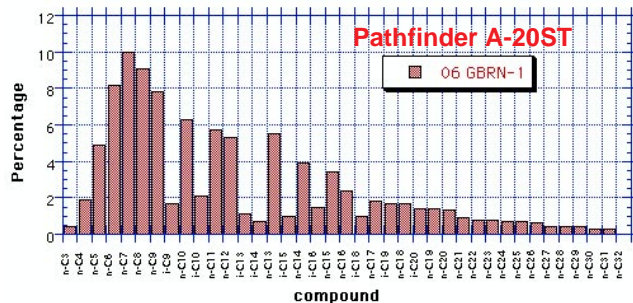
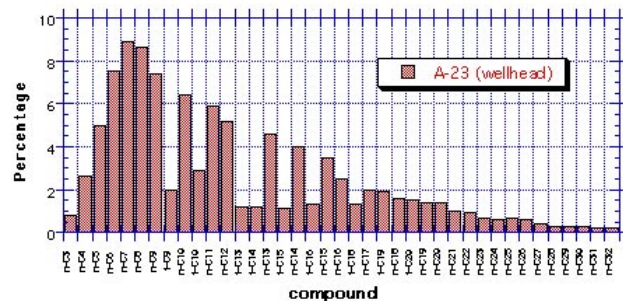


Figure I.i.14 :Whole oil chromatograms of oils sampled in 1993 from Eugene Island block 330 wells.

delta 13 C Methane (0/00)

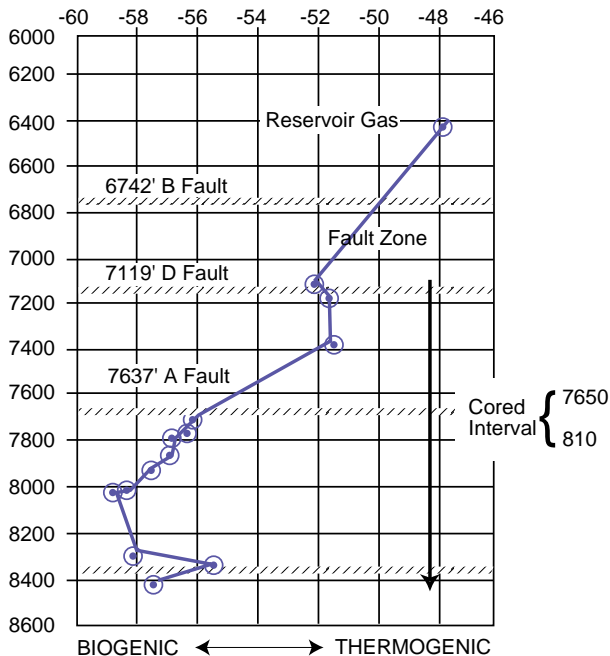


Figure I.i.15: del C17 analyses of gases collected from drilling muds from A-20ST well.

SEISMIC AMPLITUDE AS FUNCTION OF DIFFERENTIAL PRESSURE

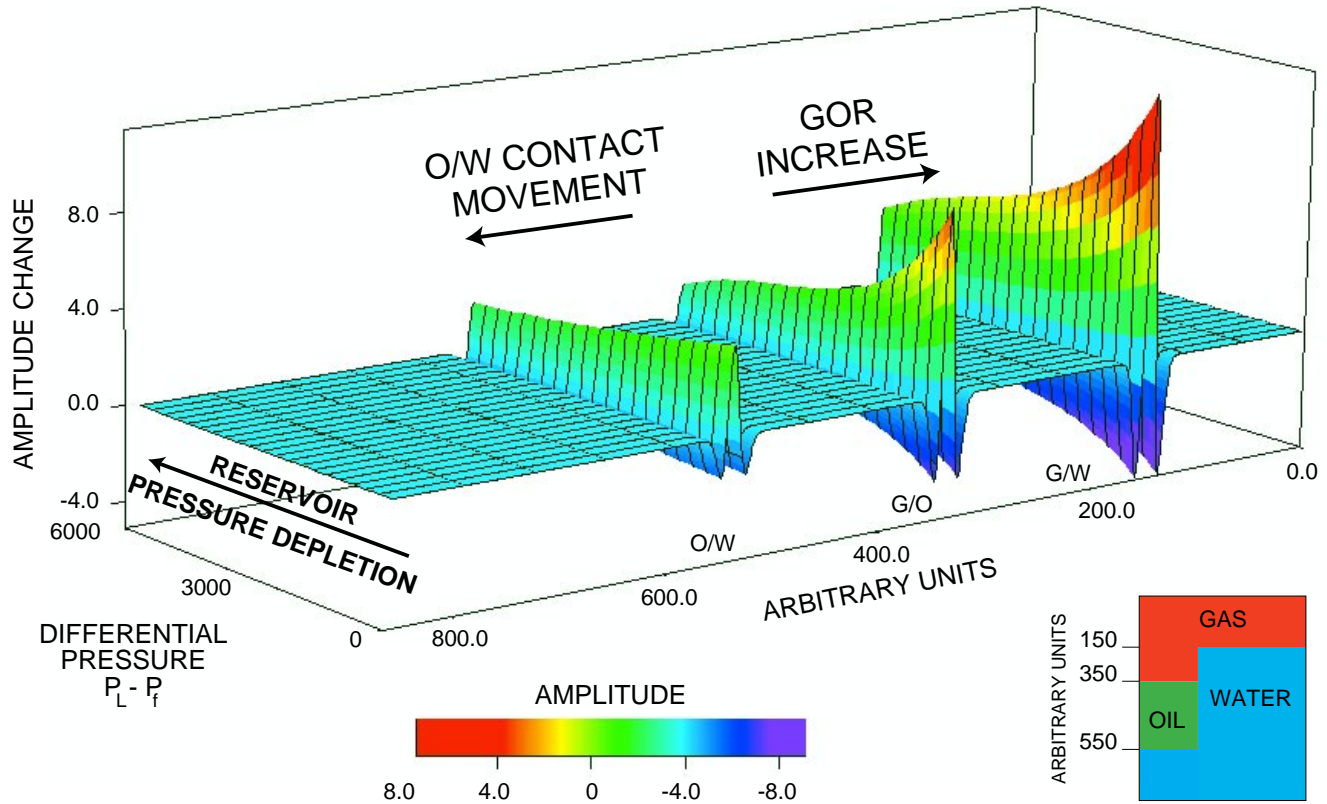


Figure 1.ii.4: Modeling study of the effects on seismic amplitude of changes in pore pressure (P_f) relative to lithostatic pressure (P_L), oil/water, gas/oil and gas/water boundary movements. Gas/oil ratio increases cause amplitudes to increase, whereas oil/water movement causes amplitudes to dim out. Production-related drops in pore pressure cause both to decrease.

4D ADIP Seismic Analysis Steps

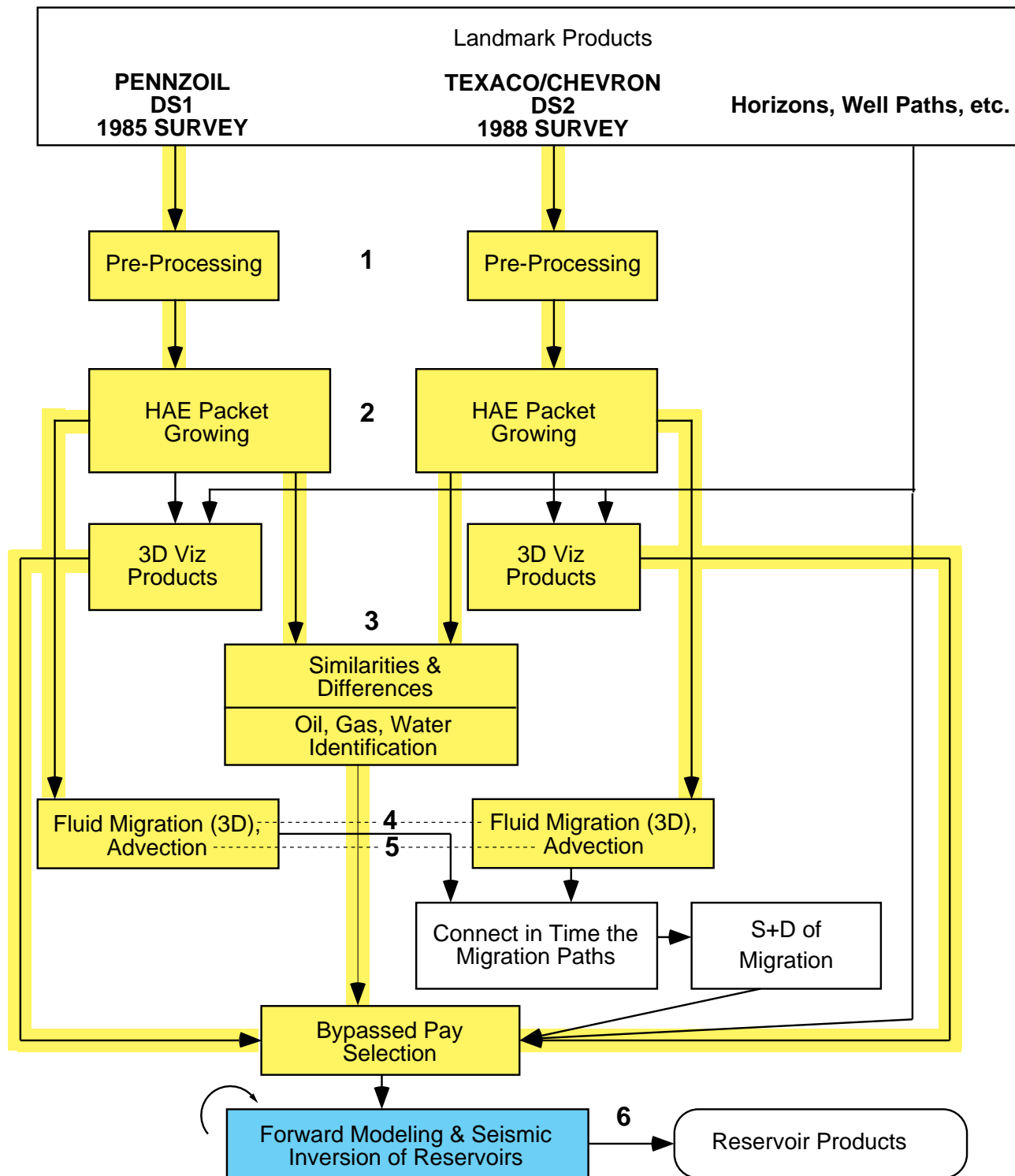


Table I.ii.1: Modules for 4-D seismic interpretation technique. Yellow boxes are operational; blue boxes are under development. (Click on any number above to go to detailed text on that subject).

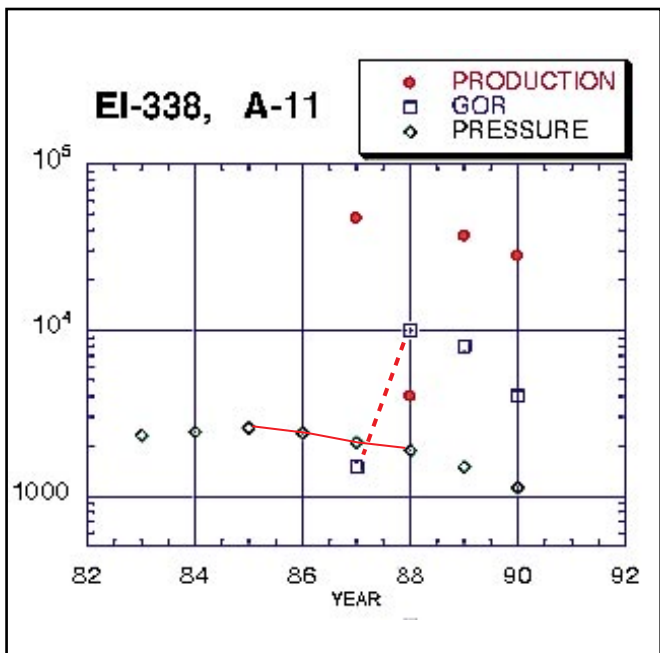


Figure I.ii.5: Production history of the A-11 well into the western fault block of the LF sand from 1982 until 1990.

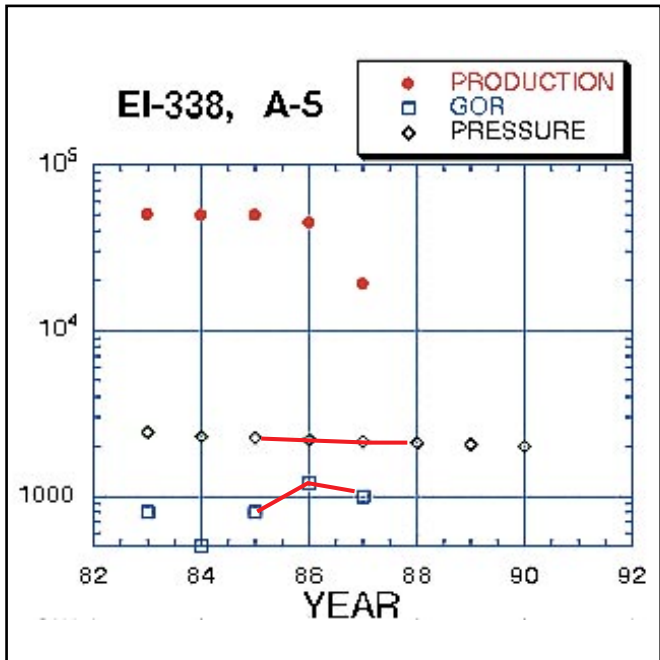


Figure I.ii.6: Production history of the A-5 well into the eastern block of the LF sand from 1982 until the well sanding out in 1988.

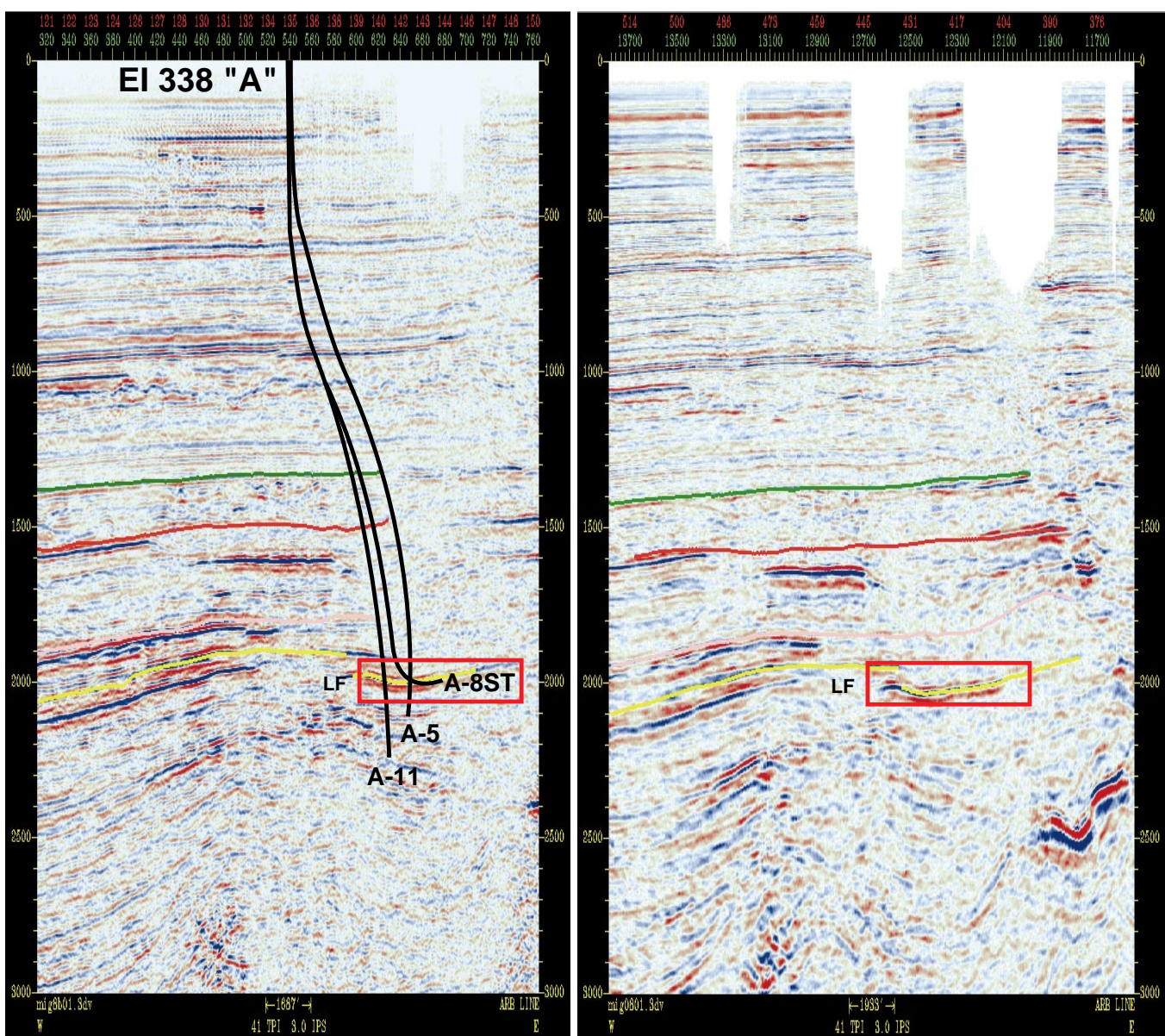


Figure I.ii.7: Seismic reflection profiles along the EI 330/338 boundary from 1988 survey (left) and 1985 survey (right), with A-8ST, A-5 and A-11 wells into the LF indicated. Note that horizontal scales are not quite the same.

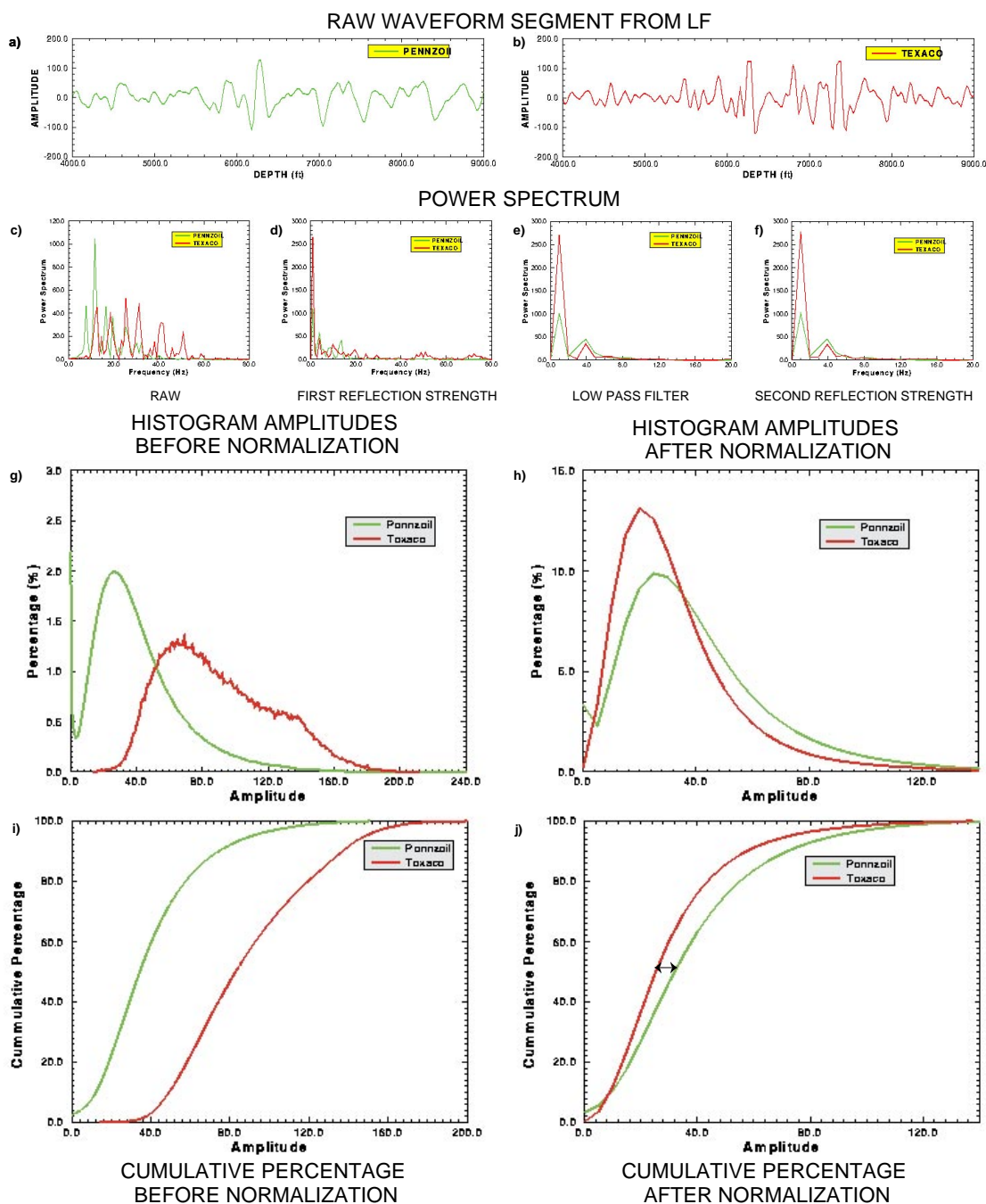


Figure I.ii.8: The first two graphs, a,b, are segments of two traces associated with LF from the Pennzoil and Texaco surveys, respectively. Note the differences in frequency content. The next graph, c, superposes the power spectra from Pennzoil and Texaco. Again, note the higher-frequency content in Texaco. The next graph, d, is the power spectra of the first-reflection strength (instantaneous amplitude) for the two datasets. Again, there is considerable difference in frequency content. The next graph, e, illustrates the use of a low-pass filter implemented via a 100ms moving window average. The frequencies are very much the same. The last graph, f, of power spectra illustrates the use of second-reflection strength after low-pass filtering. Note the similarity in frequency content. Histograms of the amplitude values of each voxel within the Pennzoil (1985) and Texaco (1988) surveys before and after normalization, g and h. Cumulative percentages of each before and after normalization, i and j, are also shown.

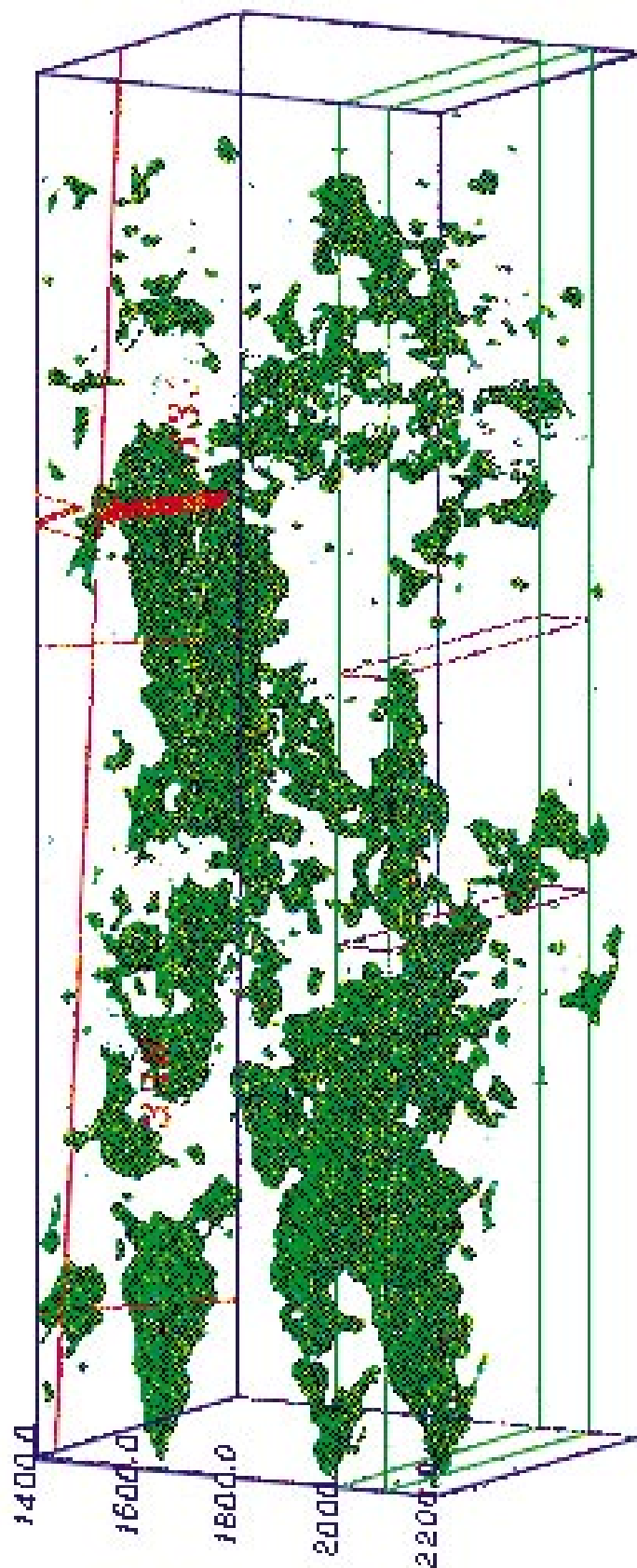


Figure I.ii.9.a: Amplitude envelopes around high seismic amplitudes from 1.4 to 2.2 seconds of travel time for the Pennzoil (1985) survey shown in green. The small box indicates the LF sand, blown up in *Figure I.ii.12*.

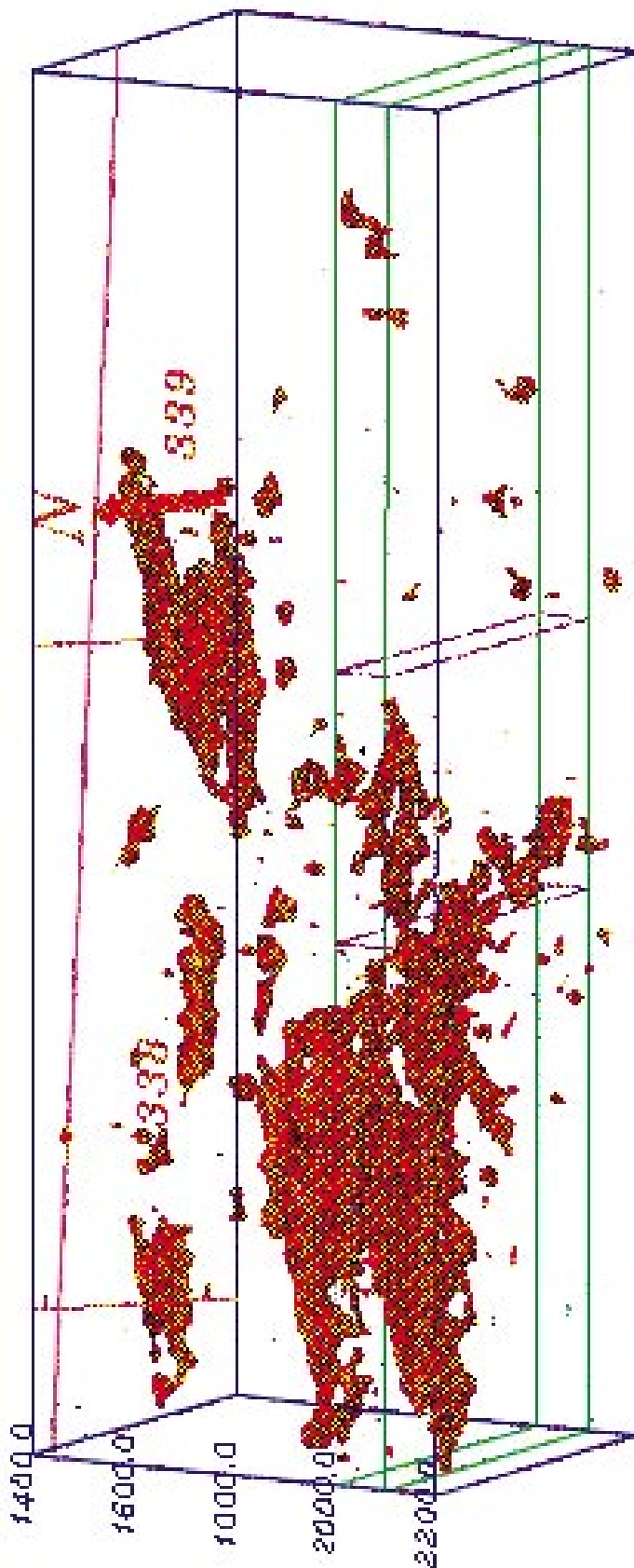


Figure I.ii.9.b: Amplitude envelopes around high seismic amplitudes from 1.4 to 2.2 seconds of travel time for the Texaco (1988) survey shown in red. The small box indicates the LF sand, blown up in *Figure I.ii.12*.

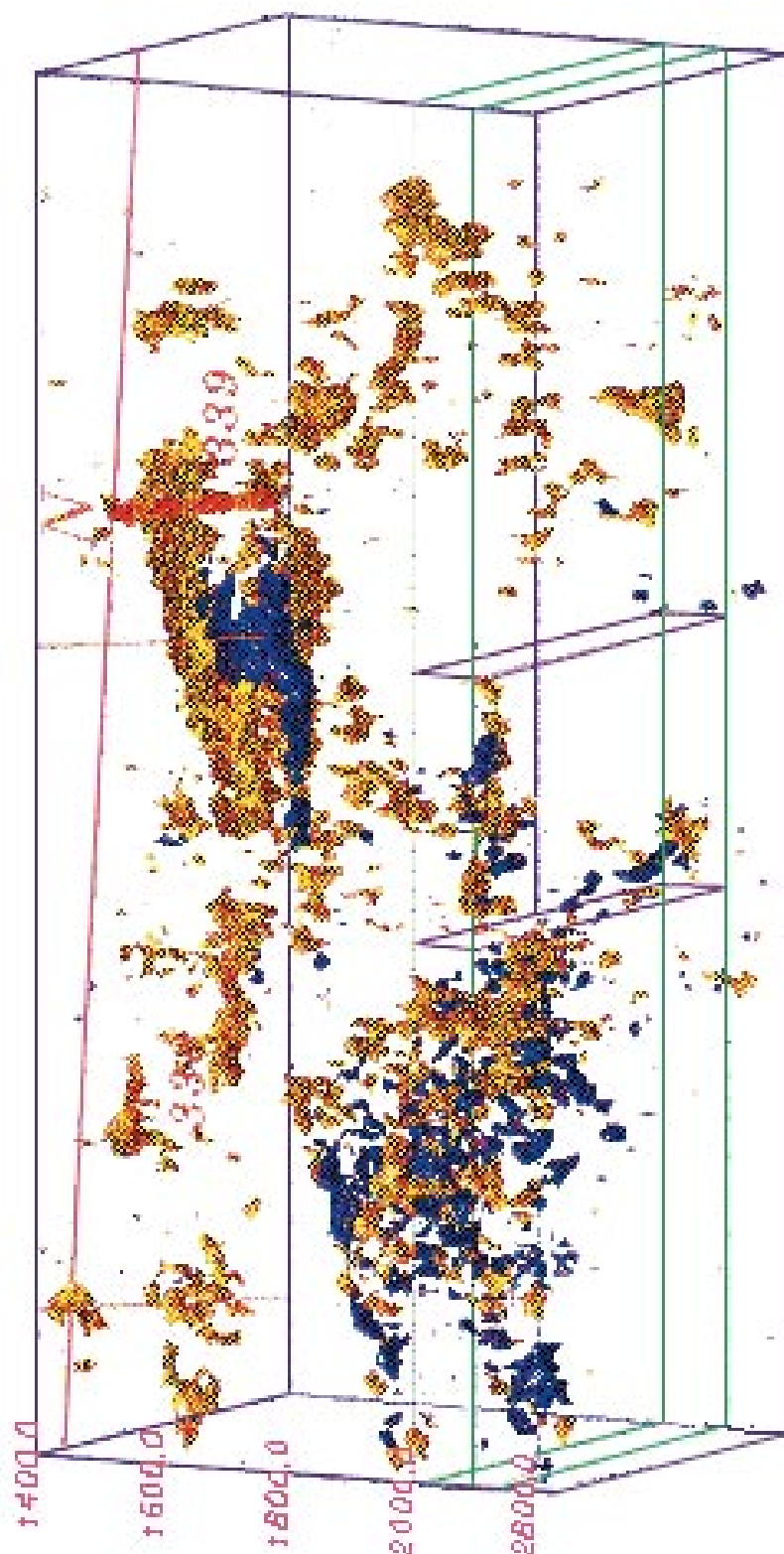


Figure I.ii.10: The differences in seismic amplitudes within the high-amplitude surfaces between *Figures 1.ii.9* and *1.ii.10*, with dimouts from 1985 to 1988 indicated in blue and amplitude increases shown in gold. The small box indicates the LF sand, blown up in *Figure 1.ii.12*.

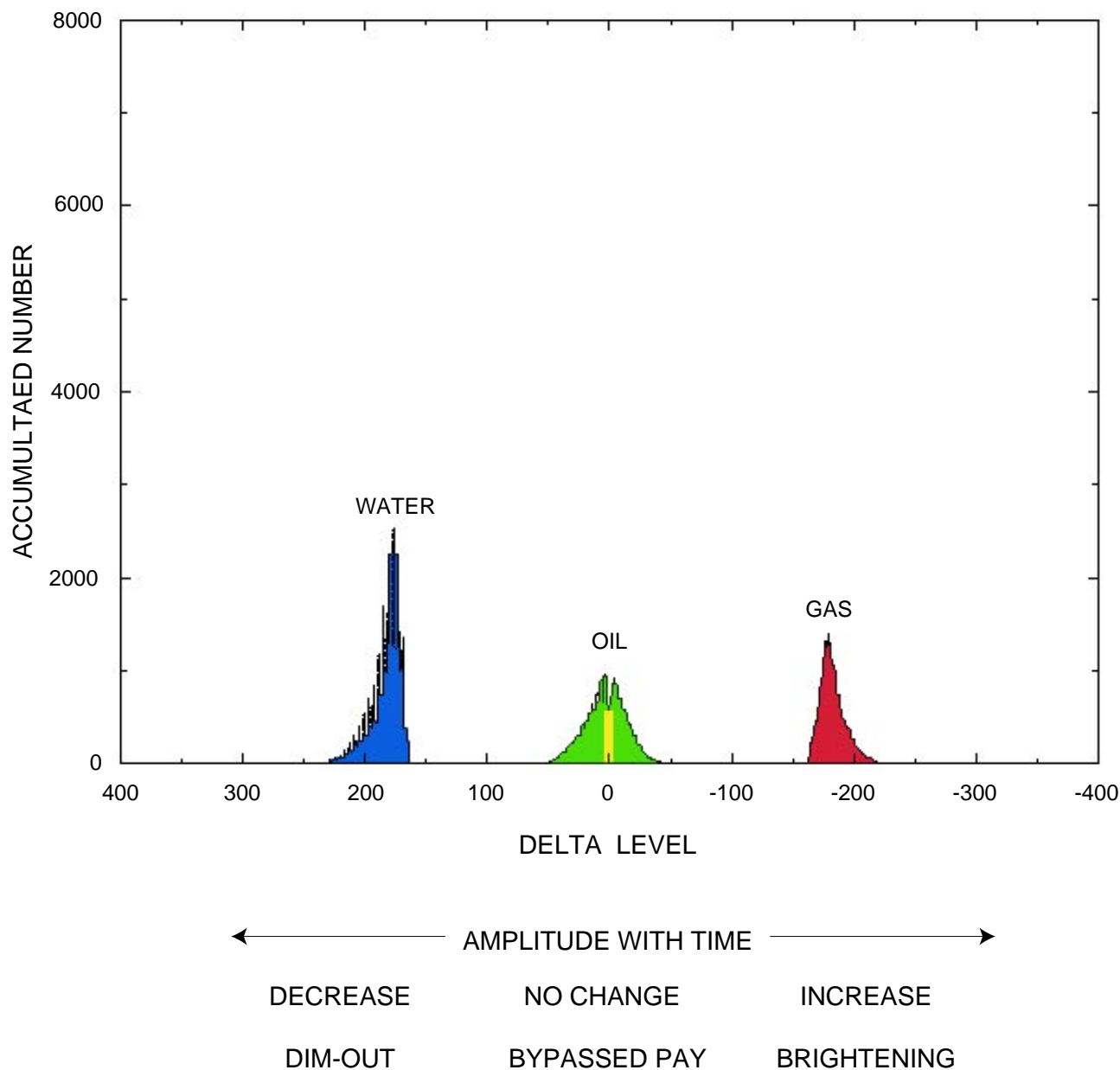


Figure I.ii.11: Histogram of reflection strength difference (1985 Pennzoil - 1988 Texaco). Color coded for use in Figure I.ii.12. These observations are consistent with model prediction in Figure I.ii.4.

Figure I.ii.12: Print onto transparency plastic each of the 11 time slices through the LF reservoir contained in this figure. Then tape onto transparency mounts, space with three blank mounts between each and assemble into 3-D physical model of the seismic changes within the LF sand caused by drainage from production from 1985 to 1988. Green is bypassed pay indicated by no change in high amplitudes, with yellow the most prospective, whereas the blue is waterfront advance that produced a dimout from production and the migration updip from the northeast of the oil/water contact. Red is amplitude increase caused by gas/oil ratio increase with production.

$t = 1980 \text{ ms}$

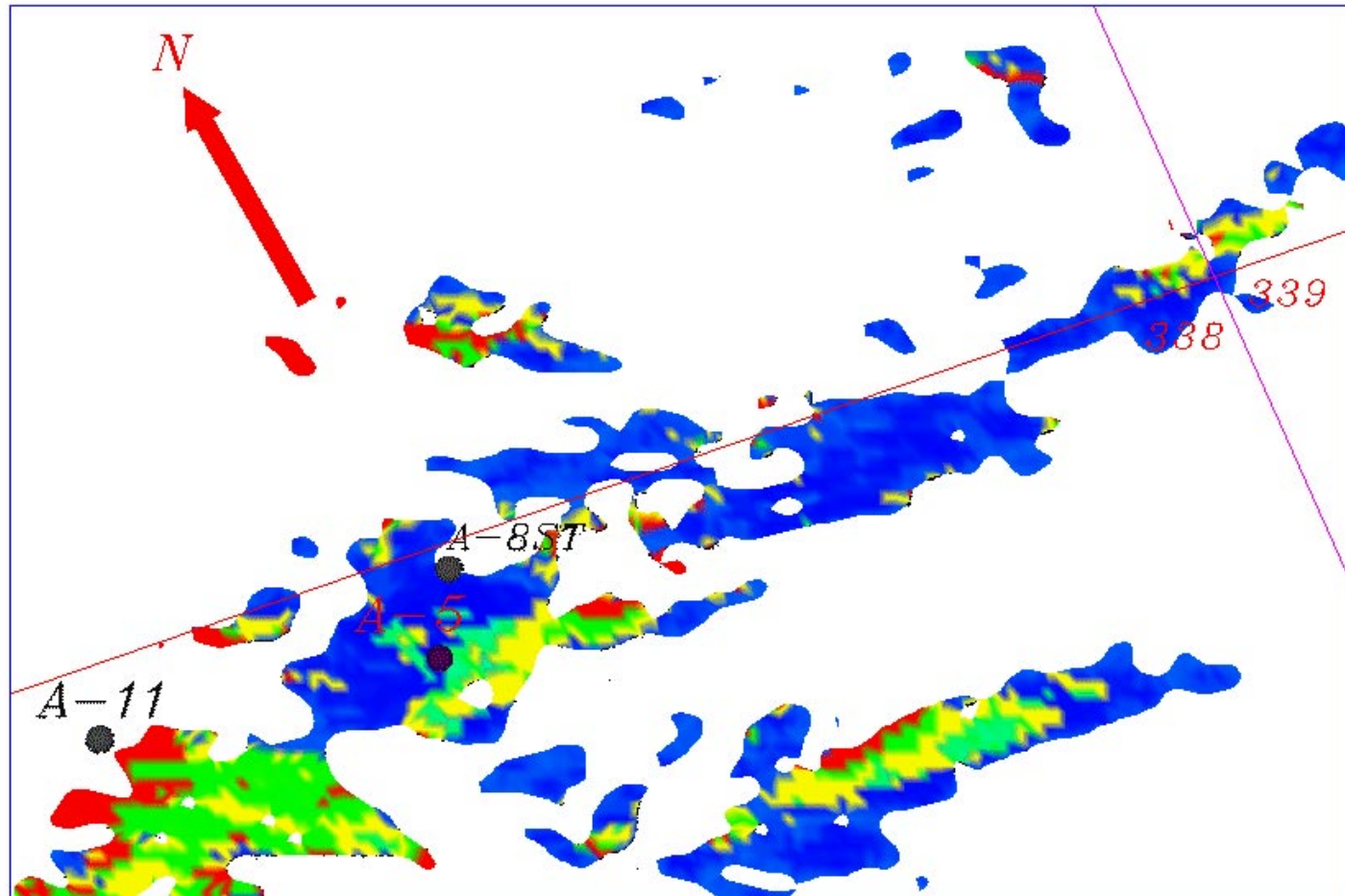


Figure I.ii.12 (continued): Print onto transparency plastic each of the 11 time slices through the LF reservoir contained in this figure. Then tape onto transparency mounts, space with three blank mounts between each and assemble into 3-D physical model of the seismic changes within the LF sand caused by drainage from production from 1985 to 1988. Green is bypassed pay indicated by no change in high amplitudes, with yellow the most prospective, whereas the blue is waterfront advance that produced a dimout from production and the migration updip from the northeast of the oil/water contact. Red is amplitude increase caused by gas/oil ratio increase with production.

$t = 1988 \text{ ms}$

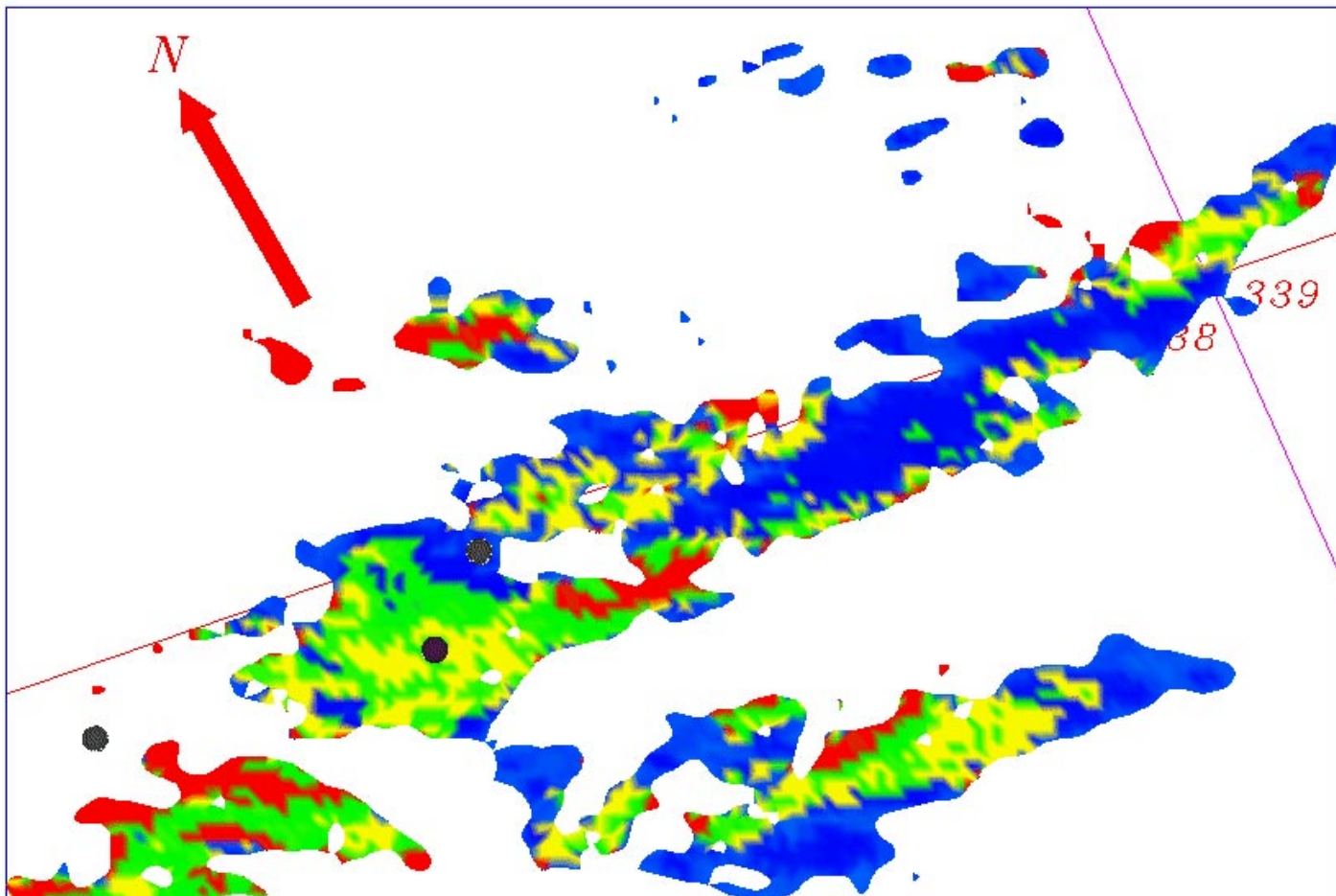


Figure I.ii.12 (continued): Print onto transparency plastic each of the 11 time slices through the LF reservoir contained in this figure. Then tape onto transparency mounts, space with three blank mounts between each and assemble into 3-D physical model of the seismic changes within the LF sand caused by drainage from production from 1985 to 1988. Green is bypassed pay indicated by no change in high amplitudes, with yellow the most prospective, whereas the blue is waterfront advance that produced a dimout from production and the migration updip from the northeast of the oil/water contact. Red is amplitude increase caused by gas/oil ratio increase with production.

$t = 1996 \text{ ms}$

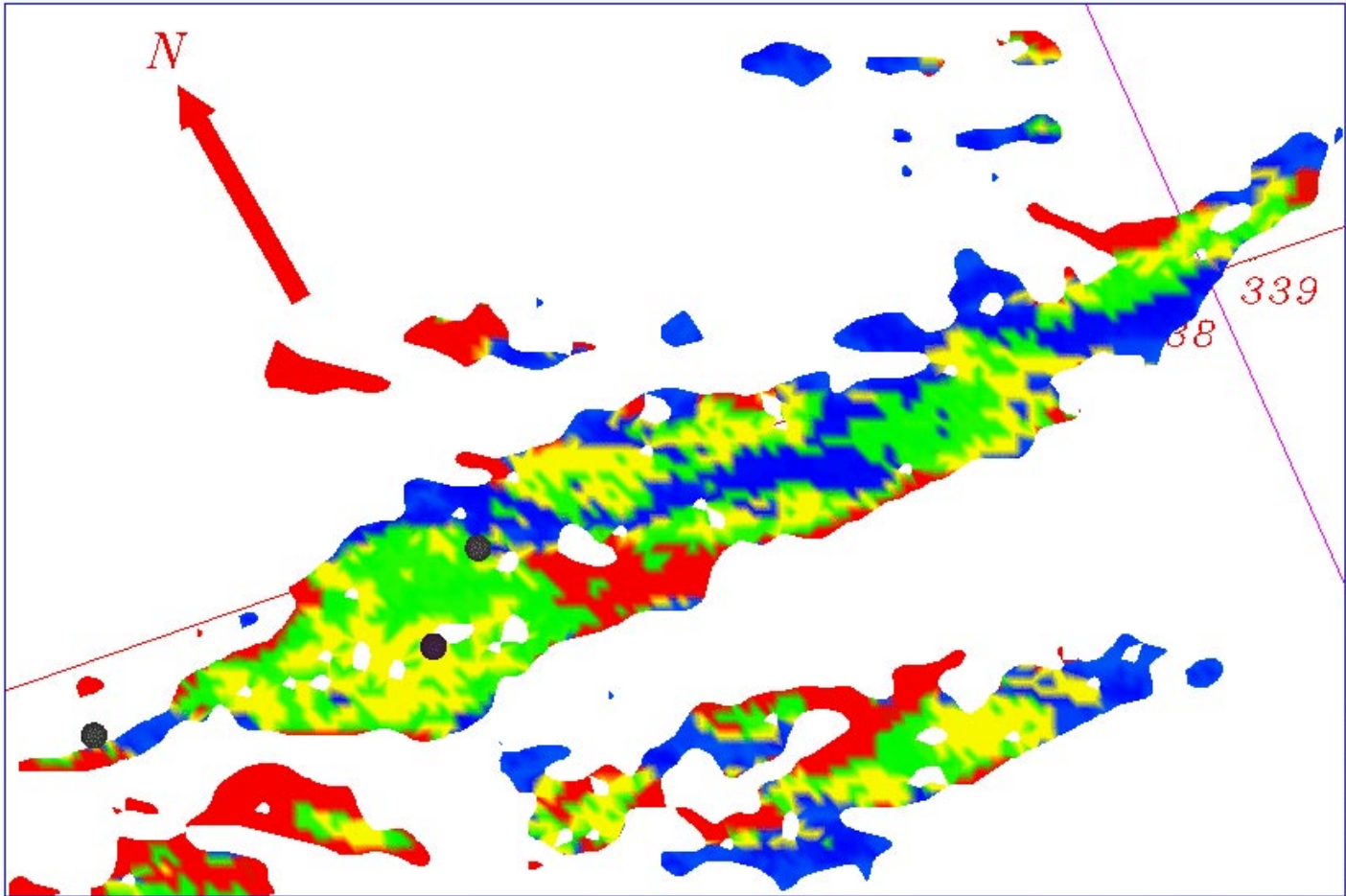


Figure I.ii.12 (continued): Print onto transparency plastic each of the 11 time slices through the LF reservoir contained in this figure. Then tape onto transparency mounts, space with three blank mounts between each and assemble into 3-D physical model of the seismic changes within the LF sand caused by drainage from production from 1985 to 1988. Green is bypassed pay indicated by no change in high amplitudes, with yellow the most prospective, whereas the blue is waterfront advance that produced a dimout from production and the migration updip from the northeast of the oil/water contact. Red is amplitude increase caused by gas/oil ratio increase with production.

$t = 2004 \text{ ms}$

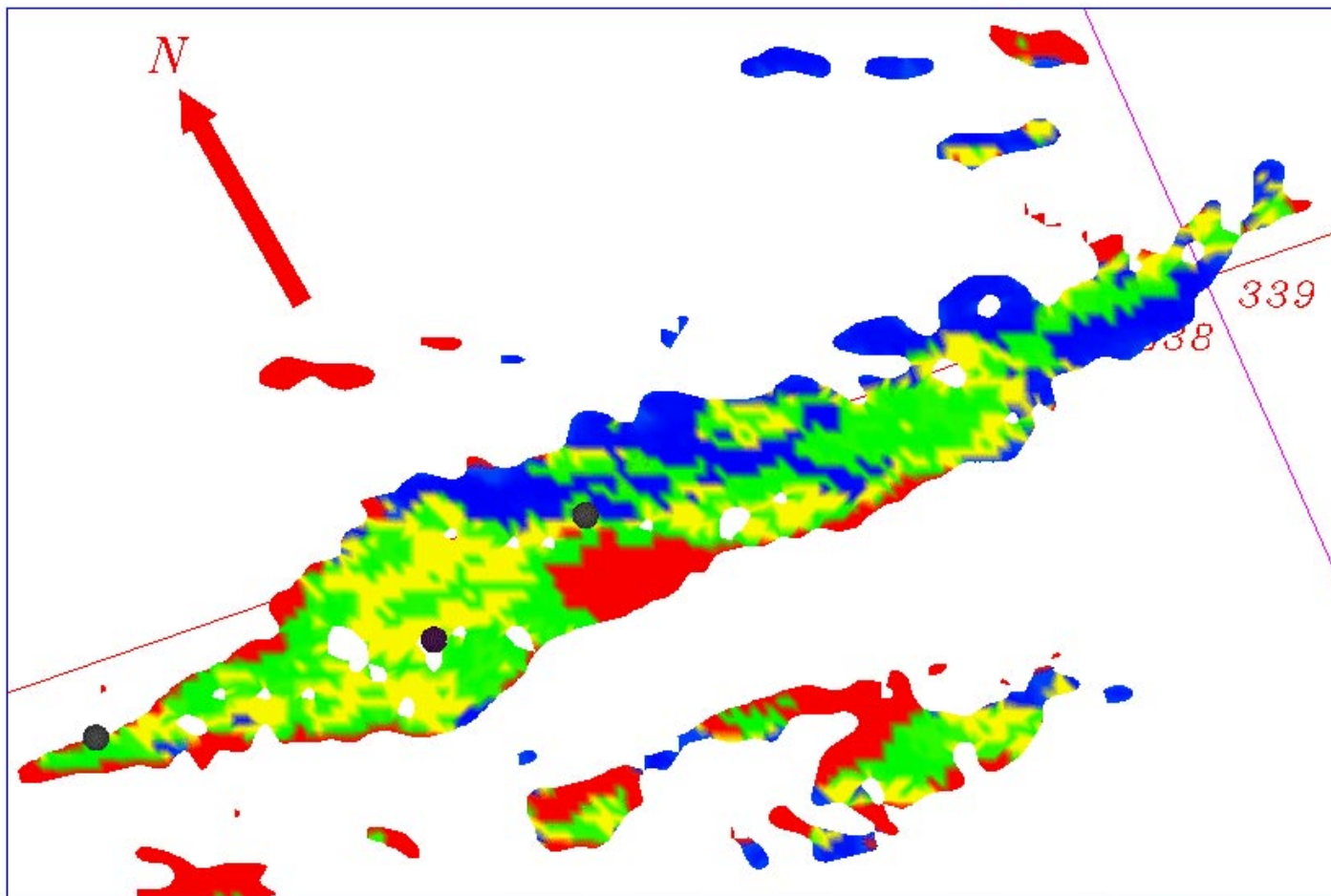


Figure I.ii.12 (continued): Print onto transparency plastic each of the 11 time slices through the LF reservoir contained in this figure. Then tape onto transparency mounts, space with three blank mounts between each and assemble into 3-D physical model of the seismic changes within the LF sand caused by drainage from production from 1985 to 1988. Green is bypassed pay indicated by no change in high amplitudes, with yellow the most prospective, whereas the blue is waterfront advance that produced a dimout from production and the migration updip from the northeast of the oil/water contact. Red is amplitude increase caused by gas/oil ratio increase with production.

$t = 2012 \text{ ms}$

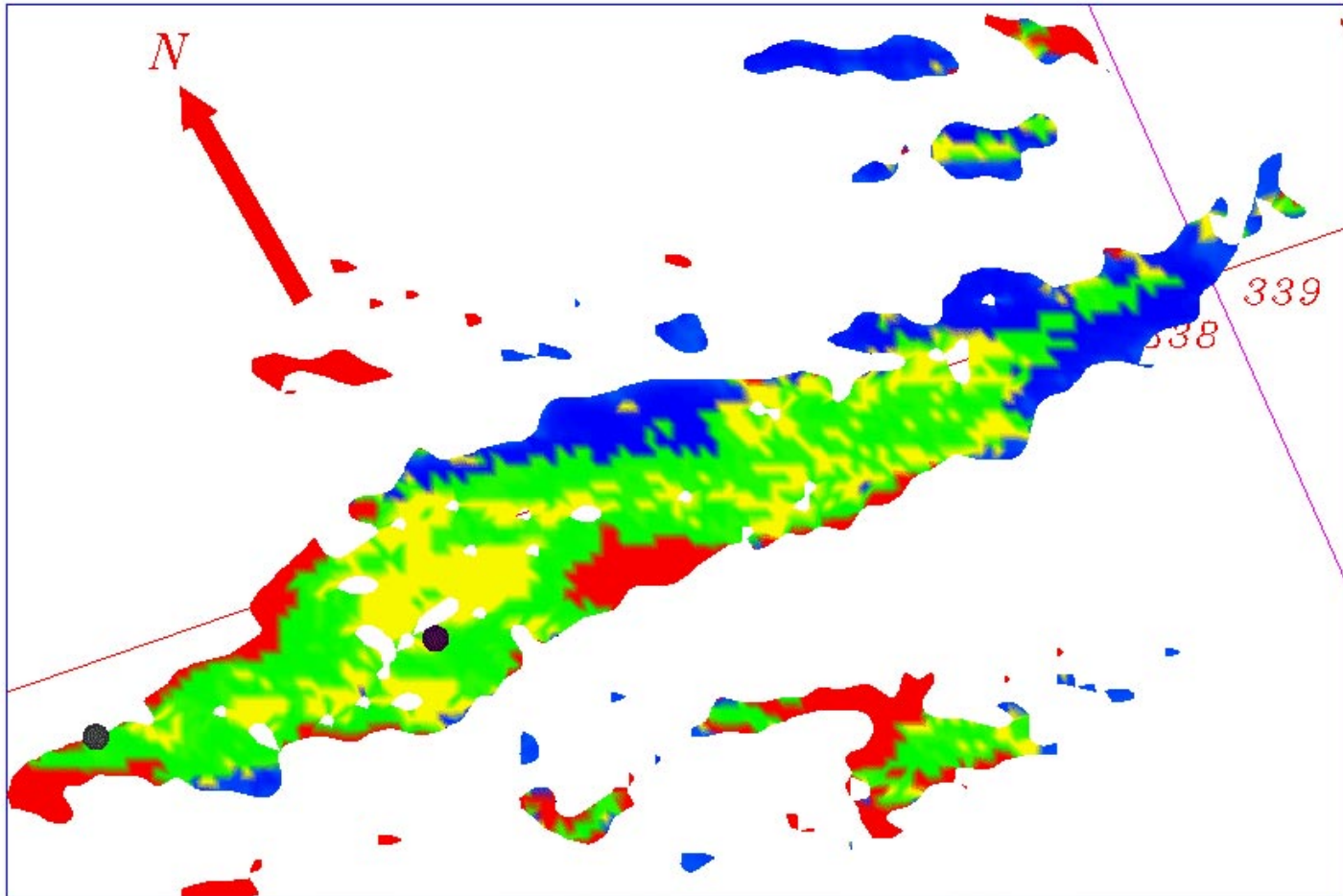


Figure I.ii.12 (continued): Print onto transparency plastic each of the 11 time slices through the LF reservoir contained in this figure. Then tape onto transparency mounts, space with three blank mounts between each and assemble into 3-D physical model of the seismic changes within the LF sand caused by drainage from production from 1985 to 1988. Green is bypassed pay indicated by no change in high amplitudes, with yellow the most prospective, whereas the blue is waterfront advance that produced a dimout from production and the migration updip from the northeast of the oil/water contact. Red is amplitude increase caused by gas/oil ratio increase with production.

$t = 2020 \text{ ms}$

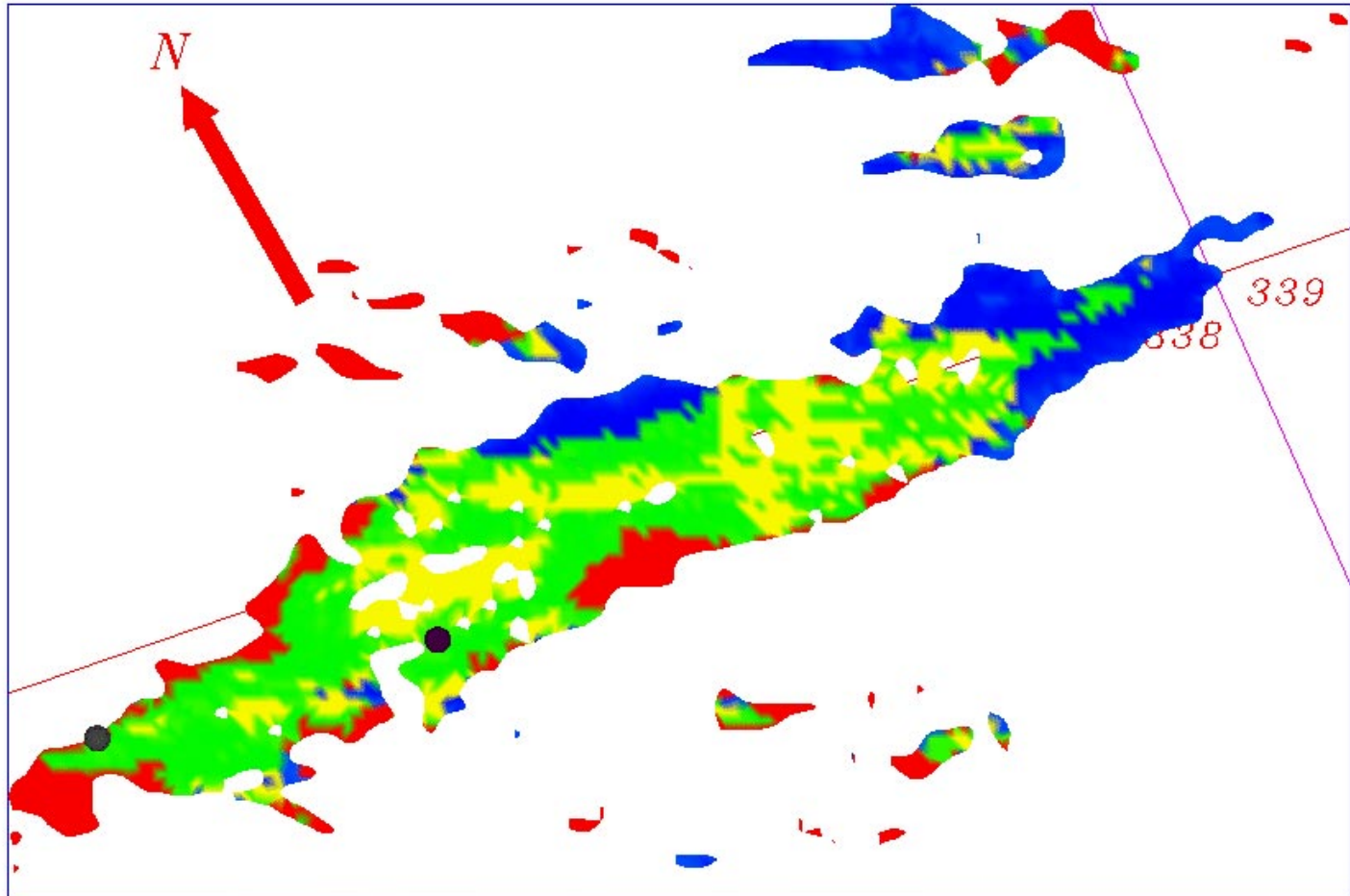


Figure I.ii.12 (continued): Print onto transparency plastic each of the 11 time slices through the LF reservoir contained in this figure. Then tape onto transparency mounts, space with three blank mounts between each and assemble into 3-D physical model of the seismic changes within the LF sand caused by drainage from production from 1985 to 1988. Green is bypassed pay indicated by no change in high amplitudes, with yellow the most prospective, whereas the blue is waterfront advance that produced a dimout from production and the migration updip from the northeast of the oil/water contact. Red is amplitude increase caused by gas/oil ratio increase with production.

$t = 2028 \text{ ms}$

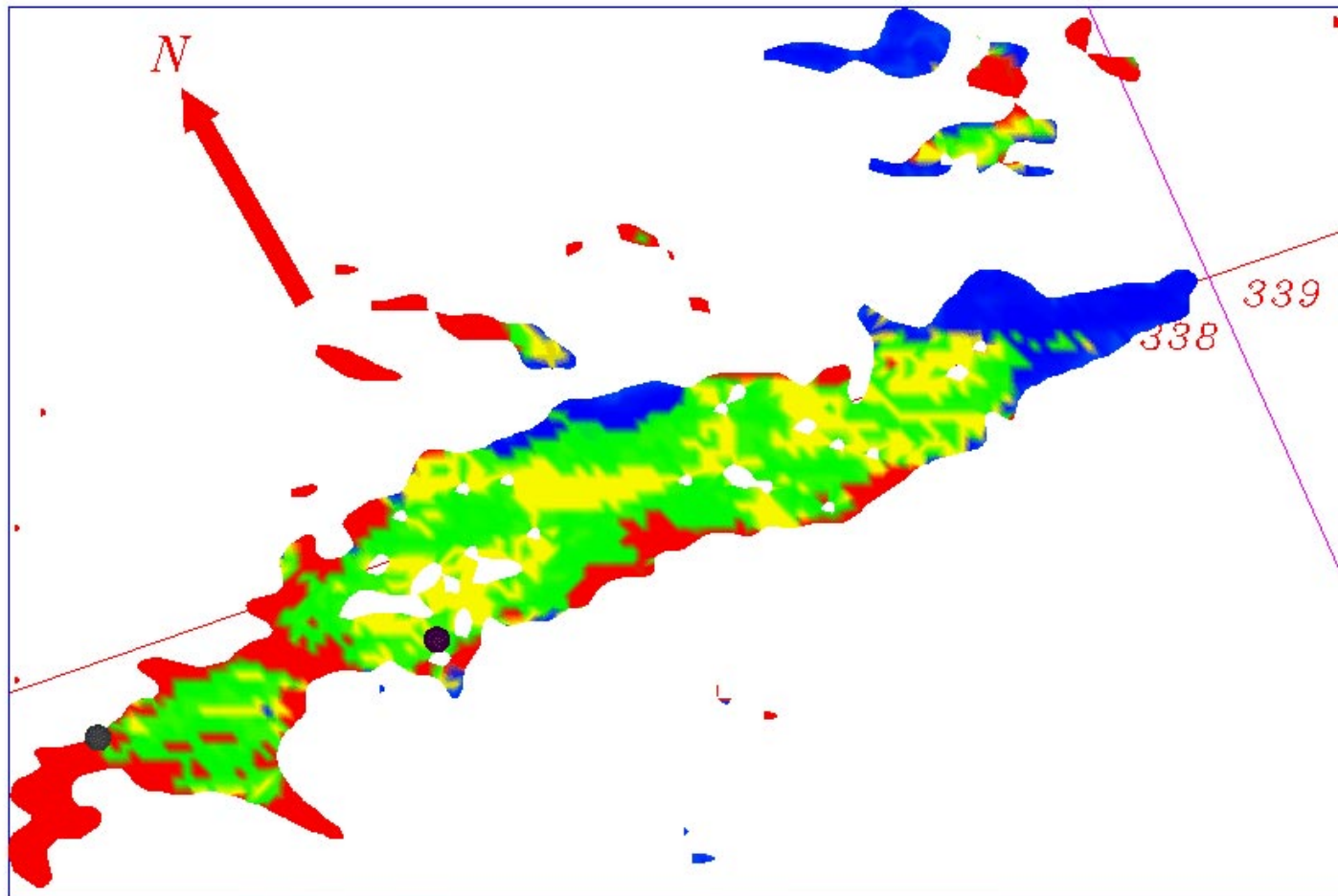


Figure I.ii.12 (continued): Print onto transparency plastic each of the 11 time slices through the LF reservoir contained in this figure. Then tape onto transparency mounts, space with three blank mounts between each and assemble into 3-D physical model of the seismic changes within the LF sand caused by drainage from production from 1985 to 1988. Green is bypassed pay indicated by no change in high amplitudes, with yellow the most prospective, whereas the blue is waterfront advance that produced a dimout from production and the migration updip from the northeast of the oil/water contact. Red is amplitude increase caused by gas/oil ratio increase with production.

$t = 2036 \text{ ms}$

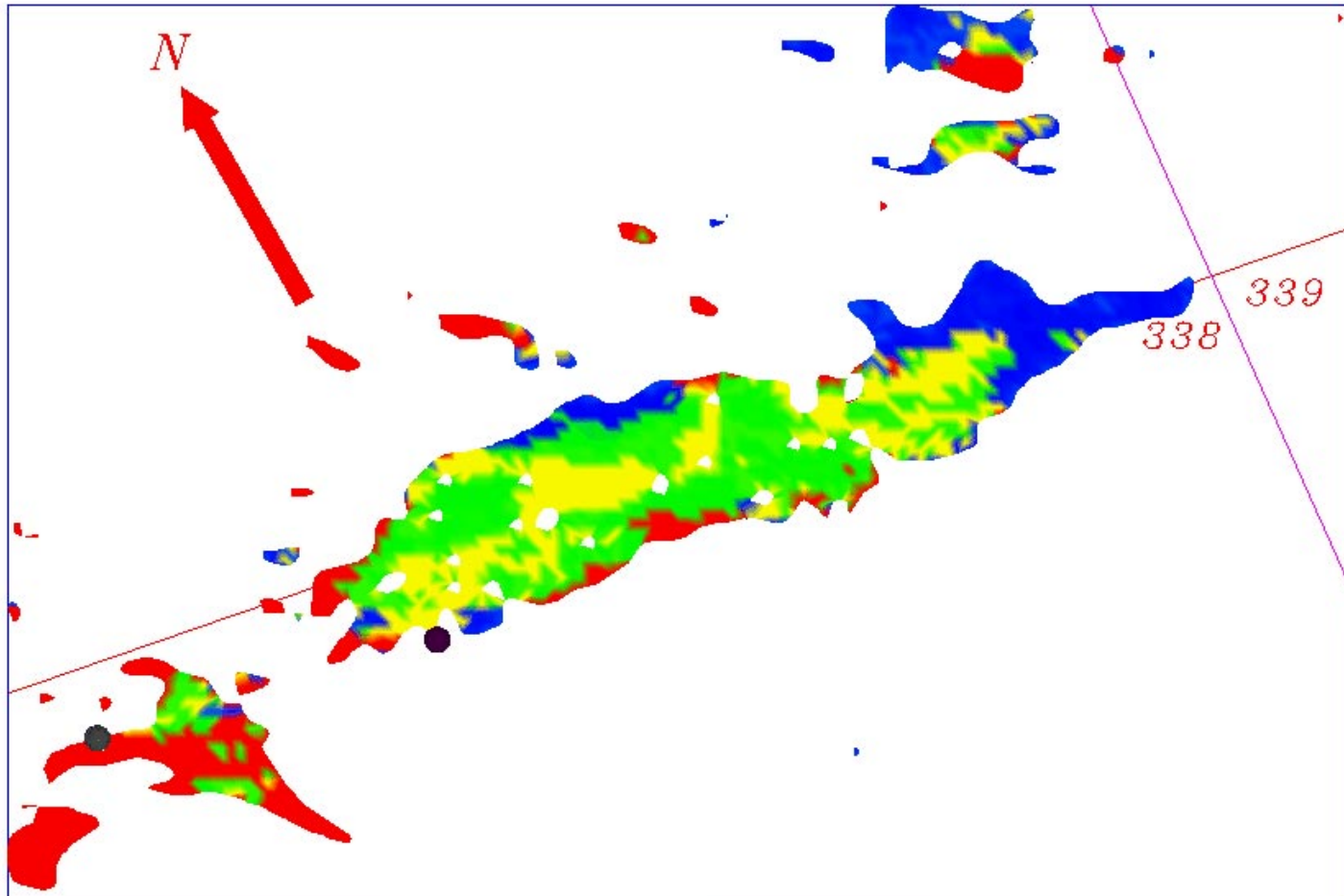


Figure I.ii.12 (continued): Print onto transparency plastic each of the 11 time slices through the LF reservoir contained in this figure. Then tape onto transparency mounts, space with three blank mounts between each and assemble into 3-D physical model of the seismic changes within the LF sand caused by drainage from production from 1985 to 1988. Green is bypassed pay indicated by no change in high amplitudes, with yellow the most prospective, whereas the blue is waterfront advance that produced a dimout from production and the migration updip from the northeast of the oil/water contact. Red is amplitude increase caused by gas/oil ratio increase with production.

$t = 2044 \text{ ms}$

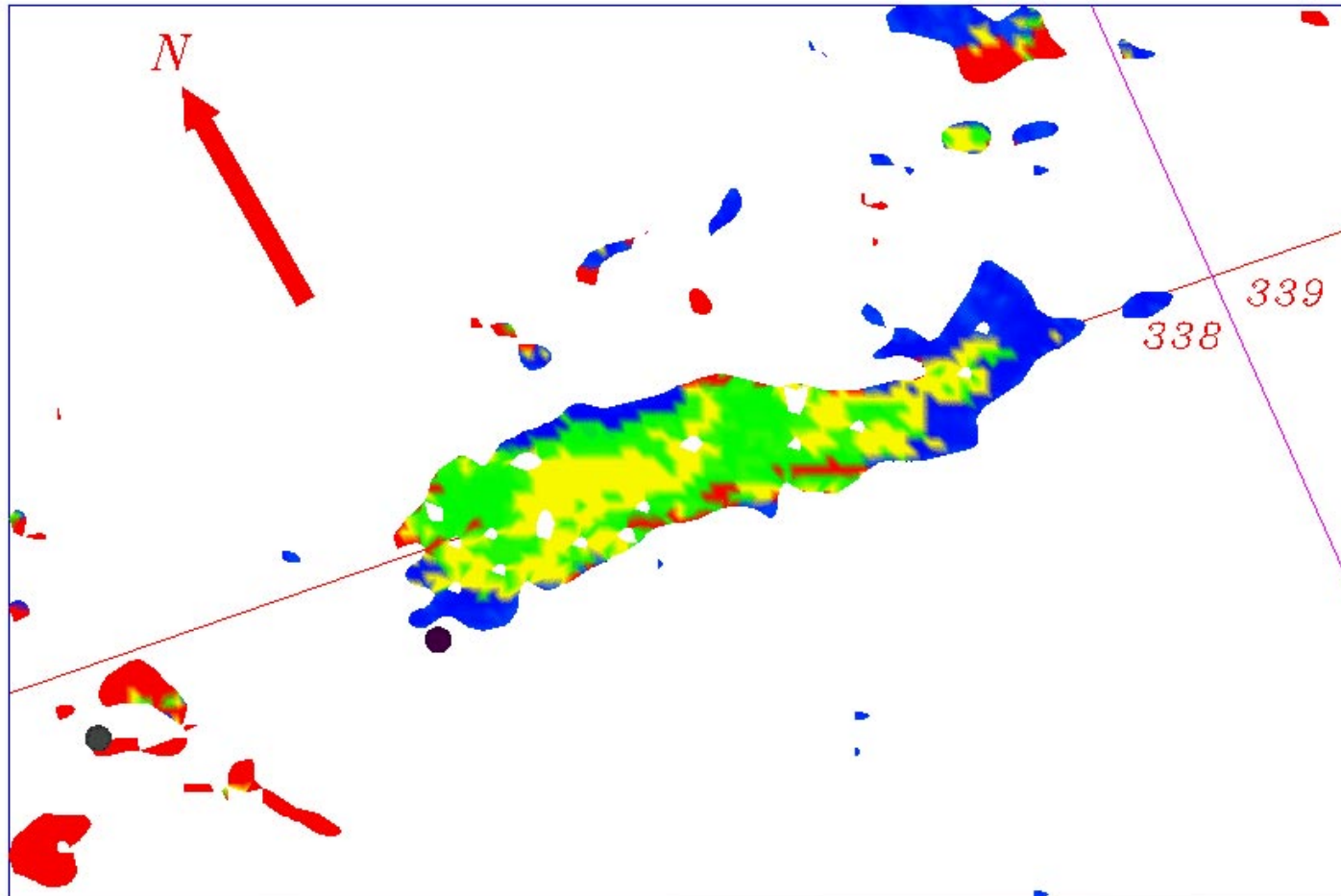


Figure I.ii.12 (continued): Print onto transparency plastic each of the 11 time slices through the LF reservoir contained in this figure. Then tape onto transparency mounts, space with three blank mounts between each and assemble into 3-D physical model of the seismic changes within the LF sand caused by drainage from production from 1985 to 1988. Green is bypassed pay indicated by no change in high amplitudes, with yellow the most prospective, whereas the blue is waterfront advance that produced a dimout from production and the migration updip from the northeast of the oil/water contact. Red is amplitude increase caused by gas/oil ratio increase with production.

$t = 2052 \text{ ms}$

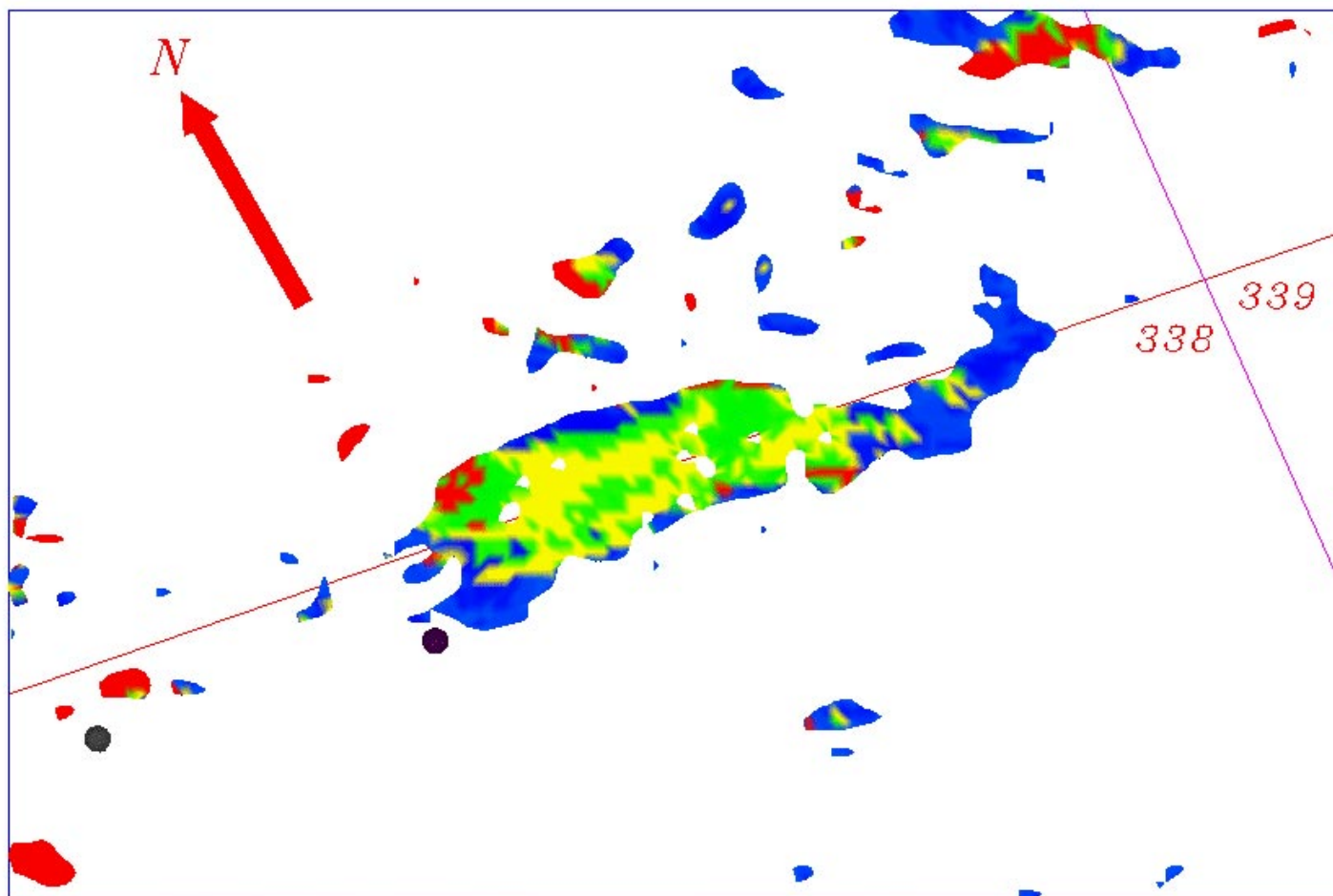
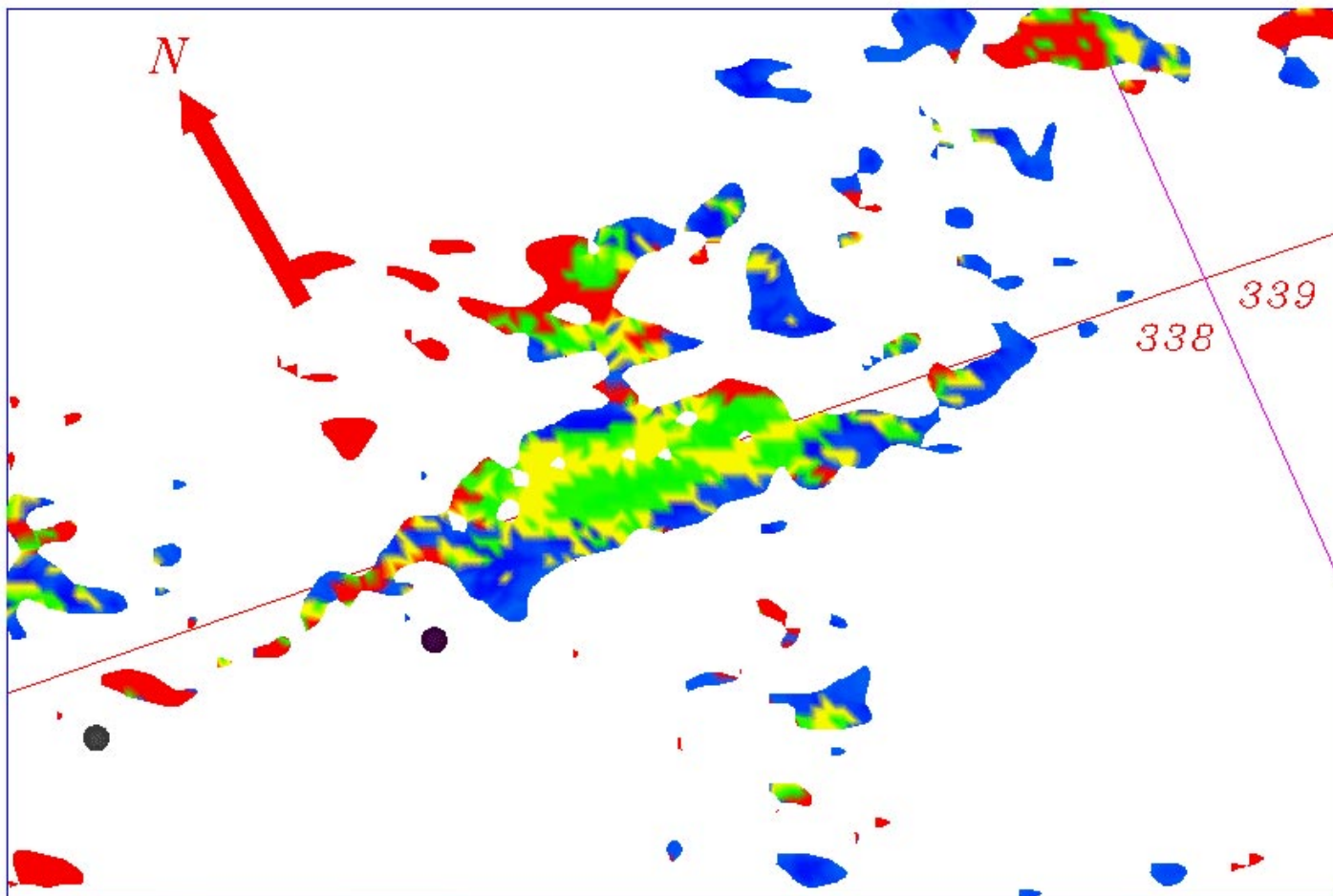


Figure I.ii.12 (continued): Print onto transparency plastic each of the 11 time slices through the LF reservoir contained in this figure. Then tape onto transparency mounts, space with three blank mounts between each and assemble into 3-D physical model of the seismic changes within the LF sand caused by drainage from production from 1985 to 1988. Green is bypassed pay indicated by no change in high amplitudes, with yellow the most prospective, whereas the blue is waterfront advance that produced a dimout from production and the migration updip from the northeast of the oil/water contact. Red is amplitude increase caused by gas/oil ratio increase with production.

$t = 2060 \text{ ms}$



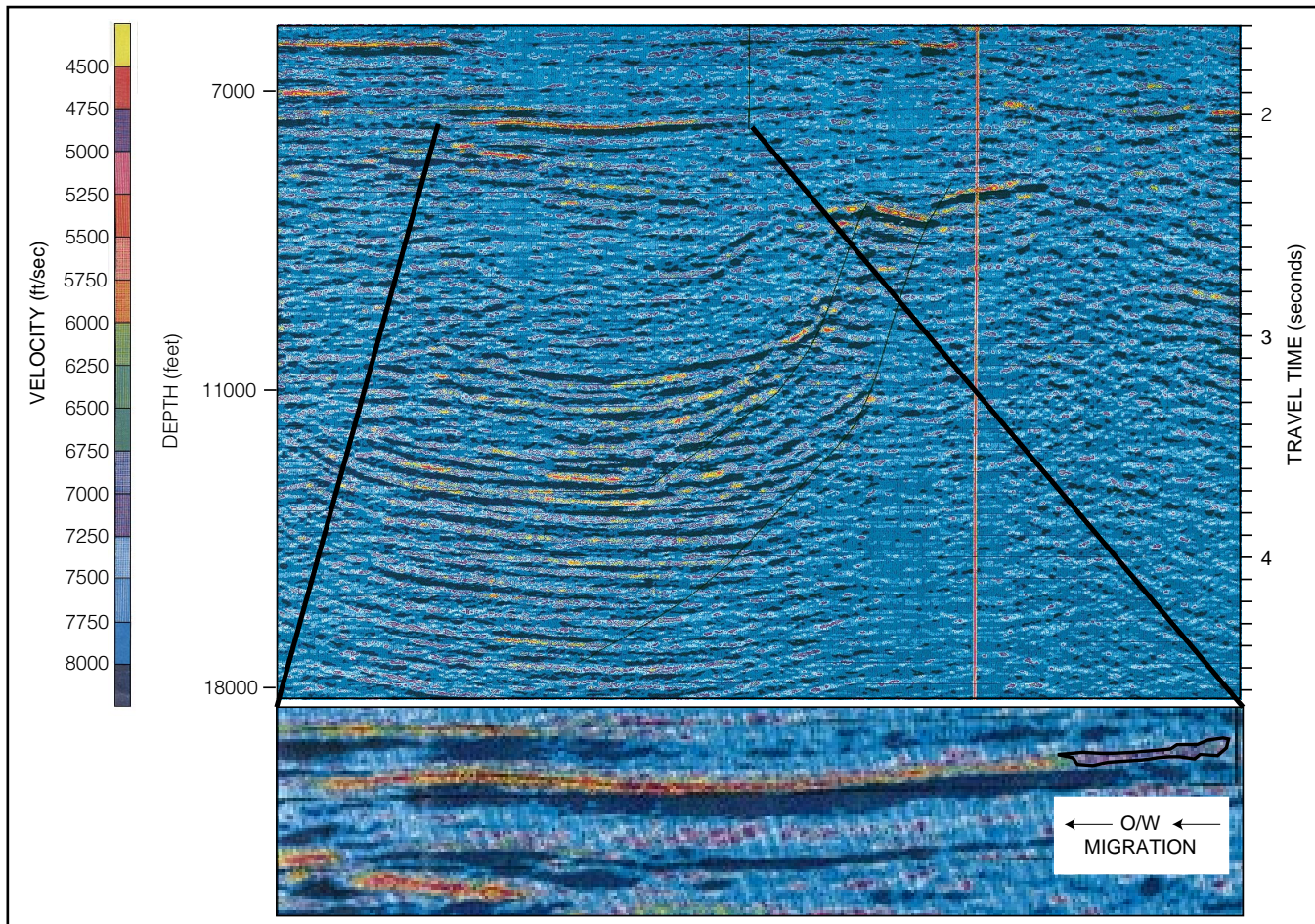


Figure I.ii.13: Seismic velocity inversion performed by Texaco along the seismic profile running along the EI 330/338 boundary, with the LF sand blown up (below). Increases in velocity are recorded in the easternmost part of the reservoir; perhaps from the movement of the oil/water contact as suggested by the 4-D seismic analysis.s.

Figure I.ii.14.a: The amplitudes extracted from a traditional “ZAP” of the trough that makes up the LF reflector from the Pennzoil (1985) survey (the yellow horizon in Figure I.ii.7, right). Hot colors are high amplitudes.

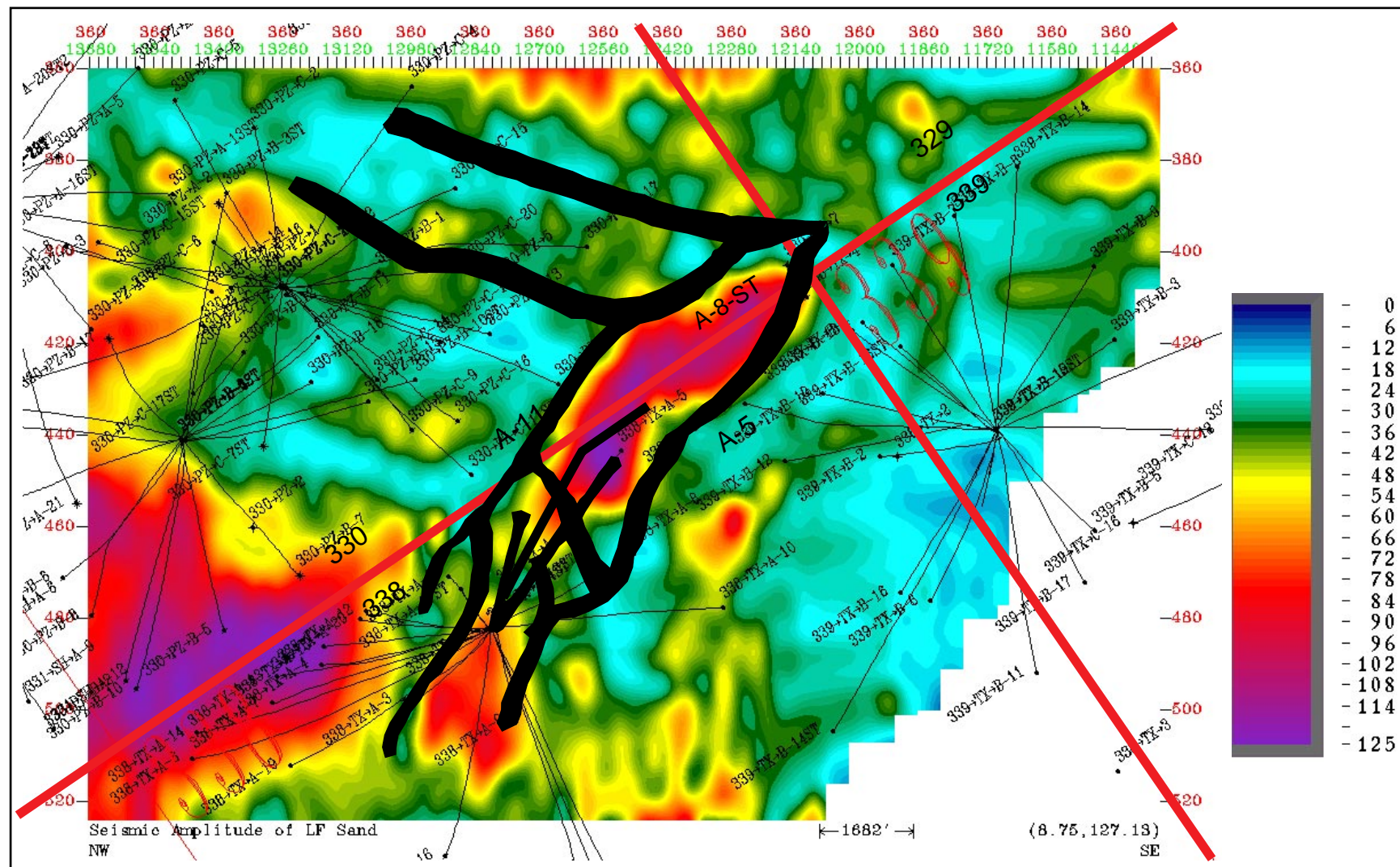


Figure I.ii.14.b: The amplitude extracted from a traditional “ZAP” of the trough that makes up the LF reflector from the Texaco (1988) survey (the yellow horizon in Figure I.ii.7, left). Note the dimout in the northeastern corner, thought to be caused by the oil/water contact movement.

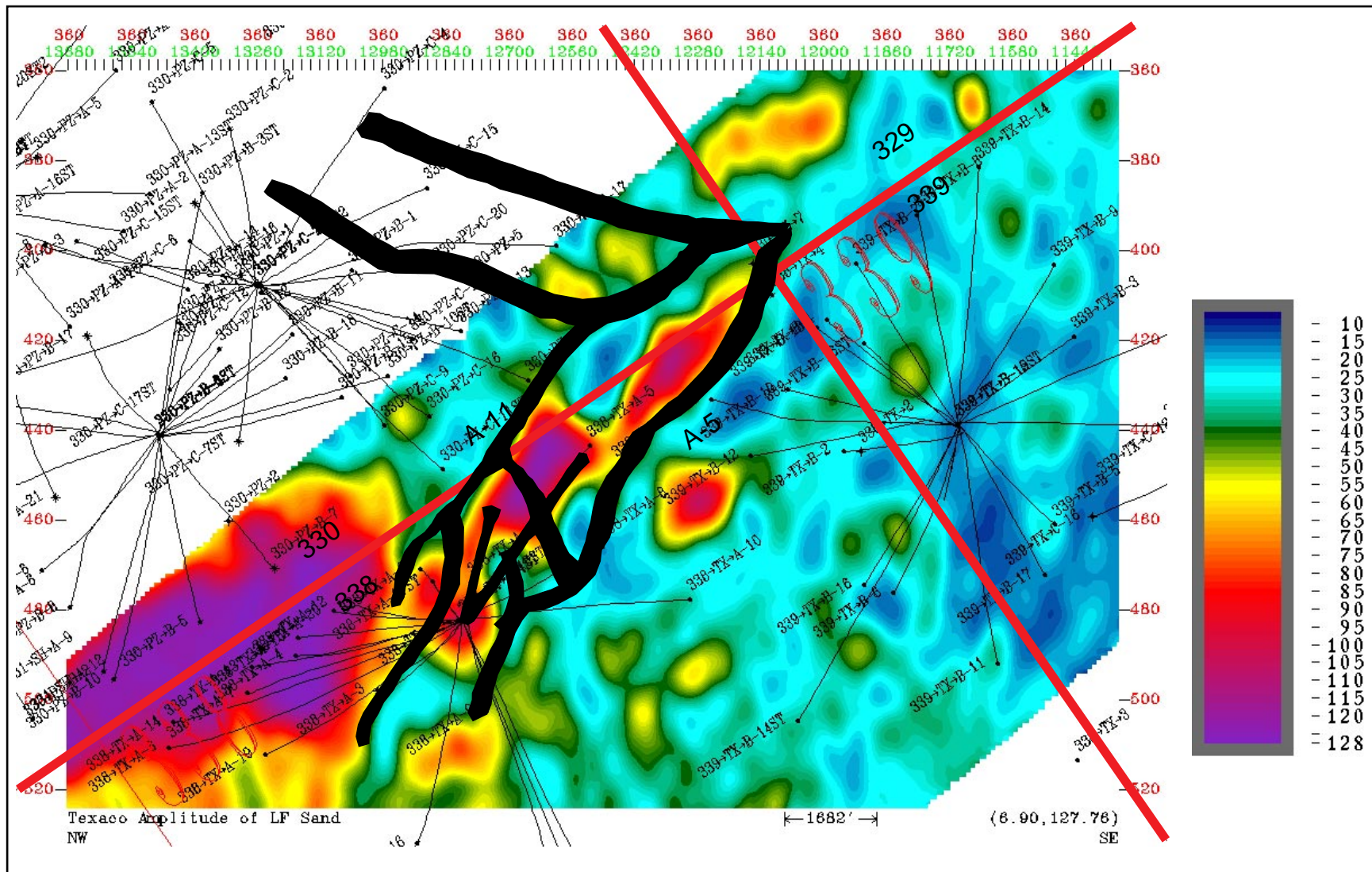
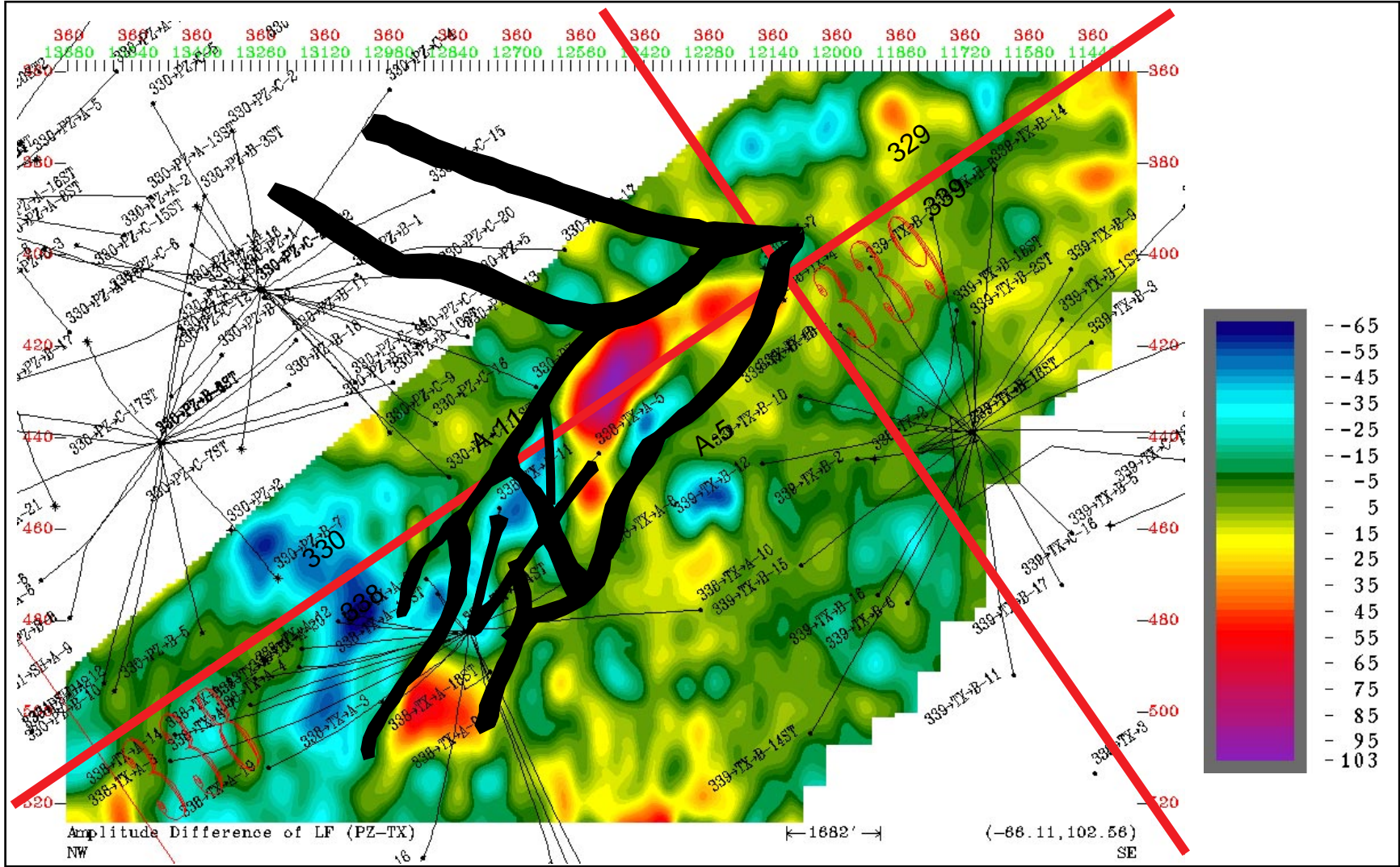
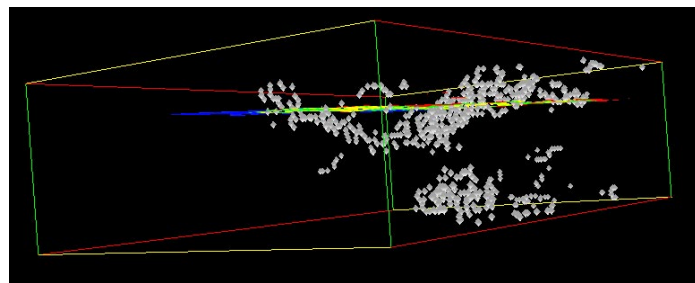


Figure 1.ii.14.c: The differences between the LF seismic troughs from 1985 to 1988 (hot colors are decreased, dimmed-out amplitudes). Note the boundary between the western and eastern fault blocks is discernible as the A Fault of Figure 1.ii.3.





PERSPECTIVE VIEW
FROM THIS DIRECTION

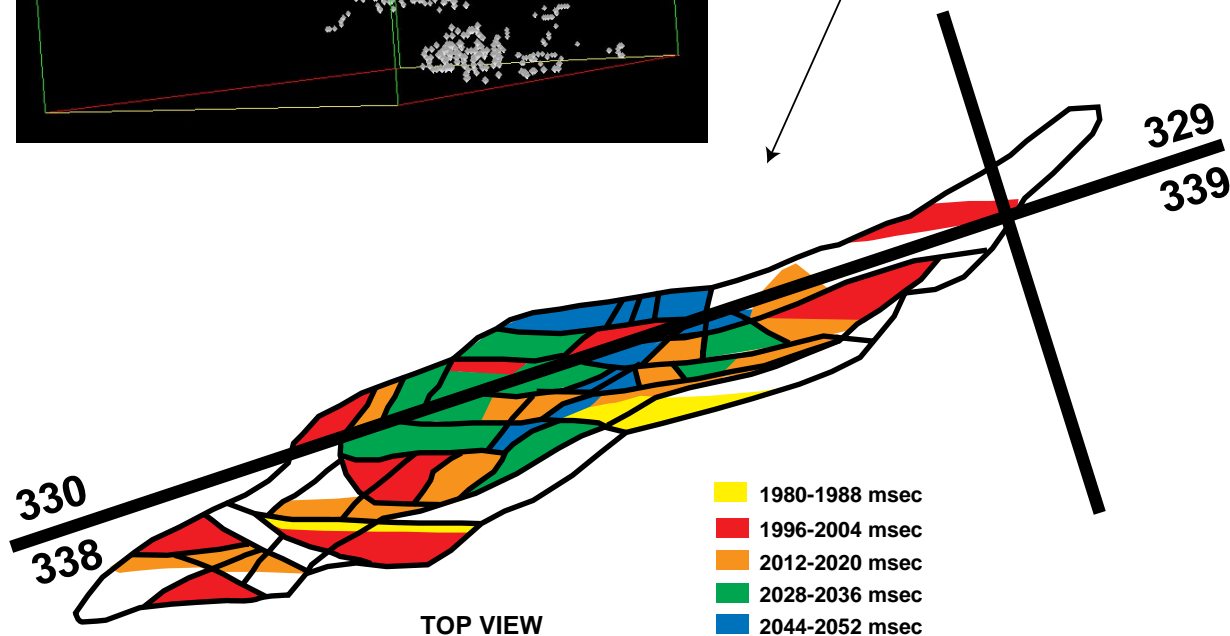


Figure I.ii.15: Permeability pattern in LF sand from connecting high-amplitude voxels, with no change between the 1985 and 1988 surveys (bypassed pay - the yellow region of Figure I.ii.12).

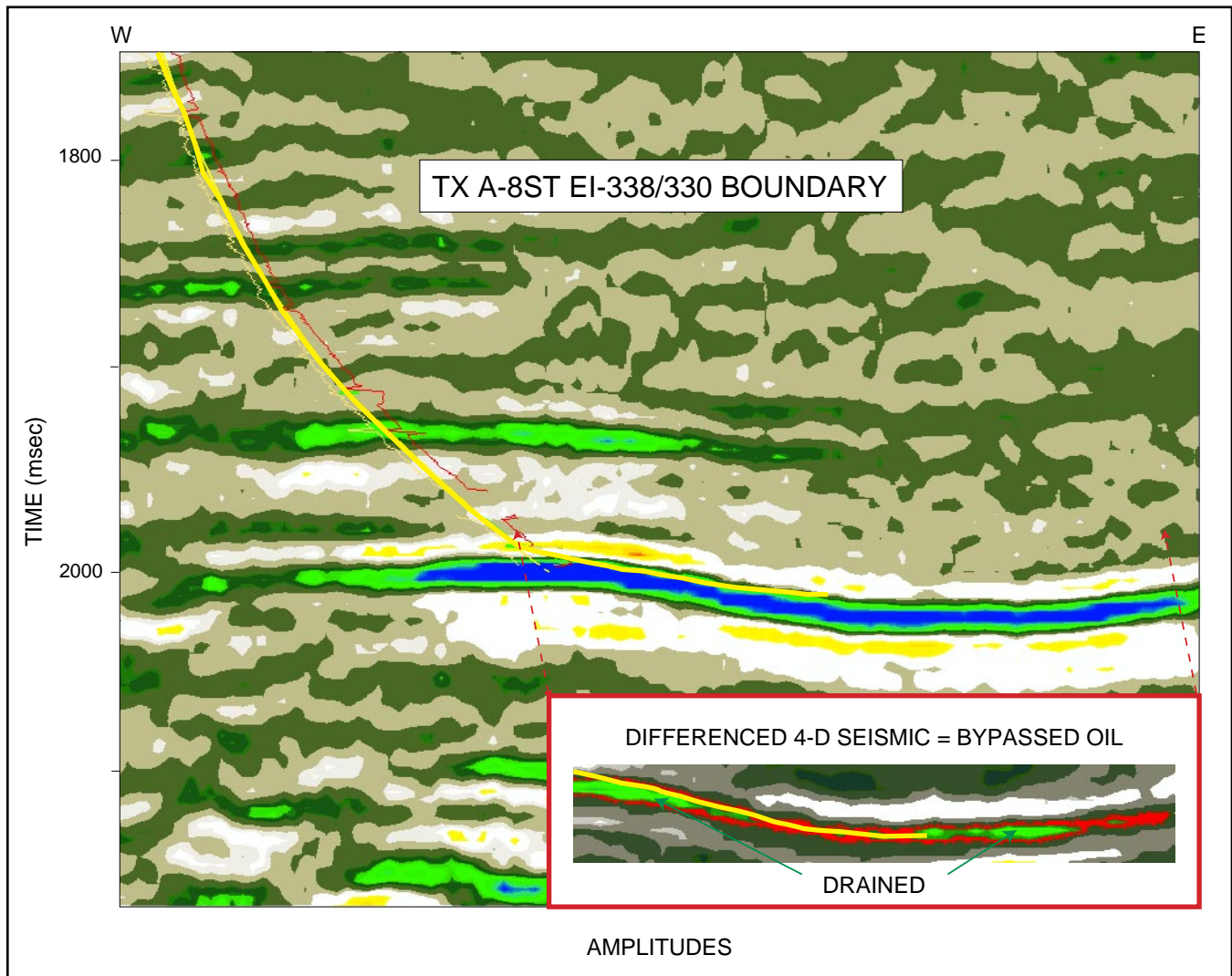


Figure I.ii.16: WE seismic profile through the property boundary of EI 330/338 showing LF sand reservoir, and a blowup of the similarities and differences between seismic amplitudes from 1985 to 1988 (similar = red, dimmed out = green). The A-8ST horizontal well targeted bypassed pay, indicated by the red.

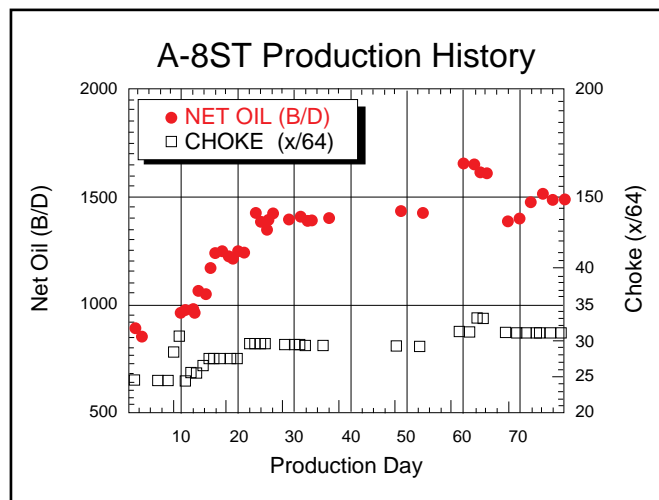


Figure I.ii.17: The production history of the A-8ST horizontal well.

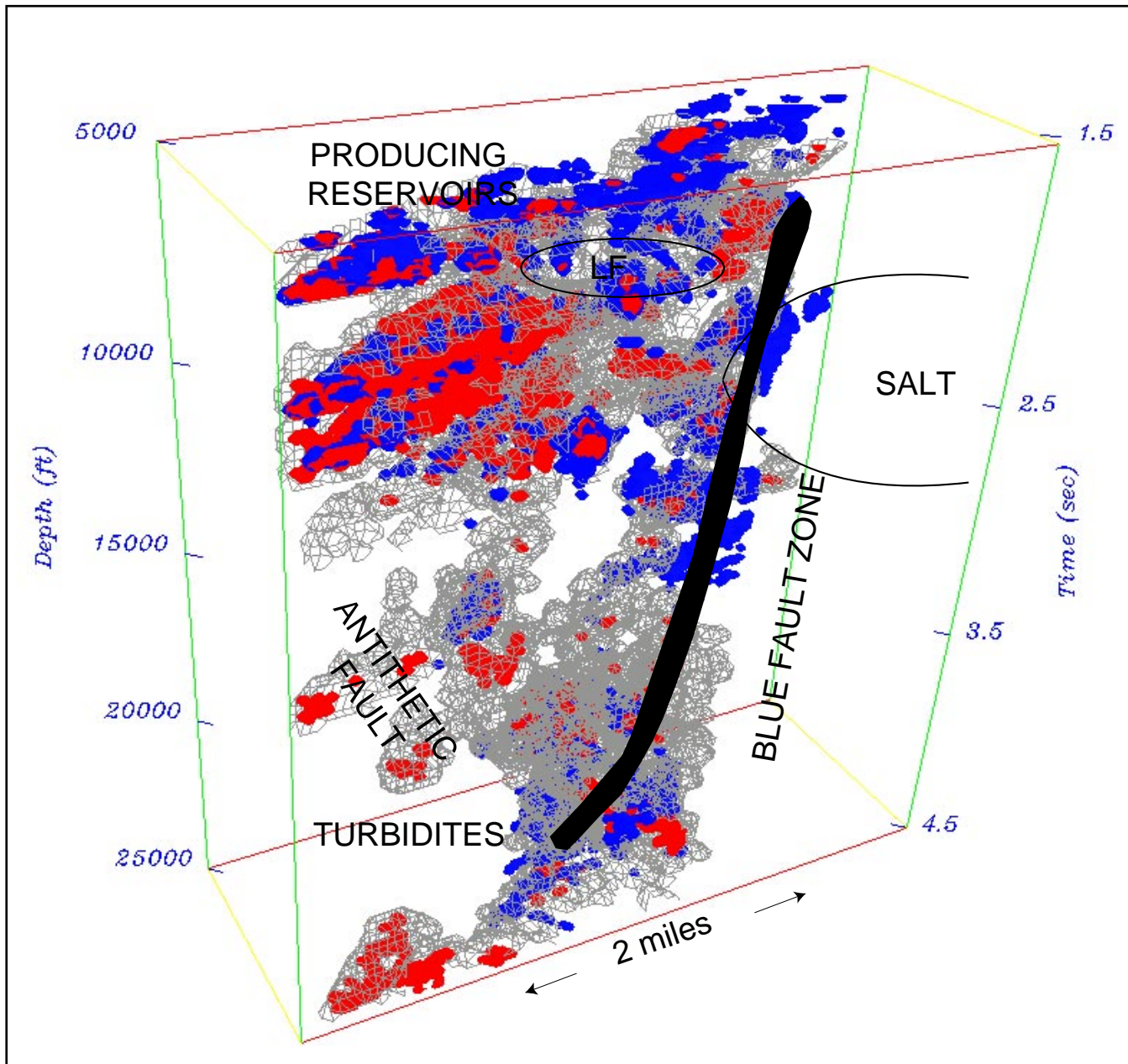


Figure I.ii.18: The gray mesh is the connectivity between the deep turbidites and the LF and shallower reservoirs, indicated by high-amplitude region tracking. Red = Texaco (1988) survey, Blue = Pennzoil (1985) survey.

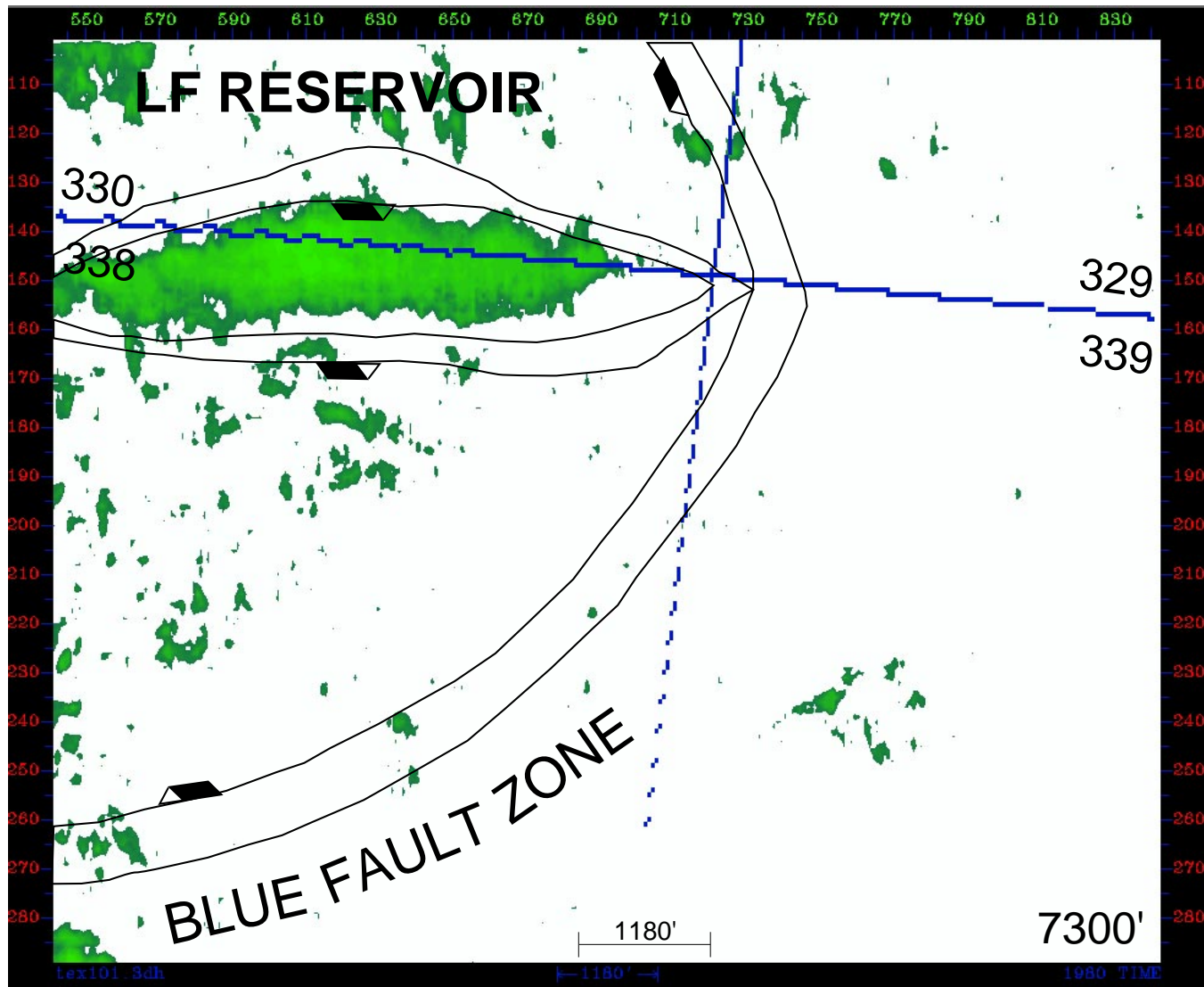


Figure I.ii.19.a: The connectivity in seismic amplitudes indicated by the white mesh in the previous figure can be illustrated by time slices through the seismic volume at 15,000', 8000' and 7300', with high amplitudes indicated in green. Note that the amplitude trail switches from the Blue Fault Zone at depth to the antithetic fault at 8000', which delivers the hydrocarbons to the LF and shallower reservoirs.

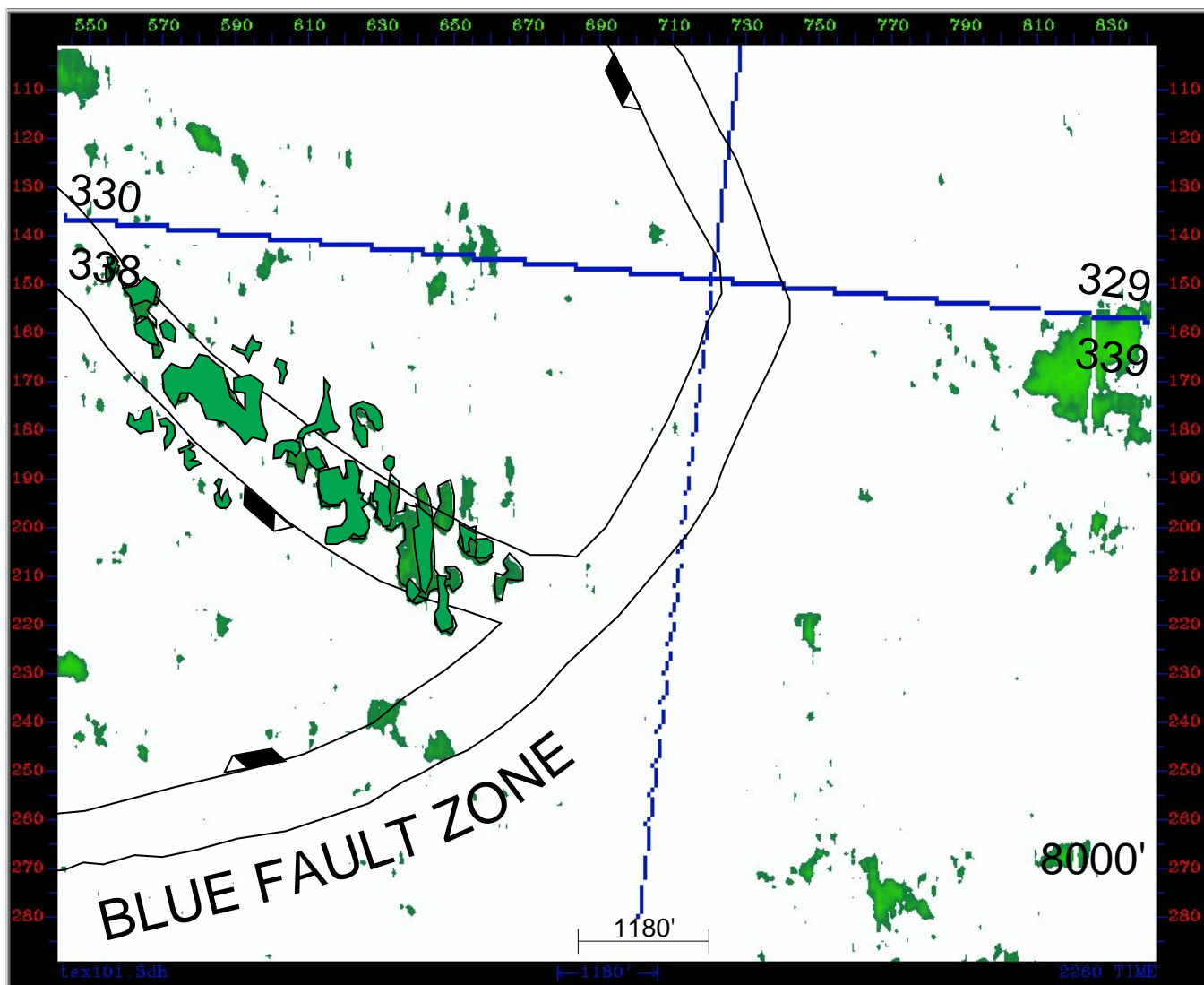


Figure I.ii.19.b (continued): The connectivity in seismic amplitudes indicated by the white mesh in the previous figure can be illustrated by time slices through the seismic volume at 15,000', 8000' and 7300', with high amplitudes indicated in green. Note that the amplitude trail switches from the Blue antithetic fault at depth to the antithetic fault at 8000', which delivers the hydrocarbons to the LF and shallower reservoirs.

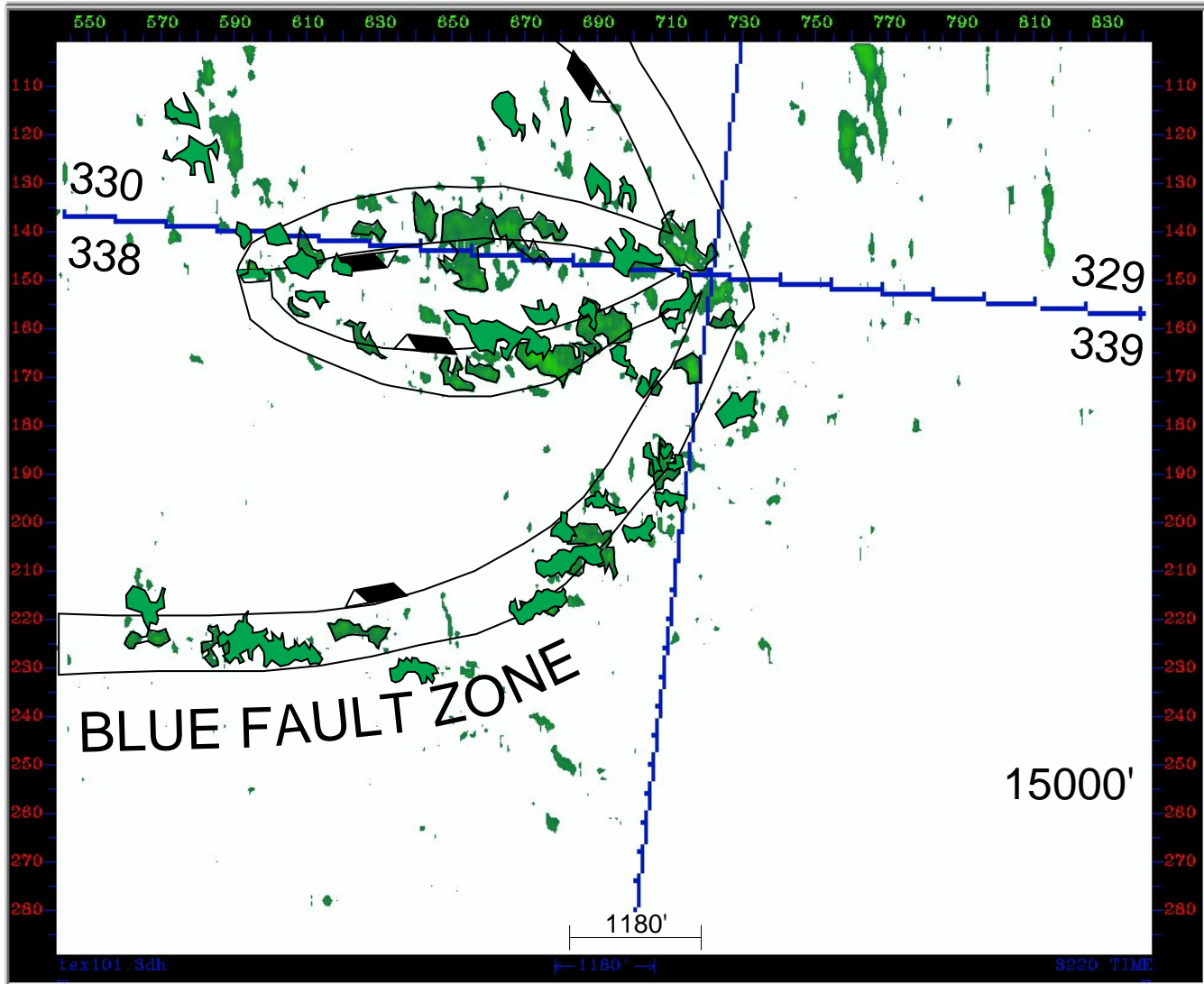


Figure 1.ii.19.c (continued): The connectivity in seismic amplitudes indicated by the white mesh in the previous figure can be illustrated by time slices through the seismic volume at 15,000', 8000' and 7300', with high amplitudes indicated in green. Note that the amplitude trail switches from the Blue antithetic fault at depth to the antithetic fault at 8000', which delivers the hydrocarbons to the LF and shallower reservoirs.

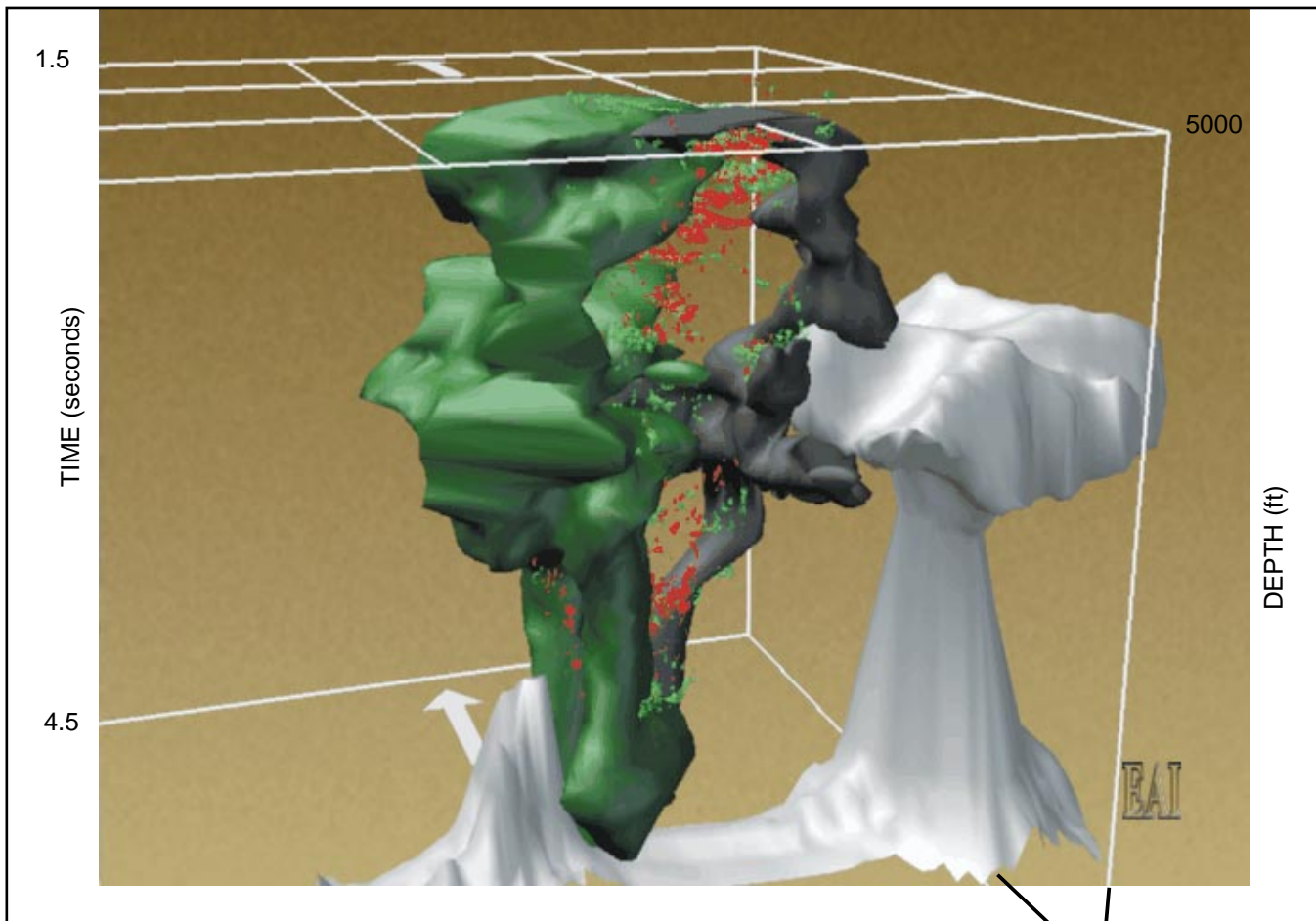


Figure 1.ii.20: The migration pathway in 3-D as indicated by connectivity of seismic amplitudes. The large green and charcoal or dark gray columns are the two separate migration pathways that are discernible in the seismic data indicated by red (1988 Texaco) and green (1985 Pennzoil) surveys. White is salt.

Variations Caused by Dilatancy,” *Ph.D. Dissertation*, Columbia University (1994).

Teng, Y.C. “Scattering of Transient Waves by Finite Cracks in an Anti-plane Strain Elastic Solid,” *Journal of Computational Acoustics*, Vol. 1, No. 1, pp. 101-116 (1993).

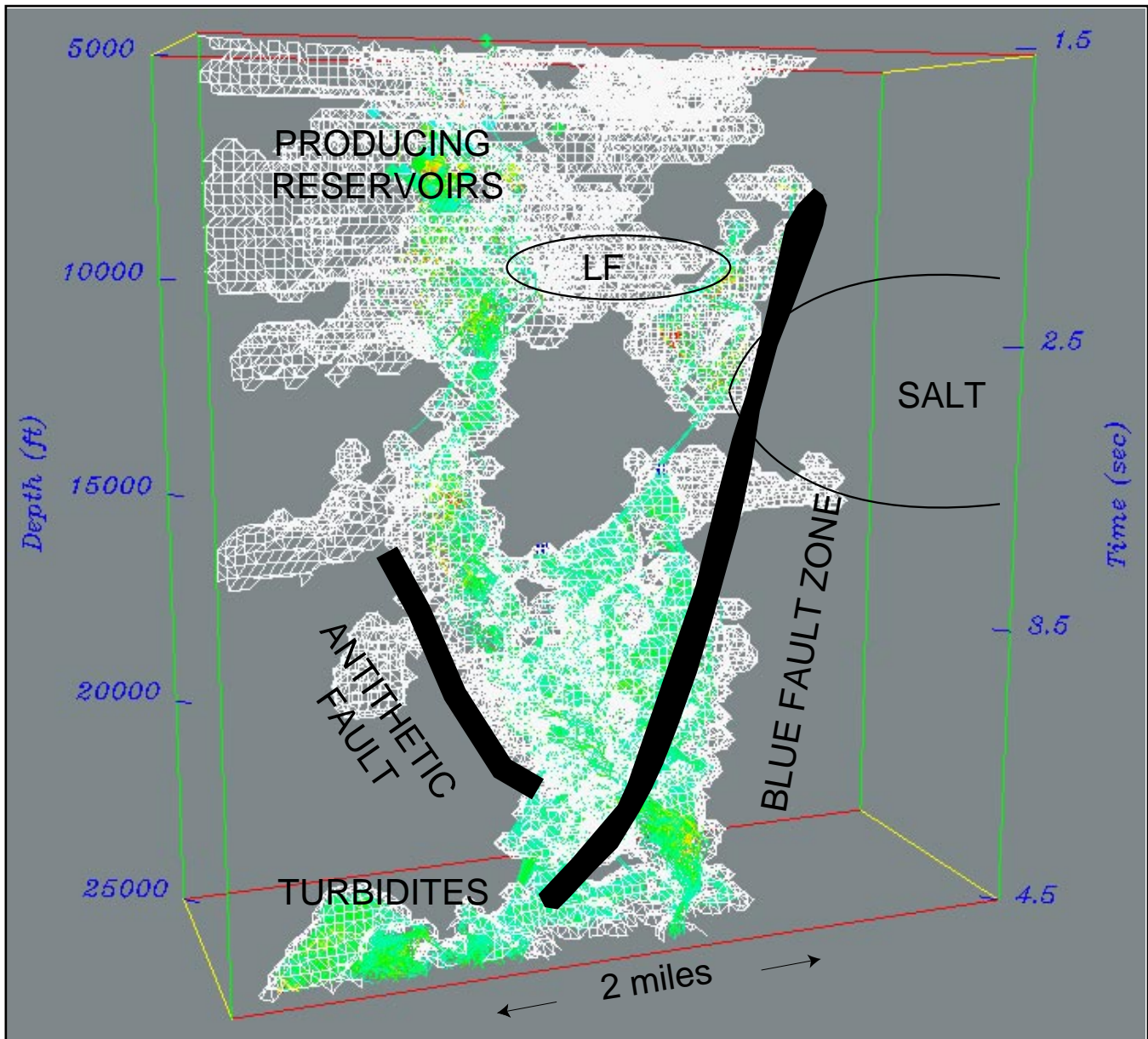


Figure I.ii.21: Buoyant balls convey the migration pathway through the high-amplitude, interconnected pathways identified within the seismic surveys.

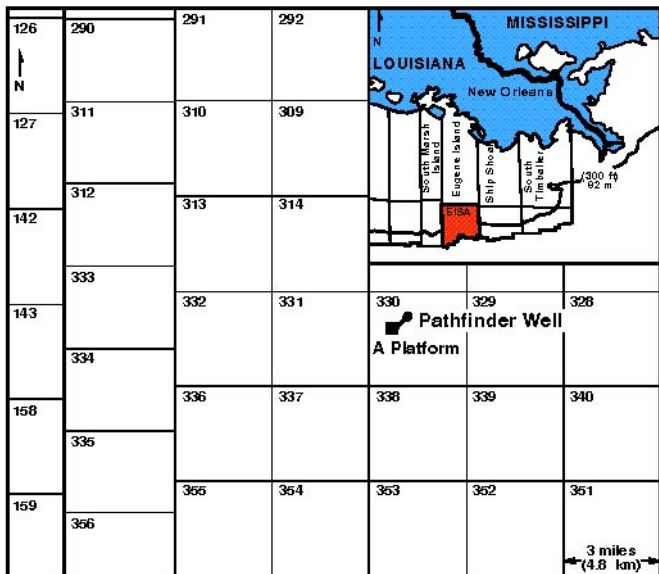


Figure I.iii.1: Basemap showing Eugene Island South Addition and location of the 330-A platform.

Map View of A-20ST2

Eugene Island Area, Offshore Louisiana

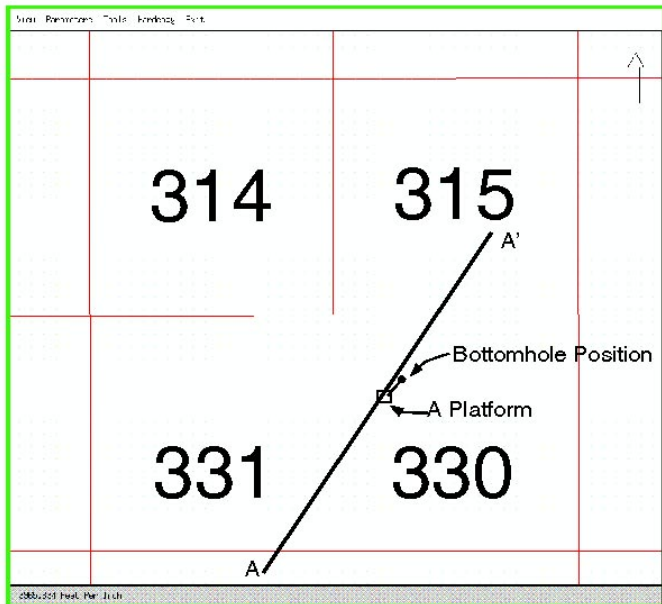


Figure I.iii.2: Expanded view of basemap, showing Pathfinder borehole path and the location of seismic line A-A'.

SW A _____ A' **NE**

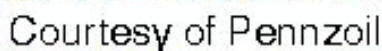


Figure I.iii.3: Seismic dipline (A-A') with Pathfinder well path, showing locations of interpreted sand tops and faults.

Time Slice at 2000 ms

NW

SE

Courtesy of Pennzoil

A Fault

**A-20ST2
(2000 ms)**

B Fault

A platform

1500 feet

Figure I.iii.4: Seismic time slice taken at 2000 ms showing 330-A platform, Pathfinder well path and interpreted faults.

Pathfinder: Deviated Well Path

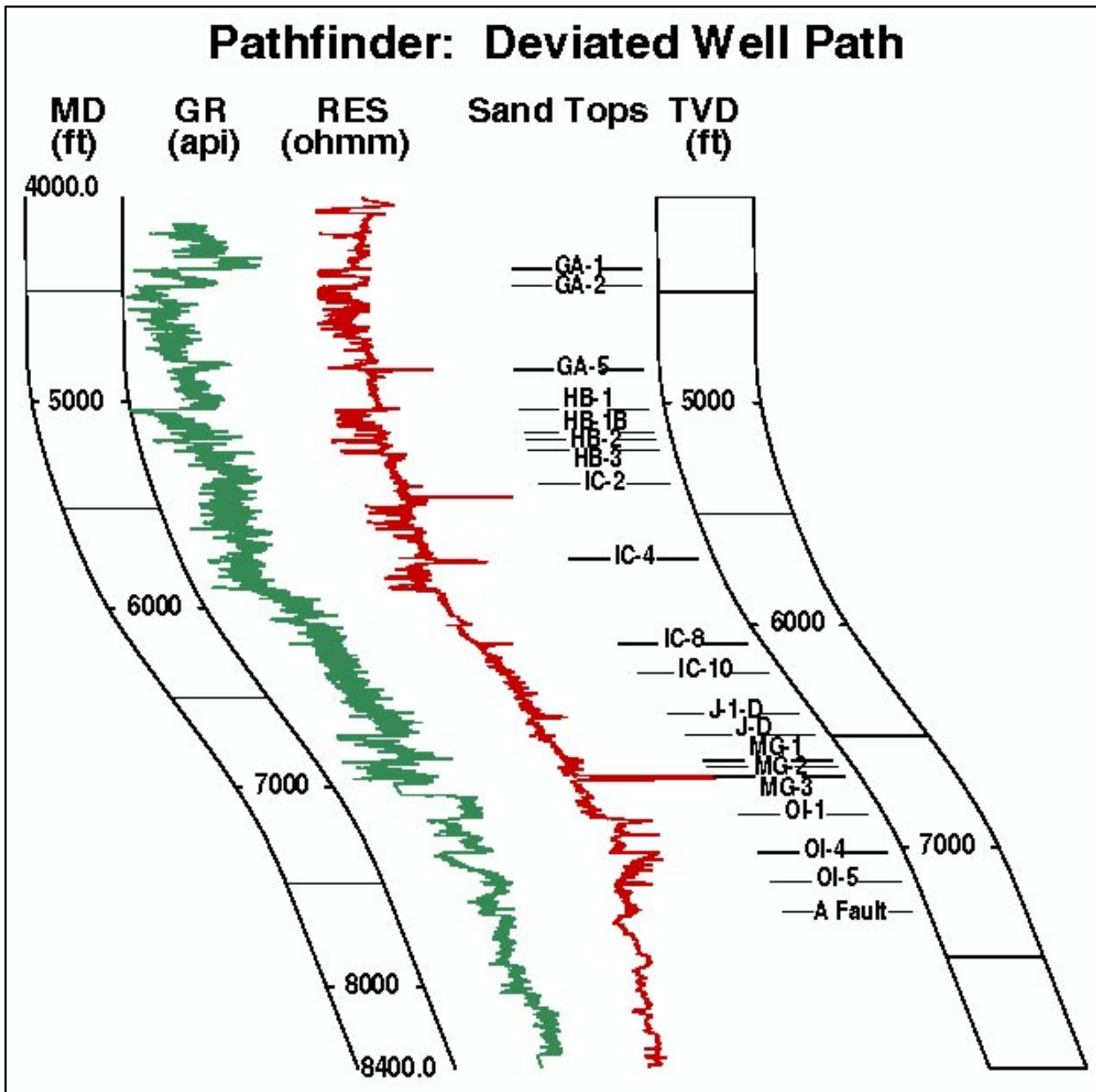


Figure I.iii.5: Deviated well display showing gamma ray, resistivity and sand tops. Reference is True Vertical Depth.

Pathfinder Well

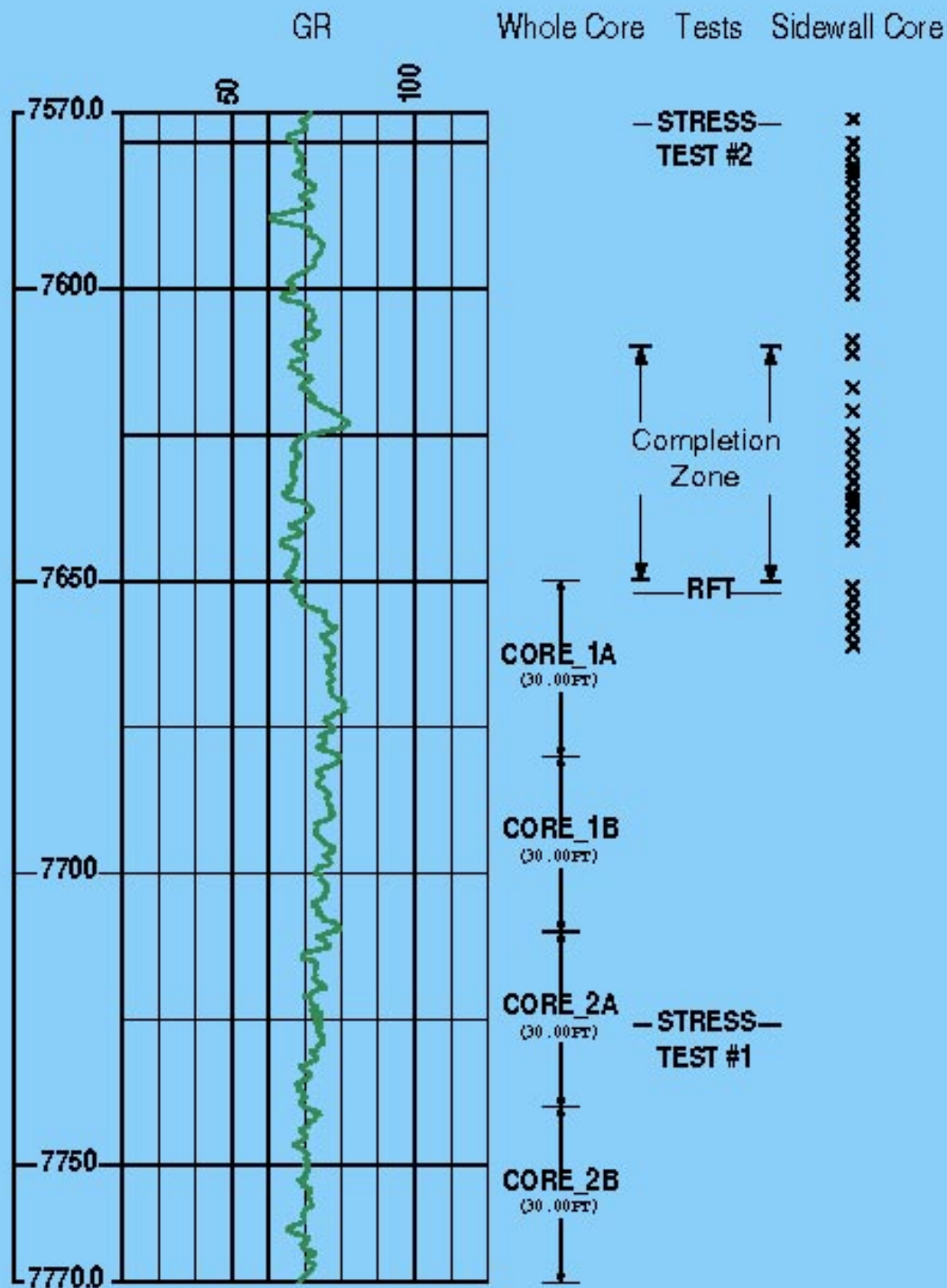


Figure I.iii.6: Type well expanded view of the fault zone showing experiment locations.

Pathfinder Well

Seismic Fault Prediction vs. Actual Location

S

N

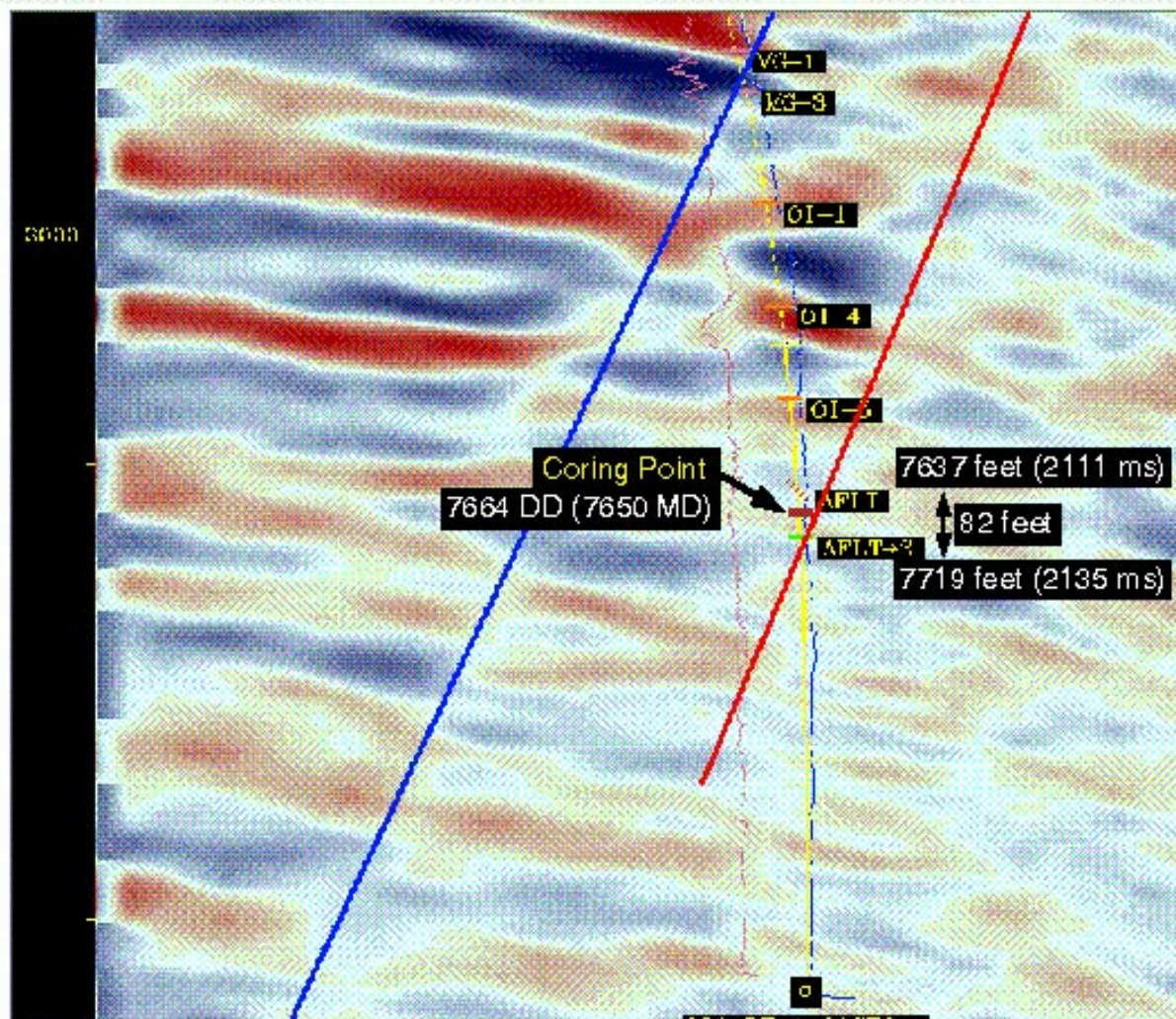


Figure 1.iii.7: Expanded view of the seismic dipline showing the A Fault as it was interpreted on the seismic profile and where it was actually encountered.

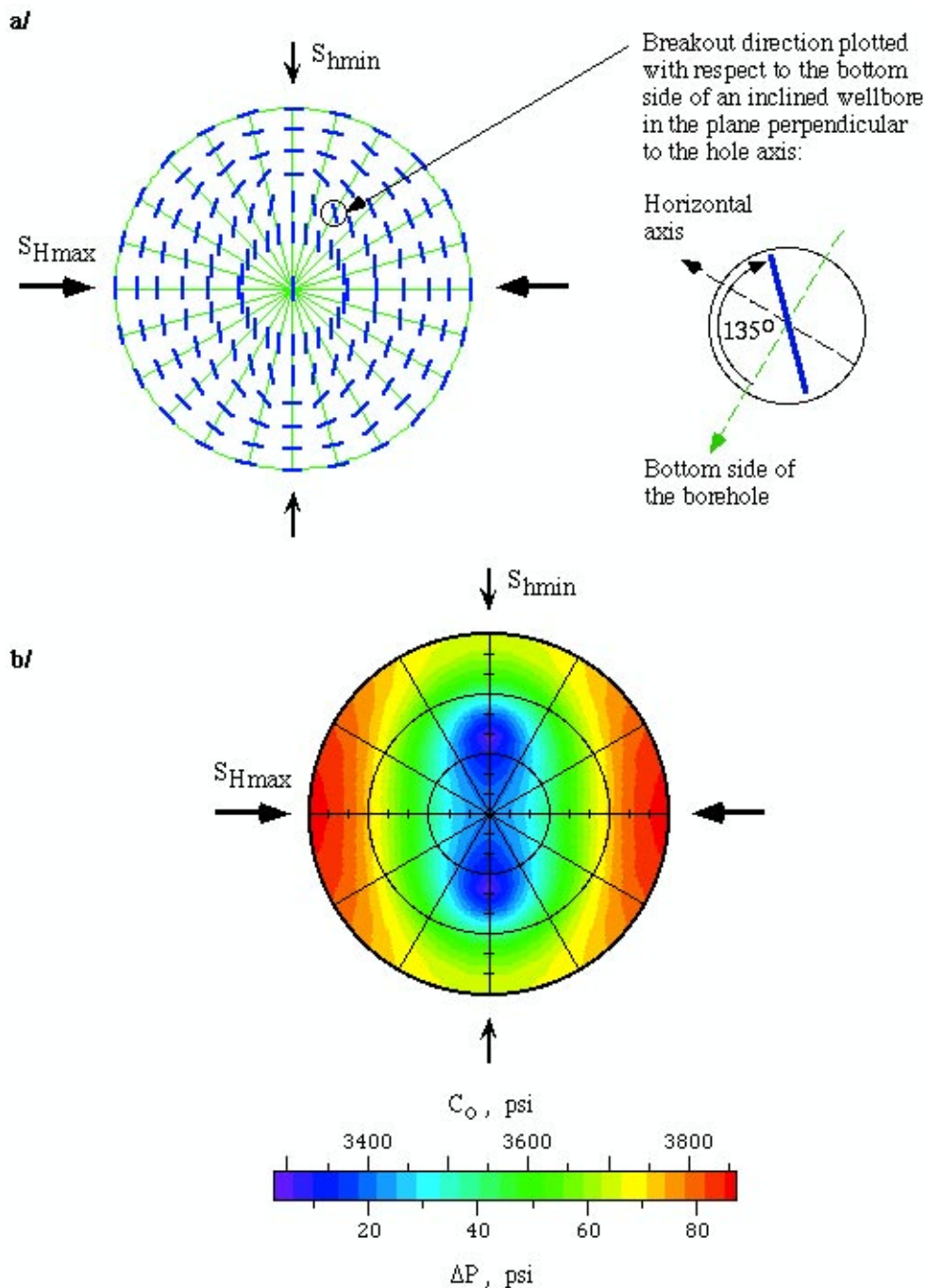


Figure IV.ii.1: Illustration of breakout directions (a) and tendency for failure (b) in boreholes of arbitrary orientations with respect to the horizontal principal stresses. The tendency for failure is expressed as a function of effective rock strength, C_0 , or differential borehole fluid pressure, ΔP , necessary to prevent borehole failure. In this illustration, the coefficient of internal friction, μ_v was assumed to be 1.0 and the magnitudes of in-situ stress and pore pressure are $S_v=6528$ psi, $S_{Hmin}=6226$ psi, $S_{Hmax}=6377$ psi and $P_p=4749$ psi. The detailed illustration in the upper right indicates that breakout orientations are shown with respect to the bottom of the hole. In other words, the orientations of breakouts are shown as if the reader is looking "down the hole."

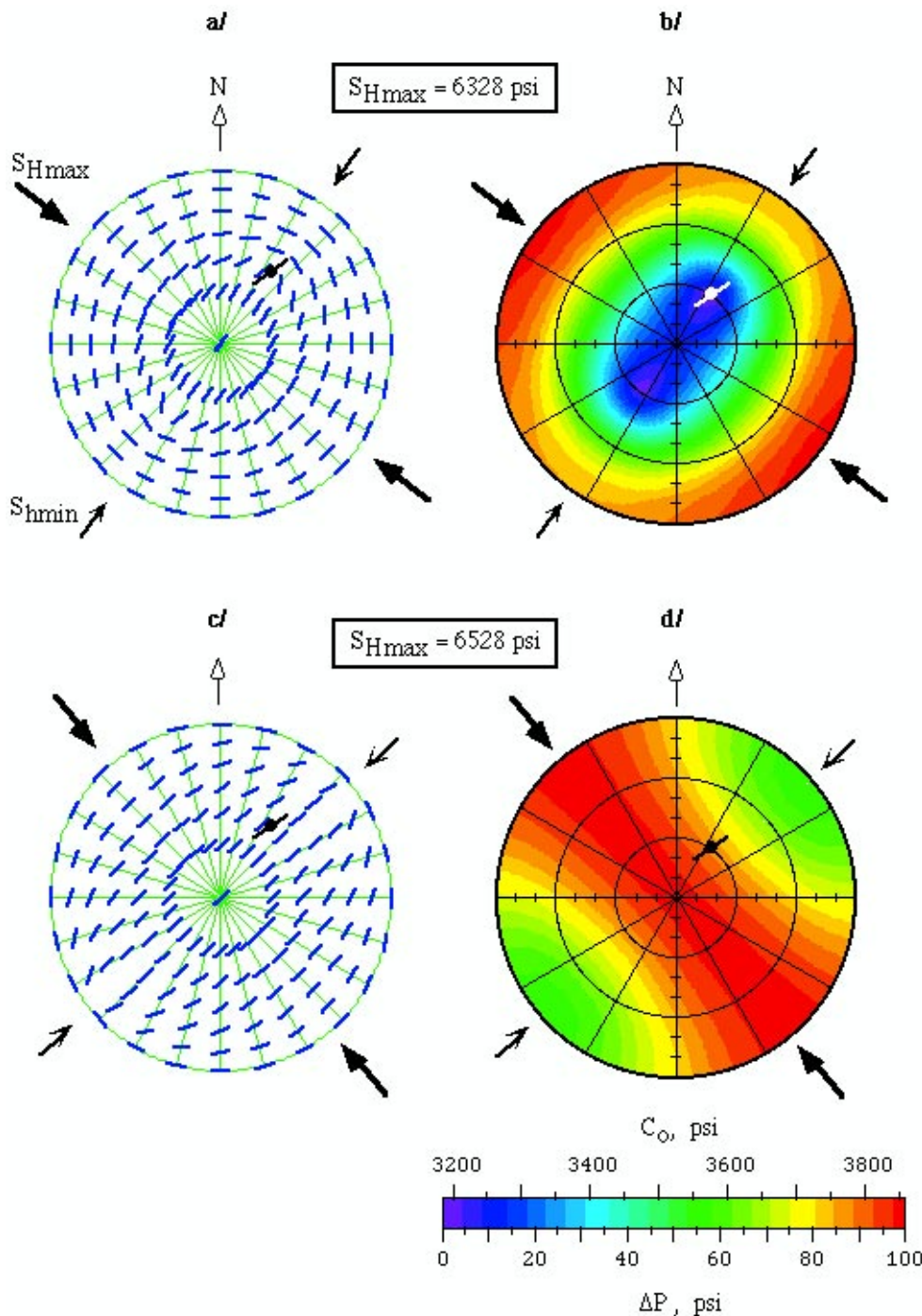


Figure IV.ii.2: Breakout orientations and the likelihood to occur in arbitrarily oriented wellbores for the orientation and upper-bound magnitude of S_{Hmax} of 6328 psi (a,b) and the orientation and lower-bound magnitude of 6528 psi (c,d). The other principal stresses and pore pressure are $S_{hmin}=6226$ psi, $S_v=6528$ psi and $P_p=4749$ psi. The tendency for failure is expressed in color either as a function of necessary uniaxial rock strength C_0 (for $\Delta P=0$) or as a function of ΔP (for $C_0=3180$ psi) which is necessary to avoid borehole failure.

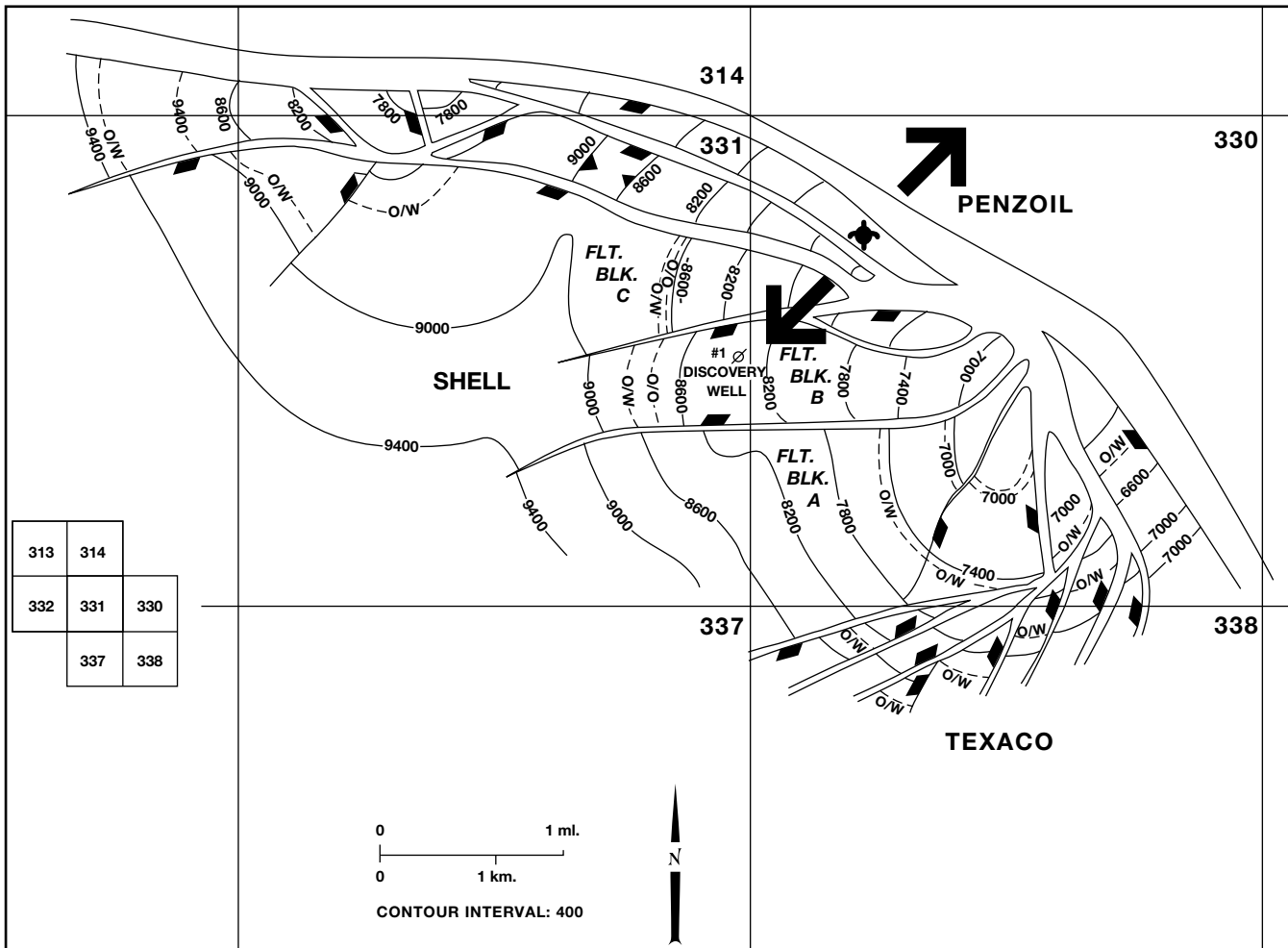
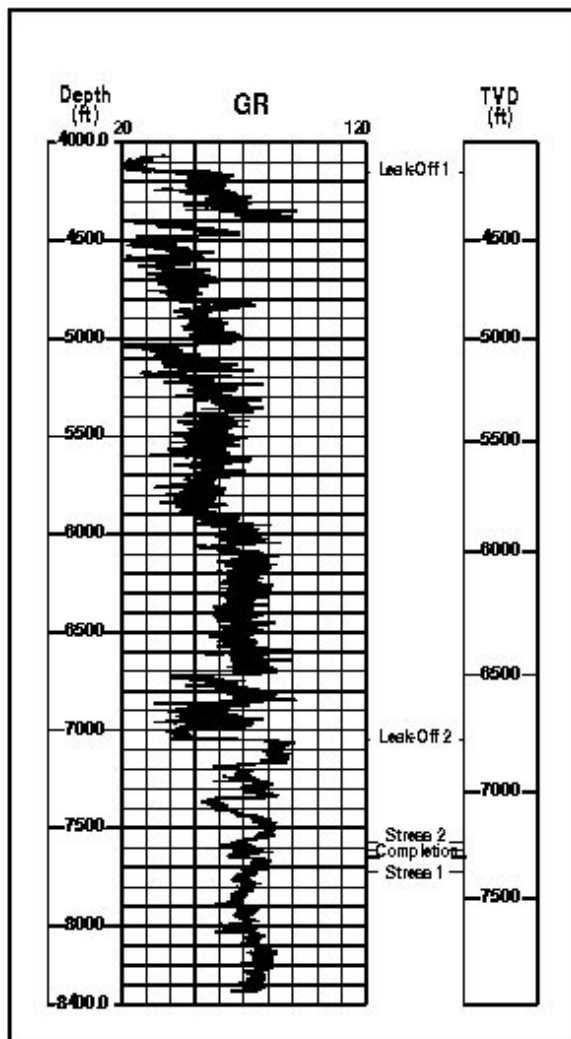


Figure IV.ii.3: Top OI sandstone structure map (after Holland et al.³²) and direction of the least horizontal principal stress S_{hmin} obtained from the analysis of leak-off data and wellbore breakouts in the Pathfinder well.

a)



b)

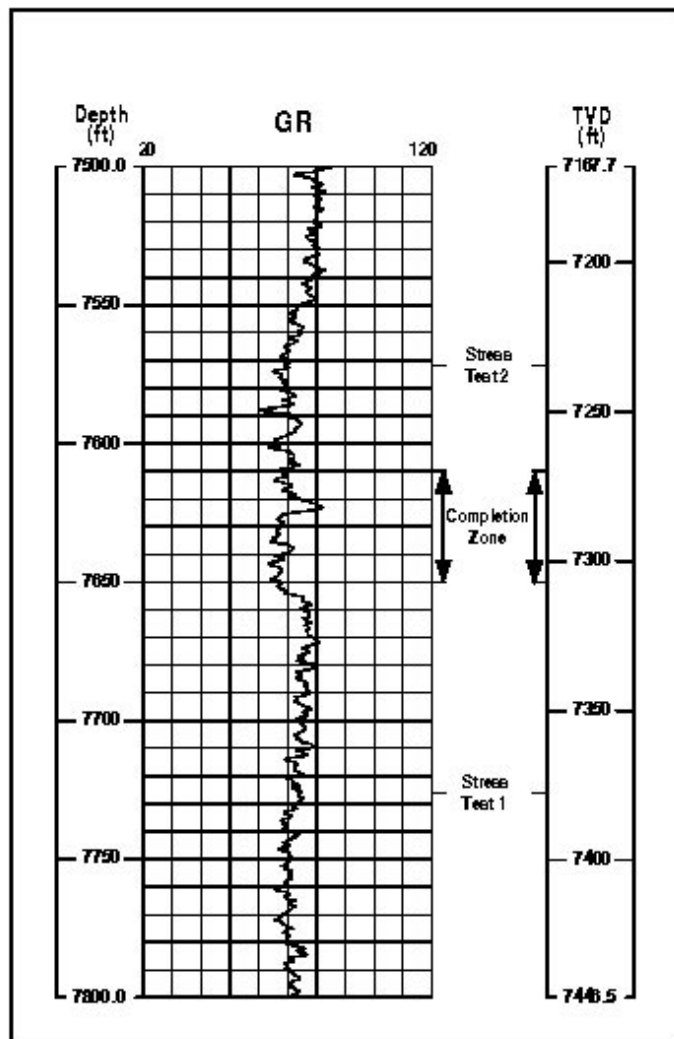


Figure IV.iii.1: Location of Pathfinder stress measurements. Measured depth in feet is on the left; true vertical depth (TVD) is on the right. **Figure IV.iii.1.a:** Entire interval. **Figure IV.iii.1.b:** Completion Zone interval.

Pathfinder Well
borehole path

Leak-off 1

$K = 0.6$
 $P = 0.5 S_v$
 $S_{hmin} - P = 1137$

$K = 1.0$
 $P = 0.7 S_v$
 $S_{hmin} - P = 1777$

Leak-off 2

Buoyant Pressure
due to gas column
in nearby sands = ~500 psi

$k = 0.9$
 $P = 0.9 S_v$
 $S_{hmin} - P = 644$

Stress Test 2

Completion

$k = 0.6$
 $P = 0.9 S_v$
 $S_{hmin} - P = 376$

Stress Test 1

$k = 0.8$
 $P = 0.9 S_v$
 $S_{hmin} - P = 515$

Fault

Figure IV.iii.19: Sketch of in-situ conditions in the Pathfinder well. K is the ratio of effective stresses ($S_{hmin} - P / S_v - P$); P is the formation pressure.